# Stony Brook University

**The official electronic file of this thesis or dissertation is maintained by the University Libraries on behalf of The Graduate School at Stony Brook University.**

# Searching for Dark Sectors

A Dissertation presented

by

**Yi-Ming Zhong**

to

The Graduate School

in Partial Fulfillment of the

Requirements

for the Degree of

**Doctor of Philosophy**

in

**Physics**

Stony Brook University

**August 2016**

**Stony Brook University**

The Graduate School

Yi-Ming Zhong

We, the dissertation committee for the above candidate for the

Doctor of Philosophy degree, hereby recommend

acceptance of this dissertation

**Rouven Essig**
**Assistant Professor, Department of Physics and Astronomy**

**John Hobbs**
**Professor, Department of Physics and Astronomy**

**Patrick Meade**
**Associate Professor, Department of Physics and Astronomy**

**Hooman Davoudiasl**
**Physicist, Department of Physics, Brookhaven National Laboratory**

This dissertation is accepted by the Graduate School

Charles Taber
Dean of the Graduate School

Abstract of the Dissertation

**Searching for Dark Sectors**

by

**Yi-Ming Zhong**

**Doctor of Philosophy**

in

**Physics**

Stony Brook University

**2016**

The existence of Dark Matter suggests the presence of a dark sector, consisting of particles neutral under all Standard Model forces. Various "portals" can connect the dark sector to the Standard Model sector. Two popular examples are the vector portal, which gives rise to a "dark photon" ($A'$), and the Higgs portal, which gives rise to a "dark Higgs". Such dark forces appear in many well-motivated extensions of the Standard Model. In some cases, they may resolve discrepancies between experimental data and theoretical predictions, such as the muon anomalous magnetic moment. We show that dark sectors and forces can be constrained from several novel probes in current and future experiments, including mono-photon searches in low-energy positron-electron colliders, rare muon decays in the Mu3e, and exotic Higgs decays at the Large Hadron Collider (LHC).

We first investigate the power of low-energy, high-luminosity electron–positron colliders to probe dark sectors with a mass below $\sim 10$ GeV, which couple to Standard Model particles through a low-mass dark mediator. Dark matter candidates in this mass range are well-motivated and can give rise to distinctive mono-photon signals at $B$-factories and similar experiments. We use data from an existing mono-photon search by *BABAR* to place new constraints on this class of models, and give projections for the sensitivity of a similar search at a future $B$-factory such as Belle II. We find that the sensitivity of such searches are more

powerful than searches at other collider or fixed-target facilities for dark-sector mediators and particles with masses between a few hundred MeV and 10 GeV. We compare our results to existing and future direct detection experiments and show that low-energy colliders provide an indispensable and complementary avenue to search for light dark matter.

We also find that dark photons with masses $\sim$ 10 MeV–80 MeV can probed in the rare muon decay process $\mu^+ \to e^+ \nu_e \bar{\nu}_\mu A'$, $A' \to e^+ e^-$, in the upcoming Mu3e experiment at the Paul Scherrer Institute without modifying the experimental set-up. We show that the Mu3e has an exciting opportunity to probe a large fraction of unexplored dark photon parameter space, probing kinetic-mixing parameter, $\epsilon$, as low as $10^{-4}$ by the end of the experiment.

The newly discovered 125 GeV Higgs boson is a scalar and has a small Standard Model decay width. Hence it can easily decay to light dark-sector particles with sizable branching ratios. We investigate several possible dark-sector searches at the LHC based on the exotic decays of the Higgs. We also analyze in detail a possible decay to $b\bar{b}\mu^+\mu^-$ via intermediate scalar states. We find the branching ratio of the exotic Higgs decay can be constrained at the few $\times 10^{-5}$ level across a wide range of mass for the intermediate scalars at the high luminosity LHC.

Finally, we show a possible dark-sector interpretation of the recently reported 750 GeV diphoton excess from the LHC 13 TeV Run, as the 750 GeV heavy resonance decaying to light dark photons or dark Higgs bosons. Such decays may pass the photon selection criteria and fake diphoton events. We investigate two scenarios where the 750 GeV heavy resonance is a spin-0 or spin-1 particle and estimate the parameters of the models to explain the existing excess.

*Dedicated to my parents.*

# Table of Contents

# List of Figures

# List of Tables

# Acknowledgements

I would like to first thank my advisor, Dr. Rouven Essig, for the opportunity he has granted to me to work on theoretical particle physics at C.N. Yang Institute for Theoretical Physics (YITP), for the sincere support on my academic career development, for many inspiring lectures, instructions, advices, and encouragements he has been delivering, and for the work and projects we together accomplished during these four years.

Also fundamental for me have been all my research collaborators: Chien-Yi Chen, David Curtin, Bertrand Echenard, Stefania Gori, Jin Huang, Prerit Jaiswal, Andrey Katz, Jun Koda, Ming-Xiong Liu, Tao Liu, Zhen Liu, Michel Lefebvre, Jeremy Mardon, Samuel McDermott, David McKeen, Patrick Meade, Michele Papucci, Maxim Pospelov, Harikrishnan Ramani, Paul Shapiro, Jessie Shelton, Matthew Strassler, Ze'ev Surujon, Brock Tweedie, Tomer Volansky, Qi-Shu Yan, Hai-Bo Yu, Xiaoran Zhao, and Zhijie Zhao. I would like to thank them sincerely. Besides I am grateful of all people who answered with patience a lot of my questions, whose help is curial for me to overcome obstacles.

A big thank to my Stony Brook professors. I have been benefited a lot from the lectures on various topics on physics and mathematics, especially from the lectures offered by Dr. Peter van Nieuwenhuizen and Dr. George Sterman. I also would like to thank George for his support of my career development. Special thanks to my PhD oral exam committee, which includes Dr. Alexander Abanov, Dr. Rouven Essig, Dr. John Hobbs, and Dr. Patrick Meade. I am grateful for their advices and encouragements. I appreciate very much of various seminars and conferences supported by the Department of Physics and Astronomy, Simons Center, and Brookhaven National Laboratory. I would like to thank Dr. Hooman Davoudiasl, Dr. Sally Dawson, and Dr. Amarjit Soni for offering me help to access BNL. I also thank ATLAS experimental group at Stony Brook, leaded by Dr. John Hobbs and Dr. Dmitri Tsybychev, for offering me valuable insights into LHC and enormous computational resource. I would like to thank people participating in the YITP lunch group. Also I would like to thank Simons Center for offering daily afternoon tea gathering, which is an excellent place to fertilize new ideas.

I also would like to thank my Stony Brook colleagues and fellows, who make my PhD

years much more colorful. Especially I would like to thank my office mates at Physics B120 and Math 6114: Kazue Matsuyama, Tyler Corbet, Qiang Deng, Andrea Massari, Jun Nian, Wolfger Peelaers, Yachao Qian, Pin-Ju Tien, Harikrishnan Ramani, Michael Spillane, Yihong Wang, Colin West, and Wanyu Ye. Besides, I would like to thank my friends outside of the Department of Physics and Astronomy, and my roommates at Chapin and Schomburg. I also thank Dr. Ning Chen and Dr. Wenbin Yan for bringing me to Stony Brook after my first arrival to US.

Moreover, I would like to extend my thanks to people at Perimeter Institute for Theoretical Physics, where I started my theoretical physics study as a master student. I would like to thank my classmates, tutors and lecturers of the Perimeter Scholars International program. In particular, I would like to thank my master advisor, Dr. David Skinner, for guiding my final project and for his later support during my PhD years.

I would like to further extend my thanks to Dr. Stephen Hawking, who visited China fourteen years ago and delivered a public lecture on holographic principle and M-theory. A teenage, watching the live broadcast, was deeply attracted by the machine voice he could not comprehensive and decided to take physics courses seriously from that day on.

Finally, I would like to thank my whole family: my mom, my dad and my grandpa. Thanks to your sacrifices and willingness I have been given the possibility to undertake this exciting adventure, from Tianjin to Waterloo then to Stony Brook. I would be always grateful to you.

# List of Publications

This thesis is based on the following original publications in refereed journals:

1. R. Essig, J. Mardon, M. Papucci, T. Volansky and YZ, JHEP **1311**, 167 (2013) doi:10.1007/JHEP11(2013)167 [arXiv:1309.5084 [hep-ph]].

2. D. Curtin *et al.*, Phys. Rev. D **90**, no. 7, 075004 (2014) doi:10.1103/PhysRevD.90.075004 [arXiv:1312.4992 [hep-ph]].

3. B. Echenard, R. Essig and YZ, JHEP **1501**, 113 (2015) doi:10.1007/JHEP01(2015)113 [arXiv:1411.1770 [hep-ph]].

4. D. Curtin, R. Essig and YZ, JHEP **1506**, 025 (2015) doi:10.1007/JHEP06(2015)025 [arXiv:1412.4779 [hep-ph]].

5. C. Y. Chen, M. Lefebvre, M. Pospelov and Y. M. Zhong, JHEP **1607**, 063 (2016) doi:10.1007/JHEP07(2016)063 [arXiv:1603.01256 [hep-ph]].

Following publication in refereed journal that is not included in the thesis:

1. C. Y. Chen, Q. S. Yan, X. Zhao, Z. Zhao and YZ, Phys. Rev. D **93**, no. 1, 013007 (2016) doi:10.1103/PhysRevD.93.013007 [arXiv:1510.04013 [hep-ph]].

Following publications in preparation that are not included in the thesis:

1. R. Essig, P. Meade, H. Ramani, and YZ, *Higgs Precision Constraints on Colored Naturalness.*

2. R. Essig, J. Koda, S. McDermott, P. Shapiro and YZ, *Gravothermal Evolution of Galactic Dark Matter Halos with Velocity Dependent Self-Interactions.*

3. R. Essig, D. McKeen, and YZ, *Constraining Light Dark Matter from Cosmological Small Scale Structures.*

4. C. Y. Chen, M. Pospelov, and YZ, *Dark Sector Searches via Muon Beam-Dump Experiments.*

# Chapter 1

# Introduction

## 1.1 The Standard Model of Particle Physics and Its Challenges

The Standard Model (SM) of particle physics is one of the greatest triumphs of 20th century physics. One central idea underlying the development of the Standard Model of particle physics is the principle of local symmetry.

### 1.1.1 Local Symmetry and the Standard Model

The marriage between particle physics and the powerful tool of local symmetry starts in the early 20th century. Hermann Weyl, motivated by unifying general relativity and electromagnetism, first introduced the notion of a $U(1)$ gauge field, $A_\mu$, in 1918 [1]. Since then, particle physicists gradually embedded local symmetries into our understandings of the strong, weak, and electromagnetic forces.[1] Important steps along the way includes Yang-Mills theory of $SU(2)$ interactions, Glashow-Weinberg-Salam $SU(2) \times U(1)$ theory of weak interactions, Nambu-Goldstone spontaneous symmetry breaking mechanism, Brout-Englert-Higgs mechanism, 't Hooft-Veltman's proof of the renormalizability of $SU(2) \times U(1)$ theory, Gell-Mann-Zweig $SU(3)$ theory of quarks, and Gross-Wilczek-Politzer $SU(3)$ theory of the strong interactions. Based on the above theoretical breakthroughs as well as experimental discoveries, by 1975 we realized the SM is essentially defined by the gauge symmetry group $SU(3)_c \times SU(2)_L \times U(1)_Y$, where $SU(2)_L \times U(1)_Y$ breaks into $U(1)_{\mathrm{EM}}$ below the electro-

---

[1]However, as another prespect about the gauge theory, many theoretical physicists have been unsatisfied with the redundancy in the gauge field and developed new formalism for quantum field theory. See *e.g.* [2] and [3].

weak scale. The theory predicts the existence of the $W$, $Z$, and Higgs bosons, which are later confirmed by CERN in 1981 and 2012.

## 1.1.2 Challenges to the Standard Model

By the mid of 1970s, the Standard Model of particle physics was mature and experimental supporting evidence kept accumulating. However, we are sure that the Standard Model of particle physics is not the end of the story. One clear piece of evidence is the discovery of neutrino oscillations. It indicates that at least two out of three SM neutrinos are massive, which contradicts the SM assumptions. Another piece of evidence is from the discovery of the dark matter from rotation curve measurements in 1970s. It suggests that a large portion of the matter in the universe is not explained the SM. Besides above problems, the SM also fails the expectations from many theorists. The model has not yet achieved the unification of the gauge symmetries, it does not explain why particles are ordered by $SU(3)_c \times SU(2)_L \times U(1)_Y$ structure. The description of its matter sector is disjointed from the one of its gauge sector. The model fails to answer the Higgs hierarchy problem as well as the origin of baryon asymmetry in the universe. Nowadays, we view the Standard Model as an effective theory, rather than a fundamental description of nature up to the Planck scale.

In this section, we will briefly discuss challenges to the SM mentioned above, but leave particle dark matter to a more detailed discussion to the next section.

1. **Grand Unification**: The SM unifies the electromagnetic force and weak force into a single electro-weak force. But it leaves the strong force untouched. Therefore, it is natural to ask if there is a single group structure that unifies the strong and electro-weak forces at a high energy scale, and if there is a single group structure that unifies the matter and force content of the SM.

2. **The Higgs Mass Hierarchy**: Quantum gravity suggests that the new physics exists at the Planck scale, $M_{\rm p} \sim 10^{19}$ GeV, which is about $\sim 10^{16}$ times greater than the electro-weak scale. The Planck scale appears in the loop corrections of the Higgs mass and makes its measured value, 125 GeV, extremely fine tuned. The unreasonable UV sensitivity of the Higgs mass is denoted as the "Higgs hierarchy problem" or the "gauge hierarchy problem".

3. **The Strong CP Problem**: Quantum Chromodynamics (QCD) allows the CP-violating terms $\theta G_{\mu\nu} \tilde{G}^{\mu\nu}$, where $G^a_{\mu\nu}$ is the $SU(3)$ field strength, and the coefficient is the so-called $\theta$-angle. In principle, the $\theta$-angle can be any value ranging from $-\pi$ to

$+\pi$. However, neutron electric dipole measurements indicate that $|\theta| < 10^{-10} - 10^{-11}$. Why $|\theta|$ is so small is called the "strong CP problem".

4. **Baryogenesis**: The Universe today exhibits a large imbalance between matter and anti-matter, which is not guaranteed from the underlying quantum field theory, unless a baryogenesis process satisfies the Sakharov conditions: baryon number violation, C and CP violation, and interactions out of thermal equilibrium. The SM is equipped with CP violation in its weak interactions. However, it may be not large enough to account for the large asymmetry.

5. **Neutrino Mass**: The SM assumes the neutrinos are left-handed particles with no mass. However, the experimental evidence of neutrino oscillation (see review *e.g.* [4]) suggests at least two out of three neutrinos are massive. Questions about the neutrino masses requires new physics beyond the SM, include whether the mass is Dirac or Majorana and the origin of their tiny values compared to other SM fermions.

6. **The Cosmological Constant Hierarchy**: Observations of supernovae in late 1990s firstly indicate our universe is expanding at an accelerating rate. Through the later years, observations from cosmic microwave background (CMB), galaxy surveies, baryon acoustic oscillations (BAO) confirms this fact. The source of the accelerated expansion is unclear, and is denoted as "dark energy" (DE). Two proposed mechanism for DE are 1) a cosmological constant and 2) a quintessence field, which can be partially distinguished in future high-precision cosmological measurements. In the cosmological constant scenario, the resulting cosmological constant from observation is $\sim 10^{120}$ times smaller than the QFT estimation ($\sim M_{\rm p}^4$). This extreme fine tuning is denoted as the Cosmological Constant hierarchy problem. Note that the quintessence scenario does not fully address this hierarchy problem.

7. **The Cosmological Coincidence**: From cosmological measurement, we learn 68% of the mass-energy content of universe are described by dark energy, 27% are dark matter and 5% are ordinary matter. Although people used to emphasise the small percentage of ordinary matter, it is also remarkable to note that 1) the densities of matter and dark energy today are at the same order-of-magnitude 2) the densities of dark matter and baryonic matter today are at the same order-of-magnitude. In principle, the difference in the three components can be much larger. Hence their rough equality raises the cosmological coincidence problem.

Besides, SM has other problems such as SM flavor problem, which may also lead to new insights of physics beyond the SM.

## 1.2 Particle Dark Matter

The concept of dark matter was proposed by astronomers in the early 1930s [5, 6] but ignored for the next 40 years. The idea was resurrected in 1970s as an explanation for the anomaly observed in the rotation curve measurements of galaxies, namely the rotational speeds of stars does not decline as its distance to the center of the galaxy increases [7]. Since then, evidence for dark matter, such as the bullet cluster and cosmic microwave background (CMB) measurement, has accumulated. Today measurements by Planck and WMAP show that 85% of the matter in our universe is dark. The search for the identity of DM remains is one of the most important experimental endeavors of particle physics. All evidence for DM comes from its gravitational interactions with ordinary matter. While we have assumed important clues from those observations, many questions about the nature of DM remains open, such as its mass and its interaction strength with ordinary matter. The success of laboratory and space-based experiments searching for DM is predicated on DM having additional non-gravitational interactions with ordinary matter. A range of DM candidates at various mass scales has been proposed. We will review three examples and explore their experimental consequences.

### 1.2.1 Weakly Interacting Massive Particle

A Weakly Interacting Massive Particle (WIMP) is a theoretically well-motivated DM candidate with mass in the 10 GeV to 10 TeV range, typically interacting with Standard Model (SM) particles through the Electroweak sector. For the DM mass range and interaction strength, WIMP particles give the DM abundance that maches closely the amount of DM experimentally observed today [8]. This unexpected coincidence is known as the "WIMP miracle" and has become the dominant paradigm of dark matter models. More importantly, WIMP hypothesis can be tested in many ongoing and upcoming colliders and direct and indirect detection experiments.

Current collider experiments, based on "mono-X" searches[2], have delivered null results on WIMP searches. On the other hand, direct detection experiments with nobel gas and semiconductor targets exclude large portions of favored WIMP parameter space. The current strongest bound, from the LUX experiment (with an exposure of $118 \times 85$ kg-day) exclude WIMP-nucleon (spin-independent) cross sections down to $10^{-44}$ cm$^2$ across the mass range from 10 GeV to 10 TeV [9]. However, it is also worthy to note that several possible ex-

---

[2]Those searches aim at the missing energy signature due to the production of DM. Examples include mono-photon, mono-$Z$, mono-jet searches.

perimental and observational anomalies are reported in direct and indirect detection. Their consistency with other DM probes requires further investigation.

## 1.2.2 Axions

Although the WIMP is the dominant paradigm of DM theories for the past decades, there are also many well-motivated non-WIMP DM candidates. The axion is another popular alternative. It first emerged from the Peccei-Quinn symmetry solution to the strong CP problem of QCD. Later it was generalized to a class of light spin-0 fields, which originate from the breaking of a shift symmetry due to instanton effects. Through collective motion, axions act like cold dark matter. And via the "misalignment mechanism"[3] [10], a sub-eV axion can provide the correct dark matter density today. Constraints on axions have been placed through astrophysical processes, such as the cooling of white dwarfs. Ground-based axion dark matter experiments, such as ADMX [11], ABRACADABRA [12], and CASPEr [13], can probe QCD axion dark matter with a mass of $10^{-4} - 10^{-6}$ eV, $10^{-6} - 10^{-9}$ eV, and $< 10^{-9}$ eV, respectively.

## 1.2.3 Sterile Neutrinos

From neutrino oscillation experiments, we learn neutrinos have non-zero but tiny masses. The smallness of the neutrino mass can be explained through the see-saw mechanism, which predicts the existence of sterile neutrinos. Sterile neutrinos are singlets under the SM gauge group and can mix with active (ordinary) neutrinos. For the so-called "$\nu$MSM" models (see review *e.g.* [14]), the see-saw scale is set to be the electroweak scale and the mass of sterile neutrino is around $\sim 10$ keV. This class of sterile neutrinos can serve as either cold dark matter or warm dark matter due to different production mechanism in the early universe. Their parameter space is restricted by astrophysical observations, such as X-ray surveys, and ground-based experiments, such as missing energy searches in low energy $e^+e^-$ colliders.

## 1.2.4 Asymmetric Dark Matter

Another popular alternative to WIMP is asymmetric DM (ADM, see review *e.g.* [15, 16]). ADM addresses the coincidence between the amount of dark matter (85% of matter) and the ordinary matter (15% of matter), which are at the same order-of-magnitude. This class

---

[3]Misalignment mechanism works for PQ phase transition occurs before inflation. In the case PQ phase transition takes place after inflation, the production of DM can be due to the decay of axionic strings or domain walls.

of models assumes an asymmetry between DM and anti-DM, which is similar to the baryon-anti-baryon asymmetry and may have a similar origin. The absence of annihilation today indicates ADM may alter the stellar evolution into black holes [17]. The dark photon is a possible candidate for complete annihilation of the symmetric part of ADM at early universe, which in turn will leave imprints in CMB and galaxy evolution. In later chapters, we will discuss dark photons in detail.

## 1.3 The Dark Sector

### 1.3.1 Extra Local Symmetry and the Dark Sector

As we learned, the SM is essentially characterized by the underlying gauge group $SU(3)_c \times SU(2)_L \times U(1)_Y$. This gauge group structure can be easily extended to include a new gauge group. Particles only charged under this new gauge group and *neutral* under the SM gauge group form a "dark" sector. This procedure can be further continued to include more "dark" gauge groups, and the resulting local group structure of the dark sector can be as rich as the SM sector.

A dark sector can be connected to the SM sector through "portals", which can be classified by the type of mediator or by the dimension of the interaction operator. Following the first classification, the so-called "vector portal" gives rise to a vector-like mediator, which denoted as a "dark photon" ($A'$). The so-called "scalar" portal gives rise to a Higgs-like mediator, which is denoted as a "dark Higgs" ($s$ for CP-even Higgs, $a$ for CP-odd Higgs). The interaction term of the vector portal and Higgs portal are both dimension-4 and renormalizable. However, it is possible to construct interaction terms with higher dimensional operators like the axion portal [18].

In this picture, particle DM can be identified as being a part of the dark sector, or with the dark force mediator itself [19, 20], or form its own sector. Moreover, different species of DM can appear in the dark sector picture, which further riches the dark sector. Some of DM exhibit significant interaction with ordinary matter or with themselves. Others may behavior as cold collisionless DM. Fig. 1.1 illustrates the above general set-up.[4]

Models of dark sectors are commonly presented as simplified models. On the one hand, they summarize various specific models. On the other hand, they link to various search channels. But fields in those simplified model Lagrangian can be often promoted to SUSY

---

[4]An analogy to this picture appears in the SUSY breaking, where the supersymmetric SM (SSM) sector connects to the hidden SUSY breaking sector via various "messengers". DM can reside either in the SSM sector, the SUSY breaking sector, or in its own sector.
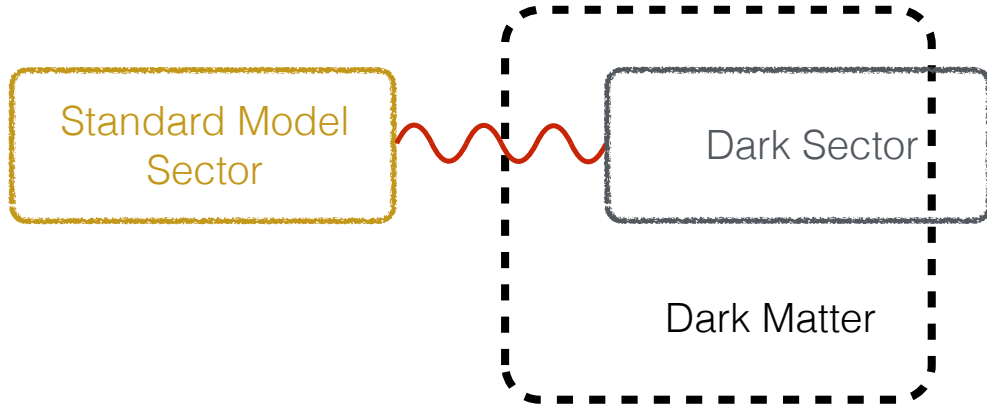
Figure 1.1: Illustration for the relation between dark sectors, portals to the SM sector and particle DM.

fields and result in a complete UV model (for example, $\text{MSSM} \times U(1)_D$ model [21, 22]).

## 1.3.2 Motivations for the Dark Sector

**Solving the Muon $g - 2$ Discrepancy**

The experimental measured anomalous magnetic moment of the muon, $a_\mu \equiv (g-2)_\mu$ [23], is different from its theoretical calculation based on the SM (see *e.g.* [24]). The two values are

$$a_\mu^{\text{SM}} = (11659180.2 \pm 4.2 \pm 2.6 \pm 0.2) \times 10^{-10}, \tag{1.1}$$

$$a_\mu^{\text{exp}} = (11659208.9 \pm 5.4 \pm 3.3) \times 10^{-10}, \tag{1.2}$$

and hence the difference

$$\Delta a_\mu = a_\mu^{\text{exp}} - a_\mu^{\text{SM}} = (28.7 \pm 8.0) \times 10^{-10} \tag{1.3}$$

is about $3.6\sigma$.

A dark photon [25] (or dark Higgs [26]) yield a positive contribute to the anomalous magnetic moment of the muon, and hence offer a possible beyond SM (BSM) explanation. The favored coupling between the dark photon (dark Higgs) is at the order of $\mathcal{O}(10^{-4})$, which is excluded by current experimental constraints of dark sector searches assuming dark photons decays 100% to the SM particles.

**Beyond the WIMP paradigm**

The dominant paradigm for particle dark matter today is WIMP and most experimental searches are focusing on detecting its non-gravitational interaction with ordinary matter. As

we mentioned in the last section, the WIMP has a typical mass between 10 GeV to 1 TeV. However, alternative DM candidates such as ADM have a mass around $\mathcal{O}(1)$ GeV, sterile neutrino DM has a mass around $\mathcal{O}(10)$ keV, and axion has a sub-meV mass. Clearly, the possible dark matter mass range can be much wider than WIMP paradigm predicts, and in particular, the range can be extended to lower masses. We denote this set of DM candidates as "Light Dark Matter" (LDM).

The parameter space of LDM is less explored in comparison to WIMPs. Part of the reason is due to the lower recoil energy and higher sensitivity requirement of the direct detection experiment. But another reason is due to theoretical prejudice. The lower mass limit of WIMPs (as well as the upper limit), $\sim 10$ GeV, is set by Lee-Weinberg limit [27]. A crucial assumption in the derivation is that the mediator between the dark matter and ordinary matter are weak-scale mediators, such as $W/Z$ bosons and Higgs, with weak scale coupling ($\sim G_F$). It is possible to break this lower limit by introducing a light mediator with an interaction strength larger than that of a weak-scale mediator. This opens a new mass window for LDM.

Equally crucially, the existence of light mediator can provide new production channels for LDM, which can be accessed in the territorial experiments, as we will see in later chapters.

## Hints from Astrophysical Anomalies

Several anomalies from astrophysical observations can be solved by introducing a new light dark force mediator in addition to DM. A detailed discussion of each anomaly is beyond the scope of this thesis. Here we list those anomalies and their sources or origins, and refer to the literature for their possible dark sector explanations.

## Solving Other Challenges

Although dark sectors are not directly motivated to answer other SM challenges listed in Sec. 1.1.2, there are concrete model building examples of dark sectors that address them as well. For example, the Higgs portal can be naturally mapped onto the twin Higgs model [60] that addresses the Higgs hierarchy problem. The dark sector opens dark baryogenesis [61] that may address the cosmological coincidence between DM and ordinary matter. Needless to say, axions in the axion portal, sterile neutrinos in the neutrino portal, and light Higgs bosons in the Higgs portal are themselves well-motivated BSM particles aiming to solve SM challenges such as strong CP problem and baryogenesis.

| Anomaly | Source/Origin | Possible DS Explanation |
|---|---|---|
| 511 keV $\gamma$-ray line | INTEGRAL [28] | kinetic mixing [29], eXciting DM [30] |
| Positron excess | PAMELA [31], Fermi-LAT [32], AMS-02 [33] | *e.g.*Sommerfeld enhancement [34], resonance enhancement [35, 36] |
| Galactic Center $\gamma$-ray excess | Fermi-LAT [37, 38] | *e.g.*kinetic mixing [39], coy DM [40] |
| 3.5 keV $\gamma$-ray line | XMM [41, 42] | eXciting DM [43] |
| Small-scale crisis of Cold Collisionless DM | Too-big-to-fail [44, 45, 46], Cusp-core [47, 48, 49, 50] | *e.g.*Yukawa type DM self-interaction, [51, 52, 53] |
| | Missing satellite [54] | late kinetic decoupling [55, 56, 57] |
| Comet strike periodicity | Earth crater record [58] | double-disk DM [58, 59] |

Table 1.1: Anomalies from Astronomy observations that can be possibly explained by Dark Sector Models.

## 1.4 Structure of the Thesis

The thesis is organized as following. In Chapter 2 we will discuss simplified models for dark force mediators. Our focus will be on two types of portals: vector portal and Higgs portal. We will present the vanilla models as well as their more specific variations. We will also scratch the phenomenology implications, which will be used in the searches in later chapters. In Chapter 3, we will present our searches for the dark photon with visible and invisible decays at the Mu3e and low-energy $e^+e^-$ experiments, respectively. We will compare their sensitivities to existing dark photon searches from existing ground-based experiments and astronomical observations. Those results have been published in [62, 63]. In Chapter 4, we will present searches for the dark Higgs through exotic Higgs decays, in particular from the $b\bar{b}\mu^+\mu^-$ channel. We find that exotic Higgs decays provide an unique opportunity to explore the dark sector with a Higgs portal, especially in a future high luminosity LHC run. These results have been published in [64, 65]. In Chapter 5, we will shift our attention to a possible dark sector explanation of the 750 GeV diphoton excess recently reported from LHC 13 TeV run. We will present the allowed dark mediator parameter space for both spin-0 excess and spin-2 excess scenarios. The corresponding analysis appears in [66] that submitted to JHEP. A summary of dark sector searches and possible further developments are finally discussed in Chapter 6.

# Chapter 2

# Models for Dark Sectors

## 2.1 Simplified Models for Dark Sectors

Dark Sector models are typically classified as different portals according to the different types of mediator connecting the SM sector and dark sector. Common portals include vector portal, Higgs portal, neutrino portal, axion portal. In this section, we focus on main features of the vector portal and Higgs portal models and their variations.

## 2.2 Vector Portal

### 2.2.1 Kinetic Mixing for $U(1)_D$ Model

A simple extension of the Standard Model gauge group is by introducing extra $U(1)$ gauge group. The new set of gauge group is

$$SU(3)_c \times SU(2)_L \times U(1)_Y \times U(1)_D \tag{2.1}$$

The gauge boson charged under the new "dark" $U(1)$ gauge group are denoted as dark photon $A'$.[1] This model has been studied extensively in the literature since the 1980's [67, 68, 69]. The relevant gauge sector of a minimal dark photon model consists of a new massive vector field that couples to the SM $U(1)_Y$ via the so-called kinetic mixing. The relevant gauge sector Lagrangian is given by

$$\mathcal{L}_{\text{gauge}} = -\frac{1}{4} B_{\mu\nu} B^{\mu\nu} - \frac{1}{4} F'_{\mu\nu} F'^{\mu\nu} + \frac{\sin \epsilon_Y}{2} F'_{\mu\nu} B^{\mu\nu} + \frac{1}{2} m_{A'}^2 A'_\mu A'^\mu \tag{2.2}$$

---

[1]In various literature, the dark photon $A'$ is also been called as "hidden photon", "U-boson", "heavy photon", "secluded photon".

where $F'_{\mu\nu} = \partial_{[\mu} A'_{\nu]}$ and $B_{\mu\nu} = \partial_{[\mu} B_{\nu]}$ are field strengths of the $U(1)_D$, $U(1)_Y$ gauge group respectively. The mass term breaks the $U(1)_D$ explicitly but does not ruin the renormalizability (the mechanism for generating this mass can be a "dark" Higgs mechanism or Stuckelberg mechanism).

$\sin \epsilon_Y$ is the kinetic mixing parameter. In the limit of $\epsilon_Y \ll 1$, we can use the approximation $\sin \epsilon_Y \simeq \epsilon_Y$. As we mentioned later, the dimensionless parameter dictates the magnitude of the coupling of $A'$ to the SM sector. Even if the boundary conditions in the deep UV are such that $\epsilon_Y(\Lambda_{UV}) = 0$, the non-zero mixing can be mediated by a one-(two-)loop interaction and naturally give $\epsilon_Y \sim 10^{-3} - 10^{-1}$ ($\sim 10^{-5} - 10^{-3}$) [70, 67, 71, 21], where the small value is justified due to the expected loop suppression.

The mixing term $F'_{\mu\nu} B^{\mu\nu}$ is removed by field redefinition

$$\begin{pmatrix} \tilde{B}_\mu \\ \tilde{A}'_\mu \end{pmatrix} = \begin{pmatrix} 1 & -\sin \epsilon_Y \\ 0 & \cos \epsilon_Y \end{pmatrix} \begin{pmatrix} B_\mu \\ A'_\mu \end{pmatrix}, \tag{2.3}$$

where the fields with tilde are the redefined fields. We follow the standard symmetry breaking conventions for the field $B$. The SM $SU(2) \times U(1)$ covariant derivative can be written as

$$D_\mu = \partial_\mu - ig W_\mu^a T^a - ig' Y B_\mu, \tag{2.4}$$

and rotated into

$$D_\mu = \partial_\mu - i\frac{g}{\sqrt{2}} \left( W_\mu^+ T^+ + W_\mu^- T^- \right) - i\frac{g}{\cos \theta_W} Z_\mu (T^3 - \sin^2 \theta_W Q) - ie A_\mu Q, \tag{2.5}$$

where $\theta_W$ is the weak mixing angle, $g$ and $g'$ are SM $SU(2)_L$ and $U(1)_Y$ gauge couplings. $SU(2)_L$ charge $T^3$, $U(1)_Y$ charge $Y$, and $U(1)_{EM}$ charge $Q$ are related by $Q \equiv T^3 + Y$. Rotating the redefined neutral vector boson fields yields $\tilde{A}_\mu$, $\tilde{Z}_\mu$ and $\tilde{Z}'_\mu$,

$$\begin{pmatrix} \tilde{A}_\mu \\ \tilde{Z}_\mu \\ \tilde{Z}'_\mu \end{pmatrix} = \begin{pmatrix} c_W & s_W & 0 \\ -s_W & c_W & 0 \\ 0 & 0 & 1 \end{pmatrix} \begin{pmatrix} \tilde{B}_\mu \\ W_\mu^3 \\ \tilde{A}'_\mu \end{pmatrix} = \begin{pmatrix} c_W & s_W & -c_W s_\epsilon \\ -s_W & c_W & s_W s_\epsilon \\ 0 & 0 & c_\epsilon \end{pmatrix} \begin{pmatrix} B_\mu \\ W_\mu^3 \\ A'_\mu \end{pmatrix} \tag{2.6}$$

Above we begin to use a short-handed notation, *i.e.*, $c$, $s$, $t$ stands for sin, cos, tan respectively. The subscript stands for the function variables and $W$ stands for $\theta_W$.

We collect $m_{A'}$ mass term in $\mathcal{L}_{\text{guage}}$ and other SM gauge boson mass terms into

$$\mathcal{L}_{\text{mass}} = \frac{1}{2}m_{A'}^2 A'^2_\mu + \frac{1}{2}m_{Z^0}^2 \begin{pmatrix} B_\mu & W_\mu^3 \end{pmatrix} \begin{pmatrix} s_W^2 & -c_W s_W \\ -c_W s_W & c_W^2 \end{pmatrix} \begin{pmatrix} B^\mu \\ W^{3,\mu} \end{pmatrix} \tag{2.7}$$

$$= \frac{1}{2}m_{A'}^2 \tilde{Z}'^2_\mu/c_\epsilon^2 + \frac{1}{2}m_{Z^0}^2 \begin{pmatrix} \tilde{A}_\mu & \tilde{Z}_\mu & \tilde{Z}'_\mu \end{pmatrix} \begin{pmatrix} 0 & 0 & 0 \\ 0 & 1 & -s_W t_\epsilon \\ 0 & -s_W t_\epsilon & s_W^2 t_\epsilon^2 \end{pmatrix} \begin{pmatrix} \tilde{A}^\mu \\ \tilde{Z}^\mu \\ \tilde{Z}'^\mu \end{pmatrix} \tag{2.8}$$

$$= \frac{1}{2} \begin{pmatrix} \tilde{A}_\mu & \tilde{Z}_\mu & \tilde{Z}'_\mu \end{pmatrix} \begin{pmatrix} 0 & 0 & 0 \\ 0 & m_{Z^0}^2 & -m_{Z^0}^2 s_W t_\epsilon \\ 0 & -m_{Z^0}^2 s_W t_\epsilon & m_{Z^0}^2 s_W^2 t_\epsilon^2 + m_{A'}^2/c_\epsilon^2 \end{pmatrix} \begin{pmatrix} \tilde{A}^\mu \\ \tilde{Z}^\mu \\ \tilde{Z}'^\mu \end{pmatrix} \tag{2.9}$$

In the last step of the above equation, the Lagrangian is expressed in the redefined fields. However, the mass matrix is still non-diagonal. We introduce one more rotation to eliminate the mixing,

$$\mathcal{L}_{\text{mass}} = \frac{1}{2} \begin{pmatrix} \tilde{A}_\mu & \tilde{Z}_\mu & \tilde{Z}'_\mu \end{pmatrix} \begin{pmatrix} 1 & 0 & 0 \\ 0 & c_\xi & -s_\xi \\ 0 & s_\xi & c_\xi \end{pmatrix} \begin{pmatrix} 0 & 0 & 0 \\ 0 & m_{\bar{Z}}^2 & 0 \\ 0 & 0 & m_{\bar{Z}'}^2 \end{pmatrix} \begin{pmatrix} 1 & 0 & 0 \\ 0 & c_\xi & s_\xi \\ 0 & -s_\xi & c_\xi \end{pmatrix} \begin{pmatrix} \tilde{A}^\mu \\ \tilde{Z}^\mu \\ \tilde{Z}'^\mu \end{pmatrix} \tag{2.10}$$

$$\equiv \frac{1}{2} \begin{pmatrix} \bar{A}_\mu & \bar{Z}_\mu & \bar{Z}'_\mu \end{pmatrix} \begin{pmatrix} 0 & 0 & 0 \\ 0 & m_{\bar{Z}}^2 & 0 \\ 0 & 0 & m_{\bar{Z}'}^2 \end{pmatrix} \begin{pmatrix} \bar{A}^\mu \\ \bar{Z}^\mu \\ \bar{Z}'^\mu \end{pmatrix} \tag{2.11}$$

We use the bar to represent fields in their physical (mass) basis. The eigenstates of the mass matrix in (2.9) yield $m_Z^2$ and $m_{Z'}^2$ as

$$m_{\bar{Z},\bar{Z}'}^2 = \frac{m_{Z^0}^2}{2} \left[ \cos^2\theta_W + \sec^2\epsilon_Y \sin^2\theta_W + \delta^2 \pm \text{sign}\,(1-\delta)\sec^2\epsilon_Y \sqrt{\Xi} \right], \tag{2.12}$$

where

$$\Xi \equiv -4\delta^2 \cos^4\epsilon_Y + \left[ \left(1+\delta^2\right)\cos^2\epsilon_Y + \sin^2\epsilon_Y \sin^2\theta_W \right]^2 \tag{2.13}$$

and

$$\delta^2 \equiv \frac{m_{A'}^2}{m_{Z^0}^2}. \tag{2.14}$$

$m_{Z^0}$ is the SM $Z$-boson mass before kinetic mixing. The appearance of the sign function is because we intend to assign $m_Z = m_{Z^0}$ when the mixing coefficient vanishes.

Comparing the mass matrix before and after the diagonalization, we found

$$\tan\xi = \frac{m_{Z^0}^2 \sin\theta_W \tan\epsilon_Y}{m_{Z'}^2 - m_{Z^0}^2} \tag{2.15}$$

$$= \frac{1 - \delta^2 - \sin^2\theta_W \tan^2\epsilon_Y - \text{sign}(1-\delta)\sec^2\epsilon_Y \sqrt{\Xi}}{2\tan\epsilon_Y \sin\theta_W}. \tag{2.16}$$

12

We have adopted multiple matrix transformations so far. The transfer matrix from the original gauge basis to the final physical basis is

$$
\begin{pmatrix} \bar{A}_\mu \\ \bar{Z}_\mu \\ \bar{Z}'_\mu \end{pmatrix} = \begin{pmatrix} c_W & s_W & -c_W s_\epsilon \\ -c_\xi s_W & c_\xi c_W & c_\epsilon s_\xi + c_\xi s_\epsilon s_W \\ s_\xi s_W & -s_\xi c_W & c_\epsilon c_\xi - s_\epsilon s_\xi s_W \end{pmatrix} \begin{pmatrix} B_\mu \\ W^3_\mu \\ A'_\mu \end{pmatrix} . \tag{2.17}
$$

The interaction part between the gauge bosons and the SM fermions can be written as

$$
\mathcal{L}_{\text{int}} = e A^\mu J_{\text{EM},\mu} + g Z^{0,\mu} J_{Z^0,\mu} \tag{2.18}
$$

where $e$ is the SM $U(1)_{EM}$ gauge coupling, and $J_{\text{EM}}$ and $J_{Z^0}$ are the SM EM and neutral current, respectively. $A$ and $Z^0$ can be expressed in the physical basis as

$$
\begin{pmatrix} A_\mu \\ Z^0_\mu \end{pmatrix} = \begin{pmatrix} c_W & s_W & 0 \\ -s_W & c_W & 0 \end{pmatrix} \begin{pmatrix} B_\mu \\ W^3_\mu \\ A'_\mu \end{pmatrix} = \begin{pmatrix} 1 & c_W t_\epsilon s_\xi & c_W t_\epsilon c_\xi \\ 0 & -s_W t_\epsilon s_\xi + c_\xi & -s_W t_\epsilon c_\xi - s_\xi \end{pmatrix} \begin{pmatrix} \bar{A}_\mu \\ \bar{Z}_\mu \\ \bar{Z}'_\mu \end{pmatrix} . \tag{2.19}
$$

Therefore the interaction in the physical basis is

$$
\mathcal{L}_{\text{int}} = \begin{pmatrix} \bar{A}_\mu & \bar{Z}_\mu & \bar{Z}'_\mu \end{pmatrix} \begin{pmatrix} 1 & 0 \\ c_W t_\epsilon s_\xi & -s_W t_\epsilon s_\xi + c_\xi \\ c_W t_\epsilon c_\xi & -s_W t_\epsilon c_\xi - s_\xi \end{pmatrix} \begin{pmatrix} e J^\mu_{\text{EM}} \\ g J^\mu_{Z^0} \end{pmatrix} . \tag{2.20}
$$

From the above expression, we read off the relevant part for the $Z' \bar{f} f$ interaction as

$$
\mathcal{L}_{\bar{Z}' \bar{f} f} = \frac{g}{\cos \theta_W} \left[ -\sin \xi \left( T^3 \cos^2 \theta_W - Y \sin^2 \theta_W \right) + \tan \epsilon_Y \cos \xi \sin \theta_W Y \right] \bar{Z}'_\mu \bar{f} \gamma^\mu f . \tag{2.21}
$$

Similarly, the $Z \bar{f} f$ interaction is modified to

$$
\mathcal{L}_{\bar{Z} \bar{f} f} = \frac{g}{\cos \theta_W} \left[ \cos \xi \left( T^3 \cos^2 \theta_W - Y \sin^2 \theta_W \right) + \tan \epsilon_Y \sin \xi \sin \theta_W Y \right] \bar{Z}_\mu \bar{f} \gamma^\mu f . \tag{2.22}
$$

Finally, to avoid the proliferation of notations, we will call the physical $\bar{Z}$ particle as $\bar{A}$, and refer to it as the dark photon. Here we discuss two limits in more details.

1. In the limit $m_{A'} \ll m_{Z^0}$ and $\epsilon_Y \ll 1$, we have

$$
\mathcal{L}_{\bar{A}' \bar{f} f} \simeq \epsilon_Y \cos \theta_W e Q \bar{A}'_\mu \bar{f} \gamma^\mu f \equiv \epsilon e Q \bar{Z}'_\mu \bar{f} \gamma^\mu f . \tag{2.23}
$$

with

$$
m^2_{\bar{A}'} \simeq m^2_{A'} \left( 1 - \epsilon^2_Y \sin^2 \theta_W \right) . \tag{2.24}
$$

Above we introduce the "usual" kinetic mixing parameter $\epsilon \equiv \epsilon_Y \cos \theta_W$. This will be the main scenario through our later discussions. As we seen in Eq. (2.23), the mixing between the dark photon and the SM photon leads to an $\epsilon$-suppressed coupling of the dark photon to SM quarks and charged leptons.

13

2. In the other limit $m_{A'} \gg m_{Z^0}$ and $\epsilon_Y \ll 1$, we obtain

$$\mathcal{L}_{\bar{A}'\bar{f}f} \simeq \epsilon_Y g' Y \bar{A}'_\mu \bar{f} \gamma^\mu f = \frac{\epsilon_Y}{\cos\theta_W} eY \bar{A}'_\mu \bar{f} \gamma^\mu f = \frac{\epsilon eY}{\cos^2\theta_W} \bar{A}'_\mu \bar{f} \gamma^\mu f \qquad (2.25)$$

with

$$m_{\bar{A}'}^2 \simeq m_{A'}^2. \qquad (2.26)$$

We will visit this scenario in Chapter 5. Note that, like the previous limit, the couplings between $Z'$ and fermions are independent of the $Z'$ mass.

Theoretically, the values of the kinetic mixing and the dark photon mass can take on a wide range of values. However, as we seen in Sec. 1.3.2, much attention has recently been focused on the MeV–GeV mass range where the dark photon could explain the $\sim$ $3.6\sigma$ discrepancy between the observed and SM value of $(g-2)_\mu$ and offer an explanation for various dark matter related anomalies through dark matter-dark photon interactions. Moreover, a dark photon mass in this range can be generated naturally in several new physics scenarios [70, 72, 21, 22, 73].

There are many experimental probes of MeV–GeV mass dark photons that decay directly to SM particles. These include collider experiments, beam dumps, rare meson decays, supernova cooling, and precision measurements [74, 75, 76, 77, 78, 79, 80, 73, 81, 82, 83, 84, 25, 85, 86, 87, 88, 89, 90, 91, 92, 93, 94, 95, 96, 97, 98, 99, 100, 101, 102, 103, 104, 105, 106]. Existing constraints have almost disfavored the entire mass and coupling range in which dark photons could explain the $(g-2)_\mu$ anomaly, assuming the dark photon decays directly to SM particles with a branching ratio close to 100%. A reduced branching ratio is possible if there exist other light particles that couple to the dark photon and open up additional decay modes.

## 2.2.2 Other Variations

The kinetic mixing with $U(1)_D$ represents one of the simplest scenario of the vector portal models. Other well-motivated, anomaly-free gauge group can be easily mapped on to $U(1)_D$ scenario. Examples include $U(1)_{B-L}$, $U(1)_{L_e-L_\mu}$, $U(1)_{L_e-L_\tau}$, and $U(1)_{L_\mu-L_\tau}$ models.

The kinetic mixing term $F'_{\mu\nu} B^{\mu\nu}$ in the $\mathcal{L}_{\text{gauge}}$ is a dim-4 renormalizable operator. However, it is also possible to construct higher dimensional operators with respect to the vector mediator. Electric dipole moment interaction (EDM) and magnetic dipole moment (MDM) interaction are two well-motivated examples:

$$\mathcal{L}_{\text{EDM}} \supset -\frac{iD}{2} \bar{f} \sigma_{\mu\nu} \gamma_5 f F'^{\mu\nu}, \quad \mathcal{L}_{\text{MDM}} \supset -\frac{iM}{2} f \sigma_{\mu\nu} f F'^{\mu\nu}, \qquad (2.27)$$

where $f$ is the SM fermion and $D$ and $M$ are couplings with dimension $[E]^{-1}$.

## 2.3 Higgs Portal

The discovery of the 125 GeV Higgs boson at the Large Hadron Collider (LHC) [107, 108] provides strong evidence for the existence of fundamental scalars in the universe. It also encourage searches for Higgs "siblings" and other searches for exotic production and decay modes of the Higgs. Among the most exciting possibilities is that the Higgs boson can provide a unique window onto light dark sectors, consisting of particles neutral under the SM gauge groups.

The Higgs boson is one of only a few SM particles that can couple to new states with an interaction that is (super-)renormalizable. In addition, the small decay width of the SM Higgs, dominated by the bottom Yukawa coupling, means that a small, $\mathcal{O}(0.01)$, renormalizable coupling of the Higgs to a new, light state can lead to an exotic Higgs decay branching ratio of $\mathcal{O}(1)$. This makes exotic Higgs decays a prime experimental target. In many cases, these exotic decays need to be searched for explicitly as they may otherwise escape detection. In particular, measurements of the Higgs couplings to SM states only constrains the Higgs branching ratio to non-SM states to $\lesssim 60\%$ [109, 110]. Thus a large branching ratio to beyond SM particles is still viable. For a detailed survey of promising exotic decay modes and their theoretical motivations we refer the reader to [64].

In this section, we will focus on two classes of Higgs portal model 1) SM with an extra singlet and 2) Two-Higgs-doublet model (2HDM) with an extra singlet and work out their phenomenology that relevant to the exotic Higgs decays. This part of introduction is based on [64]. We will describe in a particular example of the exotic Higgs decay searches in Chapter 4.1.

### 2.3.1 SM+Scalar Model and Exotic Higgs Decays

A particularly simple extension of the SM is to add to it one real scalar singlet $S$. This model can easily produce non-trivial exotic Higgs decays, since 1) the Higgs can decay to pair of singlets; and 2) the singlet decays to SM particles (by virtue of mixing with the Higgs). Singlet scalars coupled to the Higgs also provide a well-known avenue for enhancing the electroweak phase transition in the early universe, which is a necessary ingredient for electroweak baryogenesis (see *e.g.*[111]). We describe this simple model below, as well as two small variations (one with more symmetry, one with a complex scalar), but all three models, as well as other variations, can yield essentially identical phenomenology. In 4.1.1, this will be generalized to two-Higgs-doublet models with a singlet.

**Higgs potentials in SM+S**

At the renormalizable level, gauge invariance allows the singlet $S$ to couple only to itself and to $H^\dagger H \equiv |H|^2$. The resulting potential is given by

$$V(H, S) = V(H) + \hat{V}(S) + k\, S\, |H|^2 + \frac{1}{2}\, \zeta\, S^2\, |H|^2\,, \qquad (2.28)$$

where $\hat{V}(S)$ is a general quartic polynomial that may give $S$ a vacuum expectation value. The couplings $k$ and $\zeta$ generate mixings between $H$ and $S$. Assuming those mixings are small, we identify the uneaten doublet degree of freedom to be the SM-like Higgs with $m_h = 125$ GeV and take the singlet field to have a mass below $m_h/2$. The small mixings give mass eigenstates $h$ and $s$, which are mostly doublet- and singlet-like, respectively. The decays $h \to ss$ are generated by an effective cubic term, and $s$ decays to SM particles via its doublet admixture.

Imposing a $Z_2$ symmetry $S \to -S$, we can obtain a simpler version of this model with similar phenomenology. In this case, $\hat{V}(S)$ contains only quadratic and quartic terms and $k = 0$, *e.g.*

$$V(H, S) = -\mu^2\, |H|^2 - \frac{1}{2}\, \mu'^2\, S^2 + \lambda\, |H|^4 + \frac{1}{4}\, \kappa\, S^4 + \frac{1}{2}\, \zeta\, S^2\, |H|^2. \qquad (2.29)$$

Depending on the choice of couplings, the potential may have a minimum at $S = 0$, in which case the $Z_2$ is unbroken, there is no mixing between $H$ and $S$, and the $S$ does not decay; the coupling $\zeta$ induces the invisible decay $h \to ss$. If the minimum instead has $S \neq 0$, then the $Z_2$ is broken, and the coupling $\zeta$ now not only produces a cubic term but also a quadratic term that allows $H$ and $S$ to mix. In this case, the phenomenology is just as described in the previous paragraph, i.e. $h \to ss$ for $m_s < m_h/2$, with $s$ decaying to SM particles.

A third model, with essentially identical phenomenology, involves a theory with a *complex* scalar and an *approximate* $U(1)$ global symmetry.[2] Here the scalar potential is as above, with $S$ now complex, and with a small $U(1)$ breaking part:

$$V(H, S) = V_0(|H|^2, |S|^2) + V_1(|H|^2, S, S^\dagger) \qquad (2.30)$$

$$V_0 = -\mu^2\, |H|^2 - \mu'^2\, |S|^2 + \lambda\, |H|^4 + \kappa\, |S|^4 + \zeta\, |S|^2 |H|^2 \qquad (2.31)$$

$$V_1 = (\rho + \xi_S\, |S|^2 + \xi_H\, |H|^2)\, S + \text{h.c.} \; + \; \text{other terms} \qquad (2.32)$$

where we have chosen not to consider the most general $V_1$ for illustration purposes. If the potential is such that $S$ develops a non-zero vacuum expectation value, the spectrum

---

[2]An exact $U(1)$ symmetry leads to invisible decays, while a spontaneously broken $U(1)$ gives rise to an unacceptable massless Nambu-Goldstone boson; a gauged $U(1)$ will be discussed in Sec. 2.3.2.

consists of a massive scalar $S$ and a light pseudo-Nambu-Goldstone boson $a$ with mass $m_a$. If $m_s > \frac{1}{2}m_h > m_a$, then $h \to aa$ is possible, which is an invisible decay unless the $U(1)$-violating terms also violate charge conjugation. In that case, $a$ can mix with the massive state $s$, which in turn mixes with $H$ as in previous examples, allowing the $a$ to decay to SM particles, with couplings inherited from $H$.

**Phenomenology in SM+S**

After electroweak symmetry breaking there are two relevant *mass-eigenstates*: the SM-like scalar $h$ at 125 GeV containing a small admixture of $S$, and the mostly-singlet scalar $s$ containing a small admixture of $H$. The phenomenology of all three variants above is the same, as far as decays of the form $h \to ss \to$ SM are concerned. It can be captured in terms of three parameters:

1. The effective Lagrangian contains a term of the form $\mu_v \, h \, s \, s$, which gives $h \to ss$ with $\mathrm{Br}(h \to \text{exotic})$ determined by $\mu_v$.

2. The singlet's mass $m_s$ affects $\mathrm{Br}(h \to \text{exotic})$ and the type of SM final states available for $s \to$ SM.

3. The mixing angle between $S$ and $H$, denoted here by $\theta_S$, determines the overall width of $s \to$ SM. If $s$ cannot decay to other non-SM fields, $\theta_S$ controls its lifetime.

Apart from these continuous parameters, the parity of $s$ also affects the partial widths to different final states, mostly near thresholds. Note that the total width of $s$ is usually not important for phenomenology if it decays promptly. However, the lifetime of $s$ is macroscopic ($c\tau \sim$ meters) if $\theta \lesssim 10^{-6}$. This possibility is technically natural and thus the experimental search for displaced vertices deserves serious consideration [112]; however, we do not discuss this further here. Therefore, for a large part of parameter space, only $\mu_v$ and $m_s$ is relevant for collider phenomenology as this fixes $\mathrm{Br}(h \to ss)$ and $\mathrm{Br}(s \to$ SM$)$.

The partial width for exotic Higgs decays is given by

$$\Gamma(h \to ss) \;=\; \frac{1}{8\pi} \frac{\mu_v^2}{m_h} \sqrt{1 - \frac{4m_s^2}{m_h^2}} \;\approx\; \left(\frac{\mu_v/v}{0.015}\right)^2 \Gamma(h \to \text{SM}) \,, \tag{2.33}$$

where the last step assumes $m_s \ll m_h/2$. Therefore, the new branching ratio is $\mathcal{O}(1)$ even for small values of $\mu_v/v$. This is not surprising, if we recall that in the SM the bottom quark takes up almost 60% of the total width although its Yukawa coupling is only $\sim 0.017$. In Fig. 2.1, we show contours of $\mu_v/v$ in the $\mathrm{Br}(h \to ss)$ versus $m_s$ plane.
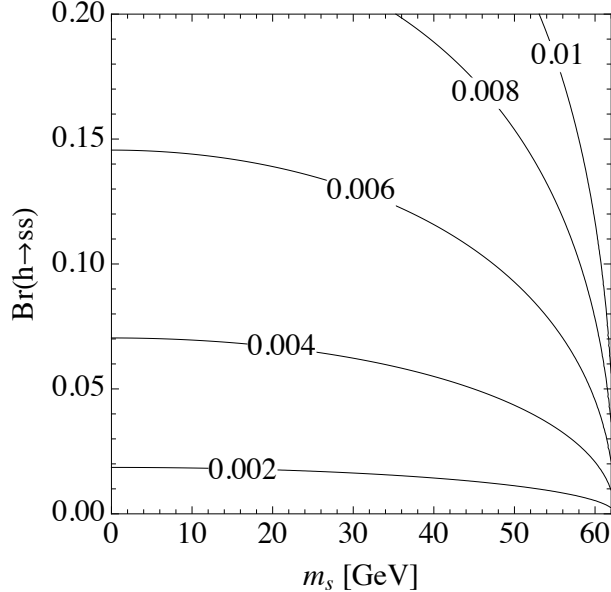
Figure 2.1: Size of the cubic coupling $\mu_v$ in units of Higgs expectation value $v$ to yield the indicated $h \to ss$ branching ratio as a function of singlet mass, as given by Eq. (2.33).

The individual partial widths of the singlet $s$ to SM particles are readily computed using existing calculations for Higgs decays, *e.g.* [113, 114]. Decays into $W^*W^*$ and $Z^*Z^*$ are negligible for $m_s < m_h/2$. At lowest order, the partial decay width to fermions is given by

$$\Gamma(s \to f\bar{f}) = \sin^2 \theta_S \frac{N_c}{8\pi} \frac{m_s m_f^2}{v^2} \beta_f^3, \tag{2.34}$$

where $\beta_f = \sqrt{1 - 4m_f^2/m_s^2}$ and $N_c$ is the number of colors, equaling 3 (1) for quarks (leptons). For the pseudoscalar singlet state $a$, $\beta_f^3$ is replaced by $\beta_f$. The mixing suppression $\sin^2 \theta_S$ is common to all partial widths, including those to gluons and photons, and thus does not affect branching ratios if $s$ only decays to SM particles. $\mathrm{Br}(s \to \mathrm{SM})$ and $\mathrm{Br}(h \to ss \to \mathrm{SM})$ are shown for $m_s > 1$ GeV in Fig. 2.2 on the **left** and **right**, respectively. It is clear that a simple singlet extension of the SM generically implies significant branching ratios of exotic Higgs decays to 4 SM objects. The indicated branching ratios include $\mathcal{O}(\alpha_s^2, \alpha_s^3)$ radiative corrections for decays to quarks, as well as NLO corrections to the loop-induced decays to photons and gluons [113].

The theoretical calculations become increasingly inaccurate as $m_s$ is lowered to $\sim 1$ GeV, where perturbative QCD breaks down, or when $m_s$ is close to a hadronic resonance, which can enhance the decay rates [115]. Decays to quarkonium states are suppressed for $s$ but may be important for $a$. For $m_s < 1$ GeV and above the pion threshold, partial widths have to be computed within a low energy effective theory of QCD, such as soft-pion theory or the
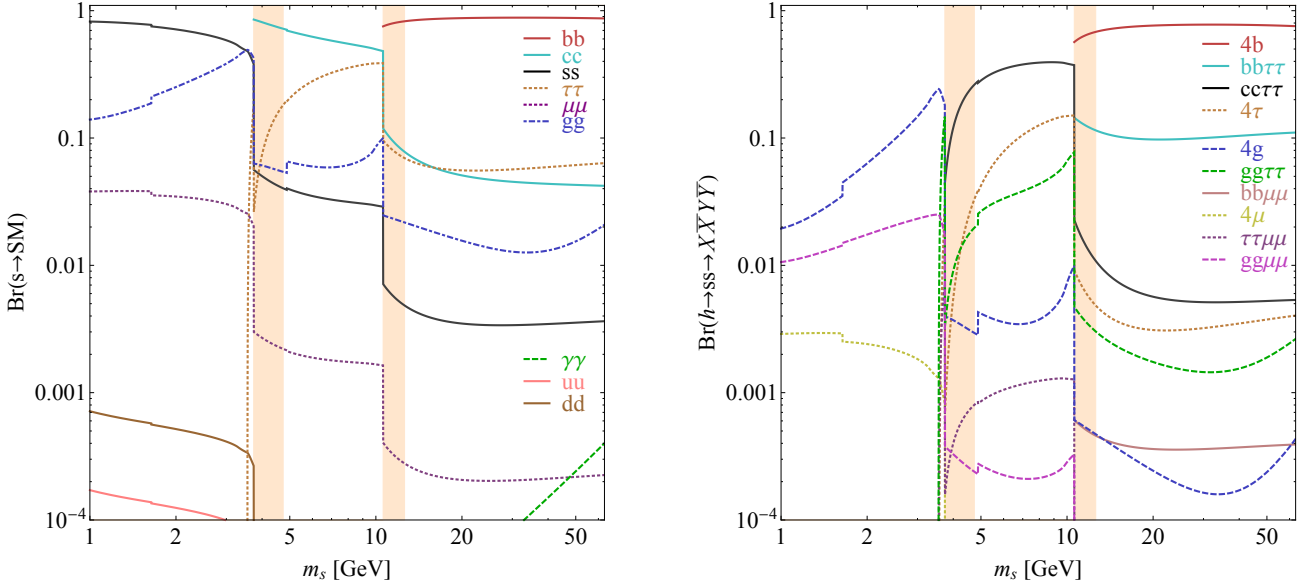
Figure 2.2: **Left**: Branching ratios of a CP-even scalar singlet to SM particles, as function of $m_s$. **Right**: Branching ratios of exotic decays of the 125 GeV Higgs boson as function of $m_s$, in the *SM + Scalar* model described in the text, scaled to $\mathrm{Br}(h \to ss) = 1$. Hadronization effects likely invalidate our simple calculation in the shaded regions.

chiral Lagrangian method. Nevertheless, it is clear that the dominant decay of the singlet is to some combination of hadrons, which are boosted due to the large mass difference between the singlet and $h$. The resulting two-track jet may look like a low-quality hadronic $\tau$-decay. Between the muon and pion thresholds (210 MeV $\lesssim m_s \lesssim$ 270 MeV), the dominant decay is to $\mu^+\mu^-$, while for $m_s \lesssim 210$ MeV, the dominant decay is to $e^+e^-$. Photons are the only possible final state for $m_s < 2\,m_e$, in which case the scalar is detector-stable.

Further details of the branching ratio calculation can be found in Sec. 2.3.2 and Appendix A.1, which also includes a more detailed discussion of pseudoscalar decays.

For $m_s \lesssim 2m_b$, the $s\bar{b}b$ coupling can in principle be probed by bottomonium decay [116, 117]. The strongest limits are $\mathrm{Br}(\Upsilon(1S) \to \gamma\tau^+\tau^-) \lesssim 10^{-5}$ by *BABAR* [118], which constraints the Yukawa coupling to satisfy $y_{sbb} \lesssim 0.4$ for $\mathrm{Br}(s \to \tau^+\tau^-) = 1$ [119, 120]. In the SM+S scenario, $y_{sbb} = \sin\theta_S\, y_{hbb}$ with $y_{hbb} \approx 0.02$ in the SM. Clearly the Upsilon decay measurement provides no meaningful bounds on singlet extensions. Similar arguments apply to pseudoscalars, and hence the 2HDM+S and NMSSM in the next sections.

### 2.3.2 2HDM (+ Scalar) Model and Exotic Higgs Decays

The SM Higgs sector is made up of a single $SU(2)_L$ doublet $H$ with hypercharge $Y = +\frac{1}{2}$, denoted by $H \sim 2_{+1/2}$. Adding a doublet to this minimal picture is one of the simplest extensions of the Higgs sector compatible with a $\rho$-parameter close to 1. Such extensions are found in several well-motivated theories, such as supersymmetry [121] and axion models [122, 123], where holomorphy and the Peccei-Quinn symmetry, respectively, necessitate an additional doublet; theories of electroweak baryogenesis, which might be made viable with additional doublets [124]; and grand unified models [115]. For this reason, it makes sense to define the most general Two-Higgs Doublet Model (2HDM) and study it in detail (for a comprehensive review, see *e.g.* [125]; for a discussion on the impact of recent SM-like Higgs boson discovery, see *e.g.* [126]). Below we will then add a light scalar to the 2HDM to obtain a rich set of exotic Higgs decays.

The most general 2HDM Higgs potential is given by [115]

$$
\begin{aligned}
V \;=\;& m_1^2|H_1|^2 + m_2^2|H_2|^2 + \frac{\lambda_1}{2}|H_1|^2 + \frac{\lambda_2}{2}|H_2|^2 + \lambda_3|H_1|^2|H_2|^2 + \lambda_4|H_1^\dagger H_2|^2 + \quad (2.35) \\
& \frac{\lambda_5}{2}\left((H_1 H_2)^2 + \text{h.c.}\right) + m_{12}^2\left(H_1 H_2 + \text{h.c.}\right) + \\
& \left(\lambda_6|H_1|^2(H_1 H_2) + \text{h.c.}\right) + \left(\lambda_7|H_2|^2(H_1 H_2) + \text{h.c.}\right) \;.
\end{aligned}
$$

We choose the charges of the Higgs fields such that $H_1 \sim 2_{-1/2}$ and $H_2 \sim 2_{+1/2}$. Note that we choose conventions that differ slightly from the "standard" conventions of [115, 125]; this will simplify the transition to supersymmetry models below.[3] The scalar doublets $H_{1,2}$ acquire vacuum expectation values $v_{1,2}$, which we assume here are real and aligned. Expanding around the minima yields two complex and four real degrees of freedom

$$
H_1 = \frac{1}{\sqrt{2}}\begin{pmatrix} v_1 + H_{1,R}^0 + iH_{1,I}^0 \\ H_{1,R}^- + iH_{1,I}^- \end{pmatrix}, \quad H_2 = \frac{1}{\sqrt{2}}\begin{pmatrix} H_{2,R}^+ + iH_{2,I}^+ \\ v_2 + H_{2,R}^0 + iH_{2,I}^0 \end{pmatrix}. \quad (2.36)
$$

The charged scalar and pseudoscalar mass matrices are diagonalized by a rotation angle $\beta$, defined as $\tan\beta = v_2/v_1$. One charged (complex) field and one neutral pseudoscalar combination of $H_{1,2,I}^0$ are eaten by the SM gauge bosons after electroweak symmetry breaking. The other complex field yields two charged mass eigenstates, $H^\pm$, which we assume are heavy and will thus play no further role in our discussions. The surviving three real degrees of freedom yield one neutral pseudoscalar mass eigenstate,

$$
A = H_{1,I}^0 \sin\beta - H_{2,I}^0 \cos\beta\,, \quad (2.37)
$$

---

[3] To recover the conventions of [115] set $\Phi_2 = H_2$, $\Phi_1 = i\sigma^2 H_1^*$.

and two neutral scalar mass eigenstates,

$$\begin{pmatrix} h \\ H^0 \end{pmatrix} = \begin{pmatrix} -\sin\alpha & \cos\alpha \\ \cos\alpha & \sin\alpha \end{pmatrix} \begin{pmatrix} H^0_{1,R} \\ H^0_{2,R} \end{pmatrix}, \tag{2.38}$$

where[4] $-\pi/2 \leq \alpha \leq \pi/2$. Our notation anticipates the assumption below that the model is in a decoupling limit, so that $h$ is the SM-like Higgs and $H^0$ is the other, heavier, scalar.

Allowing the most general Yukawa couplings to fermions would result in large Flavor-Changing Neutral Currents (FCNCs). This can be avoided by imposing $\mathbb{Z}_2$ symmetries to ensure that fermions with the same quantum numbers all couple to only one Higgs field. This results in four "standard" types of fermion couplings commonly discussed in the literature: type-I (all fermions couple to $H_2$), type-II (MSSM-like, $d_R$ and $e_R$ couple to $H_1$, $u_R$ to $H_2$), type-III (lepton-specific, leptons/quarks couple to $H_1/H_2$ respectively) and type-IV (flipped, with $u_R, e_R$ coupling to $H_2$ and $d_R$ to $H_1$). The couplings of the $h$, $H^0$, and $A$ mass eigenstates to fermions and gauge fields relative to the SM Higgs couplings are summarized in Tab. 2.1.[5]

In general, 2HDMs could allow for exotic decays of the 125 GeV state of the form $h \to AA$, $H^0 \to hh, AA$ or $h \to ZA$ (where we temporarily identified the 125 GeV state with either $h$ or $H^0$), where the daughter (pseudo)scalars decay to SM fermions or gauge bosons. However, while this possibility can be realized in certain corners of parameter space, 2HDMs are by now too constrained from existing data [130, 131] to allow for a wide variety of exotic Higgs decay phenomenology.

These restrictions are easily avoided as follows. First, we assume the 2HDM is near or in the decoupling limit,

$$\alpha \to \beta - \pi/2, \tag{2.39}$$

where the lightest state in the 2HDM is $h$, which we identify with the observed 125 GeV state. In this limit, the fermion couplings of $h$ also become identical to the SM Higgs, while the gauge boson couplings are very close to SM-like for $\tan\beta \gtrsim 5$. All of the properties of $h$ are determined by just two parameters, $\tan\beta$ and $\alpha$, and the type of fermion couplings. The remaining parameters, which control the rest of the Higgs spectrum and its phenomenology, are in general constrained by the measured production and decays of $h$ [132, 133, 134, 135, 129, 136, 137, 138, 139, 140], but plenty of viable parameter space exists in the decoupling limit.

---

[4]Contrast this to the MSSM Higgs potential, where $-\pi/2 \leq \alpha \leq 0$.

[5]More general fermion couplings are possible within the framework of Minimal Flavor Violation [127, 128]. We do not discuss this case here since we use the 2HDM to illustrate a range of possible exotic Higgs decay signatures, which would not be qualitatively different in the MFV scenarios.

| | Couplings | I | II (NMSSM-like) | III (Lepton specific) | IV (Flipped) |
|---|---|---|---|---|---|
| | $g_{hVV}$ | $\sin(\beta - \alpha)$ | $\sin(\beta - \alpha)$ | $\sin(\beta - \alpha)$ | $\sin(\beta - \alpha)$ |
| | $g_{ht\bar{t}}$ | $\cos\alpha/\sin\beta$ | $\cos\alpha/\sin\beta$ | $\cos\alpha/\sin\beta$ | $\cos\alpha/\sin\beta$ |
| $h$ | $g_{hb\bar{b}}$ | $\cos\alpha/\sin\beta$ | $-\sin\alpha/\cos\beta$ | $\cos\alpha/\sin\beta$ | $-\sin\alpha/\cos\beta$ |
| | $g_{h\tau\bar{\tau}}$ | $\cos\alpha/\sin\beta$ | $-\sin\alpha/\cos\beta$ | $-\sin\alpha/\cos\beta$ | $\cos\alpha/\sin\beta$ |
| | $g_{H^0VV}$ | $\cos(\beta - \alpha)$ | $\cos(\beta - \alpha)$ | $\cos(\beta - \alpha)$ | $\cos(\beta - \alpha)$ |
| | $g_{H^0t\bar{t}}$ | $\sin\alpha/\sin\beta$ | $\sin\alpha/\sin\beta$ | $\sin\alpha/\sin\beta$ | $\sin\alpha/\sin\beta$ |
| $H^0$ | $g_{H^0b\bar{b}}$ | $\sin\alpha/\sin\beta$ | $\cos\alpha/\cos\beta$ | $\sin\alpha/\sin\beta$ | $\cos\alpha/\cos\beta$ |
| | $g_{H^0\tau\bar{\tau}}$ | $\sin\alpha/\sin\beta$ | $\cos\alpha/\cos\beta$ | $\cos\alpha/\cos\beta$ | $\sin\alpha/\sin\beta$ |
| | $g_{AVV}$ | $0$ | $0$ | $0$ | $0$ |
| | $g_{At\bar{t}}$ | $\cot\beta$ | $\cot\beta$ | $\cot\beta$ | $\cot\beta$ |
| $A$ | $g_{Ab\bar{b}}$ | $-\cot\beta$ | $\tan\beta$ | $-\cot\beta$ | $\tan\beta$ |
| | $g_{A\tau\bar{\tau}}$ | $-\cot\beta$ | $\tan\beta$ | $\tan\beta$ | $-\cot\beta$ |

Table 2.1: Couplings of the mass eigenstates of the neutral CP-even scalars $h$ and $H^0$, and CP-odd scalar $A$ in the four types of 2HDM with a $\mathbb{Z}_2$ symmetry. The table follows the convention of [129]. All couplings are normalized to those of the SM Higgs, and only the coupling to the heaviest SM fermion with a particular set of quantum numbers is shown. Here $\tan\beta \equiv \langle H_2 \rangle / \langle H_1 \rangle$ and the mixing angle $\alpha \in (-\pi/2, \pi/2)$ defines the admixture of $H_{1,2}$ that make up the mass eigenstates $h, H^0$. In the 2HDM+S setup, the couplings of the singlet-like pseudoscalar $a$ are identical to the couplings of $A$, up to an overall mixing angle. The couplings of the singlet-like scalar $s$ can be obtained (again up to an overall mixing angle) from the $h$-couplings by replacing $\alpha \to \alpha'$, where the free parameter $\alpha'$ defines the mixture of $H_{1,2}$ that mixes with $s$ (see [64] for details). The couplings listed here can be used for the calculation of the singlet branching ratios in the 2HDM+S, as additional mixing angles drop out.

Second, we add to the 2HDM one complex scalar singlet,

$$S = \frac{1}{\sqrt{2}}(S_R + iS_I),$$

which may attain a vacuum expectation value that we implicitly expand around. This singlet only couples to $H_{1,2}$ in the potential and has no direct Yukawa couplings, acquiring all of its couplings to SM fermions through its mixing with $H_{1,2}$. This mixing needs to be small to avoid spoiling the SM-like nature of $h$.

Under these two simple assumptions, exotic Higgs decays of the form

$$h \to ss \to X\bar{X}Y\bar{Y} \quad \text{or} \quad h \to aa \to X\bar{X}Y\bar{Y} \tag{2.40}$$

22
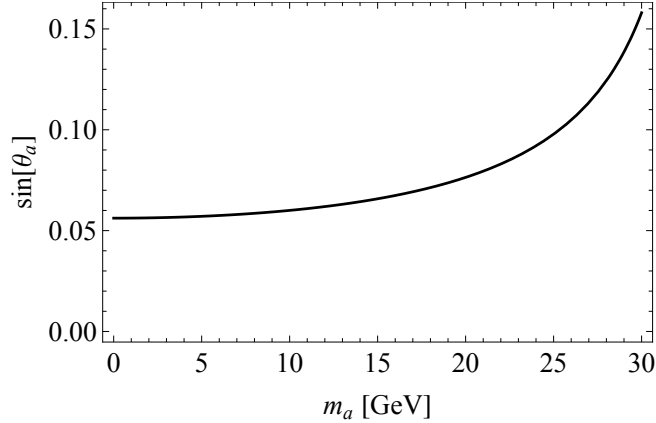
Figure 2.3: Required mixing angle between the doublet and singlet-sector pseudoscalar for $\mathrm{Br}(h \to aZ) = 10\%$, assuming no other exotic Higgs decays and $\alpha = \pi/2 - \beta$ (decoupling limit).

as well as

$$h \to aZ \to X\bar{X}Y\bar{Y} \tag{2.41}$$

are possible, where $s(a)$ is a (pseudo)scalar mass eigenstates mostly composed of $S_R(S_I)$ and $X, Y$ are SM fermions or gauge bosons. We refer to this setup as the 2HDM+S. For type-II 2HDM+S, a light $a$ corresponds roughly to the R-symmetry limit of the NMSSM. However, the more general 2HDM framework allows for exotic Higgs decay phenomenologies that are much more diverse than those usually considered in an NMSSM-type setup.

To incorporate the already analyzed constraints on 2HDMs into the 2HDM+S (*e.g.* [140]), one can imagine adding a decoupled singlet sector to a 2HDM with $\alpha, \beta$ chosen so as to not yet be excluded.[6] The real and imaginary components of $S$ can be given separate masses, and small mixings to the 2HDM sector can then be introduced as a perturbation. Approximately the same constraints on $\alpha, \beta$ apply to this 2HDM+S, as long as $\mathrm{Br}(h \to ss/aa/Za) \lesssim 10\%$. This allows for a wide range of possible exotic Higgs decays. There are some important differences depending on whether the lightest singlet state with a mass below $m_h/2$ is scalar or pseudoscalar. We will discuss them in turn.

**Light Pseudoscalar ($a$)**  There are two pseudoscalar states in the 2HDM+S, one that is mostly $A$ and one that is mostly $S_I$. One can choose the mostly-singlet-like pseudoscalar

$$a = \cos\theta_a S_I + \sin\theta_a A \quad, \qquad \theta_a \ll 1, \tag{2.42}$$

---

[6]As we have pointed out in Sec. 2.3.1, bottomonium decays provide no meaningful constraint on the 2HDM+S scenario.

to be lighter than the SM-like Higgs. There are two possible exotic Higgs decays: $h \to Za$ for $m_a < m_h - m_Z \approx 35$ GeV and $h \to aa$ for $m_a < m_h/2 \approx 63$ GeV.

The partial width $\Gamma(h \to Za)$ is entirely fixed by the 2HDM parameters $\alpha, \beta$ and the mixing angle $\theta_a$. The relevant interaction term in the effective Lagrangian is

$$\mathcal{L}_{\text{eff}} \supset g_{\text{eff}}(a\partial^\mu h - h\partial^\mu a)Z_\mu, \quad \text{where} \quad g_{\text{eff}} = \sqrt{\frac{g^2 + g'^2}{2}} \sin(\alpha - \beta) \sin\theta_a, \qquad (2.43)$$

which gives

$$\Gamma(h \to Za) = \frac{g_{\text{eff}}^2}{16\pi} \frac{[(m_h + m_Z + m_a)(m_h - m_Z + m_a)(m_h + m_Z - m_a)(m_h - m_Z - m_a)]^{3/2}}{m_h^3 m_Z^2}.$$
$$(2.44)$$

Fig. 2.3 shows that $\theta_a \sim 0.1$ gives $\text{Br}(h \to Za) \sim 10\%$ in the absence of other exotic decays.

Two terms in the effective Lagrangian give rise to $h \to aa$ decays:

$$\mathcal{L}_{\text{eff}} \supset g_{hAA} \, hAA + \lambda_S |S^2|^2. \qquad (2.45)$$

In terms of mass eigenstates, this contains

$$\mathcal{L}_{\text{eff}} \supset g_{hAA} \sin^2\theta_a \, haa + 4\lambda_S v_s \sin\zeta_1 \cos^2\theta_a \, haa, \qquad (2.46)$$

where $\langle S \rangle = v_s$ is the singlet vacuum expectation value, and the (presumably small) mixing angle $\zeta_1$ determines the singlet scalar content of the SM-like Higgs, see Eq. (2.47). The first term by itself can easily give rise to $\text{Br}(h \to aa) \sim 10\%$ if $g_{hAA} \sim v$ and $\theta_s \sim 0.1$, see Fig. 2.1. (Fig. 2.1 shows the results for Higgs partial widths to scalars, but these are almost identical to pseudoscalars, except near threshold.) The additional contribution from the second term (even without a singlet scalar below the Higgs mass) means that $\text{Br}(h \to aa)$ and $\text{Br}(h \to Za)$ can be independently adjusted.

The decay of $a$ to SM fermions proceeds via the $A$ couplings in Tab. 2.1, multiplied by $\sin\theta_a$. Therefore, once the type of 2HDM model has been specified, the exotic Higgs decay phenomenology is entirely dictated by the two exotic branching ratios $\text{Br}(h \to aa)$ and $\text{Br}(h \to Za)$, as well as $\tan\beta$, which determines $a$'s fermion couplings. Perturbative unitarity of the Yukawa couplings sets a lower bound of $\tan\beta > 0.28$ [140]; we will show results for $\tan\beta$ as low as $\sim 0.5$.

In Figs. 2.5–2.7, we show $\text{Br}(a \to X\bar{X})$, where $X$ is a SM particle. These include $\mathcal{O}(\alpha_s^2, \alpha_s^3)$ radiative corrections for decays to quarks, which can be readily computed [114, 113] (for details see Appendix A.1). As mentioned in Section 2.3.1, perturbative QCD can be used for pseudoscalar masses above $\sim 1$ GeV, though the calculation breaks down near quarkonium states [141]. A detailed investigation of this is beyond the scope of this thesis. The results can be summarized as follows:

- type-I (Fig. 2.4): Since all fermions couple only to $H_2$, the branching ratios are independent of $\tan\beta$. The pseudoscalar couplings to all fermions are proportional to those of the SM Higgs, all with the same proportionality constant, and the branching ratios are thus very similar to those of the SM+S model with a complex $S$ and a light pseudo-scalar $a$ (i.e., for example, proportional to the mass of the final state fermions).

- type-II (Fig. 2.5): The exotic decay branching ratios are those of NMSSM models. Unlike type-I models, they now depend on $\tan\beta$, with decays to down-type fermions suppressed (enhanced) for down-type fermions for $\tan\beta < 1$ ($\tan\beta > 1$).

- type-III (Fig. 2.6): The branching ratios are $\tan\beta$ dependent. For $\tan\beta > 1$, pseudoscalar-decays to leptons are enhanced over decays to quarks. For example, unlike the NMSSM above the $b\bar{b}$-threshold, decays to $\tau^+\tau^-$ can dominate over decays to $b\bar{b}$; similarly, above the $\mu^+\mu^-$ threshold, decays to $\mu^+\mu^-$ can dominate over decays to heavier, kinematically accessible quark-pairs. This justifies extending, for example, NMSSM-driven $4\tau$ searches over the entire mass range above the $b\bar{b}$-threshold. For $\tan\beta < 1$, decays to quarks are enhanced over decays to leptons.

- type-IV (Fig. 2.7): The branching ratios are $\tan\beta$ dependent. For $\tan\beta < 1$ and compared to the NMSSM, the pseudoscalar-decays to up-type quarks and leptons can be enhanced with respect to down-type quarks, so that branching ratios to $b\bar{b}$, $c\bar{c}$ and $\tau^+\tau^-$ can be similar. This opens up the possibility of detecting this model in the $2b2\tau$ or $2c2\tau$ final state.

Note that the branching ratios are only independent of $\tan\beta$ for type-I, and all types reduce to type-I for $\tan\beta = 1$.

A sizable $\mathrm{Br}(h \to Za)$ would open up additional exciting search channels with leptons that reconstruct the $Z$-boson. A detailed discussion for the sencario can be found in [142].

For $3m_\pi < m_a < 1$ GeV the decay rate calculations suffer large theoretical uncertainties but the dominant decay channels will likely be muons and hadrons. Below the pion, muon, and electron thresholds, the pseudoscalar decays dominantly to muons, electrons, and photons, respectively, except for $\tan\beta < 1$ in type-II, III and $\tan\beta > 1$ in type-IV, where the suppressed lepton couplings can also cause decays to photons to dominate below the pion threshold. If the pseudoscalar couples to both quarks and leptons, then requiring its mixing angle to be small enough to not conflict with constraints from *e.g.* meson decays and the muon anomalous magnetic moment implies that any allowed decay to two muons (for $2m_\mu < m_a < 3m_\pi$) is likely to have at least a displaced vertex (or be detector-stable), while any allowed decay to two electrons (for $2m_e < m_a < 2m_\mu$) will be detector stable [143]. For
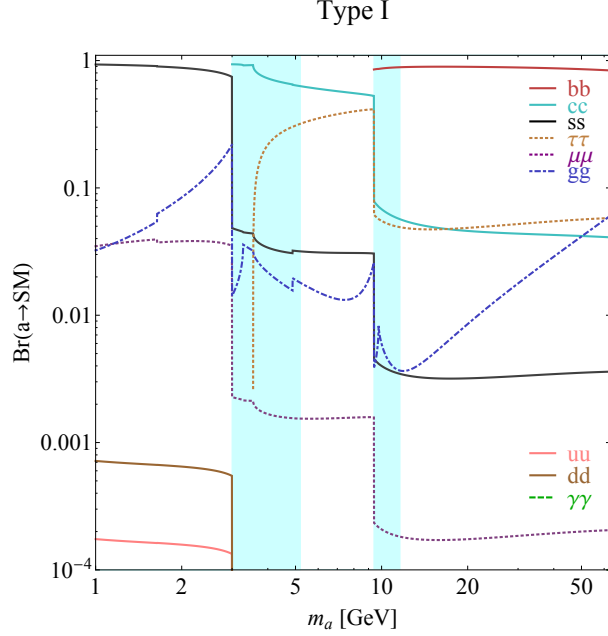
Figure 2.4: Branching ratios of a singlet-like pseudoscalar in the 2HDM+S for type-I Yukawa couplings. Decays to quarkonia likely invalidate our simple calculations in the shaded regions.
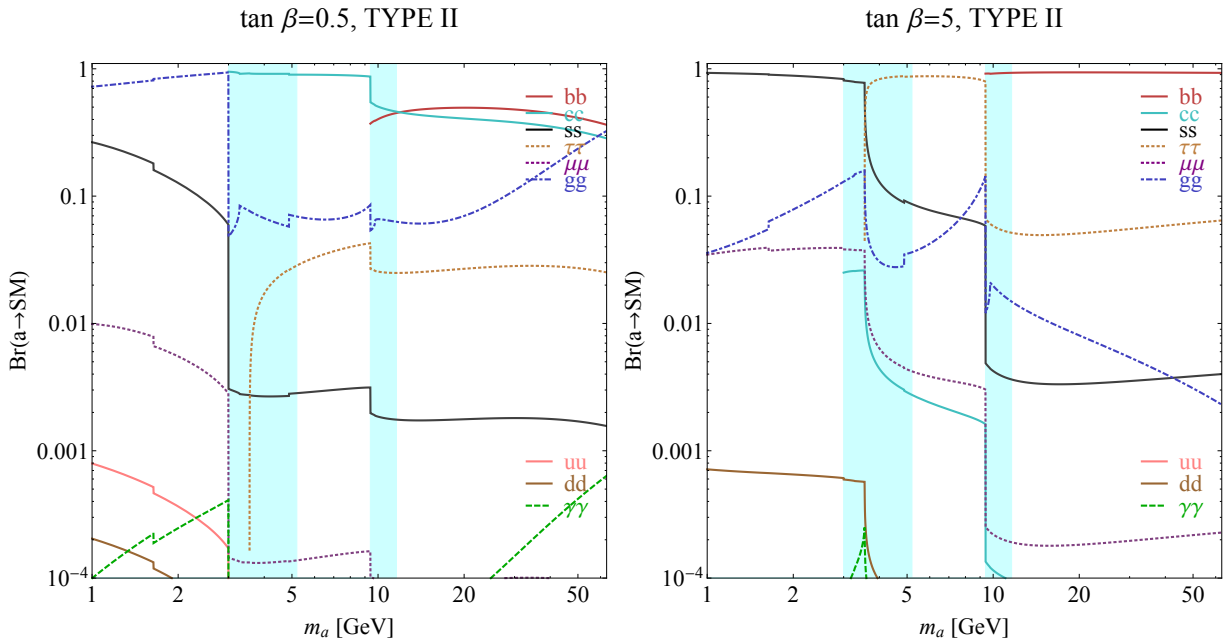


Figure 2.5: Branching ratios of a singlet-like pseudoscalar in the 2HDM+S for type-II Yukawa couplings. Decays to quarkonia likely invalidate our simple calculations in the shaded regions.
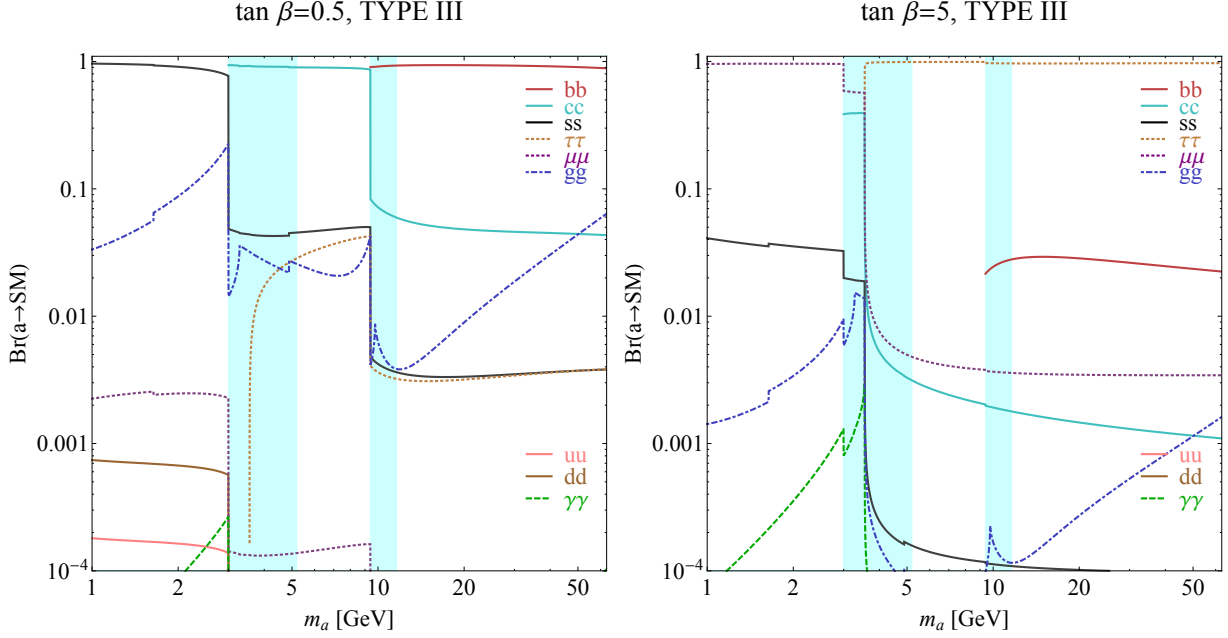
Figure 2.6: Branching ratios of a singlet-like pseudoscalar in the 2HDM+S for type-III Yukawa couplings. Decays to quarkonia likely invalidate our simple calculations in the shaded regions.
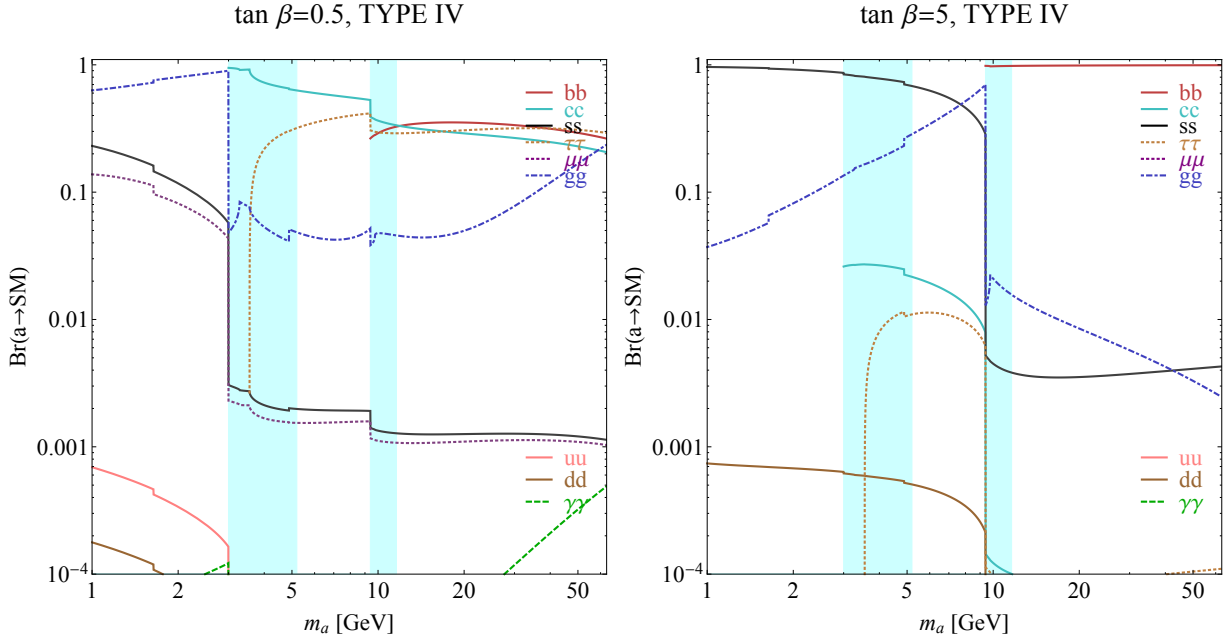


Figure 2.7: Branching ratios of a singlet-like pseudoscalar in the 2HDM+S for type-IV Yukawa couplings. Decays to quarkonia likely invalidate our simple calculations in the shaded regions.

pseudoscalars that couple preferentially to leptons, the meson-decay constraints are absent and prompt decays to muons are allowed; however, allowed decays to electrons will likely have at least a displaced vertex, and need to be detector-stable as $m_a$ is decreased well below the muon threshold [143].

**Light Scalar ($s$)**   We now assume that the mass of the real singlet $S_R$ is below $m_h/2$. The scalar Higgs spectrum, Eq. (2.38), gets extended by the additional real singlet, which mixes with the doublet sector

$$
\begin{pmatrix} h \\ H^0 \\ s \end{pmatrix} = \begin{pmatrix} 1 & 0 & 0 \\ 0 & \cos\zeta_2 & \sin\zeta_2 \\ 0 & -\sin\zeta_2 & \cos\zeta_2 \end{pmatrix} \begin{pmatrix} \cos\zeta_1 & 0 & \sin\zeta_1 \\ 0 & 1 & 0 \\ -\sin\zeta_1 & 0 & \cos\zeta_1 \end{pmatrix} \begin{pmatrix} -\sin\alpha & \cos\alpha & 0 \\ \cos\alpha & \sin\alpha & 0 \\ 0 & 0 & 1 \end{pmatrix} \begin{pmatrix} H^0_{1,R} \\ H^0_{2,R} \\ S_R \end{pmatrix}.
$$

If we assume that the mixing angles $\zeta_{1,2}$ are small, this simplifies to

$$
\begin{pmatrix} h \\ H^0 \\ s \end{pmatrix} = \begin{pmatrix} -\sin\alpha & \cos\alpha & \zeta_1 \\ \cos\alpha & \sin\alpha & \zeta_2 \\ (-\zeta_2\cos\alpha + \zeta_1\sin\alpha) & (-\zeta_1\cos\alpha - \zeta_2\sin\alpha) & 1 \end{pmatrix} \begin{pmatrix} H^0_{1,R} \\ H^0_{2,R} \\ S_R \end{pmatrix}. \tag{2.47}
$$

In this approximation, $h$ and $H$ have the same Yukawa couplings as in the regular 2HDM but now contain a small $S_R$ component that allows the decay $h \to ss$. The mostly-singlet state $s$ on the other hand mixes with some admixture of $H^0_{1,R}$ and $H^0_{2,R}$. This can be expressed in more familiar notation by adopting the following parameterization for the small singlet-doublet mixing angles

$$
\zeta_1 = -\zeta\cos(\alpha - \alpha') \quad , \quad \zeta_2 = -\zeta\sin(\alpha - \alpha') \, , \tag{2.48}
$$

$$
\implies \begin{pmatrix} h \\ H^0 \\ s \end{pmatrix} = \begin{pmatrix} -\sin\alpha & \cos\alpha & -\zeta\cos(\alpha - \alpha') \\ \cos\alpha & \sin\alpha & -\zeta\sin(\alpha - \alpha') \\ -\zeta\sin\alpha' & \zeta\cos\alpha' & 1 \end{pmatrix} \begin{pmatrix} H^0_{1,R} \\ H^0_{2,R} \\ S_R \end{pmatrix}. \tag{2.49}
$$

The *arbitrary* angle $\alpha'$ determines the $H^0_{1R,2R}$ admixture contained within $s$, while the *small* mixing parameter $\zeta$ gives its overall normalization. The couplings of $s$ to SM fields are now identical to those of the SM-like Higgs $h$ in Tab. 2.1, scaled down by $\zeta$ and with the replacement $\alpha \to \alpha'$. Since $\alpha$ and $\alpha'$ can be independently chosen, $s$ can have an even broader range of branching ratios than $a$ and mirrors the range of possible $h$-decays in the regular 2HDM, but without a mass restriction beyond $m_s < m_h/2$. Just as for $h$, choosing $\alpha' \to \frac{\pi}{2} - \beta$ amounts to giving $s$ fermion couplings that are SM-Higgs-like (up to the overall mixing factor $\zeta$). In this limit, the 2HDM+S theory reduces to the SM+S case discussed in
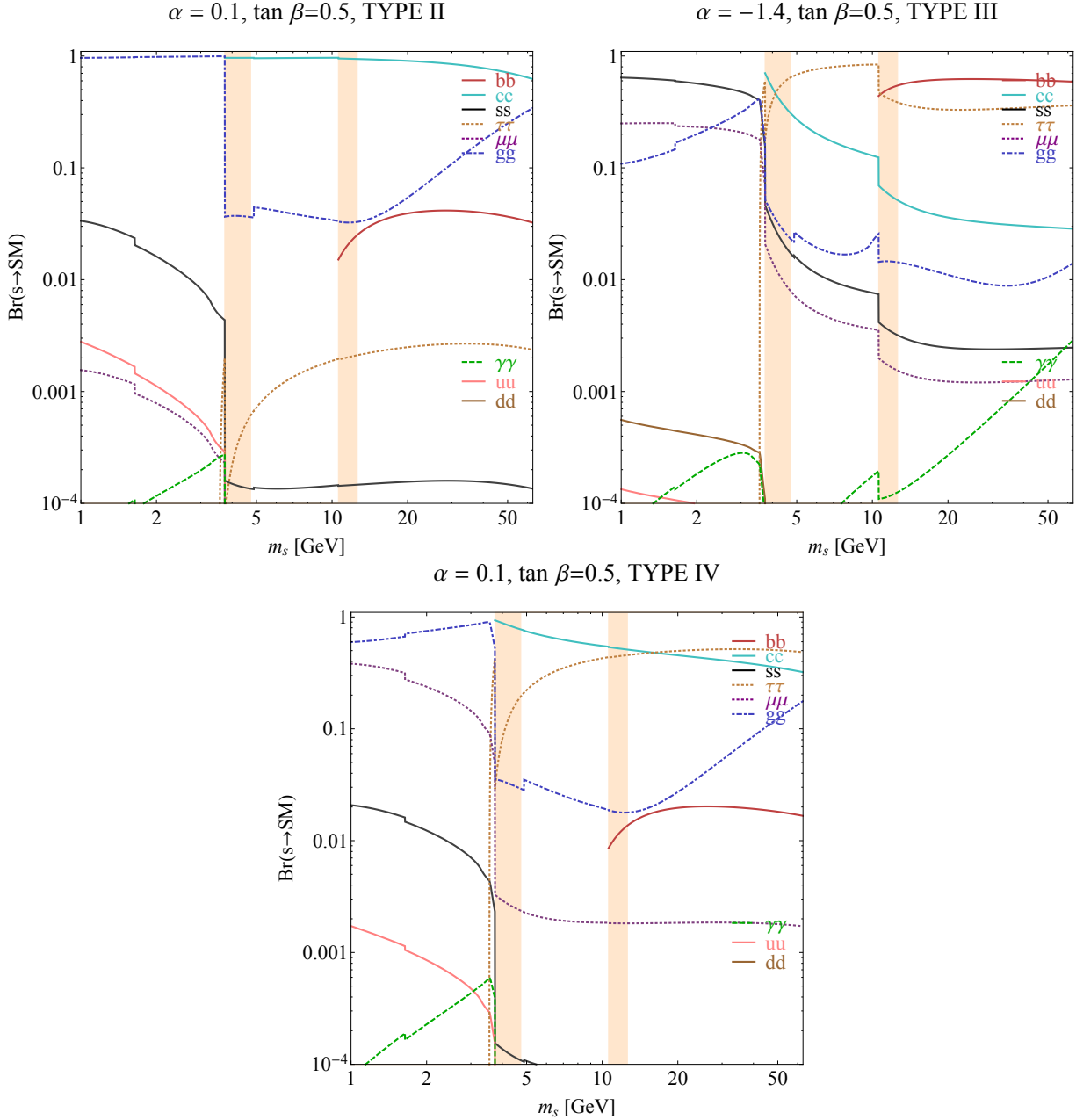
Figure 2.8: Singlet-like scalar branching ratios in the 2HDM+S for different $\tan\beta, \alpha'$ and Yukawa coupling type. These examples illustrate the possible qualitative differences to the pseudoscalar case, such as dominance of $s \to c\bar{c}$ decay above $b\bar{b}$-threshold; democratic decay to $b\bar{b}$ and $\tau^+\tau^-$; and democratic decay to $c\bar{c}$ and $\tau^+\tau^-$. Hadronization effects likely invalidate our simple calculations in the shaded regions.

Sec. 2.3.1. On the other hand, choosing $\alpha' = \beta$ gives the same couplings as the pseudoscalar case.

The $s \to X\bar{X}$ branching ratios are computed analogously to the pseudoscalar case, with further details again given in Appendix A.1. There is a large range of possible decay phenomenologies. Fig. 2.8 illustrates some examples that have qualitatively new features compared to the pseudoscalar case, namely the possible dominance of $s \to c\bar{c}$ decays above the $b\bar{b}$-threshold; similar decay rates to $b\bar{b}$ and $\tau^+\tau^-$; and similar decay rates to $c\bar{c}$ and $\tau^+\tau^-$.

To sum up, 2HDM+S model allows for a large variety of Higgs decay phenomenologies $h \to aa \to X\bar{X}Y\bar{Y}$, $h \to ss \to X\bar{X}Y\bar{Y}$, and $h \to aZ \to X\bar{X}Y\bar{Y}$ by coupling the SM-like Higgs $h$ to a singlet-like scalar $s$ or pseudoscalar $a$. While the singlet's couplings within each fermion "family" (down-type quarks, up-type quarks, or leptons) are ranked by their Yukawa couplings, the relative coupling strength to each family can be adjusted, and arbitrarily so in the scalar case. In Chapter 4.1, we will illustrate the rich decay phenomenology of exotic Higgs decays through a detailed analysis for $h \to aa(ss) \to b\bar{b}\mu^+\mu^-$.

# Chapter 3

# Searching for Dark Photons

For light dark photon with a mass far smaller than that of $Z$-boson mass, the mixing between dark photon and the SM photon leads to an $\epsilon$-suppressed coupling of the dark photon and SM charge current, where $\epsilon$ stands for the kinetic mixing parameter. Consequently a substantial effort is underway to search for a dark photon in a variety of high-intensity experiments. In this chapter, we will show two examples for dark photon searches. The first is based on the upcoming Mu3e experiment at the Paul Scherrer Institute (PSI) in Switzerland. Novel probes aiming dark photons with visible decays are proposed. The second is based on low energy $e^+e^-$ colliders, such as *BABAR* and upcoming Bell-II experiment in Japan. There are we focus on searching for dark photons with invisible decays.

## 3.1  Searching for Dark Photon with Rare Muon Decays at the Mu3e

The Mu3e experiment use an unprecedented number of muon decays[1] in their search for the lepton flavor violating decay $\mu^+ \to e^+e^-e^+$, the Mu3e can also search for the decay $\mu^+ \to e^+ \nu_e \bar{\nu}_\mu A'$, $A' \to e^+e^-$ shown in Fig. 3.1. This allows them to probe currently unexplored regions of the dark photon parameter space. We note that while our focus will be on vector bosons (the dark photon), other particles that couple to electrons and/or muons and decay to an $e^+e^-$ pair could also be probed with the Mu3e.

Here we will show that the Mu3e can probe dark photons in the mass range $2m_e < m_{A'} < m_\mu$, where $m_e$ ($m_\mu$) is the electron (muon) mass, and improve upon current constraints on $\epsilon$ in the range $10 \text{ MeV} \lesssim m_{A'} \lesssim 80 \text{ MeV}$, down to $\epsilon^2 \sim 10^{-8}$. This probes well into the mentioned above parameter region motivated from embedding the $U(1)_Y$ in a GUT, as well

---

[1] "Muon" refers to $\mu^+$ in this section.
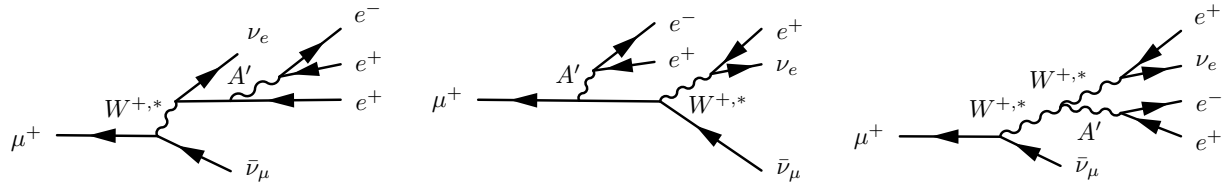
Figure 3.1: Feynman diagrams for (on-shell) dark photon production in muon decays, $\mu^+ \to e^+ \nu_e \bar{\nu}_\mu A'$, $A' \to e^- e^+$.

as probing $a_\mu$ favored dark photon to SM branching ratios significantly less than 100%. Depending on the performance of the detector, Mu3e may also be sensitive to long-lived dark photons, which produce displaced vertices.

### 3.1.1   The Search Set-up with the Mu3e

The Mu3e experiment at PSI [144] has been proposed to search for the charged lepton flavor violating decay $\mu^+ \to e^+ e^- e^+$ with an ultimate sensitivity of $10^{-16}$, four orders below the current limits. It will take advantage of one of the most intense sources of muons in the world. During its first phase (2015 – 2016), Mu3e will probe $10^{15}$ muon decays, and more than $5.5 \times 10^{16}$ muon decays by the end of phase II (2018 and beyond). To achieve the required sensitivity, a novel design based on high-granularity thin silicon pixel detectors, supplemented by a fast timing system, has been proposed.

The large statistics and excellent detector resolution offer an ideal setup to search for dark photon production in muon decays as well. The production mechanism is illustrated in Fig. 3.1: the dark photon can be either emitted from the initial state radiation off the $\mu^+$, or final state radiation off the $e^+$, or radiate off the internal $W$-boson. The latter process is suppressed by $\sim m_\mu^2/m_W^2 \sim 10^{-6}$ at the amplitude level compared to the other processes due to the different propagators appearing in the diagrams (this is similar for the corresponding SM process where the dark photon is replaced by the SM photon, see also [145]). The corresponding decay width of $\mu^+ \to e^+ \nu_e \bar{\nu}_\mu A'$, is evaluated using `MadGraph5_aMC@NLO` [146] for $m_{A'}$ ranging from 1.1 MeV to 100 MeV. Approximating the total decay width, $\Gamma_{\text{tot}}$, as the SM muon decay width, the resulting branching ratio $B_{\text{sig}}$ is presented in Fig. 3.2 for $\epsilon = 0.1$. We also include a parametrized curve (red, labeled "fit") of the form $B_{\text{sig}} = B_{\text{sig}}(\epsilon, m_{A'})$ with

$$B_{\text{sig}} = \frac{1}{3 \times 10^{-19}} \left(\frac{\epsilon}{0.1}\right)^2 \exp\left(\sum_{i=0}^{5} a_i \left(\frac{m_{A'}}{\text{GeV}}\right)^i\right), \tag{3.1}$$

where $a_0 = -50.866$, $a_1 = -360.93$, $a_2 = 13998.59$, $a_3 = -3.731 \times 10^5$, $a_4 = 4.442 \times 10^6$, $a_5 = -2.015 \times 10^7$, and we take the fine structure constant $\alpha = 1/137.036$ and $\Gamma_{\text{tot}} \simeq$
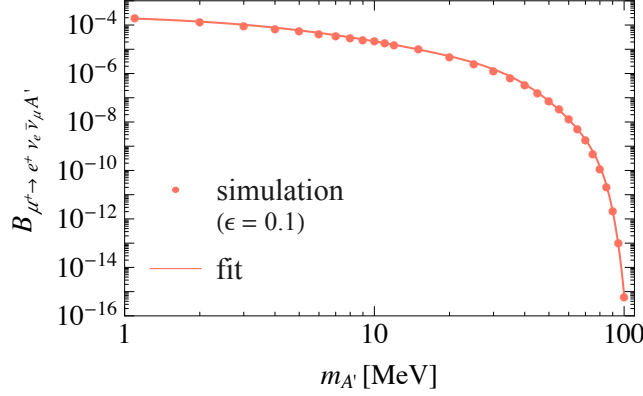
Figure 3.2: The branching ratio of the muon decay channel $\mu^+ \to e^+ \nu_e \bar{\nu}_\mu A'$ with $\epsilon = 0.1$. Shown are the numerical values computed with `MadGraph5_aMC@NLO` (red points) and a parametrized fit to these numerical values (red solid line), which is given by Eq. (3.1).
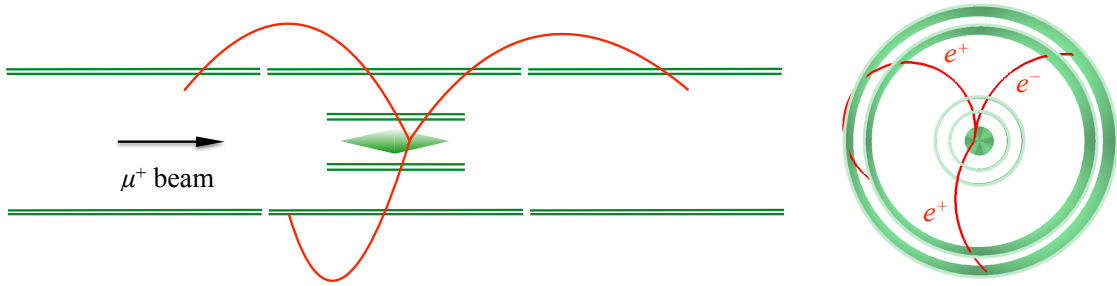


Figure 3.3: **Left:** Side view of the experimental setup (adapted from [144]). A muon beam impinges on a target consisting of two hollow aluminum cones connected at their base. A silicon tracker composed of two inner and two outer double layers of cylindrical pixel silicon surrounds the target. Although not included in the simulation, a time-of-flight device provides a timing measurement with a resolution of 250 ps. A simulated $\mu^+ \to e^+ \nu_e \bar{\nu}_\mu A'$, $A' \to e^+ e^-$ event is shown. **Right:** Transverse view of the experimental setup. The stopping target is shown at the center, surrounded by two inner and two outer cylindrical layers of silicon detectors.

$3 \times 10^{-19}$ GeV [147].

For $2m_e \leq m_{A'} \leq 2m_\mu$, the dominant decay is $A' \to e^+ e^-$ (the loop-induced decay $A' \to 3\gamma$ is highly suppressed and only important for $m_{A'} < 2m_e$). The main signature of such a dark photon is that the invariant mass of the $e^+ e^-$-pair from the dark photon decay must equal $m_{A'}$. The invariant mass spectrum is dominated by SM background events (see Sec. 3.1.2), but a resonance search or "bump-hunt" can be used to search for a dark photon.

In addition to a resonance search, displaced $e^+e^-$ vertices can also be used to probe long-lived dark photons. The dark photon width and the proper decay length are given by, respectively,

$$\Gamma_{A'\to e^+e^-} = \frac{\alpha\,\epsilon^2}{3}\,m_{A'}\,\sqrt{1 - \frac{4m_e^2}{m_{A'}^2}}\left(1 + \frac{2m_e^2}{m_{A'}^2}\right), \tag{3.2}$$

$$c\,\tau_{A'\to e^+e^-} \simeq 0.8 \text{ mm}\,\left(\frac{10^{-4}}{\epsilon}\right)^2\frac{10 \text{ MeV}}{m_{A'}}\,. \tag{3.3}$$

For small-enough values of $\epsilon$, the dark photon will travel a finite distance and the $e^+e^-$-pair will be reconstructed as a displaced vertex (for even smaller values, the decay length will be large enough to allow for the shielding of almost any backgrounds, as in beam-dump experiments). Since the backgrounds are expected to be greatly reduced with respect to prompt decays, displaced vertices could provide sensitivity to low values of the kinematic mixing.

### 3.1.2 Projections for Dark Photon Searches with the Mu3e

The sensitivity to dark photons with an experimental setup similar to that of Mu3e is studied using a simulation program, `FastSim`, that was originally developed for the Super$B$ experiment [148], based on the software framework and analysis tools used by the *BABAR* collaboration [149, 150]. Detector components are described in `FastSim` as two-dimensional shells of geometric objects, such as cylinders, disks, or planes, and the effect of the physical thickness is modeled parametrically. Coulomb scattering and energy loss by ionization are described with the standard parametrization in terms of radiation length and particle momentum. Simplified cross sections are used to describe Bremsstrahlung and pair production. Tracking measurements are simulated in terms of single-hit and two-hit resolutions, while silicon strip detectors are modeled as two independent orthogonal projections. Tracks are reconstructed from the simulated hits passed to the *BABAR* Kalman filter track fitting algorithm. Uncertainties associated with pattern recognition algorithms traditionally used to form track hits are introduced using models based on the *BABAR* pattern recognition algorithm performance.

The `FastSim` model is a simplified version of the proposed Mu3e detector [144], which consists of a silicon tracker composed of two inner and two outer double layers of cylindrical pixel silicon detectors surrounding the target. The inner layers have a length of 12 cm, while the outer silicon layers are extended to a length of 180 cm to improve the momentum resolution of recurling tracks. The innermost (outermost) silicon detectors are placed at a radius of 1.9 cm (8.9 cm). Silicon sensors are simulated as 50 $\mu$m thick double-sided

striplet sensors mounted on 50 $\mu$m of kapton in `FastSim`. The spatial resolution of the hits is modeled as a sum of two components with resolutions of 8 $\mu$m and 20 $\mu$m. Although Mu3e uses pixel silicon sensors, we expect the performances of both tracking system to be comparable. The target is composed of two hollow aluminum cones connected at their base. Each cone is 5 cm long, 50 $\mu$m thick with a base radius of 1 cm. The entire detector is placed in a 1 T solenoidal magnetic field. Although not included in `FastSim`, a time-of-flight device provides a timing measurement. We assume a time resolution of 250 ps, averaging the values of the corresponding Mu3e detector systems. We define a coordinate system having the $z$-axis aligned along the axis of the cylindrical silicon detectors, with the transverse plane oriented perpendicular to the $z$-axis. The apparatus layout is displayed in Fig. 3.3, together with a simulated $\mu^+ \to e^+ \nu_e \bar{\nu}_\mu A'$, $A' \to e^+ e^-$ event.

## Promptly Decaying Dark Photons

We begin by studying the sensitivity of prompt dark photon decays in $\mu^+ \to e^+ \nu_e \bar{\nu}_\mu A'$, $A' \to e^+ e^-$ events. Large samples of signal and background events are generated to study the signal efficiency and background levels. We assume that muons decay uniformly at rest in the target. Signal events are generated with `MadGraph5_aMC@NLO` for 5 MeV $< m_{A'} <$ 100 MeV. The background processes can be classified as either *irreducible* or *accidental*:

- *Irreducible backgrounds* arise from events with internal conversions of the photon in $\mu^+ \to e^+ \nu_e \bar{\nu}_\mu \gamma^* (\to e^+ e^-)$ decays, or from radiative muon decays where the radiated photon converts into an electron-positron pair inside the target material. Conversion outside the target material, *i.e.* in the detector material, can be efficiently tagged and are not considered. These background processes are simulated using the matrix element and differential decay width given in [151, 145], and the events are normalized using the following branching ratios: $B_{\mu^+ \to e^+ \nu_e \bar{\nu}_\mu e^+ e^-} = (3.4 \pm 0.4) \times 10^{-5}$ and $B_{\mu^+ \to e^+ \nu_e \bar{\nu}_\mu \gamma} = (1.4 \pm 0.4)\%$ [147]. As the probability of photon conversion inside the target is of $\mathcal{O}(10^{-3})$, both channels contribute roughly equally to the irreducible background.

- *Accidental backgrounds* arise mainly from the combination of several muon decays where, *e.g.*, one of the positrons is misreconstructed as an electron. We consider background sources from the following accidental combinations: (1) three Michel decays ($\mu^+ \to e^+ \nu_e \bar{\nu}_\mu$) where one positron is misreconstructed as an electron ("3M decays"), (2) a Michel decay and a radiative Michel decay ($\mu^+ \to e^+ \nu_e \bar{\nu}_\mu \gamma$) where the photon converts to a $e^+ e^-$ pair in the target material and one positron remains undetected ("2M$_\gamma$ decays"), and (3) a Michel decay and a radiative Michel decay with internal conversion where one positron again remains undetected ("2M$_{3e}$ decays"). Another
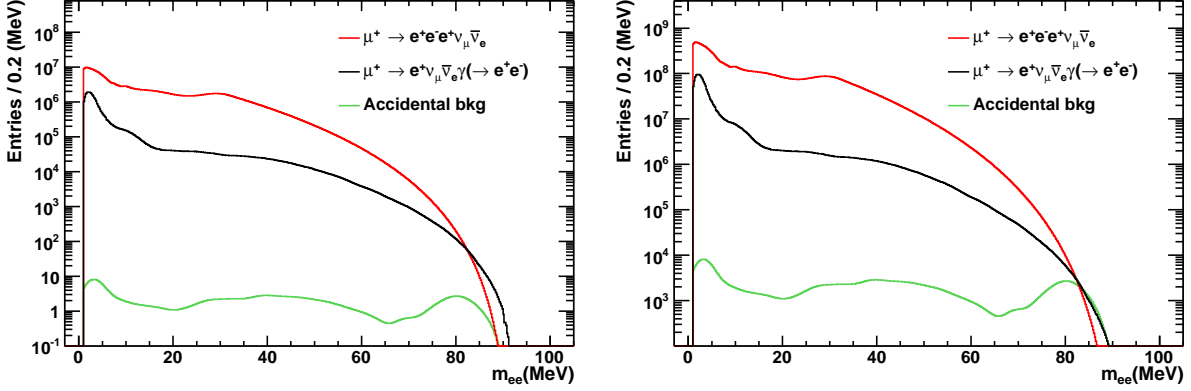
Figure 3.4: The expected $e^+e^-$ invariant mass distribution from the various sources of background displayed assuming a total number of $10^{15}$ (**top**) or $5.5 \times 10^{16}$ (**bottom**) muon decays for the phase I and II of Mu3e, respectively. The accidental backgrounds include the 3M, $2M_\gamma$, and $2M_{3e}$ backgrounds but not the $2M_{\text{Bhabha}}$ background (see text for details).

source of accidental background, which we will not include, arises from two Michel decays where the outgoing positron from one of the Michel decays produces an electron by interacting with the detector material via Bhabha scattering ("$2M_{\text{Bhabha}}$ decays"). Other sources of accidental backgrounds are expected to be smaller.

We generate signal and background events and process them with `FastSim` to determine the detection efficiency and the invariant mass distribution, $m_{e^+e^-}$. We require all electrons and positrons to have a minimum transverse momentum of 10 MeV to match the Mu3e tracker acceptance. The $\mu^+ \to e^+\nu_e\bar{\nu}_\mu e^+e^-$ candidates are formed by combining two positrons and an electron, and fit with the constraint that the tracks originate from the same position at the surface of the target. We select only well reconstructed candidates by requiring the probability of the $\chi^2$ of the constrained fit to be greater than 1%. Additional kinematic constraints can further distinguish $\mu^+ \to e^+\nu_e\bar{\nu}_\mu e^+e^-$ decays from accidental backgrounds. The magnitude of the sum of the momenta of the electron and two positrons ($|\vec{p}_{3e}| \equiv |\vec{p}_{e^-} + \vec{p}_{e^+,1} + \vec{p}_{e^+,2}|$) must be compatible with the muon decay hypothesis, requiring

$$|\vec{p}_{3e}| \leq \frac{m_\mu^2 - m_{3e}^2}{2m_\mu}, \tag{3.4}$$

where $m_{3e}$ is the invariant mass of the three tracks.

While we can reliably determine the efficiency of the signal and irreducible backgrounds, it is more challenging to estimate the accidental backgrounds with very high accuracy. However, the following approach, which is similar to that described by Mu3e [144], is sufficient for our purposes.

36
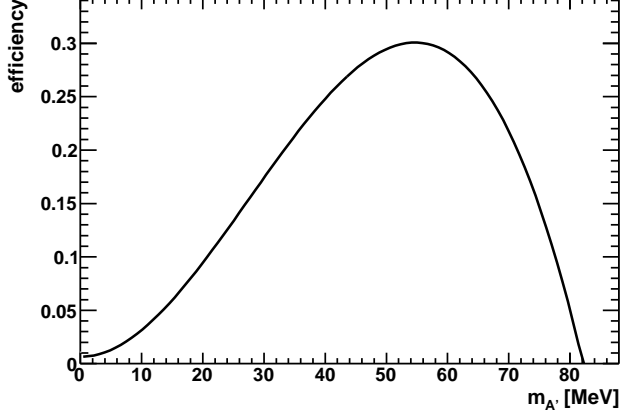
Figure 3.5: The signal efficiency as a function of the dark photon mass ($m_{A'}$) for prompt $\mu^+ \to e^+ \nu_e \bar{\nu}_\mu A'$, $A' \to e^+ e^-$ decays.

We first estimate the accidental background arising from three Michel decays, where one positron is misreconstructed as an electron ($N_{3M}$). We assume a measurement takes place in a time interval $T \gg \delta t$, where $\delta t$ is the time resolution. The probability for three decays to occur in the same time window is $(\delta t / T)^2$ and at the same position is $P_p^2$, where $P_p$ is the position suppression factor. Multiplying these probabilities with the branching ratio for three Michel decays, $B^3_{\mu^+ \to e^+ \nu_e \bar{\nu}_\mu}$, and the probability for one out of three positrons to be misreconstructed as an electron, $P_{e^+ \to e^-}$, the total probability for the 3M pile-up is given by

$$P_{3M} = \left( \frac{\delta t}{T} \right)^2 P_p^2 \, B^3_{\mu^+ \to e^+ \nu_e \bar{\nu}_\mu} \binom{3}{1} P_{e^+ \to e^-}. \tag{3.5}$$

During the time $T$, the total number of stopped muons, $N_\mu \equiv R_\mu T$, where $R_\mu$ is the instantaneous stopped muon rate for Mu3e phase I (II). The number of 3M pile-up event, $N_{3M}$, are related by

$$N_{3M} = \binom{N_\mu}{3} P_{3M}. \tag{3.6}$$

Substituting Eq. (3.5) into Eq. (3.6) yields the number of 3M event,

$$N_{3M} = \frac{1}{2} T R_\mu \left( R_\mu - \frac{1}{T} \right) \left( R_\mu - \frac{2}{T} \right) \delta t^2 P_p^2 B^3_{\mu^+ \to e^+ \nu_e \bar{\nu}_\mu}$$
$$\simeq \frac{1}{2} N_\mu R_\mu^2 \, \delta t^2 \, P_p^2 \, B^3_{\mu^+ \to e^+ \nu_e \bar{\nu}_\mu}, \tag{3.7}$$

which is Eq. (3.14). The approximation is valid in the limit $R_\mu T \gg 1$.

Similarly, the total probabilities for the $2M_\gamma$ and $2M_{3e}$ accidental backgrounds are given

by

$$P_{2\mathrm{M}_\gamma} = \binom{2}{1} B_{\mu^+\to e^+\nu_e\bar\nu_\mu} B_{\mu^+\to e^+\nu_e\bar\nu_\mu\gamma} P_\gamma, \tag{3.8}$$

$$P_{2\mathrm{M}_{3e}} = \binom{2}{1} B_{\mu^+\to e^+\nu_e\bar\nu_\mu} B_{\mu^+\to e^+\nu_e\bar\nu_\mu e^+e^-}, \tag{3.9}$$

respectively. Given the number of $2\mathrm{M}_\gamma$ and $2\mathrm{M}_{3e}$ as

$$N_{2\mathrm{M}_\gamma} = \binom{N_\mu}{2} P_{2\mathrm{M}_\gamma}, \tag{3.10}$$

$$N_{2\mathrm{M}_{3e}} = \binom{N_\mu}{2} P_{2\mathrm{M}_{3e}}, \tag{3.11}$$

one finds

$$
\begin{aligned}
N_{2\mathrm{M}_\gamma} &= TR_\mu\left(R_\mu - \frac{1}{T}\right)\delta t P_\mathrm{p} B_{\mu^+\to e^+\nu_e\bar\nu_\mu} B_{\mu^+\to e^+\nu_e\bar\nu_\mu\gamma} P_\gamma \\
&\simeq TR_\mu^2 \delta t P_\mathrm{p} B_{\mu^+\to e^+\nu_e\bar\nu_\mu} B_{\mu^+\to e^+\nu_e\bar\nu_\mu\gamma} P_\gamma,
\end{aligned}
\tag{3.12}
$$

$$
\begin{aligned}
N_{2\mathrm{M}_{3e}} &= TR_\mu\left(R_\mu - \frac{1}{T}\right)\delta t P_\mathrm{p} B_{\mu^+\to e^+\nu_e\bar\nu_\mu} B_{\mu^+\to e^+\nu_e\bar\nu_\mu e^+e^-} \\
&\simeq TR_\mu^2 \delta t P_\mathrm{p} B_{\mu^+\to e^+\nu_e\bar\nu_\mu} B_{\mu^+\to e^+\nu_e\bar\nu_\mu e^+e^-}.
\end{aligned}
\tag{3.13}
$$

The approximations in the above equations are again valid for $R_\mu T \gg 1$. Substituting $N_\mu \equiv R_\mu T$ back to Eq. (3.7), Eq. (3.12), and Eq. (3.13), we obtain

$$N_{3\mathrm{M}} \simeq \frac{1}{2} N_\mu R_\mu^2\, \delta t^2\, P_\mathrm{p}^2\, B_{\mu^+\to e^+\nu_e\bar\nu_\mu}^3\, P_{e^+\to e^-}, \tag{3.14}$$

$$N_{2\mathrm{M}_\gamma} \simeq N_\mu R_\mu\, \delta t\, P_\mathrm{p}\, B_{\mu^+\to e^+\nu_e\bar\nu_\mu} B_{\mu^+\to e^+\nu_e\bar\nu_\mu\gamma}\, P_\gamma, \tag{3.15}$$

$$N_{2\mathrm{M}_{3e}} \simeq N_\mu R_\mu\, \delta t\, P_\mathrm{p}\, B_{\mu^+\to e^+\nu_e\bar\nu_\mu} B_{\mu^+\to e^+\nu_e\bar\nu_\mu e^+e^-}, \tag{3.16}$$

where $N_\mu = 10^{15}$ ($2\times10^{16}$) and $R_\mu = 10^8/\mathrm{s}$ ($2\times10^9/\mathrm{s}$) for Mu3e phase I (II), $\delta t = 2.5\times10^{-10}\,\mathrm{s}$, $P_\mathrm{p} = 10^{-4}$, $P_{e^+\to e^-} = 0.5\%$, and $P_\gamma = 8\times10^{-4}$. Inserting the numbers, we find that the expected number of accidental background events over the lifetime of the experiment (before correcting for the efficiency) are given by, roughly, $N_{3\mathrm{M}} \sim 15,000$ (60,000), $N_{2\mathrm{M}_\gamma} \sim 30,000$ ($6\times10^6$), and $N_{2\mathrm{M}_\mathrm{e}} \sim 75,000$ ($2\times10^7$) for phase I (II). We use these numbers to normalize each accidental background component. We note that we will not consider the $2\mathrm{M}_\mathrm{Bhabha}$ background, as it is challenging to simulate reliably. More study is needed by the Mu3e Collaboration to determine its size, but preliminary estimates suggest that in the 10 MeV to 80 MeV mass range, this background should be at most comparable, but more likely subdominant, to the irreducible backgrounds.
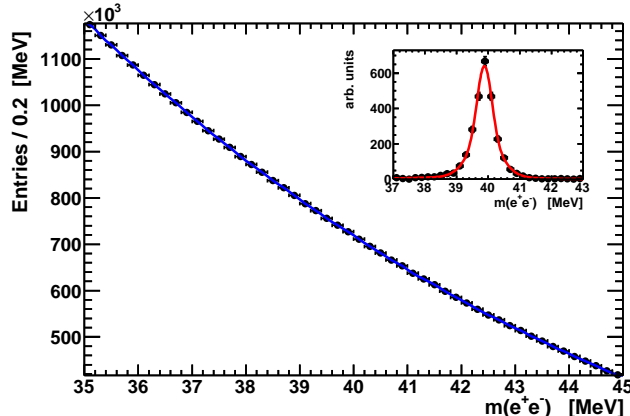
Figure 3.6: Fit to the $e^+e^-$ invariant mass distribution for a dark photon mass hypothesis of 40 MeV. The blue line shows the expected background. The signal probability density function, as obtained from a fit to the signal Monte Carlo sample, is shown as the red line in the insert.

The $e^+e^-$ invariant mass distribution of the most important irreducible and accidental backgrounds, after applying all selection criteria, is shown in Fig. 3.4, assuming a total number of $10^{15}$ (top plot) and $5.5 \times 10^{16}$ (bottom plot) muon decays for the two phases of Mu3e, respectively. Both combinations per muon candidate are considered and included in the corresponding histograms. The signal reconstruction efficiency is shown in Fig. 3.5 and varies between 7% and 41%, depending on the dark photon mass.

As expected, the distribution peaks towards low values of $m_{e^+e^-}$. The spectrum is dominated by $\mu^+ \to e^+\nu_e\bar{\nu}_\mu e^+e^-$ events (red line in Fig. 3.4) with an additional contribution from $\mu^+ \to e^+\nu_e\bar{\nu}_\mu\gamma$ with the conversion $\gamma \to e^+e^-$ in the target material (black line). The accidental backgrounds (green line) are subdominant, except for $m_{e^+e^-} \gtrsim 80$ MeV, where they become comparable to the irreducible contribution. However, as we will discuss below, this region is already well explored by existing experiments. Therefore, even if our accidental background estimate is off by a factor of a few, it will have little impact on the the dark-photon parameter region probed by Mu3e that is currently unexplored ($m_{A'} \lesssim 70$ MeV).

A dark photon signal would appear as a narrow peak over the smooth background distribution. The signal resolution is determined by fitting the corresponding mass spectrum with a sum of three Gaussians. The central mass resolution is at the level of $0.2-0.3$ MeV, almost independent of $m_{A'}$. We checked that these results are similar to the expected performance of the Mu3e detector [144].

We estimate the signal sensitivity by fitting a signal component on top of the expected
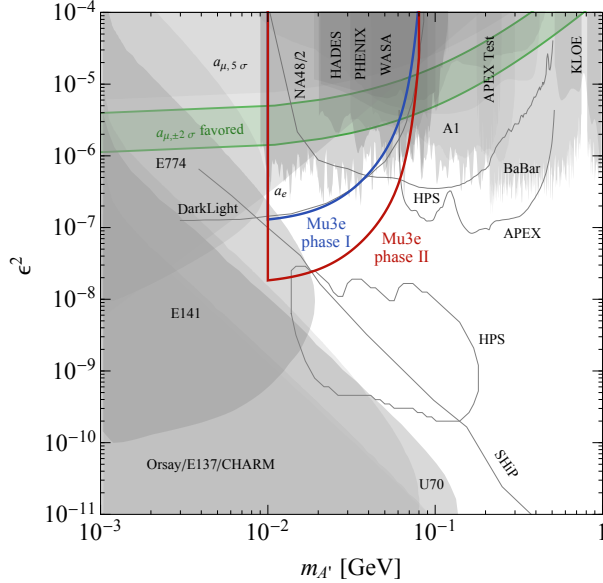
Figure 3.7: Prospects and constraints in the $\epsilon^2$ versus $m_{A'}$ plane for dark photons that decay directly to SM particles (see *e.g.* [152]). The projected sensitivity of a resonance search for promptly decaying dark photons with the Mu3e experiment is shown in blue (red) assuming $10^{15}$ ($5.5 \times 10^{16}$) muon decays for Mue3 phase I (II).

background in the range 10 MeV $< m_{A'} <$ 80 MeV. Each fit is performed over an interval of $\pm$ 5 MeV around the nominal dark photon mass.. An example of a fit is displayed in Fig. 3.6. We extract a 95% confidence level (CL) limit on the number of signal events, and derive a bound on the $\mu^+ \to e^+ \nu_e \bar{\nu}_\mu A'$, $A' \to e^+ e^-$ branching ratio by dividing by the signal efficiency and the number of muon decays. These results are translated into limits on the kinetic mixing parameter, $\epsilon$, and shown as a blue (red) solid line for Mu3e's phase I (II) in Fig. 3.7, together with existing constraints and prospects for upcoming experiments.

A substantial fraction of open parameter space in the low $m_{A'}$ region can be explored, complementing or overlapping the reach of currently planned experiments, including APEX [82, 90], HPS [101], DarkLight [81, 97], and an experiment at the SPS [100] (the latter is not shown). As mentioned in the introduction, if $U(1)_Y$ is embedded in a GUT, the mixing that is generated by a one-(two-)loop interaction naturally gives $\epsilon^2 \sim 10^{-6}-10^{-2}$ ($\sim 10^{-10}-10^{-6}$). Mu3e has the opportunity to explore part of this theoretically interesting parameter space.

### Displaced Vertices From Dark Photons

For sufficiently small values of $\epsilon$, the dark photon lifetime can be sizable (see Eq. (3.3)), leading to displaced decay vertices observable in the laboratory frame. While smaller values

of $\epsilon$ lead to smaller muon branching ratios to dark photons, the backgrounds associated with displaced vertices are substantially reduced, providing an opportunity to observe a signal. The discovery potential depends on the geometrical acceptance of the detector, the vertex resolution, and the backgrounds. The assumptions introduced in the prompt decay scenario to treat the accidental backgrounds, *i.e.* pile-up events arising from muons decaying within the same time window and at the same position in the target, might not be valid anymore for displaced vertices. A full analysis should include contributions from pile-up of several (radiative) muon decays generated everywhere in the target, which is beyond the scope of this thesis, given the large number of muon decays involved. Furthermore, a small residual background from misreconstructed $\mu^+ \to e^+\nu_e\bar{\nu}_\mu e^+e^-$ events is expected to remain, and the accuracy of `FastSim` might be too limited to reliably predict its level. We encourage the Mu3e Collaboration to perform a detailed reach estimate, both because the tools at our disposal are not sufficient for a reliable estimate and because the sensitivity that could potentially be achieved is well worth the effort.

### 3.1.3 Summary

In this section, we have studied the possibility to search for dark photon in $\mu^+ \to e^+\nu_e\bar{\nu}_\mu A'$, $A' \to e^+e^-$ decays with an apparatus similar to the Mu3e experiment. We derive sensitivity estimates for both prompt and displaced dark photon decays. Mu3e has the exciting opportunity to probe a substantial fraction of currently unexplored parameter space in the mass range $10\text{ MeV} \lesssim m_{A'} \lesssim 80\text{ MeV}$ for $\epsilon^2 \gtrsim 10^{-8}$, using a resonance search, overlapping or complementing the reach of currently planned experiments. This opportunity does not require any modifications of their existing setup. A search for displaced vertices may have sensitivity to lower values of $\epsilon$, but the precise reach estimate depends on the backgrounds, which require a careful modeling by the Mu3e Collaboration.

## 3.2 Searching for Dark Photons with Low Energy $e^+e^-$ Colliders

As we mentioned in Sec. 1.3.2, Light Dark Matter (LDM), within a mass smaller than 10 GeV, are important alternative to WIMP paradigm and a nature composite of the dark sector picture. LDM can be tested in various collider searches, as well as direct and indirect detection experiments. As we will show later in this section, among collider experiments, low-energy $e^+e^-$ colliders such as $B$-factories and $\Phi$-factories are particularly well suited to exploring this mass range.

DM searches at colliders have received much attention in the past. However, most of the focus has been on searches with high-energy colliders such as LEP, the Tevatron, the LHC, and an ILC, see *e.g.* [153, 154, 155, 156, 157, 158, 159, 160, 161, 162, 163, 164, 165, 166, 167, 168, 169]. These colliders are ideally suited for probing Weak-scale DM, and for DM whose interactions with ordinary matter are mediated by heavy particles. In contrast, $B$-factories ($\Phi$-factories) operate at much lower center-of-mass energies of $\sqrt{s} \approx 10$ GeV (1 GeV). Their sensitivity is therefore highest to LDM with low-mass mediators.

DM particles produced in colliders do not scatter in the detector, and appear as missing energy, $\not{E}$. A particularly clean channel to study is LDM produced in association with a single photon, resulting in a mono-photon signature ($\gamma + \not{E}$). Here we study the sensitivity of mono-photon searches at low-energy $e^+e^-$ colliders to LDM. While LDM production has been studied before in the context of rare meson decays, *e.g.* [170, 171, 172, 173, 174, 175, 176, 177, 178, 179, 180, 181, 182, 183, 184, 185], here we consider a complementary possibility: non-resonant production of mono-photon events directly in the $e^+e^-$ collisions, see Fig. 3.8 (this possibility has previously been considered in less detail in *e.g.* [186, 178, 73, 85, 169]). We first reanalyse the results of an existing search by the *BABAR* collaboration for mono-photon events in decays of the $\Upsilon(3S)$ [187]. While *BABAR* had an active mono-photon trigger for only $\sim 55$/fb (including $\sim 30$/fb on the $\Upsilon(3S)$) out of a total of $\sim 500$/fb of data collected over its lifetime, and performed only a very limited background estimate on these events, the resulting bounds on LDM improve significantly upon existing bounds in parts of the LDM parameter space. A similar analysis with Belle or KLOE data is not possible, due to the lack of a single-photon trigger.

We also estimate the possible sensitivity of Belle II to LDM. This will depend strongly on the ability to implement a mono-photon trigger, and to reduce or subtract backgrounds, but should reach substantially beyond the constraints from *BABAR* in parts of parameter space. Our results stress the importance for Belle II to *include a mono-photon trigger during the entire course of data taking.*

The rest of the section is organized as follows. In Sec. 3.2.1 we give a brief theoretical overview of LDM coupled through a light mediator. Sec. 3.2.2 contains a more detailed discussion of the production of such LDM at low-energy $e^+e^-$ colliders. In Sec. 3.2.3 we describe the *BABAR* search [187], and extend the results to place constraints on LDM. In Sec. 3.2.4 we compare our results to existing constraints such as LEP, rare decays, beam-dump experiments, and direct detection experiments. In Sec. 3.2.5 we estimate the reach of a similar search in a future $e^+e^-$ collider such as Belle II. We conclude in Sec. 4.1.4. A short appendix discusses the constraints on invisibly decaying dark photons for some additional scenarios.
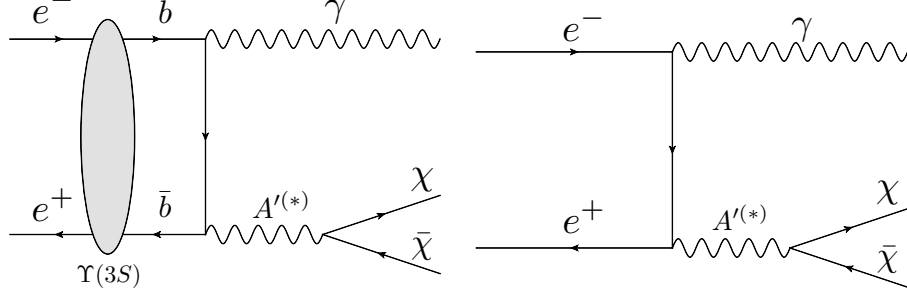
Figure 3.8: $\gamma + \not{E}$ production channels for LDM coupled through a light mediator. **Left:** Resonant $\Upsilon(3S)$ production, followed by decay to $\gamma + \chi\,\overline{\chi}$ through an on- or off-shell mediator. **Right:** The focus of this section – non-resonant $\gamma + \chi\,\overline{\chi}$ production in $e^+e^-$ collisions, through an on- or off-shell light mediator $A'^{(*)}$. (Note that in this section, the symbol $A'$ is used for vector, pseudo-vector, scalar, and pseudo-scalar mediators.)

## 3.2.1 Light Dark Matter with a Light Mediator

A LDM particle is a natural member of a dark sector. Generally speaking, the dark sector may generally contain a multitude of states with complicated interactions among themselves. However, for the context of this section, it is sufficient to characterize it by a simple model with just two particles, the DM particle $\chi$ and the mediator $A'$ (which, with abuse of notation, may refer to a generic (pseudo-)vector, or (pseudo-)scalar, and does not necessarily indicate a dark photon), and four parameters:

(i) $m_\chi$ (the DM mass)

(ii) $m_{A'}$ (the mediator mass)

(iii) $g_e$ (the coupling of the mediator to electrons)

(iv) $g_\chi$ (the coupling of the mediator to DM).

In most of the parameter space only restricted combinations of these four parameters are relevant for $\chi\overline{\chi}$ production in $e^+e^-$ collisions; we describe this in more detail in Sec. 3.2.2. The spin and $CP$ properties of the mediator and DM particles also have a (very) limited effect on their production rates, but will have a more significant effect on comparisons to other experimental constraints, as will the couplings of the mediator to other SM particles. For the rest of the section, the "dark matter" particle, $\chi$, can be taken to represent any dark-sector state that couples to the mediator and is invisible in detectors; in particular, it does not have to be a (dominant) component of the DM.

43

The simplest example of such a setup is DM that does not interact with the SM forces, but that nevertheless has interactions with ordinary matter through a *dark photon*. The variables $\varepsilon$, $g_\chi$, $m_\chi$, and $m_{A'}$ are the free parameters of the model. We restrict

$$g_\chi < \sqrt{4\pi}\,, \qquad \text{(perturbativity)} \tag{3.17}$$

in order to guarantee calculability of the model. Such a constraint is also equivalent to imposing $\Gamma_{A'}/m_{A'} \lesssim 1$ which is necessary for the $A'$ to have a particle description. We will refer in the following to this restriction as the "perturbativity" constraint.

In this section, we discuss this prototype model as well as more general LDM models with vector, pseudo-vector, scalar, and pseudo-scalar mediators. We stress that in UV complete models, scalar and pseudo-scalar mediators generically couple to SM fermions through mixing with a Higgs boson, and consequently their coupling to electrons is proportional to the electron Yukawa, $g_e \propto y_e \sim 3 \times 10^{-6}$. As a result, low-energy $e^+e^-$ colliders are realistically unlikely to be sensitive to them. Nonetheless, since more intricate scalar sectors may allow for significantly larger couplings, we include them for completeness.

For simplicity we consider only fermionic LDM, as the differences between fermion and scalar production are very minor. We do not consider models with a $t$-channel mediator (such as light neutralino production through selectron exchange). In these, the mediator would be electrically charged and so could not be light.

### 3.2.2   Production of Light Dark Matter at $e^+e^-$ Colliders

Fig. 3.8 illustrates the production of $\gamma + \not{E}$ events at low-energy $e^+e^-$ colliders in LDM scenarios. The channel shown on the left of Fig. 3.8 is the resonant production of a heavy meson such as $\Upsilon(3S)$, followed by its decay to $\gamma + \chi\overline{\chi}$ through an on- or off-shell mediator. This channel probes the couplings of the mediator to the $b$-quark (specifically its pseudo-vector or pseudo-scalar couplings if the mediator is on shell). The focus of this section, however, is a complementary channel, shown on the right of Fig. 3.8, where LDM is produced through an on- or off-shell mediator, which couples directly to electrons.

The collider signal consists of mono-photon events, $\gamma + \not{E}$. The photon energy spectrum can vary quite significantly depending on the masses of the DM and mediator, and we divide the $m_\chi$–$m_{A'}$ plane into three regions with distinct kinematics, as illustrated in Fig. 3.9. Typical spectra for each region are shown in Fig. 3.10 as a function of the $\chi\overline{\chi}$ invariant mass, which is related to the photon energy by

$$m_{\chi\overline{\chi}}^2 \equiv s - 2\sqrt{s}E_\gamma^*\,. \tag{3.18}$$

The regions are as follows:
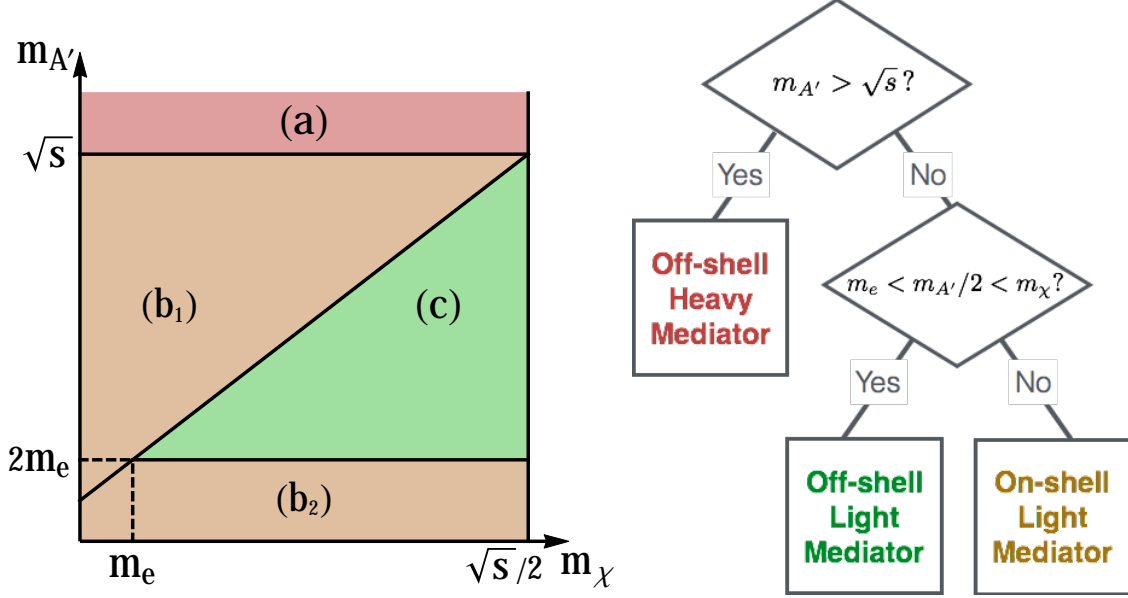
Figure 3.9: **Left**: Regions in the $m_\chi$–$m_{A'}$ plane with different characteristic $\gamma + \not{E}$ signals ($A'$ is any type of mediator). **Region (a)** corresponds to an off-shell heavy mediator, for which an effective operator analysis holds if $m_{A'} \gg \sqrt{s}$. In **Region (b)** the mediator is invisible and is produced on-shell. In **Region (c)**, while the mediator is light enough to be produced on shell, $\chi\overline{\chi}$ production occurs through an off-shell mediator. **Right**: Decision tree that summarize the search plan.

(a): $\mathbf{m_{A'} > \sqrt{s}}$. Here the mediator is too heavy to be produced on shell, and $\chi\overline{\chi}$ production proceeds through an off-shell mediator. In this case, the photon is dominantly produced in the form of initial state radiation, and so has a spectrum rising towards low energies (high $m_{\chi\overline{\chi}}$), illustrated by the red histogram in Fig. 3.10.

(b): $\mathbf{\sqrt{s} > m_{A'} > 2m_\chi}$ or $\mathbf{m_{A'} < 2m_e}$. In region ($b_1$), the mediator decays to $\chi\overline{\chi}$ (the branching ratio to SM particles is assumed to be negligible). In region ($b_2$), it is too light to decay to either $\chi\overline{\chi}$ or $e^+e^-$; if *e.g.* $A'$ is a dark photon, it eventually decays to (three) photons far outside the detector. Both cases result in a mono-energetic $\gamma + \not{E}$ signature. The spectrum is peaked at $m_{\chi\overline{\chi}}^2 = m_{A'}^2$, but the finite detector resolution gives a width of

$$\sigma_{m_{\chi\overline{\chi}}^2} = 2\sqrt{s}\,\sigma_{E_\gamma} = (s - m_{\chi\overline{\chi}}^2) \times (\sigma_{E_\gamma}/E_\gamma), \tag{3.19}$$

where $\sigma_{E_\gamma}$ is the experimental photon energy resolution. This is illustrated by the two orange histograms in Fig. 3.10.

(c): $\mathbf{2m_\chi > m_{A'} > 2m_e}$. In this region, the mediator can be produced on shell, but is

too light to decay to $\chi\bar{\chi}$. It could either decay to another light dark-sector state (if available) or it will instead decay to SM fermions, an interesting signature, which is not the topic of this section (see *e.g.* [186, 178, 73, 85]). In the latter case, while direct searches for the *visible* decay are likely to be more sensitive (see *e.g.* [74, 188] and references therein), $\gamma + \not{E}$ events can occur in the production of $\chi\bar{\chi}$ through an off-shell mediator. Probing these decays is necessary to assess whether such light mediator couples to invisible particles such as LDM and therefore is complementary to visible searches. The mediator propagator contributes a factor $1/m^4_{\chi\bar{\chi}}$ to the cross-section, resulting in the broad, flat photon spectrum illustrated by the green histogram in Fig. 3.10.
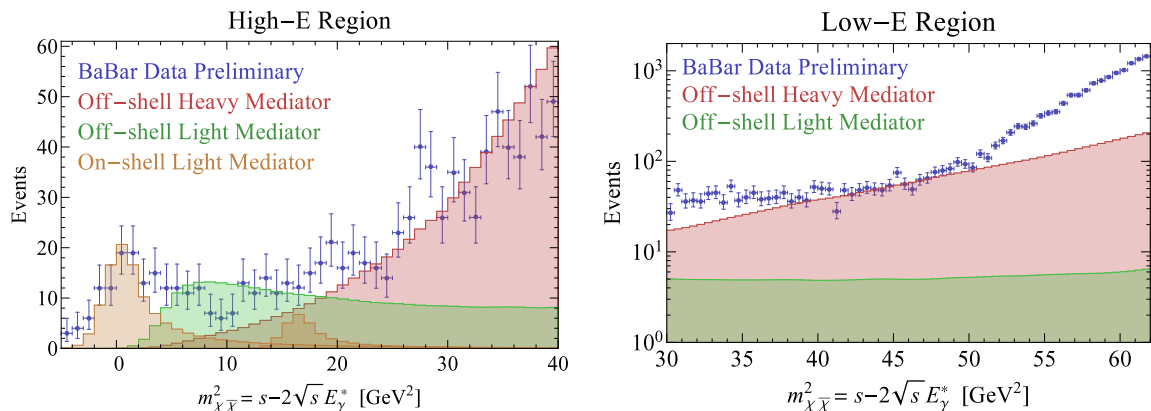


Figure 3.10: Typical simulations of $\gamma + \not{E}$ signals compared to data that was scanned from the *BABAR* Collaboration (unpublished) [187], in both the "High-E" (**left**) and "Low-E" (**right**) search regions (where 3.2 GeV $< E^*_\gamma <$ 5.5 GeV and 2.2 GeV $< E^*_\gamma <$ 3.7 GeV, respectively; see Sec. 3.2.3 for more details). The **red** histogram illustrates $\chi\bar{\chi}$ production through an off-shell heavy mediator (region (a)), resulting in a rising spectrum. The histogram corresponds to $m_\chi = 1$ GeV and $m_{A'} = 12$ GeV. The **orange** histograms show the peaked spectra arising from on-shell production of an invisible mediator (region (b)), with $m_{A'} = 0.5$ MeV (left) or 4 GeV (right). The **green** histogram shows the typical broad spectrum resulting from $\chi\bar{\chi}$ production through an off-shell light mediator (region (c)) (we show $m_\chi = m_{A'} = 1$ GeV). In each case the cross-section is scaled to lie at the 95% CL limits presented in Sec. 3.2.3.

## Relevant Parameters

In each of the three regions, only limited combinations of the four model parameters presented in Sec. 3.2.1 determine the $\gamma + \not{E}$ signal, with the remaining combinations being redundant

(or giving small corrections), as follows:

(a): When $m_{A'} \gg \sqrt{s}$, the mediator can be integrated out of the theory and the interaction described by a 4-point vertex. For fermionic LDM coupling through a vector, pseudo-vector, scalar or pseudo-scalar mediator, the effective operator describing the interaction is given by (respectively)

$$\mathcal{O}_V = \frac{1}{\Lambda^2} \left( \bar{\chi} \gamma_\mu \chi \right) \left( \bar{e} \gamma^\mu e \right) , \tag{3.20}$$

$$\mathcal{O}_A = \frac{1}{\Lambda^2} \left( \bar{\chi} \gamma_\mu \gamma^5 \chi \right) \left( \bar{e} \gamma^\mu \gamma^5 e \right) , \tag{3.21}$$

$$\mathcal{O}_S = \frac{1}{\Lambda^2} \left( \bar{\chi} \chi \right) \left( \bar{e} e \right) , \tag{3.22}$$

$$\mathcal{O}_{PS} = \frac{1}{\Lambda^2} \left( \bar{\chi} \gamma^5 \chi \right) \left( \bar{e} \gamma^5 e \right) . \tag{3.23}$$

where $\Lambda$ is given by

$$\Lambda \equiv \frac{m_{A'}}{\sqrt{g_e g_\chi}} . \tag{3.24}$$

The signal spectrum depends on $m_\chi$, and the rate is proportional to $\Lambda^{-4}$, with corrections of order $m_{\chi\bar{\chi}}^2 / m_{A'}^2$, relevant only for $A'$ masses close to the center-of-mass energy.

(b): For mediators produced on shell, $m_\chi$ and $g_\chi$ are irrelevant as long as the mediator does not have a significant branching ratio to SM fermions. The signal spectrum is controlled by $m_{A'}$, and the rate is proportional to $g_e^2$, with corrections of order $g_e^2 / g_\chi^2$.

(c): For $m_{A'} \ll m_\chi$, the signal spectrum depends on $m_\chi$ but not on $m_{A'}$, and the rate is proportional to $(g_e g_\chi)^2$, with corrections of order $m_{A'}^2 / m_{\chi\bar{\chi}}^2$.

### 3.2.3 Constraints from BABAR Data

The BABAR Collaboration performed an unpublished analysis of mono-photon events in a search for decays of the $\Upsilon(3S)$ to $\gamma A^0$, where $A^0$ is an invisible pseudoscalar particle [187]. We reproduce their preliminary data in Fig. 3.10. The search was performed on a sample of $122 \times 10^6$ $\Upsilon(3S)$ decays, corresponding to about 28/fb of data at $\sqrt{s} \approx m_{\Upsilon(3S)} \approx$ 10.355 GeV [189]. The data was analyzed in two overlapping photon CM energy regimes with distinct trigger requirements: 3.2 GeV $< E_\gamma^* <$ 5.5 GeV and 2.2 GeV $< E_\gamma^* <$ 3.7 GeV, referred to respectively as the High-E and Low-E regions. The former used the full dataset, and the latter a subset corresponding to 19/fb. The main SM backgrounds are a peak at $m_{\chi\bar{\chi}}^2 = 0$
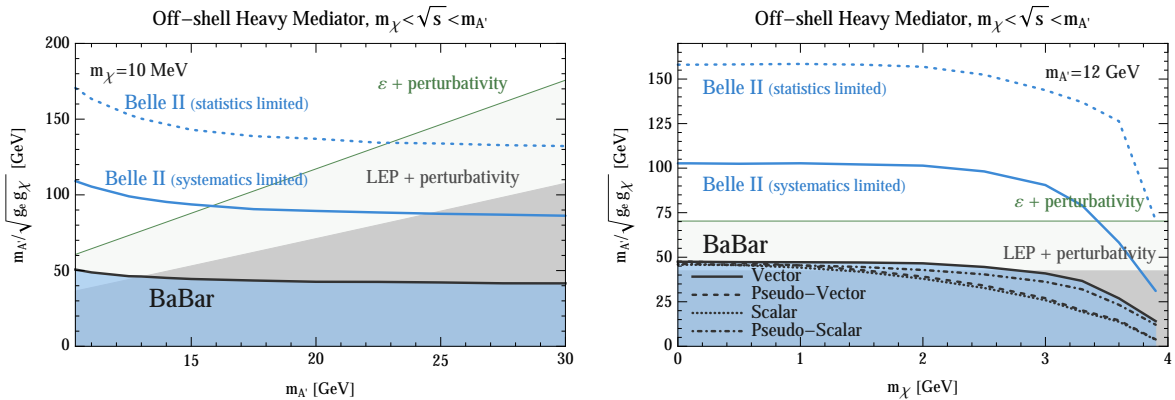
Figure 3.11: Lower bounds on $m_{A'}/\sqrt{g_e g_\chi}$ in region (a) of Fig. 3.9 (production of $\chi\overline{\chi}$ through a heavy off-shell mediator), for (**left**) a fixed DM mass of 10 MeV, and (**right**) a fixed mediator mass of 12 GeV. The solid black line / blue shaded region show the bounds from *BABAR* data (this work) with a vector mediator. On the right, the bounds with other mediators are shown with different line styles, while on the left they are almost identical to the vector case and thus not shown separately. The solid and dotted blue line both show the projected reach of Belle II in the vector-mediated case assuming that the various background components are known at the $5-20\%$ level ("systematics" limited) or, more idealistically, is known perfectly up to statistical fluctuations ("statistics" limited) (see Sec. 3.2.5 for details). The gray shaded region is excluded by combining LEP bounds [157] with $g_\chi$-perturbativity. For the dark photon case, this limit is strengthened by including $Z$-pole constraints [87] on $\varepsilon$, as shown by the green line. See text for more details.

from $e^+e^- \to \gamma\slashed{\gamma}$, a continuum background from $e^+e^- \to \gamma\slashed{\ell}^+\slashed{\ell}^-$, $e^+e^- \to \gamma\slashed{\gamma}\slashed{\gamma}$, where $\slashed{\ell}^\pm$ and $\slashed{\gamma}$ represent particles that escape undetected (down the beam pipe or in a detector crack) and, to a lesser extent, two-photon production of hadronic states decaying to photons where only one is detected. The results of a bump hunt in the photon spectrum were presented as preliminary upper limits on the branching ratio (BR) $\mathcal{B}(\Upsilon(3S) \to \gamma A^0) \times \mathcal{B}(A^0 \to inv.)$.

We use this data below to constrain the non-resonant production of LDM in $e^+e^-$ collisions as shown in Fig. 3.8-*right*, for the three regions shown in Fig. 3.9. (A similar analysis is performed in Ref. [180] to constrain LDM couplings to $b$-quarks through an effective dimension-6 operator.) The *BABAR* analysis applies both geometric and non-geometric cuts to the mono-photon data, with total efficiency for signal events given as 10-11% (20%) in the High-E (Low-E) region. By simulating $e^+e^- \to \Upsilon(3S) \to \gamma A^0$ events, we find that geometric acceptance accounts for 34% and 37% of this efficiency in the two respective regions, with non-geometric cuts therefore having about 30% and 55% efficiencies. In our analysis, we

determine the geometric cut acceptances for each search region from simulation, and apply a further cut of 30% (55%) in the High-E (Low-E) region to account for the efficiencies of other cuts. Photon energies are smeared using a crystal-ball function, with tail parameters $\alpha = 0.811$ and $n = 1.79$, obtained from fitting the $E_\gamma^*$ distribution of $e^+e^- \to \gamma\slashed{\gamma}$ to the data in [187]. We take the width, $\sigma_{E_\gamma}/E_\gamma$, to be $1.5\%/(E_\gamma/\text{ GeV})^{1/4} \oplus 1\%$ to match the values of $\sigma_{m_{\chi\overline{\chi}}^2}$ given in [187]. The signal was simulated with `Madgraph 5` [190].

**Constraints for Off-shell Heavy Mediators**

When $\gamma + \chi\overline{\chi}$ events are produced through a heavy off-shell mediator (region (a) of Fig. 3.9), the mono-photon spectrum has a shape very similar to that of the background, as can be seen in Fig. 3.10. Because of this, and since no background estimate was performed in [187], we place constraints by requiring that the expected signal does not exceed the observed number of events by more than $2\sigma$ in any bin.

Fig. 3.11 (*left*) shows lower limits on $m_{A'}/\sqrt{g_e g_\chi}$ as a function of $m_{A'}$ for a fixed DM mass of 10 MeV, while Fig. 3.11 (*right*) shows limits as a function of $m_\chi$ for a fixed mediator mass of 12 GeV, and various mediators. The dependence on the type of mediator is negligible for $m_\chi \lesssim 1$ GeV. The solid blue curves show projections for a similar search at Belle II (see Sec. 3.2.5). These rely on the possibility of performing an estimate of the background and hence could also apply to a reanalysis of the data by the *BABAR* collaboration if they are able to calculate the backgrounds and/or determine them from data.

These models are also constrained by mono-photon searches at LEP, which in this regime place an upper bound on $g_e$ (see Sec. 3.2.4). Combining this with the requirement $g_\chi < \sqrt{4\pi}$ (for perturbativity) gives the gray shaded region shown in Fig. 3.11. LEP's high CM energy makes it more effective at constraining heavier mediators, and the LEP bounds are stronger than those from *BABAR* for $m_{A'} \gtrsim 15$ GeV. In the case of a dark photon mediator, there is an even stronger constraint of $g_e < 0.026e$ from $Z$-pole measurements [87], shown by the green lines.

**Constraints for On-Shell Light Mediators**

Production of on-shell invisible mediators in $e^+e^- \to \gamma A'$ events (region $(b_{1,2})$ of Fig. 3.9) gives a mono-photon signal with a distinct bump at $m_{\chi\overline{\chi}}^2 = m_{A'}^2$, as illustrated in Fig. 3.10. The backgrounds are smooth functions, except for a bump at $m_{\chi\overline{\chi}}^2 = 0$ from $\gamma\slashed{\gamma}$ events. We set limits on $g_e$ by performing our own bump hunt on the *BABAR* data, as described below.

Following [187], we model the background in the High-E region by combining a crystal ball peaked at $m_{\chi\overline{\chi}}^2 = 0$ with an exponential $\exp(c\, m_{\chi\overline{\chi}}^2)$. In the Low-E region we combine an
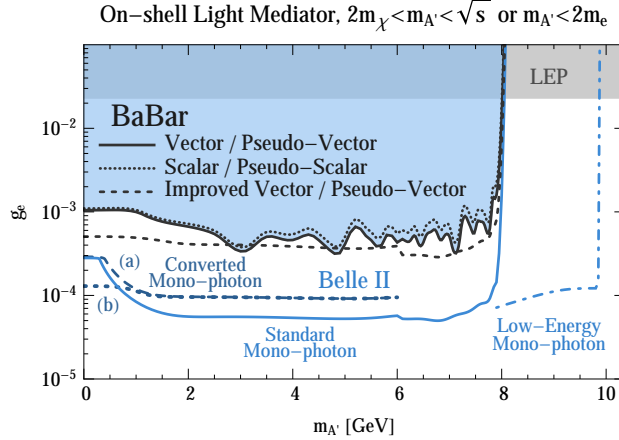
Figure 3.12: Upper bounds on the coupling of electrons to a mediator decaying invisibly to dark-sector states (region (b) of Fig. 3.9). The solid black line / blue shaded region shows the bound from *BABAR* data (this work), for a vector or pseudo-vector mediator. The dotted line shows the bound for a scalar or pseudo-scalar mediator. The black dashed line shows the projected upper limit from an "improved *BABAR*" analysis for a vector or pseudo-vector mediator, where the $\gamma\not\gamma$ background has been reduced by a factor of 10. The projected reaches of four possible searches for a vector mediator at Belle II are shown by the solid blue lines: a converted mono-photon search (dashed, labelled (a) and (b), which respectively assume no (a factor of 10) improvement in the $\gamma\not\gamma$ background rejection over the "improved *BABAR*" projection), a standard mono-photon search (solid), and a low-energy mono-photon search (dot-dashed) (see Sec. 3.2.5). The gray shaded region is excluded by LEP [157]. Additional limits relevant for sub-GeV mediators are shown in Fig. 3.15. See text for more details.

exponential $\exp(c_1 m_{\chi\overline{\chi}}^2 + c_2 m_{\chi\overline{\chi}}^4)$ with a constant. The normalizations of each component, and the exponents $c$, $c_1$, $c_2$, are treated as free nuisance parameters, with the normalizations constrained to be positive. We model the signal with a crystal ball peaked at $m_{\chi\overline{\chi}}^2 = m_{A'}^2$, and integrated area $N_{\text{signal}}$. The width of the crystal ball functions is as described above.

For any given value of $m_{A'}$, we bin the expected rates using the same binning as the *BABAR* data, construct a likelihood function based on the signal and various background components, with the various nuisance parameters kept unconstrained except for the normalizations, which are kept positive. We then set 95% C.L. limits on $N_{\text{signal}}$ using the profile likelihood method.

The absence of features in the non-$\gamma\not\gamma$ backgrounds makes the bump-hunt an effective procedure to discriminate a signal from background for heavier $A'$. In the analysis of [187],

only a limited background estimate was done on the $\gamma\not\gamma$ peak, using off-resonance data to estimate the background rate. We cannot use this approach in our analysis, since our signal would also appear in the off-resonance sample. The search becomes therefore background-limited for $m_{A'} \lesssim 1$ GeV in the current *BABAR* data. However, an improved background estimate may be possible. We therefore show a projection for an "improved *BABAR*" limit, assuming that the $\gamma\not\gamma$ background can be reduced by a factor of 10. For this case, we fit smooth curves to the current *BABAR* data to show the expected limit. At Belle II, additional improvements in both background rejection and resolution may decrease the value of $m_{A'}$ at which the search becomes background-limited to a few hundred MeV, see Sec. 3.2.5.

We convert the limits on $N_{\mathrm{signal}}$ into limits on $g_e$ using simulation, accounting for the cut efficiency as described above. The limits are shown in Fig. 3.12, along with projections for Belle II and limits from LEP (see Secs. 3.2.5 and 3.2.4). In Figs. 3.15 and 3.14 we show our limits in the $\varepsilon$ versus $m_{A'}$ plane for the special case of an invisibly decaying dark photon. The bounds and projected reach of various other experiments are also shown, and are discussed further in Sec. 3.3.

**Constraints for Off-Shell Light Mediators**

When $2m_e < m_{A'} < 2m_\chi$ (region (c) of Fig. 3.9), $\gamma + \chi\overline{\chi}$ production proceeds through a light off-shell mediator, giving a broad mono-photon spectrum as seen in Fig. 3.10. This spectrum has a kinematic edge at $m_{\chi\overline{\chi}}^2 = 4m_\chi^2$. Without good control over backgrounds, this spectrum is difficult to distinguish from backgrounds, and we conservatively place constraints by requiring that the expected signal does not exceed the observed number of events by more than $2\sigma$ in any bin.

Fig. 3.13 shows the upper limit on $g_e g_\chi$ as a function of $m_\chi$ for a fixed mediator mass of 100 MeV, for various mediator types. The constraint on $g_e g_\chi$ from LEP (see Sec. 3.2.4) is shown by the gray shaded region. In the case of a dark photon mediator there is a stronger constraint, shown by the green line. This combines the requirement $g_\chi < \sqrt{4\pi}$ (for perturbativity) with bound on a visibly-decaying dark photon by the KLOE experiment, which constrains $g_e < 0.002$ for $m_{A'} = 100$ MeV [89]. We note that if the mediator can decay to a second light state in the dark sector then the visible constraints do not apply. However, this second light state is then constrained by the on-shell constraints in Sec. 3.2.3, which are of comparable strength.

Also shown is the projected reach of Belle II for the vector-mediated case (see Sec. 3.2.5). As for the heavy off-shell region, these rely on the possibility of performing a background estimate and hence could also apply to a reanalysis of the data by the *BABAR* collaboration
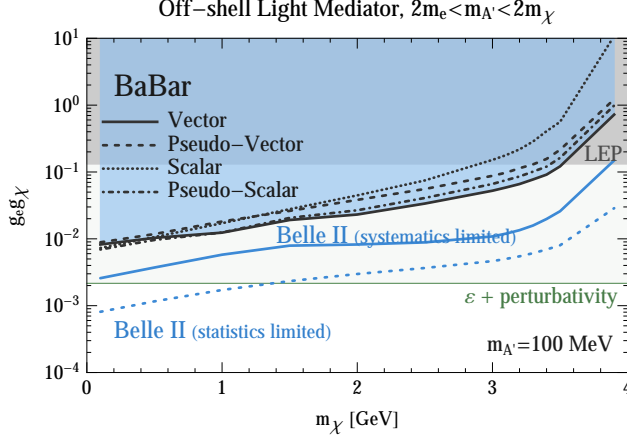
Figure 3.13: Upper limits on $g_e g_\chi$ for the off-shell light mediator region (region (c) of Fig. 3.9), for a fixed mediator mass of 100 MeV. The coloring and assumptions of the *BABAR* and Belle II curves are as in Fig. 3.11. The gray shaded region is excluded by LEP [157]. With a hidden-photon mediator, there is a stronger constraint from combining $g_\chi$-perturbativity with a search for visibly-decaying hidden-photons at KLOE (green line). The possible reach of an edge search is not shown, but may allow some improvement. The solid and dotted blue line both show the projected reach of Belle II in the vector-mediated case assuming that the various background components are known at the $5 - 20\%$ level ("systematics" limited) or, more idealistically, are known perfectly up to statistical fluctuations ("statistics" limited) (see Sec. 3.2.5 for details). See text for more details.

if control over the various background components can be obtained. In addition, a search for a kinematic edge may allow for an improvement of the bounds, but is not shown here. As can be seen from the figure, for the case of a dark photon mediator, stronger constraints can be obtained from the direct production and (visible) decay of the $A'$.

## 3.2.4 Comparison with LEP

The search for mono-photon events in $e^+e^-$ collisions is also possible with the $\mathcal{O}(1)/\text{fb}$ of data collected with a mono-photon trigger at LEP, and in [157] this was used to place constraints on DM coupled to electrons through a mediator or a higher-dimension four-point interaction. Because LEP operated at $\sqrt{s} \sim 200$ GeV, the DM and mediators of interest in this section are light by LEP standards. There are therefore two regimes of interest to us: $2m_\chi < m_{A'} \ll 200$ GeV, for which the mono-photon signal rate is controlled by the single parameter $g_e$, and $m_{A'} < 2m_\chi \ll 200$ GeV, for which it is controlled by the combination $g_e g_\chi$.

In Ref. [157] (Fig. 7) bounds are presented in terms of the parameters $m_\chi$, $m_{A'}$, the effective cutoff scale $\Lambda \equiv m_{A'}/\sqrt{g_e g_\chi}$, and the $A'$ decay width $\Gamma_{A'}$. However, in the two respective mass regimes of interest these are consistent with a single bound on either $g_e$ or $g_e g_\chi$, of

$$g_e < 0.023 \qquad\qquad (2m_\chi < m_{A'}) , \qquad\qquad (3.25)$$

$$g_e g_\chi < 0.13 \qquad\qquad (m_{A'} < 2m_\chi) . \qquad\qquad (3.26)$$

The former is extracted from the "minimum width" curves of Ref. [157], which correspond approximately to the assumption $g_\chi = g_e$.

In Figs. 3.12 and 3.13 we show these two bounds directly with gray shaded regions. In Fig. 3.11 we show a combination of the bound on $g_e$ with the requirement $g_\chi < \sqrt{4\pi}$ (for perturbativity). LEP is more suited to probing higher mass scales, and becomes more sensitive than *BABAR* for mediator masses above about 15 GeV assuming $g_\chi = \sqrt{4\pi}$. For the on- and off-shell light mediator regimes, the bounds from *BABAR* are significantly stronger than those from LEP, due largely to *BABAR*'s higher luminosity and larger production cross-section.

### 3.2.5  Projections for Belle II

The bounds placed on LDM by the *BABAR* data are competitive with existing constraints, and in many cases stronger. In particular, for on-shell invisible mediators the bounds exclude a large region of previously-allowed parameter space. In this section, we make projections for the sensitivity to LDM of future high-luminosity $e^+ e^-$ colliders, notably the next-generation $B$-factory Belle II, which could significantly improve on these results.

Belle II is an upgrade of the Belle experiment, using the SuperKEKB asymmetric $e^+ e^-$ collider currently under construction [191]. It is expected to start taking data in 2016 and obtain 50/ab of integrated luminosity at $\sqrt{s} \approx 10.5$ GeV by 2022 [192]. The average energy resolution is slightly improved over *BABAR* $\sigma_{E_\gamma}/E_\gamma = 1.7\%$. The implementation of a mono-photon trigger will require a dedicated study by the Belle II collaboration to ensure that the high luminosity and pile-up do not lead to an unacceptably high trigger rate. It will hopefully be possible to implement such a trigger for the full Belle II run for energetic mono-photons without prescaling, and possibly with a prescaled version also at lower photon energies ($E_\gamma \lesssim 2$ GeV). An interesting possibility is the study of a dedicated trigger for mono-photons that convert in the tracker. While paying a high price in signal rate, this may overcome significant issues (discussed below) with the standard mono-photon search.

A precise estimate of the reach of Belle II depends on various unknowns, such as the amount of data taken with the mono-photon trigger, the trigger and cut efficiencies, and most crucially the background rate and the ability to perform a careful background estimate. In order to make illustrative projections, we make plausible assumptions about these factors. We emphasize that the actual reach of Belle II may prove somewhat different than our projections.

**Standard Mono-Photon Search**

We assume that Belle II can implement a mono-photon trigger on the full 50/ab of data, but restricted to the energy range 2.2 GeV $< E_\gamma^* \lesssim$ 5.5 GeV, corresponding to $-5$ GeV$^2 <$ $m_{\chi\bar{\chi}}^2 \lesssim 62$ GeV$^2$. This avoids the excessive rates coming from the radiative Bhabha contributions and other soft photon and instrumental backgrounds at lower energies. In analogy with the current *BABAR* search [187], we divide the energy range again into High-E and Low-E regions. This allows us to scale up the current *BABAR* background estimates. We determine these by fitting the *BABAR* data with the smooth functions described in 3.2.3. We then assume the same geometric acceptance in each region as *BABAR*, neglecting $\mathcal{O}(1)$ differences between the geometric acceptances of the two experiments due to differences in the beam energies and calorimeter rapidity coverage. We further assume a constant efficiency for non-geometric cuts of 50% and finally scale up all the smoothed *BABAR* backgrounds by the ratio of the luminosities, except for the $\gamma\gamma\!\!\!/$ background. For the latter, we assume a baseline improvement in the background rejection by a factor of 10 over the current *BABAR* analysis [187] (so that it corresponds to the "improved *BABAR*" version discussed in Sec. 3.2.3 and shown in Figs. 3.12 and 3.15) before scaling by the ratio of luminosities. We note that the real backgrounds may of course differ significantly from these simple scalings using the *BABAR* data.

For on-shell mediators, we set limits following the same procedure described in Sect. 3.2.3. For off-shell mediators, we assume the expected continuum background rate can be determined using some combination of Monte Carlo and data-driven techniques, allowing one to estimate and effectively "subtract" part of the background (there would be no improvement in the Belle II sensitivity over the current *BABAR* limits without an improved understanding of the backgrounds, since we showed "signal-only" limits for *BABAR*). Without a realistic estimate of the range of shape variations for the various background components, it is hard to estimate the power of the limits that can be obtained by such subtraction procedure. Instead, we provide a conservative and an aggressive estimate of the limits, labeled "systematics-limited" and "statistics-limited", respectively. In both cases, we present single-

bin limits, where the signal is constrained not to exceed the 95% C.L. in any single bin. In the "systematics-limited" case, we assume that the bin uncertainties are dominated by systematic uncertainties due to the subtraction procedure: we set them at 5% for the radiative Bhabha, 10% for the $\gamma\gamma\!\!\!/$ peak (whose size assumes that Belle II can reach the same level of rejection as the *BABAR* analysis) and at 20% for the other continuum components. In the "statistics-limited" case, we consider only statistical uncertainties. While it is almost impossible to achieve this limit, good control of the background shapes and the simultaneous fit of many bins could yield a significant improvement over our "systematics-limited" reach, so that it is instructive to show both.

The sensitivity reach from both these estimates are shown by the solid and dashed blue curves in Figs. 3.11 and 3.13, while only the "systematics-limited" reach is shown with the solid blue curves in Figs. 3.12, 3.15, and 3.14. In Figs. 3.16 and 3.17, the "systematics-limited" curve is shown under two assumptions for the value of $g_\chi$.

**Low-Energy Mono-Photon Search**

We also consider the possibility that Belle II can implement a prescaled trigger for low-energy mono-photons, $0.5~\text{GeV} < E_\gamma^* \leq 2.2~\text{GeV}$. We will assume a prescale factor of 10 (corresponding to 5/ab of collected data), although a dedicated study by the Belle II collaboration is necessary to see whether this is sufficient to avoid background events overwhelming the data acquisition. We estimate the background by extrapolating the fit in the Low-E region described in the previous section, Sec. 3.2.5, and otherwise follow the same assumptions and procedures. The result is shown by the blue dot-dashed lines in Figs. 3.12 and 3.15.

**Converted Mono-Photon Search**

A small fraction of photons convert to $e^+e^-$ pairs in the inner detector (see *e.g.* [193]). While the rate of these events is significantly lower than for non-converted photons, they do allow for significantly better pointing and energy resolution. The combination of the lower rate and the distinctive nature of the events should make it possible to implement a dedicated trigger for converted mono-photons. The improved pointing resolution may make it significantly easier to veto mono-photons that are back-to-back with detector regions responsible for photon losses, such as azimuthal gaps in calorimeter coverage. This would reduce the background from $\gamma\gamma\!\!\!/$ events, and improve the reach around the peak at $m_{\chi\bar\chi}^2 = 0$ compared to what *BABAR* achieved in the current analysis [187], or even compared to our "improved *BABAR*" projection, which already assumed a factor of 10 reduction in the $\gamma\gamma\!\!\!/$ background over [187]. Moreover, away from the $\gamma\gamma\!\!\!/$ peak, the improved energy resolution

may increase the power of a bump hunt (although this may not compensate for the reduced amount of data). Thus these factors can potentially strengthen the search for LDM and are worth a dedicated study by the Belle II collaboration.

We make projections for such a search assuming that 50/ab of data is collected with a converted-mono-photon trigger, over the energy range 3.2 GeV $< E_\gamma^* <$ 5.5 GeV (*BABAR*'s High-E region). We take the fraction of photons that convert in the tracker to be 5%, and assume the same cut efficiency as for the standard mono-photon search, giving a combined trigger efficiency of 0.85%. We present two scenarios, one assuming a $\gamma\gamma$ background reduction factor comparable with our baseline assumption of the "improved *BABAR*" version, the other assuming a further factor of 10 improvement relative to the "improved *BABAR*" version, i.e. a factor of 100 improvement over the *BABAR* analysis in [187]. In both cases, we assume that the continuum background rate is unchanged. These two scenarios are labeled as "(a)" and "(b)" in Fig. 3.12 and 3.15. We take the energy resolution to be a factor of 2 better than for non-converted photons. Extension to lower $E_\gamma$ should also be possible without prescaling given the low conversion fraction (but we do not consider this further). An additional improvement of the photon energy resolution by up to a factor of $\sim 2$ may be possible [193] due to the improved momentum resolution of low $p_T$ tracks.

We show the results with the blue dashed curves in Figs. 3.12 and 3.15. The improvement over current bounds is potentially very substantial, but clearly a dedicated analysis by the Belle II collaboration is required.

**B-factory Prospects on Additional Dark Photon Scenarios**

We also show the constraints on invisibly decaying dark photons, assuming they can decay either invisibly to a dark-sector state $\chi$ or visibly to SM matter for $m_{A'} < 2m_\chi$. While Fig. 3.15 showed the constraints assuming $m_{A'} < 2m_\chi$, Fig. 3.14 shows the constraints for a fixed LDM mass, $m_\chi = 10$ MeV (left) or 100 MeV (right). Note that the LSND limit, taken from [194], weakens significantly for larger $m_\chi$ and disappear completely for $m_\chi > m_{\pi^0}/2$. The limit from rare Kaon decays $K^\pm \to \pi^\pm A'$ disappears when $m_{A'} > 2m_\chi$. The other constraints are as discussed in Sec. 3.3. We do not show the prospects of the experiments that have been proposed to search for visible $A'$ decays, but see *e.g.* [188].

## 3.2.6   Summary

Light Dark Matter, coupled to the Standard Model through a light mediator, offers an attractive alternative to the WIMP paradigm. However, the parameter space of LDM remains largely unexplored. With their large integrated luminosities, current and future low-energy

$e^+e^-$ colliders offer a uniquely powerful window into LDM parameter space.

We constrained LDM parameter space using an existing *BABAR* search [187]. We compared this to constraints from direct detection experiments and LEP, and in the case of a hidden-photon mediator, also from rare Kaon decays, proton beam dumps, supernova cooling, and QED precision measurements.

Mono-photon searches at future high-luminosity $e^+e^-$ colliders, such as Belle II, can potentially provide an even more powerful probe of LDM and light mediators. The most crucial requirement is the implementation of a mono-photon trigger. In searching for invisible on-shell mediators, it is important that this be applied for as much run-time as possible (preferably for the entire experiment). For searches that are currently background-limited, the identification of suitable control regions is necessary to estimate the various backgrounds that cannot be computed theoretically in a reliable way, together with the collection of sufficient statistics in such control regions. In fact, if background estimates can be performed with small uncertainties, significant improvements over existing bounds are also possible in the off-shell mediator regions, even with a fraction of the total Belle II mono-photon data. Additionally, a study of converted mono-photons, using a dedicated trigger, could be extremely powerful.

Low-energy $e^+e^-$ colliders are one of the most effective probes for light dark matter and light mediators.

## 3.3 Other Searches

In this section, we discuss various other probes related to the specific case of dark photons that couple to light dark-sector states, possibly DM. Projections and/or constraints from these other probes are shown in Figs. 3.15 and 3.14, together with the $B$-factory constraints and projections shown already in Fig. 3.12. We focus on rare kaon decays, precision measurements of the anomalous magnetic moment of the electron and muon, and fixed-target experiments.[2]

### 3.3.1 Rare Kaon Decay Limits

Meson decays involving dark photons can constrain parts of the parameter space. A particularly important rare decay mode is $K^+ \to \pi^+ A'$, with $A' \to$ invisible. A search for the SM process $K^+ \to \pi^+ \nu \bar{\nu}$ by the BNL experiments E787 [197] and E949 [198] found a total of

---

[2]We do not discuss or show a constraint from invisible $J/\psi$-decays [195], since it is much weaker than other constraints, except in a very narrow mass range near the $J/\psi$-mass — see *e.g.* [196].
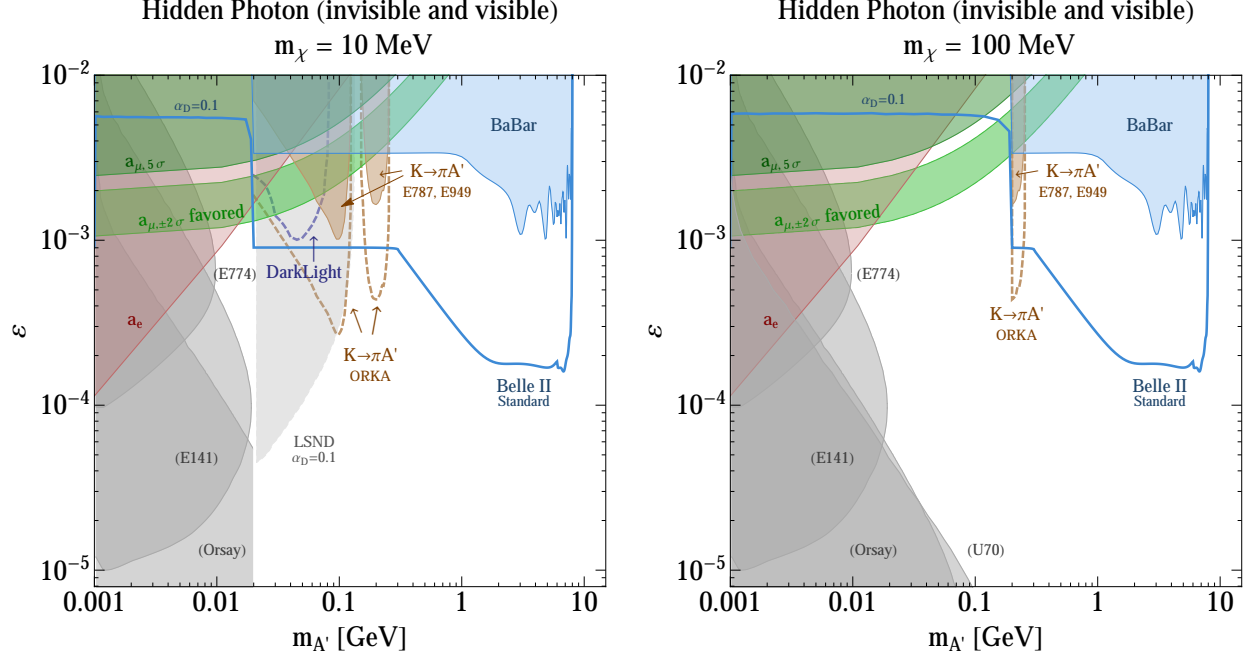
Figure 3.14: Constraints in the $\varepsilon$ versus $m_{A'}$ plane for **invisibly-decaying** dark photons assuming they can decay either invisibly to a dark-sector state $\chi$ or visibly to SM matter for $m_{A'} < 2m_\chi$. We show the constraints for fixed mass $m_\chi = 10$ MeV (**left**) or 100 MeV (**right**). The bounds from the *BABAR* mono-photon data are shown by the blue shaded region. Projections for a possible Belle II search is shown with a solid blue line, corresponding to the "standard" mono-photon search discussed in Sec. 3.2.5. Various other constraints (shaded regions) and projected sensitivities (dashed lines) are also shown: the anomalous magnetic moment of the electron ($a_e$, red) and muon ($a_\mu$, blue), rare kaon decays (brown), the upcoming electron fixed-target experiment DarkLight (light blue; shown when kinematically relevant), and LSND (light gray; assuming $\alpha_D = 0.1$ and that there are no other light dark-sector states that $\chi$ decays to, which do not interact with the dark photon). In the green shaded region an $A'$ could explain the discrepancy between the measured and predicted SM value of $a_\mu$. For $m_{A'} < 2m_\chi$, we show with gray shaded regions the constraints from visible searches (E141, E774, Orsay, U70 etc.) that apply unless there are other decay modes (besides $A' \to \bar{\chi}\chi$) available for the $A'$. We do not show the experimental prospects in this case of visible decays. More details and references are given in Sec. 3.3.

seven events. The SM predicted value [199],

$$B_{\mathrm{SM}}(K^+ \to \pi^+ \nu\bar\nu) = (7.81 \pm 0.80) \times 10^{-11}, \tag{3.27}$$
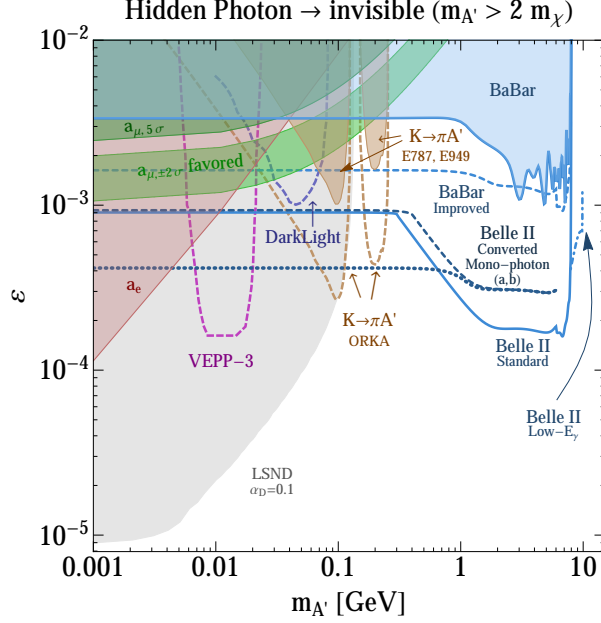
Figure 3.15: Constraints in the $\varepsilon$ versus $m_{A'}$ plane for **invisibly-decaying** dark photons. The bounds from the *BABAR* mono-photon data are shown by the blue shaded region. The blue dashed line shows a "*BABAR* improved" projection that assumes a factor of 10 reduction in the $\gamma\gamma$ background. Projections for four possible Belle II searches are shown by the four blue lines, with line styles matching Fig. 3.12 (see Sec. 3.2.5): a converted mono-photon search (dashed, labelled (a) and (b), which respectively assume no (a factor of 10) improvement in the $\gamma\gamma$ background rejection over the "*BABAR* improved" projection), a standard mono-photon search (solid), and a low-energy mono-photon search (dot-dashed) (see Sec. 3.2.5). Various other constraints (shaded regions) and projected sensitivities (dashed lines) are also shown: the anomalous magnetic moment of the electron ($a_e$, red) and muon ($a_\mu$, green), rare kaon decays (brown), and the upcoming electron/positron fixed-target experiments DarkLight and VEPP-3. In the green shaded band an $A'$ could explain the discrepancy between the measured and predicted SM value of $a_\mu$. The gray shaded region is a constraint from LSND [194], assuming $\alpha_D = 0.1$ and that $\chi$ has no decay modes available to other light dark-sector states that do not couple to the $A'$. More details are given in Sec. 3.3, and we show the corresponding plot for $m_\chi = 10$ MeV and 100 MeV in Fig. 3.14 in Appendix 3.2.5.

is consistent with a combined result of E787 and E949 of the branching ratio measurement [198]

$$B_{\text{measured}}(K^+ \to \pi^+ \nu\bar{\nu}) = (17.3^{+11.5}_{-10.5}) \times 10^{-11} \,. \tag{3.28}$$

For the two-body decay $K^+ \to \pi^+ A'$ (where the $A'$ is on-shell), the $\pi^+$-momentum spectrum is peaked at

$$|\vec{p}_\pi| = \frac{1}{2m_K} \left(m_K^4 + m_\pi^4 + m_{A'}^4 + \right.$$
$$\left. - 2\left(m_K^2 m_\pi^2 + m_K^2 m_{A'}^2 + m_\pi^2 m_{A'}^2\right)\right)^{\frac{1}{2}}, \tag{3.29}$$

while for three-body decay $K^+ \to \pi^+ A'^* \to \pi^+ \bar{\chi}\chi$ through an off-shell $A'$, the $\pi^+$-momentum has a continuous distribution, making it more difficult to distinguish from the SM decay $K^+ \to \pi^+ \nu\bar{\nu}$. The constraints are thus much stronger for the on-shell decay compared to the off-shell decay, and we only consider the former.

Both E787 and E949 published results on the branching ratio limit for on-shell decays [197, 200], which we can use to constrain $\varepsilon$. Following [25], and using results from [201], the two-body decay width is given by

$$\Gamma(K^+ \to \pi^+ A') = \frac{\varepsilon^2 \alpha m_{A'}^2}{2^{10} \pi^4 m_K} \left|W(m_{A'}^2/m_K^2)\right|^2$$
$$\times \left(1 + \frac{(m_\pi^2 - m_{A'}^2)^2}{m_K^4} - \frac{2(m_\pi^2 + m_{A'}^2)}{m_K^2}\right)^{\frac{3}{2}}, \tag{3.30}$$

where

$$|W(x)|^2 \simeq 10^{-12} \left(3 + 6x\right). \tag{3.31}$$

Using now the measured total width of the $K^+$ of $\Gamma_{\text{total}}(K^+) \simeq 5.3 \times 10^{-14}$ MeV, and taking the E949 limit on the branching ratio $K^+ \to \pi^+ A'$ from Fig. 18 in [200] (scaled to 95% C.L.), we derive the limit on $\varepsilon$ versus $m_{A'}$ shown in the shaded brown region in Figs. 3.15 and 3.14. There are two separated excluded regions (as opposed to a single continuous region), since the search $K^+ \to \pi^+ \bar{\nu}\nu$ was restricted to certain values of $|\vec{p}_\pi|$ to avoid backgrounds.

Several experiments have been proposed with an improved sensitivity to $K^+ \to \pi^+ \bar{\nu}\nu$ decays. ORKA [202] is a proposed experiment to measure this branching ratio to much higher precision using stopped kaons from the Fermilab Main Injector high-intensity proton source. Its detector design is based on the E787 and E949 experiments, and it is expected to detect $\sim 1000$ decays over five years of data taking, improving the branching ratio measurement to 5%. ORKA is expected to be able to take data five years after funding becomes available. A rough sensitivity estimate of ORKA to $K^+ \to \pi^+ A'$ decays can be obtained by scaling the E949 limit in [200] used above. First, we assume a factor of 100 increase in the luminosity. In addition, we assume that the background rate of $K^+ \to \pi^+ \bar{\nu}\nu$ decays agrees with the SM prediction (in E787 and E949 the observed background rate was found to be twice as large as the SM prediction, but still consistent with it, thereby weakening the limits slightly).

ORKA can thus be expected to improve the branching ratio limit by at least $\sim \sqrt{200} \sim 14$, and improve the sensitivity to $\varepsilon$ by $\sqrt[4]{200} \sim 3.8$, which is shown in Figs. 3.15 and 3.14 with dashed brown lines. Note that this ignores expected improvements in the $\pi^+$-momentum resolution. This projected improvement in sensitivity to the branching ratio is also weaker than what is projected by the ORKA collaboration for $m_{A'} = 0$, namely from $0.73 \times 10^{-10}$ (at 90% C.L.) to $2 \times 10^{-12}$, a factor of 36.5 as opposed to 14 (see *e.g.* [203]). The ORKA sensitivity shown in Figs. 3.15 and 3.14 should thus be viewed as conservative.

Another experiment with excellent sensitivity to $K^+ \to \pi^+ \bar{\nu}\nu$ decays is NA62 at CERN (with $\sim 50$ events/year) [204]. NA62 may begin data taking within a year. It uses decay-in-flight kaons and may be sensitive to lower $\pi^+$-momenta and thus slightly higher $m_{A'}$. We do not show a sensitivity estimate for NA62, although it would be interesting for the NA62 collaboration to look at this decay mode in detail. Finally, we note that a future Project X facility could reach even higher sensitivity than ORKA or NA62 [188].

### 3.3.2 QED Precision Measurements

As we discussed in Sec. 1.3.2, the $3.6\sigma$ discrepancy in $a_\mu$ can be solved by introducing a dark photon. In Figs. 3.15 and 3.14, we show the "$2\sigma$" region in which an $A'$ helps solve this disagreement by contributing $a_\mu^{A'} = (28.7 \pm 16.0) \times 10^{-10}$. We also show a "$5\sigma$" line, where the $A'$ contributes "too much", $a_\mu^{A'} = 68.7 \times 10^{-10}$.

The appearance of $A'$ also effect electron anomalous magnetic moment measurement $a_e \equiv (g-2)_e$. Current measurements of $a_e$ agree well with SM theory [205, 206] and experiment [207]. One finds (see also [93, 96]),

$$\Delta a_e = a_e^{\text{exp}} - a_e^{\text{SM}} = (-1.06 \pm 0.82) \times 10^{-12}. \tag{3.32}$$

The contribution from an $A'$ would introduce a disagreement between the theory and experimental value. In Figs. 3.15 and 3.14, we show the shaded region labelled $a_e$ in which $a_e^{A'} > (-1.06 + 3 \times 0.82) \times 10^{-12} = 1.4 \times 10^{-12}$.

### 3.3.3 Fixed-target and Beam-dump Experiments

Several existing and proposed experiments are sensitive to visible $A'$ decays, usually to $e^+e^-$ (see *e.g.*, [74, 85, 78, 73, 81, 208, 209, 210, 82, 143, 211, 89, 90, 212, 213]). These searches were motivated in part by astrophysical anomalies connected to Weak-scale DM [34, 35]. However, if the $A'$ can decay to light dark-sector states, then many of these experiments lose all their sensitivity. There are some exceptions, including the electron/positron fixed-target experiments DarkLight [81, 214] and VEPP-3 [215], which have sensitivity also to invisible

$A'$ decays by performing a missing mass measurement. In Fig. 3.15, for DarkLight, we show the reach as shown in Fig. 18 of [216] (for 95% photon efficiency); for VEPP-3, we show the reach given in [215].

Other experiments sensitive to invisible $A'$ decays include proton fixed-target experiments, in which a proton beam incident on a target produces a large number of mesons that decay to an $A'$ (*e.g.* $\pi^0 \to \gamma A'$), which in turn decays to LDM [208]. LSND in particular provides strong, but model-dependent, constraints [194], which we show with gray shaded regions on Figs. 3.15 and 3.14. Further searches are possible at several neutrino facilities [208, 194, 217], and a proposal has been submitted to the MiniBooNE Collaboration [196]. We do not show the reach for these experiments on our plots. Note that the constraints on $\varepsilon$ are proportional to $\sqrt[4]{\alpha_D}$, and thus disappear for small $\alpha_D = g_\chi^2/4\pi$. The constraints from these experiments also disappear if $\chi$ can decay into lighter dark-sector particles that do not interact with the $A'$.

### 3.3.4 Supernova

An $A'$ can increase the cooling rate of supernovae. Visible decays, with *e.g.* $A' \to e^+e^-$, $\varepsilon \sim 10^{-10} - 10^{-7}$, are constrained for $m_{A'} \lesssim 100 - 200$ MeV due to the cooling constraints on SN1987A [74, 92] (see also [218]). There is no bound for very small $\varepsilon$, since not enough $A'$ are produced to contribute significantly to the cooling. For larger $\varepsilon$, the $A'$ lifetime becomes short enough for it to decay inside the supernova, and so does not contribute to any cooling.

For the case where $A'$ predominantly decays to LDM or other dark-sector states, the situation is more complicated. As in the previous case, there is no constraint if $\varepsilon$ is small enough, since not enough $A'$s are produced. For larger $\varepsilon$, $A'$ decay to LDM inside the supernova, and there is potentially a bound if the LDM can escape the supernova. While a careful calculation of the supernova bound is beyond the scope of this thesis, we make a few remarks below to evaluate their relevance to the region probed by *BABAR* and Belle II. A dedicated discussion of the bound will appear in [219]. (We note that there are also constraints from white-dwarf cooling, but only if the $A'$ decays to LDM states with a mass $\lesssim 1$ keV [220].)

The mean free path of the LDM is given by $\ell \sim 1/n\sigma$, where $n \simeq 2 \times 10^{38}/\text{cm}^3$ is the number density of nucleons or electrons in a supernova. The cross section for LDM to scatter off an electron is

$$\sigma_{e\chi \to e\chi} \simeq \begin{cases} \alpha g_\chi^2 \varepsilon^2/m_{A'}^2 & m_{A'} \ll T \\ \alpha g_\chi^2 \varepsilon^2 T^2/m_{A'}^4 & m_{A'} \gg T \end{cases} . \tag{3.33}$$

For a typical supernova temperature of $T \simeq 30$ MeV, $g_\chi \varepsilon = 10^{-4}$ and $m_{A'} = 10$ MeV, the

free-streaming length is $R_{\mathrm{FS}} \simeq 10^{-11}$ km, while for significantly larger masses, $m_{A'} \gtrsim 10$ GeV, one finds $R_{\mathrm{FS}} \simeq 10$ km. For most of the parameter space that can be probed by *BABAR* and Belle II, the free-streaming length is thus smaller than the supernova radius.

The production rate of LDM through an $A'$ is proportional to $\varepsilon^2$. In addition, for a large parameter region of relevance to *BABAR* and Belle II, $m_{A'} \gg T$, so that the production is through an off-shell $A'$ and thus also proportional to $1/m_{A'}^4$. Ignoring the diffusion of LDM through the supernova, the cooling occurs via the escaping LDM produced close to the free-streaming surface. For small free-streaming lengths, the overall energy that escapes (proportional to the production rate times the free-streaming length) is therefore independent of $\varepsilon$ and $m_{A'}$. However, both the production rate and free-streaming length depend strongly on the density and temperature profiles, which are highly uncertain very close to the edge of the supernova. Thus the computation of the cooling rate suffers from very large uncertainties and for small free-streaming lengths cannot be used to place a robust limit.

When the free streaming length becomes of order the size of the supernova, i.e. for $m_{A'} \gtrsim 10$ GeV and sufficiently small $\varepsilon$, any DM particles that are produced in the supernova will escape. However, the temperature profile and size of a supernova, and of SN1987A in particular (which is the only available data), is not known precisely, so that the precise value of $m_{A'}$ at which the free-streaming length equals the supernova radius is not known. For instance, for the same $g_\chi \epsilon = 10^{-4}$ as above and under the assumption of a homogeneous temperature, $T_{\mathrm{SN}} = 25$ MeV, throughout the supernova, one finds $R_{\mathrm{FS}} = R_{\mathrm{SN}} = 10$ km for $m_{A'} = 8.5$ GeV. For $g_\chi \epsilon = 5 \times 10^{-4}$, $T_{\mathrm{SN}} = 40$ MeV and $R_{\mathrm{FS}} = R_{\mathrm{SN}} = 20$ km, the required $A'$ mass is $m_{A'} = 35$ GeV. Thus it is not clear if the supernova bounds apply at all to the $A'$ masses and couplings that can be probed by *BABAR* or Belle II.

### 3.3.5 LDM Direct Detection

Elastic nuclear recoils from DM scattering in current direct detection experiments are not able to probe DM with masses below a few GeV. However, it has recently been demonstrated that direct detection experiments can probe LDM below the GeV scale if the DM scatters instead off electrons [221, 222]. While the limits in [222] were derived from only a small amount of data taken with an experiment focused on probing heavier DM, near-future experiments such as CDMS, LUX, DAMIC and XENON100 are expected to significantly improve their sensitivity in upcoming years. Such constraints are somewhat complementary to the ones derived here, due to their sensitivity to distinct kinematical regimes. Nonetheless, under certain assumptions, the constraints can be directly compared.

In order to make such a comparison, we assume below that the mediator mass is larger

than the typical momentum transfer, $q \sim \text{keV}$, relevant for electron scattering in direct detection experiments. Consequently, effective operators of the form of Eq. (3.20)-Eq. (3.23) can be used to describe the relevant interactions at direct detection experiments, where the cut-off scale, $\Lambda$, is once again taken to be $\Lambda = m_{A'}/\sqrt{g_e g_\chi}$. For a sufficiently heavy mediator, corresponding to region (a) of Fig. 3.9, the limit on $\Lambda$ is directly obtained from Fig. 3.11. For lighter mediators, the mass $m_{A'}$ must also be specified. For a mediator in region (c), this is combined with the *BABAR* limit on $g_e g_\chi$ from Fig. 3.13 to set a bound on $\Lambda$. For a light invisible mediator, in region $(b_{1,2})$, the bound on $g_e$ from Fig. 3.12 applies for any value of $g_\chi$ in the range $g_e \lesssim g_\chi \lesssim \sqrt{4\pi}$. To set a bound on $\Lambda$, we conservatively fix $g_\chi = \sqrt{4\pi}$, at the limit of perturbativity.

Under the above assumptions, the DM-electron cross-section is simply given by

$$\sigma_e = Q \frac{\mu_{\chi e}^2}{\pi \Lambda^4} \,. \tag{3.34}$$

Here $Q = 1$ for the vector and scalar mediator while $Q = 3$ for the pseudo-vector mediator. $\mu_{\chi e}$ stands for the DM–electron reduced mass. In the case of a pseudo-scalar mediator, direct detection rates are velocity suppressed and hence are not shown. We also do not show the results for a pseudo-vector and scalar; for a scalar, there is no generic expectation for the mediator couplings when they are not proportional to the fermion yukawa couplings.

The *BABAR* results may also be translated to DM-proton scattering rates, under assumptions about how the mediator couples to quarks. For a vector mediator, motivated by kinetic mixing with the photon, we assume that the couplings are proportional to the electric charge of the SM particles. One then finds the cross-section for a vector mediated DM-proton interaction to be,

$$\sigma_p = \frac{\mu_{\chi p}^2}{\pi \Lambda^4} \,, \tag{3.35}$$

where $\mu_{\chi p}$ stands for the reduced DM-proton mass.

The resulting direct detection limits on the non-relativistic scattering cross-section of DM with electrons and with protons from the *BABAR* search are shown in Figs. 3.16 and 3.17 for the case of a vector mediator. Results are shown as a function of $m_\chi$, for fixed mediator masses of 3 GeV and 300 MeV. The plots are discontinuous for $m_\chi = m_{A'}/2$, due to the transition between an on-shell and off-shell mediator. In addition, constraints from existing experiments are presented. The LEP mono-photon searches [157] are shown for comparison as a gray shaded region. The green line shows other bounds on a dark photon mediator: $\varepsilon < 0.026$ for $m_{A'} = 3$ GeV from precision $Z$-pole measurements [87]; $\varepsilon < 0.01$ for $m_{A'} = 300$ MeV from muon $(g - 2)$ constraints (see Sec. 3.3); and for $m_\chi > m_{A'}/2$, $\varepsilon \lesssim 1.5 \times 10^{-3}$ from a search for $\Upsilon \to \gamma \mu^+ \mu^-$ by *BABAR* [74]. Finally, limits from DM direct detections
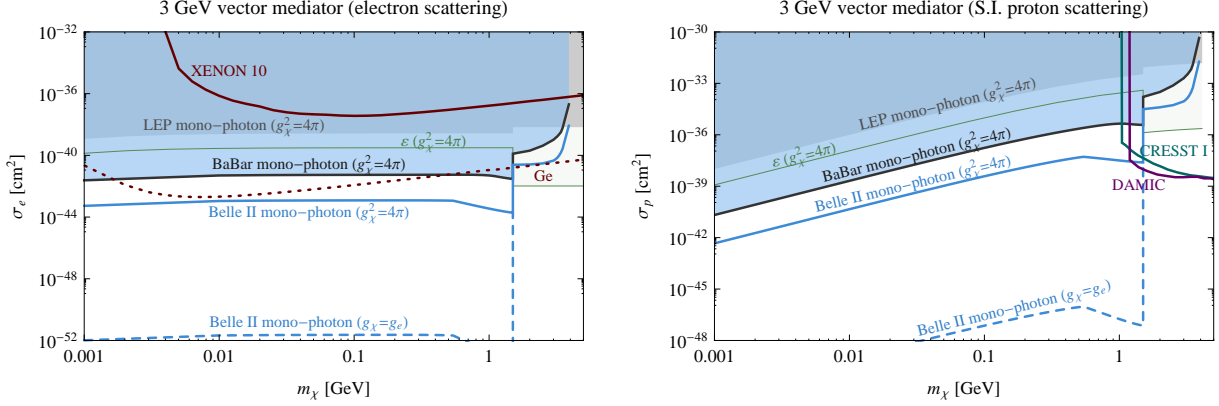
Figure 3.16: A comparison of the sensitivities of mono-photon searches and direct detection experiments to LDM, taking a 3 GeV vector mediator for illustration. Constraints and projections are shown on the non-relativistic scattering cross-section of DM with electrons (**left**), and with protons (**right**), assuming for the latter that the coupling of the mediator to SM particles is proportional to their charge (as with a dark photon). Existing direct detection bounds on proton scattering: CRESST [223] (solid turquoise) and DAMIC [224] (solid purple), are shown. For electron scattering we show the XENON10 limit [222] (solid dark red). In addition, the dotted dark red line shows a projection for a germanium-based electron recoil experiment [221]. The constraint from *BABAR* (this work) is shown as solid black line / blue shaded region. The discontinuity at $m_\chi = 1.5$ GeV corresponds to the transition between on-shell to off-shell light mediator regimes. In the latter regime we fix $g_\chi = \sqrt{4\pi}$ (smaller $g_\chi$ would correspond to stronger bounds). LEP mono-photon searches [157] are shaded in gray and limits from precision dark photon searches are shown by the thin green line labeled "$\varepsilon$" (see text). For the projected reach of Belle II mono-photon searches (blue lines) we use the "systematics limited" bound for $m_\chi > 1.5$ GeV, and otherwise the stronger of the "converted" and "standard" mono-photon searches shown in Fig. 3.15 (see Sec. 3.2.5). For $m_\chi < 1.5$ GeV we also show the projected reach of Belle II assuming $g_\chi = g_e$ (the boundary between visibly- and invisibly-decaying mediators).

experiments are also shown: the XENON10 limits [222] (solid dark red) are presented for DM-electron scattering, while limits from CRESST [223] (solid turquoise) and DAMIC [224] (solid purple) are shown in the DM-proton case. The dotted dark red line shows a possible projection for a germanium-based electron recoil experiment [221], assuming a 1 kg-year exposure and no backgrounds.

In each of the plots we demonstrate the projected Belle II sensitivity as discussed in Sec 3.2.5. For $m_\chi > m_{A'}/2$ we show the "systematics limited" bound for a light off-shell mediator, while for $m_\chi < m_{A'}/2$ we show the stronger of the projections for a converted
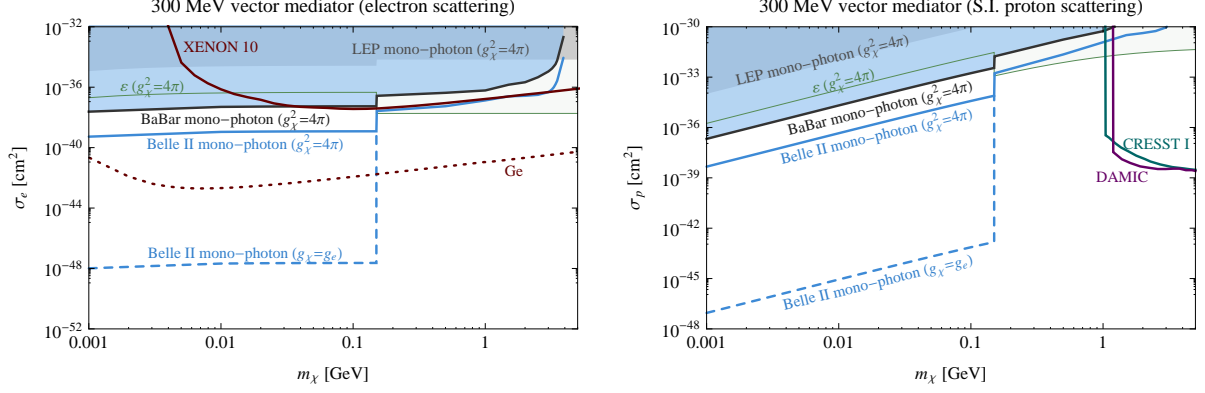
Figure 3.17: A comparison of mono-photon searches and direct detection experiments, as in Fig. 3.16, but for a mediator mass of 300 MeV.

mono-photon search and a standard mono-photon search shown in Figs. 3.12 and 3.15. In the latter case, the solid blue line shows the conservative assumption $g_\chi = \sqrt{4\pi}$. The dashed blue line assumes $g_\chi = g_e$ (the boundary between visibly- and invisibly-decaying mediators), illustrating how much more powerful mono-photon searches are than direct detection experiments at constraining the dark photon with a small $g_\chi$ scenario.

The results above demonstrate the strength of low-energy collider experiments in searching for DM in regimes where direct detection experiments are still lacking. Results from the future Belle II experiment and from future direct detection searches (along the lines suggested in [221, 222]) are competitive (although complimentary) for the case of a heavy mediator. For a light mediator, direct detection experiments are expected to be crucial as their sensitivity is significantly better due to the distinct kinematics.

# Chapter 4

# Searching for Dark Scalars

## 4.1  Searching for Dark Scalars through Exotic Higgs Decays to $b\bar{b}\mu^+\mu^-$

Exotic Higgs decays are effective ways to probe the Higgs portal. One interesting category of exotic Higgs decays contains final states with four SM fermions and no missing energy: $h \to XX' \to 2f2f'$, where $X$ and $X'$ are on-shell, and we here assume that they are the same particle, $X = X'$.[1] Generically, the couplings of $X$ determine the optimal search strategy. If $X$ is a dark photon, i.e. the mediator of a new, broken $U(1)$ gauge theory which kinetically mixes with the SM hypercharge gauge boson [67, 68, 69], then the couplings of $X$ to SM particles are gauge-ordered, i.e. the $X$ couplings are related to the SM $Z$-boson and photon couplings to SM fermions. In this case, the $X$ has an $\mathcal{O}(1)$ branching ratio to light leptons, making $h \to 4\ell$ the best discovery channel [225, 226, 94, 95, 227, 64, 228, 229, 230, 142]. On the other hand, if $X$ is a CP-odd[2] scalar $(a)$ or a CP-even scalar $(s)$, it generically inherits its couplings from the SM Higgs sector. This means that the couplings of $X$ to the SM fermions are typically Yukawa-ordered, so that its largest branching ratio is to the heaviest fermion that is kinematically accessible. For this reason, previous LHC studies have extensively focused on the decay channels $h \to 4b$ [231, 232, 233, 234, 235, 236] and $h \to 2b2\tau$ [237, 235] for $m_X > 2m_b$, $h \to 4\tau$ [238, 239] and $h \to 2\tau2\mu$ [120, 240] for $2m_\tau < m_X < 2m_b$, and $h \to 4\mu$ [240, 241, 242, 243] for $2m_\mu < m_X < 2m_\tau$. These searches are motivated in the context of, for example, the SM with a singlet (see *e.g.* [64]); the two-Higgs-doublet model with an additional singlet (2HDM+S, see *e.g.* [244, 64]), including the next-to-minimal supersymmetric standard model (NMSSM) [245, 246, 247]; the minimal

---

[1]We use the shorthand, for example, '$2f$' or '$4f$' to denote $f\bar{f}$ of $f\bar{f}f\bar{f}$, respectively.

[2]In this study, we will only consider CP-conserving Higgs sectors.

supersymmetric standard model (MSSM) with a singlet [244]; as well as many hidden valley models [80, 79, 112, 248].

In this section we propose a new search channel, $h \to 2b2\mu$, as a promising discovery avenue for Higgs decays to light scalars with a mass above $2m_b$. As we will see below, this channel represents a compromise between the dominant but difficult $4b$ and $2b2\tau$ channels, and the spectacular but very rare $4\mu$ channel. In [64], two scenarios for realizing this decay via intermediate on-shell states were considered: $h \to Za$ (see also [249]) and $h \to XX$ with $X = s$ or $X = a$. Sensitivity to the latter scenario was only estimated at parton-level. Here we expand on this estimate and provide a more detailed and comprehensive collider study for $h \to 2X \to 2b2\mu$ at the LHC. We also discuss how the projected sensitivity compares to the results of previous collider studies in the $4b$, $4\tau$, $2\tau2\mu$, and $2b2\tau$ channels.

The section is organized as follows. We first review the theoretical motivation for a search of $h \to 2X \to 2b2\mu$ in Sec. 4.1.1. We then discuss the sensitivity projections of this channel at the LHC 8 and LHC 14 in Sec. 4.1.2, discuss and compare these with existing sensitivity projections for other decay modes in Sec. 4.1.3, and finally conclude in Sec. 4.1.4. Some details about fake-lepton background estimates are included in Appendix A.2.

### 4.1.1 Predicted Branching Ratios of $h \to 2b2\mu$

Here we discuss a non-exhaustive set of models that contain the $h \to 2b2\mu$ decay and what theoretical predictions on branching ratio is. We only consider the SM with a singlet and the 2HDM+S models, as well as the NMSSM in particular. In these models, the $h$ decays to an intermediate on-shell scalar, which is either CP-even (and denoted by $s$) or CP-odd (and denoted by $a$), i.e. we consider $h \to ss$, or $h \to aa$. We will not consider other models that can lead to this decay. It is also possible that the Higgs decays to two scalars with *different* masses and/or couplings, *e.g.* $h \to ss'$ or $h \to aa'$, where $s$ and $a$ ($s'$ and $a'$) have large branching ratios to $b\bar{b}$ ($\mu^+\mu^-$). We do not consider this possibility in detail here. However, if it was realized, the $2b2\mu$ channel would obviously offer the best sensitivity to the total exotic Higgs decay branching ratio.

**SM+Salar scenario**

As we mentioned in Sec. 2.3.1, the dominate decay channel for intermediate scalar $s$ in SM+S $s \to bb$ if $m_s > 2m_b$. We quantify other decay branching ratio with respect to $H \to b\bar{b}$ by

$$\epsilon_{\mu b} \equiv \frac{\mathrm{Br}(s \to \mu^+\mu^-)}{\mathrm{Br}(s \to b\bar{b})} \approx \frac{m_\mu^2}{3m_b^2} \approx 2 \times 10^{-4} \tag{4.1}$$

68

| Final State | $\mathrm{Br}(h \to 2s \to 2f2f')/\mathrm{Br}(h \to 2s)$ |
|---|---|
| $b\bar{b}b\bar{b}$ | 0.77 |
| $b\bar{b}\tau^+\tau^-$ | 0.10 |
| $\tau^+\tau^-\tau^+\tau^-$ | $3.5 \times 10^{-3}$ |
| $b\bar{b}\mu^+\mu^-$ | $3.7 \times 10^{-4}$ |
| $\tau^+\tau^-\mu^+\mu^-$ | $2.5 \times 10^{-5}$ |
| $\mu^+\mu^-\mu^+\mu^-$ | $4.5 \times 10^{-8}$ |

Table 4.1: $\mathrm{Br}(h \to 2s \to 2f2f')/\mathrm{Br}(h \to 2s)$ in the SM+S model, with $m_s = 40$ GeV. These numbers are relatively constant across the mass range $15 \text{ GeV} \leq m_s \leq 60 \text{ GeV}$.

The small value of $\epsilon_{\mu b}$ explains the hierarchical structure of the $s$ branching ratios to $4\mu$, $2b2\mu$, and $4b$. At leading order, and ignoring phase space corrections, the Higgs branching ratios satisfy

$$\mathrm{Br}(h \to 2s \to 4\mu) = \frac{\epsilon_{\mu b}}{2}\mathrm{Br}(h \to 2s \to 2b2\mu)$$
$$= \epsilon_{\mu b}^2\mathrm{Br}(h \to 2s \to 4b). \tag{4.2}$$

Precise values, including QCD corrections that are calculated following [250, 251], are shown in Tab. 4.1.

Assuming that the Higgs is produced with SM rates, and that $\mathrm{Br}(h \to 2s) = 10\%$, one can estimate that $\mathcal{O}(20)$ $h \to 2s \to 2b2\mu$ events could be observed from gluon-gluon fusion (ggF) Higgs production at the LHC Run I (compared to zero $h \to 2s \to 4\mu$ events). While this is much less than the few hundred $h \to 2s \to 4b$ events expected from associated production, the backgrounds for a $W(h \to 4b)$ search are very challenging. As we discuss in Sec. 4.1.3, $2b2\mu$ provides complementary information to the the usual $4b$ channel for an SM+S-like scenario, and may be superior, depending on how well relatively soft $b$-jets can be reconstructed.

## 2HDM+Scalar

The simple SM+S set-up can be generalized to 2HDM+S as shown in Sec. 2.3.2. Much of the parameter space of 2HDM+S models remains unexplored by existing experimental data. (Note that the unaugmented 2HDM can also generate exotic higgs decays of the $h \to aa$ type, see *e.g.*[252].)

The general 2HDM+S setup generates a rich phenomenology. In particular, the simple scaling of the branching ratios given in Eqs. (4.1) and (4.2) does not hold in all regions of
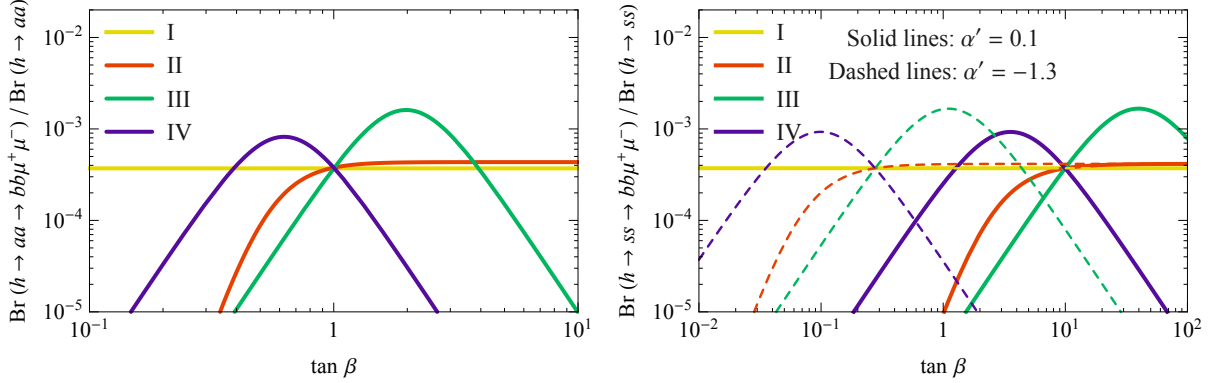
Figure 4.1: $\mathrm{Br}(h \to 2a \to 2b2\mu)/\mathrm{Br}(h \to 2a)$ of a CP-odd scalar, $a$, (**left**) and CP-even scalar, $s$, (**right**) in 2HDM+S with a fixed mass $m_{a(s)} = 40$ GeV.

parameter space. Of interest to us here are scenarios for which the Higgs decay branching ratio to $2b2\mu$ is enhanced compared to its value in the SM+S model. Fig. 2.5 and Fig. 2.6 shows the branching ratios of the CP-odd scalar $a$ as a function of $m_a$ for a particular choice of $\tan\beta$ in the type-II and type-III 2HDM, respectively. While the type-II case shown provides an example with a very similar phenomenology to the SM+S model in Sec. 4.1.1, the type-III case shown features significantly larger $\mathrm{Br}(h \to aa \to 2b2\mu)$.

Above the $b\bar{b}$ threshold, the relevant branching ratios depend only weakly on mass. It is therefore instructive to look at $\mathrm{Br}(h \to 2a(s) \to 2b2\mu)$ as a function of $\tan\beta$ (and $\alpha'$) for the four 2HDM model types. The **left** plot in Fig. 4.1 shows $\mathrm{Br}(h \to 2a \to 2b2\mu)/\mathrm{Br}(h \to 2a)$ as a function of $\tan\beta$ for a CP-odd scalar $a$, while in the **right** plot we consider a CP-even scalar $s$ for two choices of $\alpha'$ (the scalar mass is set to 40 GeV). In both cases, the maximum value of $\mathrm{Br}(h \to 2a(s) \to 2b2\mu)/\mathrm{Br}(h \to 2a(s))$ of the type-III 2HDM+S ($\simeq 0.0016$) is about four times greater than that for type-I or II ($\simeq 0.0004$).

The maximum value of $\mathrm{Br}(h \to 2a \to 2b2\mu)/\mathrm{Br}(h \to 2a)$ in the type-III 2HDM+S model can be understood simply as follows. From Tab. 2.1, the coupling of $ab\bar{b}$ ($a\tau^+\tau^-$ and $a\mu^+\mu^-$) scales as $1/\tan\beta$ ($\tan\beta$). Thus, keeping only the most important terms and ignoring phase space and QCD corrections,

$$\frac{\mathrm{Br}(h \to 2a \to 2b2\mu)}{\mathrm{Br}(h \to 2a)} \sim \frac{6m_b^2 m_\mu^2}{m_\tau^4 \tan^4\beta + 9m_b^4 \cot^4\beta + 6m_b^2 m_\tau^2} . \tag{4.3}$$

This is maximized for $\tan\beta \sim (\sqrt{3}\, m_b/m_\tau)^{1/2} \sim 2$, with the maximum value given by

$$\frac{\mathrm{Br}(h \to 2a \to 2b2\mu)}{\mathrm{Br}(h \to 2a)} \simeq \frac{\epsilon_{\mu\tau}}{2}, \tag{4.4}$$

70

where

$$\epsilon_{\mu\tau} \equiv \frac{\text{Br}(a \to 2\mu)}{\text{Br}(a \to 2\tau)} \approx \frac{m_\mu^2}{m_\tau^2} \approx 0.0035. \tag{4.5}$$

(The derivation for the CP-even scalar is identical, up to the replacement $\tan\beta \to -\sin\alpha/\cos\beta$.) Interestingly, as we discuss in Sec. 4.1.3, the sensitivity of a $2b2\mu$ search to $\text{Br}(h \to 2a)$ in these somewhat leptophilic scenarios is competitive with purely leptonic searches like $h \to 2\tau2\mu$, while providing a potentially cleaner final state for experimental reconstruction.

## NMSSM

An important example of a model with a non-minimal scalar sector is the NMSSM (see, *e.g.*, [247] for review). An additional Higgs singlet superfield $\hat{S}$ is introduced to address the $\mu$ problem of the MSSM. The Higgs superpotential is given by

$$\mathcal{W}_{\text{Higgs}} \supset \lambda \hat{S}\hat{H}_u \cdot \hat{H}_d + \frac{\kappa}{3}\hat{S}^3, \tag{4.6}$$

which together with the soft supersymmetry breaking terms results in the Higgs potential

$$V_{\text{soft}} \supset m_{H_d}^2|H_d|^2 + m_{H_u}^2|H_u|^2 + m_S^2|S|^2 + \left(\lambda A_\lambda H_u \cdot H_d S + \frac{1}{3}A_\kappa \kappa S^3 + \text{h.c.}\right), \tag{4.7}$$

where $\hat{H}_u$ and $\hat{H}_d$ are MSSM Higgs doublet superfields (unhatted fields indicate complex scalar components of the hatted superfields). The parameters $\lambda$ and $\kappa$ are Yukawa couplings, while $A_\lambda$ and $A_\kappa$ are soft-breaking $A$-parameters. The resulting neutral Higgs sector contains three CP-even scalars $(h_1, h_2, h_3)$ and two CP-odd ones $(a_1, a_2)$, labelled in order of increasing mass. Its phenomenology, in the context of exotic Higgs decays, can be seen as a type-II 2HDM+S model with restricted parameter choices.

A light CP-odd scalar can be realized in the NMSSM by taking the $R$-symmetry limit $(A_\lambda, A_\kappa \to 0)$ [253, 254, 255] or the Peccei-Quinn-symmetry limit $(\kappa, A_\kappa \to 0)$ [123, 256, 257, 258]. A light CP-even or odd scalar can also occur via an accidental cancellation among parameters that control their mass. Parameter scans have been conducted to search for NMSSM scenarios with a SM-like $\sim 125$ GeV Higgs as well as light scalars with $m_a < m_h/2$ [259, 260, 233, 261, 262, 263]. If the $a$ is light, current LHC Higgs data favors it to be singlet-dominated, but $\text{Br}(h \to 2a) \sim \mathcal{O}(10\%)$ is possible in the surviving parameter space.

It is interesting to consider the possible connection between $h \to 2a$ decays and naturalness in NMSSM models. An NMSSM scenario can be considered potentially natural if radiative Higgs mass corrections are small compared to tree-level contributions.

If $h = h_1$ and $a = a_1$, the tree-level SM Higgs mass is given by

$$m_{h,\text{tree}}^2 \simeq m_Z^2 \cos^2 2\beta + \lambda^2 v^2 \sin^2 2\beta - \frac{\lambda^2 v^2}{\kappa^2}\left[\lambda - \sin 2\beta\left(\kappa + \frac{A_\lambda}{2s}\right)\right]^2, \tag{4.8}$$

where $s \equiv \langle S \rangle$ and $\tan \beta \equiv \langle H_u \rangle / \langle H_d \rangle$. As argued in [247, 264], the naturalness limit of the NMSSM is reached for low $\tan \beta$ and $\lambda$ as large as possible (perturbativity at the GUT scale bounds $\lambda \lesssim 0.7$). Since the triple Higgs coupling $h_1 a_1 a_1$ is proportional to $\lambda$ at tree-level in the NMSSM, $\lambda \approx 0.7$ would imply $\mathrm{Br}(h_1 \to 2a_1) \approx 100\%$ if the channel is kinematically accessible, which is strongly disfavored by current LHC data. Therefore, the surviving parameter space with a sufficiently small $\mathrm{Br}(h_1 \to 2a_1) \lesssim 0.1$ requires a somewhat unnatural realization of the NMSSM in this scenario.

For $h = h_2$ and $a = a_1$, mixing in the CP-even scalar sector can help to increase $m_{h_2}$ [265]. The naturalness limit with $m_{a_1} < m_{h_2}/2$ is accommodated with $\tan \beta \sim 4 - 6$ and the comparatively smaller $\lambda \lesssim 0.4 - 0.5$ [263]. This allows for $\mathrm{Br}(h_2 \to 2a_1) \lesssim 0.1$, consistent with current LHC data. This conclusion is supported by [233].

## 4.1.2 Reach Estimate

In this section, we estimate the reach of the search for $h \to 2a \to 2b2\mu$ with $20\,\mathrm{fb}^{-1}$ at the 8 TeV LHC, and with $30\,\mathrm{fb}^{-1}$, $300\,\mathrm{fb}^{-1}$, and $3000\,\mathrm{fb}^{-1}$ at the 14 TeV LHC. For simplicity, we only consider $a$ to be a CP-odd scalar and the two intermediate $a$'s to be identical and on-shell. These results should apply, with little modification, to the case where the intermediate state is CP-even, as we do not make explicit use of any angular information of the decay.

We assume that the 125 GeV Higgs boson, $h$, is SM-like except for a non-zero branching ratio for the exotic decay $h \to 2a$. In particular, we assume that $h$ is mainly produced through ggF and has a non-zero branching ratio for the decay $h \to 2a \to 2b2\mu$. Higgs production via vector boson fusion is not included in our analysis, making our projected sensitivities slightly pessimistic. The signal is simulated for the mass of $a$ ranging from 15 GeV to 60 GeV. Lower masses of $a$ (but still above the $2b$ threshold) may involve complicated decays to bottomonium and are beyond the scope of this study [141].

We will consider three types of analyses below. A "conventional analysis" (Sec. 4.1.2) will make use of standard anti-$k_t$ jets (from $a \to 2b$) with a radius of $R = 0.4$ or $R = 0.5$. For low $m_a$, these jets are boosted and merge, so that an analysis with $R = 0.2$ is more sensitive (Sec. 4.1.2). Finally, we use jet-substructure techniques to improve the low-$m_a$ reach further (Sec. 4.1.2).

The dominant backgrounds are Drell-Yan (DY) production with associated jets, *i.e.*, $Z^{(*)}/\gamma^* + 2b/2c/2j$, where $Z^{(*)}/\gamma^*$ produces a muon pair.[3] A secondary background arises from $t\bar{t}$ production. Backgrounds from diboson production ($ZZ$, $WW$, $WZ$) have small

---

[3]We have checked that the corresponding background where $Z^{(*)}/\gamma$ produces two leptonic $\tau$'s is negligible in our analysis, due to the larger amount of missing energy and our strict $m_h$ reconstruction requirement.

|  | 8 TeV cross section (pb) | 14 TeV cross section (pb) |
|---|---|---|
| $b\bar{b}\mu^+\mu^-$ | 6.11 | 12.16 |
| $c\bar{c}\mu^+\mu^-$ | 60.44 | 109.50 |
| $jj\mu^+\mu^-$ | 151.65 | 275.17 |
| $t\bar{t}$ | 0.68 | 2.49 |
| $jj\mu^+\mu^{-*}$ | 152.24 | 279.17 |

Table 4.2: Cross sections for various backgrounds after applying generator level cuts as described in Sec. 4.1.2, given by `Sherpa 2.1.1`. The last row refers to DY $Z^{(*)}/\gamma^* + 2j$ background with different generator level cuts, as required for the small-radius jets and jet substructure analyses in Sec. 4.1.2 and Sec. 4.1.2. These cross sections are scaled in our reach estimates by a pessimistic $K$-factor of 2 to account for higher-order effects.

enough cross sections so that we can neglect them. Finally, it is possible for QCD multi-jet events, with two jets being mis-identified as muons, to contribute to the background. These 'lepton fakes' are notoriously difficult to simulate. In Appendix A.2, we use the methods of [266] to estimate their importance compared to the irreducible DY backgrounds. We find that it is reasonable to neglect muon fakes for an analysis with 0 or 2 $b$-tags, but they may be competitive if we require only a single $b$-tag. We therefore limit ourselves to using either 0 or 2 $b$-tags in Sec. 4.1.2 and Sec. 4.1.2; in these analyses, we find in any case that the sensitivity is not noticeably improved by including a single $b$-tag. However, in Sec. 4.1.2, we consider the possibility of requiring a single fat jet with a single $b$-tag. For this, a data-driven estimate of lepton-fakes to determine their importance will be needed by the experimental collaborations.

**Conventional analysis**

Signal, as well as DY $Z^{(*)}/\gamma^* + 2b/2c/2j$ and $t\bar{t}$ backgrounds, are simulated at leading-order (LO) by `Sherpa 2.1.1` [267] for the 8 and 14 TeV LHC with the CT10 [268] parton distribution function (PDF), and matched up to three jets (i.e., for example, we include one extra jet for the signal). We ignore lepton fakes from pure QCD, as justified in Appendix A.2. At generator level, no cut is imposed on the signal. The generator-level cuts for the backgrounds are: $p_{T\mu} > 5$ GeV, $|\eta_\mu| < 5$ and $10$ GeV $< m_{\mu\mu} < 70$ GeV. Additionally, for $Z^{(*)}/\gamma^* + 2j$ we require at least two partons with $p_{Tj} > 10$ GeV and $|\eta_j| < 5$. Here, $j$ refers to partons clustered into jets with the anti-$k_t$ algorithm with radius $R = 0.2$.

The signal cross sections are normalized to $\sigma_{ggF} \times \mathrm{Br}(h \to 2b2\mu)$, where $\sigma_{ggF} \simeq 19.3\,\mathrm{pb}^{-1}$ and $49.47\,\mathrm{pb}^{-1}$ are the next-to-leading-order (NLO) ggF Higgs production cross section for

|  | ATLAS | CMS |
|---|---|---|
| $\epsilon_\mu$ | $\left\{\begin{array}{ll} 0.98 & p_T > 6 \text{ GeV} \\ 0 & \text{otherwise} \end{array}\right.$ | $\left\{\begin{array}{ll} 0.96 & p_T > 6 \text{ GeV} \\ 0 & \text{otherwise} \end{array}\right.$ |
| $\Delta R_\mu^{\text{iso}}$ | 0.3 | 0.4 |
| $\max\left(p_T^{\text{cone}}/p_T^\mu\right)$ | 1.13 | 1.10 |
| $R_{\text{jet}}$ | 0.4 | 0.5 |
| $R_{\text{microjet}}$ | 0.2 | 0.2 |

Table 4.3:   Relevant object reconstruction parameters assumed for the ATLAS and CMS detectors. $\epsilon_\mu$ is the muon tagging efficiency for $|\eta| < 2.4$ (Note that our analysis relies on a dimuon trigger, which has a higher threshold than 6 GeV.) For a muon with $p_T^\mu$ to pass the isolation criteria, the $p_T$ of all the objects in a cone of radius $\Delta R_\mu^{\text{iso}}$ around the muon must be less than the shown $\max\left(p_T^{\text{cone}}/p_T^\mu\right)$. Jets are anti-$k_T$ clustered [270] with a radius given by $R_{\text{jet}}$. For the analysis in Sec. 4.1.2, this is reduced to 0.2. See text for details on $b$-tagging.
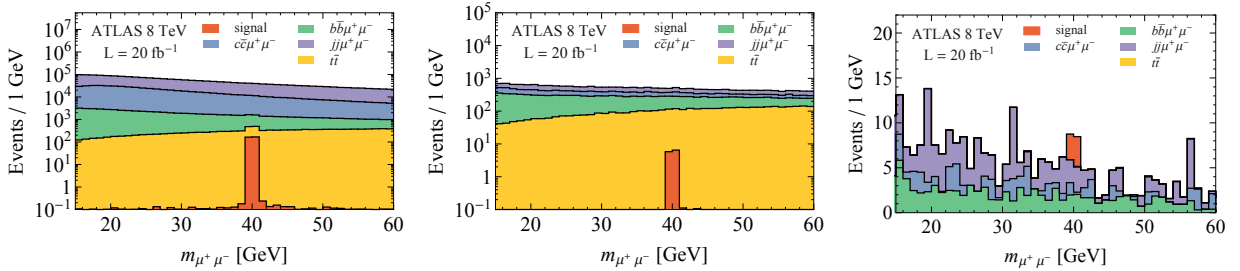


Figure 4.2: Stacked $m_{\mu^+\mu^-}$ distributions for signal ($m_a = 40$ GeV) and backgrounds with 2 $b$-tags at ATLAS 8 TeV for $20\,\text{fb}^{-1}$. The *left*, *center*, and *right* plots represent the distributions after passing the generator level cuts, preselection cuts, and higher level cuts respectively. In the **right** plot, all cuts have been included *except* for the cut on $m_{\mu_1\mu_2}$. We choose the signal size to correspond to $\sim 2\sigma$ sensitivity of our analysis. The assumptions for cross sections and branching ratios are the same as in Tab. 4.4.

8 TeV and 14 TeV, respectively [269]. Given the generator level cuts as described above, the cross sections for the backgrounds given by `Sherpa 2.1.1` are shown in Tab. 4.2. We then scale all backgrounds by a pessimistic $K$-factor of 2, to account for higher-order effects in our sensitivity estimates.

Detector simulation and data analysis are performed by an in-house software framework also used *e.g.* in [271, 266, 272]. This includes jet clustering with `FastJet 3.0.6` [273], application of realistic efficiency curves and isolation requirements for $b$-jet and lepton re-

| Selection Criteria | $S$ | $b\bar{b}\mu^+\mu^-$ | $c\bar{c}\mu^+\mu^-$ | $jj\mu^+\mu^-$ | $t\bar{t}$ |
|---|---|---|---|---|---|
| Generator level cuts | no cuts | $p_{T\mu} > 5$ GeV, $|\eta_\mu| < 5$ and 10 GeV $< m_{\mu\mu} < 70$ GeV for $jj\mu^+\mu^-$, we require in addition two partons with $p_{Tj} > 10$ GeV and $|\eta_j| < 5$ | | | |
| $N_{\text{ev, gen.}}$ $(20\,\text{fb}^{-1})$ | $6.3 \times 10^2$ | $2.4 \times 10^5$ | $2.4 \times 10^6$ | $6.1 \times 10^6$ | $2.7 \times 10^4$ |
| pass OS dimuon trigger $p_{T\mu_1,\mu_2} > (13,13)$ GeV or $(18,8)$ GeV | 50% | 27% | 19% | 29% | 60% |
| at least two $b$-jets with $p_{Tb} > 25$ GeV and $|\eta_b| < 2.5$ | 3.8% | 17% | 1.3% | 0.45% | 37% |
| $\Delta R_{b_1b_2,b\mu,\mu_1\mu_2} > 0.4, 0.4, 0.3$ | 99% | 99% | 99% | 99% | 99% |
| $N_{\text{ev,presel.}}$ $(20\,\text{fb}^{-1})$ | 12 | $1.1 \times 10^4$ | $5.7 \times 10^3$ | $7.9 \times 10^3$ | $5.9 \times 10^3$ |
| $\not{E}_T < 30$ GeV | 98% | 90% | 95% | 92% | 12% |
| $|m_{b_1b_2\mu_1\mu_2} - m_h| < 15$ GeV | 54% | 4.7% | 3.3% | 3.3% | 0.6% |
| $|m_{b_1b_2} - m_a| < 15$ GeV | 97% | 25% | 31% | 61% | 24% |
| $|m_{\mu_1\mu_2} - m_a| < 1$ GeV | 100% | 3.4% | 2.9% | 3.7% | 7.6% |
| $N_{\text{ev, final}}$ $(20\,\text{fb}^{-1})$ | 6.2 | 4.0 | 1.6 | 5.3 | 0.1 |

$$S = 6.2, \quad B_{\text{tot}} = 11, \quad S/B_{\text{tot}} = 0.6, \quad S/\sqrt{B_{\text{tot}}} = 1.9$$

Table 4.4: Relative efficiencies for the signal $(S)$ $h \rightarrow aa \rightarrow b\bar{b}\mu^+\mu^-$ $(m_a = 40$ GeV$)$ and indicated backgrounds, with 2 $b$-tags at ATLAS 8 TeV. All signals and backgrounds listed are simulated with `Sherpa 2.1.1`. The number of signal and background events after passing the generator level cuts, preselection cuts, and higher level cuts are also listed as $N_{\text{ev, gen.}}$, $N_{\text{ev,presel.}}$, and $N_{\text{ev,final}}$, respectively. (Meaningful comparisons are only possible between the latter two as $N_{\text{ev, gen.}}$ is biased by different generator-level cuts on signal and background.) For the signal normalization, we take the NLO ggF production cross section $\sigma_{ggF} = 19.3\,\text{pb}^{-1}$ [269], and assume $\text{Br}(h \rightarrow aa) \approx 100\%$, $2 \times \text{Br}(a \rightarrow b\bar{b})\text{Br}(a \rightarrow \mu^+\mu^-) = 1.6 \times 10^{-3}$. The latter branching ratio factor corresponds to a 2HDM model of type-III plus a singlet with $\tan\beta = 2$ (see Sec. 4.1.1 and Fig. 4.1 ). For the background normalization, we adopted cross sections at generator level from `Sherpa` (see Tab. 4.2) and scaled them by a pessimistic $K$-factor of 2.
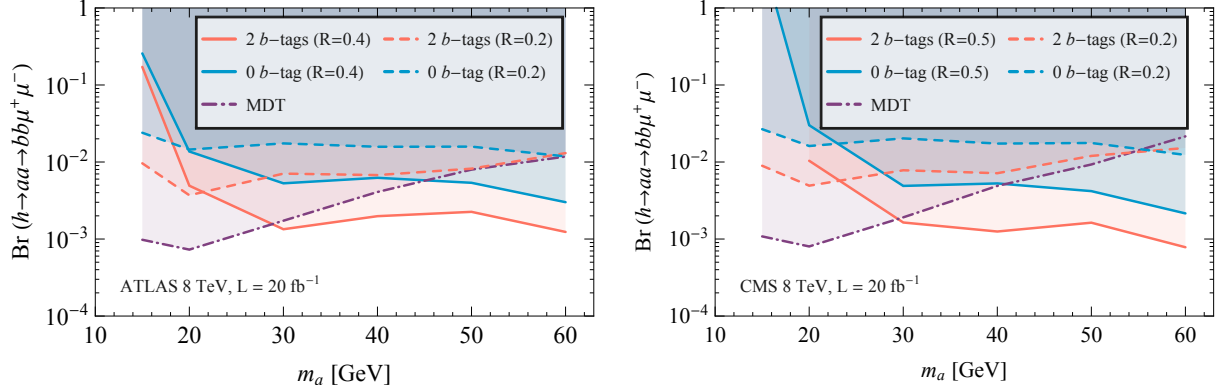
Figure 4.3: Expected 95% CL sensitivity to $\text{Br}(h \to aa \to b\bar{b}\mu^+\mu^-)$ for 20 fb$^{-1}$ data at 8 TeV ATLAS (*left*) and CMS (*right*). The solid line is the sensitivity of the "conventional" analysis (Sec. 4.1.2) with a jet-clustering radius of either $R = 0.4$ (ATLAS) or 0.5 (CMS). The sensitivities when using a smaller jet radius of $R = 0.2$ (Sec. 4.1.2) is shown with dashed lines. The purple dot-dashed line is the sensitivity from a jet substructure analysis that makes use of the mass drop tagger (MDT) (Sec. 4.1.2).

construction, and geometric detector acceptances. The relevant detector parameters for our analysis are given in Tab. 4.3. The differences between the two detectors' capabilities are relatively minor and the projected limits for both will be similar. However, the larger jet clustering radius in the CMS conventional analysis will affect the low-mass limit. We adopt the $b$-tagging efficiency curve for the "MV1" algorithm at the 70% $b$-jet efficiency working point in [274, 275] and the $c$/light-jet rejection curves with respect to $b$-jet efficiency (also for the MV1 algorithm) in [276]. For jet $p_T$ of around 200 GeV, the $b$-tagging efficiencies for $(b, c, \text{light})$ jets are $(0.78, 0.3, 0.03)$. These efficiencies drop to $(0.54, 0.1, 0.001)$ at $p_T = 25$ GeV. We use the same $b$-tagging efficiencies for both the ATLAS and CMS analyses.

The events will be recorded using a di-muon trigger. For the LHC 8 TeV search, we impose the dimuon trigger used in [277], requiring $|\eta_{\mu_1,\mu_2}| < 2.4$ and $p_{T\,\mu_1,\mu_2} > 13$ GeV, 13 GeV or $p_{T\,\mu_1,\mu_2} > 18$ GeV, 8 GeV (objects are labelled in order of decreasing $p_T$). We then impose several "preselection cuts". The leading jets are required to satisfy $p_T > 25$ GeV, $|\eta| < 2.5$, and $\Delta R_{J_1 J_2} > 0.4$. On the two (leading) muons we impose $\Delta R_{\mu_1\mu_2} > 0.3$. The distances between the two leading jets and the two leading muons must satisfy $\Delta R_{J\mu} > 0.4$ ($J$ stands for the two leading jets ($b$-jets) for the analysis with 0 (2) $b$-tags). Events with either 0 or 2 $b$-tags are selected.

Following this preselection, we now impose cuts to separate the signal from background. A missing transverse energy cut of $\not{E}_T < 30$ GeV suppresses $t\bar{t}$ background. We also make

use of the double-resonance structure of the signal by imposing mass reconstruction cuts

$$|m_{J_1 J_2 \mu_1 \mu_2} - m_h| < 15 \text{ GeV},$$
$$|m_{J_1 J_2} - m_a| < 15 \text{ GeV},$$
$$|m_{\mu_1 \mu_2} - m_a| < 1 \text{ GeV}, \tag{4.9}$$

separately for each $m_a$.

Tab. 4.4 shows an example of the relative efficiencies for the signal with $m_a = 40$ GeV and backgrounds with 2 $b$-tags for ATLAS at 8 TeV. Fig. 4.2 shows the corresponding stacked histograms for the signal and backgrounds after passing the generator level, preselection level, and higher level cuts (except for the cut on $m_{\mu_1 \mu_2}$). Despite simulating a very large number of events, our background $m_{\mu\mu}$ spectra display some fluctuations after all the other cuts with two $b$-tags are applied. This can partially be attributed to the way `Sherpa` generates weighted events, but is more generally due to the difficulty of overpopulating each small $m_{\mu\mu}$ bin in our signal region with DY+jets Monte Carlo, in order to determine the expected number of background events with high precision. However, at the level of precision of our study, this will not significantly affect our derived sensitivity reach, for which we assume a simple counting experiment after applying the above cuts, with the background expectation taken directly from the Monte Carlo prediction. For an experimental study, a side-band-type analysis would be used to estimate the SM contribution in a particular $m_{\mu\mu}$ bin directly from data. Since the aim of our study is merely to estimate the $2\sigma$ exclusion potential, we can neglect these details, including systematic uncertainties, which we have no way of reliably determining. In particular, we also do not show the $5\sigma$ discovery reach, as this would require an estimate of the look-elsewhere effect, which depends on how the analysis is done.

The expected 95% confidence level (CL) sensitivity to $\text{Br}(h \to aa \to b\bar{b}\mu^+\mu^-)$ from 8 TeV data are shown in Fig. 4.3 for both ATLAS and CMS. Requiring 2 $b$-tags increases the sensitivity by about a factor of 3 compared to requiring no $b$-tags. The expected bounds are approximately independent of scalar mass for $m_a \geq 30$ GeV. For $m_a < 20$ GeV, the signal efficiency drops dramatically because the two $b$'s from the $a$-decay become collimated. In fact, in our CMS analysis (which required the jets to satisfy $R = 0.5$), no signal events passed the cuts for this low $m_a$ region. However, as we show in the next sections, $b$-tagging with a smaller jet radius or the use of jet substructure can dramatically improve sensitivity in this region.

The analysis proceeds nearly identically for the 14 TeV LHC. We apply the same dimuon trigger, reconstruction criteria, and cuts. The higher luminosity may present challenges in the form of pile-up or higher reconstruction thresholds, but they are beyond the scope of our analysis. The resulting sensitivity to $\text{Br}(h \to aa \to b\bar{b}\mu^+\mu^-)$ are shown in Fig. 4.4.
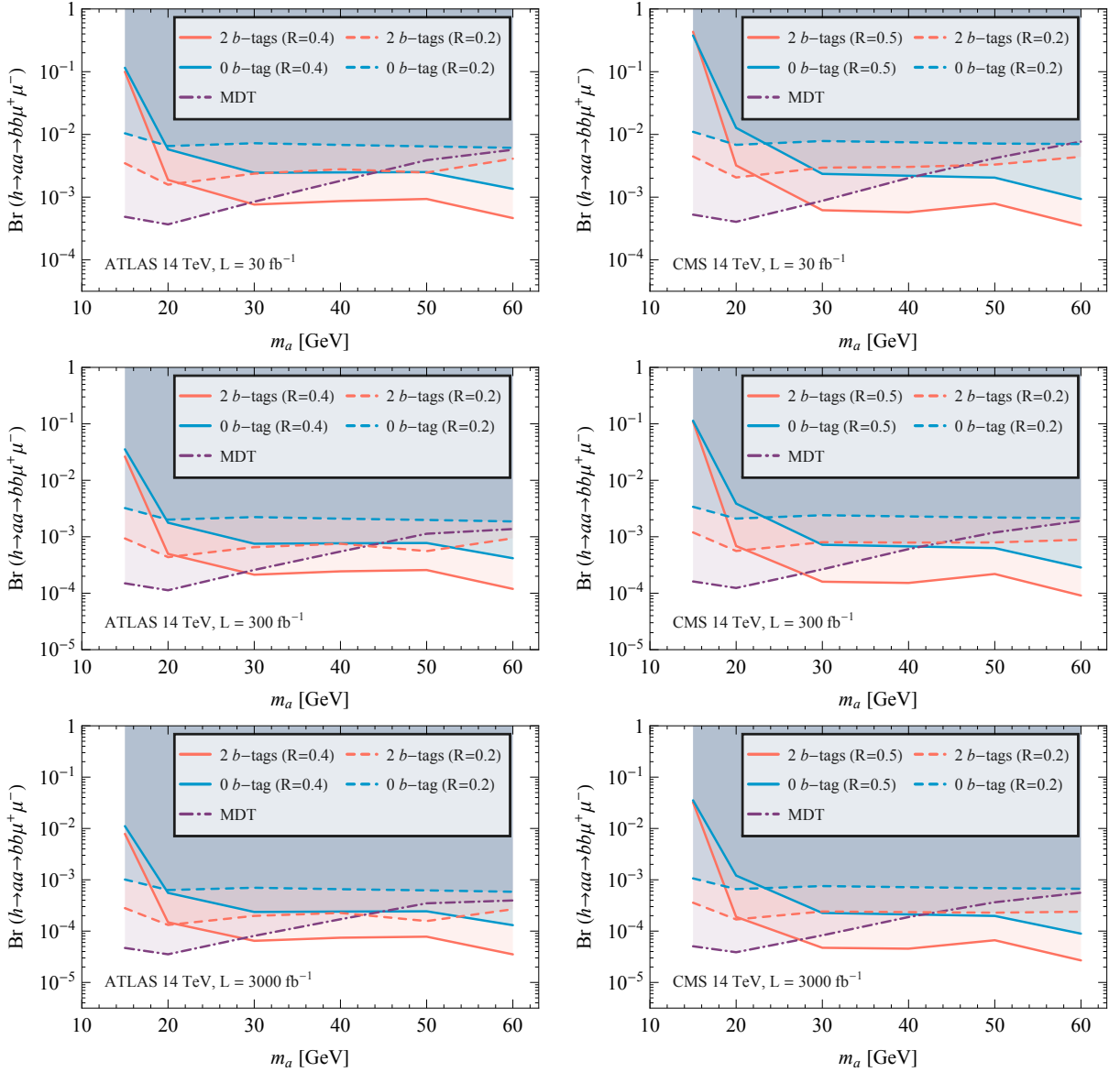
Figure 4.4: Expected 95% CL reach on Br($h \to aa \to b\bar{b}\mu^+\mu^-$) for 30 (*top*), 300 (*center*), and 3000 (*bottom*) fb$^{-1}$ at 14 TeV, for ATLAS (*left*) and CMS (*right*). The solid line is the sensitivity of the "conventional" analysis (Sec. 4.1.2) with a jet-clustering radius of either $R = 0.4$ (ATLAS) or 0.5 (CMS). The sensitivities when using a smaller jet radius of $R = 0.2$ (Sec. 4.1.2) is shown with dashed lines. The purple dot-dashed line is the sensitivity from a jet substructure analysis that makes use of the mass drop tagger (MDT) (Sec. 4.1.2).

**Analysis with smaller jet radius**

A straightforward solution to the loss of sensitivity at low $m_a$ is to reduce the clustering radius of $b$-jets. Since $b$-tagging dominantly makes use of track-based information, and since the small-radius jets would not be used for triggering, there is in principle no obstacle to implementing such a modified $b$-tagger for a well-motivated analysis. The achievable $b$-tagging efficiencies should be comparable, and the use of smaller $b$-jets significantly improves sensitivity of $2b2\mu$ searches in the low $m_a$ regime.[4]

We estimate the sensitivity possible with such a modified $b$-tagging system. The $Z^{(*)}/\gamma^* + 2j$ background is regenerated with the same generator level cuts as for the conventional analysis in Sec. 4.1.2, except that we change the parton separation criterion from $\Delta R = 0.2$ to 0.1. (No such requirement was imposed on the other generated backgrounds.) The resulting cross section for this background is shown in the last row of Tab. 4.2. Jets are then clustered with a radius of $R = 0.2$ for both ATLAS and CMS, and the cut on $\Delta R_{J_1 J_2}$ is relaxed to be $> 0.2$. Except for these two changes, we assume the analysis, including $b$-tagging efficiencies, proceeds identically as in Sec. 4.1.2.

The dashed lines in Fig. 4.3 and Fig. 4.4 show the resulting reach for 8 and 14 TeV. The sensitivity is significantly improved for $m_a \leq 20$ GeV. At higher masses, the $b$-jets are less collimated, and the smaller jet radius reduces the suppression of backgrounds compared to the conventional analysis, so that the sensitivity is reduced. A combination of both approaches therefore seems useful to achieve good sensitivity to all of the mass range. However, we will now show that a substructure analysis may have superior reach to the low $m_a$ region than the simple small-jet analysis presented in this subsection.

**Jet substructure analysis**

Sensitivity to the low-$m_a$ region can be further enhanced by making use of jet substructure techniques [279, 280, 281, 282, 283, 284, 285]. The main goal is to increase signal acceptance without eroding background rejection. Since the two $b$-jets from $a$ decays should be symmetric, we propose a jet substructure procedure based on the mass drop tagger (MDT) [286].

The substructure analysis proceeds as follows. Triggered events satisfying the OS muons selection criterion are clustered into $R_f = 0.8$ fat jets with the Cambridge/Aachen (C/A) algorithm [287, 288]. The (leading) fat jet is required to have one $b$-tag, and satisfy $p_T > 25$ GeV, $|\eta| < 2.5$. We use the same $b$-tag efficiencies as in Sec. 4.1.2. We note that requiring *two* $b$-tags within the fat-jet will remove too much signal, as the $b$-tagged subjets need to presumably have a $p_T$ of at least 25 GeV to qualify as a proper subjet. If this threshold

---

[4]For a recent theoretical discussion of small jet radius effects see [278].
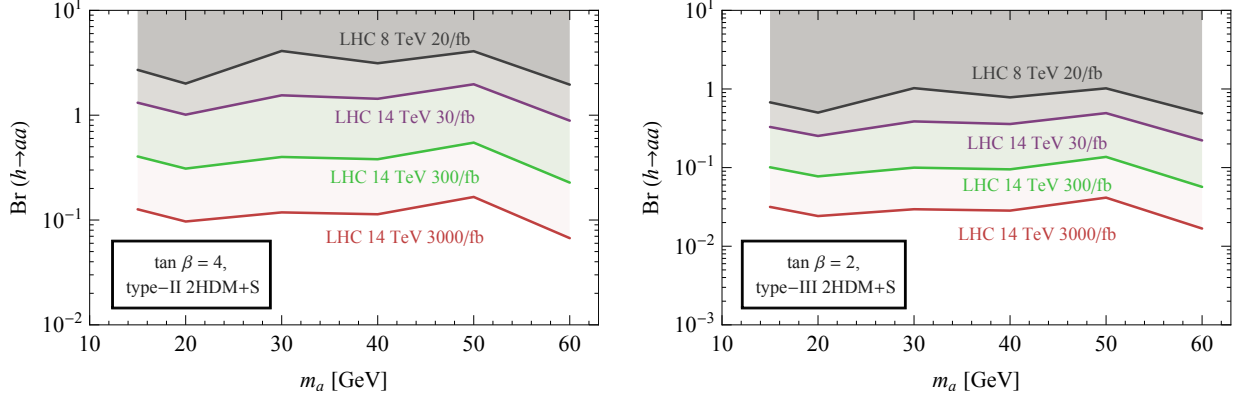
Figure 4.5: Combined 95% CL projected CMS sensitivities to $\mathrm{Br}(h \to aa)$ for the LHC at 8 and 14 TeV. To derive these sensitivities we need to make particular assumptions about how the scalar couples to the Standard Model fermions. **Left:** Type-II 2HDM+S with $\tan\beta = 4$, as in the left plot of Fig. 4.1 in Sec. 4.1.1. The sensitivity to the SM+S model discussed in Sec. 4.1.1 is almost identical. **Right:** Type-III 2HDM+S with $\tan\beta = 2$, as in the right plot of Fig. 4.1 in Sec. 4.1.1.

could be lowered, it would significantly improve sensitivity.

We then analyze the substructure of the leading fat jet passing these criteria. The two hardest subjets, identified by undoing the last step of the C/A clustering, have to satisfy the MDT criteria

$$\mu \equiv \frac{\max(m_{j_1}, m_{j_2})}{m_j} < 0.67 \,, \tag{4.10}$$

$$y \equiv \frac{\min(p_{T\,j_1}^2, p_{T\,j_2}^2)}{m_j^2} \Delta R_{j_1 j_2}^2 > 0.09 \,, \tag{4.11}$$

and $p_{T\,j_{1,2}} > 15$ GeV. We then apply the same $\Delta R$, missing energy, and invariant mass cuts for the two subjets and the two muons as in Sec. 4.1.2, with the exception of again relaxing the $\Delta R_{j_1 j_2}$ cuts to $> 0.2$.

The resulting 95% CL sensitivities are shown as dot-dashed purple lines in Fig. 4.3 and Fig. 4.4 for 8 TeV and 14 TeV, respectively. The low-mass sensitivity is significantly enhanced compared to the previous two analysis approaches. Similarly to Sec. 4.1.2, the conventional analysis does better at higher $m_a$ due to increased background rejection for an uncollimated signal.

The impact of QCD multi-jet events with lepton fakes is hard to quantify for this substructure analysis without a data-driven study. For the resolved analyses, we found that muon fakes are reasonable to neglect if 0 or 2 $b$-tags are required. This substructure study requires only one fat-jet $b$-tag, but imposes strict kinematic requirements on its subjets. This

may be enough to suppress multi-jet background, or it may be necessary to require both sub-jets to be $b$-tagged. As mentioned above, the $p_T$ threshold for $b$-tagging could weaken our projected sensitivity for small $m_a$, but determining whether this is necessary is beyond the scope of our analysis.

### 4.1.3 Discussion

We have seen that combining the substructure and conventional analyses yields a fairly flat sensitivity of about $\mathrm{Br}(h \to 2a \to 2b2\mu) \lesssim 10^{-3}$ for the 8 TeV LHC in the range $15\ \mathrm{GeV} \leq m_a \leq 60\ \mathrm{GeV}$. At 14 TeV with either 30, 300, and 3000 fb$^{-1}$ of data, the projected sensitivity increases to several times $10^{-4}$, $10^{-4}$, and several times $10^{-5}$, respectively.

We can convert the projected reach on $\mathrm{Br}(h \to 2a \to 2b2\mu)$ to the projected reach on $\mathrm{Br}(h \to 2a)$, but this is model-dependent. In a 2HDM+S model, for example, it depends on the Yukawa coupling type, see Sec. 4.1.1. In Fig. 4.5, we show the projected sensitivity to $\mathrm{Br}(h \to 2a)$ from combining the substructure and conventional analyses for two 2HDM+S models, type-II with $\tan\beta = 4$ (very similar to SM+S) and type-III with $\tan\beta = 2$. In both cases, data at 14 TeV is required to meaningfully constrain exotic Higgs decays in these models, though in the latter case the 8 TeV constraint derived for $\mathrm{Br}(h \to 2a)$ is less than 1. With the full HL-LHC (LHC at 14 TeV with 3000 fb$^{-1}$) dataset, the exotic Higgs decay branching ratio can be constrained at the 10% and 2% level in these two scenarios, respectively.

In motivating a $2b2\mu$ search, it is useful to compare its sensitivity to $\mathrm{Br}(h \to 2a)$ to that achievable in other channels. In particular:

- Earlier collider studies for the 14 TeV LHC [236, 233] found $2\sigma$ sensitivity to $\mathrm{Br}(h \to 2a \to 4b) \approx 10\%$ with 300 fb$^{-1}$ of data.

- In constraining $\mathrm{Br}(h \to 2a \to 4\tau)$ (and assuming Yukawa-ordered couplings, as we do here), the $(a \to 2\mu, a \to 2\tau)$ channel was found to be greatly superior to the $4\tau$ channel [64]. Depending on assumptions for reducible background, data from the LHC Run I can exclude $\mathrm{Br}(h \to 2a \to 4\tau) \lesssim 2 - 8\%$.

- A recent study of $h \to 2a \to 2b2\tau$ decay from ggF Higgs production [263] claims considerably greater sensitivity to $\mathrm{Br}(h \to 2a)$ in an NMSSM-like scenario than we find for $2b2\mu$. However, we find their study to be difficult to interpret, since it makes no attempt to incorporate trigger cuts. In addition, highly optimistic $b$- and $\tau$-tag rates are assumed for a low $p_T > 15$ GeV threshold. The very tight mass windows employed

also seem challenging at the LHC. For this reason, we will not consider their results in what follows, but the considered channel is interesting and deserves further study.

Based on the existing theory-level studies done thus far, in a SM+S-like scenario (which generally includes the NMSSM and type-I and II 2HDM+S), the $4b$ search may be somewhat superior to $2b2\mu$, offering a sensitivity to $\mathrm{Br}(h \to 2a)$ that is better by a factor of a few; the $4\tau/2\tau2\mu$ channel has no exclusion power. For more leptophilic scenarios, like the type-III 2HDM+S, the $2\tau2\mu$ search now constrains $\mathrm{Br}(h \to 2a) \lesssim 10 - 40\%$ with LHC Run I data [64], performing much better than a $4b$ search. Here, the $2b2\mu$ channel should provide competitive sensitivity.

The search for $h \to 2b2\mu$ is therefore motivated for several reasons. Its sensitivity to the total exotic Higgs decay branching ratio is either competitive, or close to competitive, to searches involving $\tau$'s or only $b$'s. Apart from the complementarity of discovering new physics in several different channels, the much cleaner nature of the $2b2\mu$ signal makes our conclusions less reliant on the detailed modeling of $\tau$ and $b$-jet reconstruction at low $p_T$. It could therefore turn out that $2b2\mu$ is the preferred channel in either leptophilic or NMSSM-type scenarios, although of course all the above-mentioned decay modes should be studied experimentally. Finally, although we did not consider this in detail here, it is also possible that $h \to XX'$ is the dominant exotic decay mode, where each scalar decays dominantly to $2b$ and $2\mu$, respectively (with *e.g.* $X$ above the $2b$ threshold and $X'$ below the $2\tau$ threshold).

### 4.1.4 Summary

Exotic Higgs decays are uniquely sensitive to light scalars that are uncharged under the SM gauge groups. We have demonstrated the sensitivity of a $h \to 2a \to 2b2\mu$ search for constraining theories with light scalars at the LHC. This channel can arise naturally in models like the NMSSM or other 2HDM+S scenarios, as well as in general hidden valley scenarios. We performed a detailed collider analysis for an on-shell intermediate CP-odd scalar, though the results should be applicable to CP-even scalars as well, since we did not explicitly use any angular information of the scalar decay. Already the 8 TeV LHC can probe $\mathrm{Br}(h \to 2a) < 1$ in some 2HDM+S scenarios. With its full dataset, the 14 TeV LHC will probe the exotic Higgs decay branching ratio to light scalars at the 1 - 10% level. Depending on the details of soft $b$ and $\tau$ reconstruction, this sensitivity can be competitive or even superior to that offered by other channels that contain these final states.

For low intermediate scalar masses, a conventional resolved-jet analysis loses sensitivity due to the collimation of boosted $b$-jet pairs. Simply reducing the clustering radius of $b$-jets greatly enhances sensitivity in this region, but a dedicated jet substructure analysis may be

even more powerful, fully exploiting the discovery potential for $m_a < 25$ GeV.

# Chapter 5

# Dark sector interpretation of the 750 GeV diphoton excess

The start of the LHC run at 13 TeV center-of-mass energy has brought an unexpected – from the minimalist point of view – excess of events in the diphoton channel with the invariant mass of about 750 GeV [289, 290]. In the Standard Model (SM) of particles and fields this energy is not associated with any known resonance, and may be the first sign for elusive New Physics (NP). The appearance of the "bump" in the diphoton spectrum, despite its rather limited statistical significance that may disappear or strengthen with more data, has generated a lot of excitement among physicists who wait for *any* manifestation of NP beyond SM (BSM) at the weak scale.

It is true that in most models of NP, the diphoton channel would not necessarily be the "discovery mode". That is, other manifestations of a (tenuous) 750 GeV resonance might have been expected first. Nevertheless, large classes of models where said resonance is produced from the fusion of the SM gauge bosons and/or quark-antiquark pairs with subsequent decay to the diphoton states have appeared in the literature, with most of them being tailored for the occasion. While the mass of a new resonance suggested by the CMS and (mostly) ATLAS data is to be around 750 GeV, its spin and parity remain open for discussion. Spin-zero and spin-two resonances come as the most natural candidates, while the spin-one resonance is disfavored by the so-called "Landau-Yang theorem" that forbids two photons in any state with the total angular momentum equal to one [291, 292]. The couplings of the spin-zero resonances to photons or gluons cannot be expected to arise at dimension four or lower operator level, and therefore it is reasonable to expect that 750 GeV resonance is also coupled to the weak-scale particles, charged under the SM gauge groups. The loops of these particles (for example, vector-like fermions [293, 294, 295, 296, 297, 298, 299, 300, 301, 302])

may have led to the effective couplings of the NP resonance to gauge bosons [303, 304, 305, 306, 307, 308, 309, 310, 311, 312, 313, 314, 315, 316, 317, 318, 319, 320, 321, 322, 323]. If this picture is indeed valid, then more signatures of weak-scale NP are likely to come from future data.

While noting the significance of the excess is limited, it is reasonable to question every element of the existing anomaly. In particular, it is important to ask whether *light* BSM final states may be confused with the diphoton signal. A general framework for such a scenario has been already discussed in several publications [324, 325, 326, 327]. A heavy resonance $X$ produced by the gluon-gluon or quark-antiquark fusion may decay to a pair of light BSM states $Y$ that have weak instability against subsequent decays to electron-positron pairs or photon pairs. We will call the $Y$ states "dark mediators" (see *e.g.* Refs. [328, 29, 329, 34, 152, 188]). If the decay length of $Y$ is commensurate with the linear geometry of the detector (*e.g.*, of the inner tracker and eletro-magnetic calorimeter) and its mass is in the MeV-GeV range, then emergent highly collimated pairs of photons and/or electron-positron pairs may successfully mimic actual photons. Therefore, the interesting part of this scenario is that a new 750 GeV resonance opens the door to light weakly coupled states coupled to the SM sector, which is a particular realization of the "hidden valley" idea [79, 330, 331, 332, 333, 334, 335, 336, 337, 338, 339, 340].

The purpose of this chapter is to explore the consequences of the scenario where a 750 GeV resonance decays to dark mediators in terms of its implications for the intensity frontier searches. To that effect, we construct two explicit models, with heavy spin-zero and spin-one resonances, that decay to dark mediators. The parameters of the models are chosen to fit the current ATLAS excess of the diphoton events under the assumption that decaying mediators do indeed pass the selection criteria for photon identification. In the process, we make careful accounting for the ATLAS geometry and the distribution of dark mediators over the effective decay length. The end result is a suggested range for masses and couplings of dark mediators that falls largely within reach of the next generation of intensity frontier experiments (*e.g.* [90, 82, 341, 81, 97, 62, 342, 343]).

The chapter is organized as follows. We first introduce the theoretical framework for the dark mediator explanation of the 750 GeV candidate resonance in Sec. 5.1. We then calculate the strength of expected signal, evaluate the probability of light particles decays inside the relevant parts of ATLAS detector, and present favored parameter spaces for various models in Sec. III. Different experimental strategies that would allow differentiating diphoton from di-dark mediator events are discussed in Sec. 5.3. We conclude in Sec. 5.4.

## 5.1 Theoretical motivation

### 5.1.1 750 GeV Scalar Resonance

In this sub-section, we consider a model of a heavy dark scalar (or pseudo-scalar) resonance $S$ produced via gluon fusion that decays to the pair of two metastable "dark photon" particles $A'$. Each $A'$ gives displaced decays to $e^+e^-$ pairs so that the whole chain can be represented as

$$gg \to S \to A'A' \to (e^+e^-)(e^+e^-). \tag{5.1}$$

Here we explore a possibility that $m_S \simeq 750$ GeV, but $A'$ is light, $m_{A'} < \mathcal{O}(\text{few GeV})$. Because each dark photon carries a significant fraction of energy of the 750-GeV scalar, the $e^+e^-$ pair from the decay of $A'$ are extremely collimated. The opening angle of $e^+e^-$ pair is around $2m_{A'}/E_{A'}$, where $m_{A'}$ and $E_{A'}$ are the mass and energy of $A'$, respectively. For sub-GeV $A'$s this angle is less than 0.01. Therefore it is plausible that events originating from the decay of $A'$ could pass the selection criteria for a real photon setting by $e.g.$ the ATLAS collaboration.

Dark photon models have been studied extensively in the literature since 1980's [67, 68]. In recent years, the attention to dark photons have been spearheaded by their possible connection to various particle physics and astrophysical "anomalies" (see $e.g.$ [344, 329, 34, 25]). The minimal dark photon model consists of a new massive vector field that couples to the SM $U(1)$ via the so-called "kinetic mixing" operator,

We apply the dark photon model with $U(1)_D$ symmetry to the scenario. Detailed model description is shown in Sec. 2.2.1. After EWSB, the SM gauge field $B_\mu$, and $W_\mu^3$ mix with the new gauge field $A'_\mu$. The resulting mass eigenstate $Z'$ couples to the SM electromagnetic and weak neutral currents. In the limit

$$m_{Z'} \ll m_Z, \quad \epsilon_Y \ll 1,$$

the mixing between $A'$ and the SM $Z$-boson is negligible, while the coupling between $Z'$ and SM fermions are given by

$$\epsilon_Y \cos\theta_W eQ \equiv \epsilon eQ, \tag{5.2}$$

where we introduce $\epsilon \equiv \epsilon_Y \cos\theta_W$. Finally, to avoid the proliferation of notations, we will call the physical $Z'$ particle as $A'$, and refer to it as the dark photon.

Our goal is to derive the acceptable range for masses and couplings in the proposed scenario. To achieve this, we need to specify the couplings of scalar $S$ to gluons and dark photons beyond the effective dim $= 5$ operators. To that effect, we introduce a vector-like
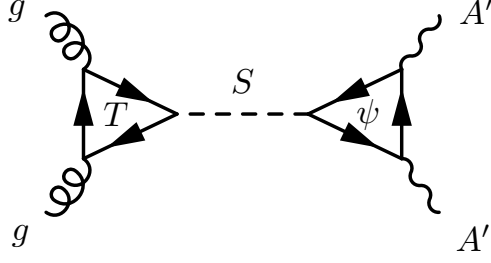
Figure 5.1: Representative Feynman diagrams for $gg \to S \to A'A'$, where $S$ is the 750 scalar resonance and $A'$ is the light on-shell dark photon that faking photons.

colored fermion, $T$, and a dark fermion, $\psi$, which is a singlet under the SM gauge group. The resulting Lagrangian reads

$$\mathcal{L}_S = \frac{1}{2}(\partial_\mu S)^2 - \frac{1}{2}m_S^2 S^2 + \bar{f}i\slashed{D}f + \bar{T}(i\slashed{D} - m_T)T - \lambda_T S\bar{T}T + \bar{\psi}(i\slashed{D} - m_\psi)\psi - \lambda_d S\bar{\psi}\psi \quad (5.3)$$

where $f$ stands for a generic SM fermion. The covariant derivative here is

$$D_\mu = \partial_\mu - i(g_d Q_d + e\epsilon Q_f)A'_\mu - ieQ_f A_\mu - ig_s G^a_\mu t^a, \quad (5.4)$$

where $Q_f$ and $Q_d$ are $U(1)_{\text{EM}}$ and $U(1)_D$ charges, respectively. $e$, $g_s$ and $g_d$ are $U(1)_{\text{EM}}$, $SU(3)_c$, and $U(1)_D$ gauge couplings, respectively. $\lambda_T$ and $\lambda_d$ are the Yukawa couplings of $S$ to $T$ and $\psi$ fermions, respectively. Notice that one does not have to choose positive parity, and $S\bar{T}i\gamma_5 T$ pseudo-scalar couplings could also serve the same purpose. $T$ and $\psi$ fermion loops mediate the production and decay of $S$ resonance, as shown in Fig. 5.1.

Having formulated the model, we are now ready to evaluate the strength of the fake diphoton signal in it. We start from the master formula for the signal,

$$\sigma_{\text{Signal}} = \sigma_{pp \to S} \times \text{Br}_{S \to A'A'} \times P\left(A'A' \to (e^+e^-)(e^+e^-)\big|\,\gamma\gamma\right), \quad (5.5)$$

where $\sigma_{pp \to S}$ is the cross section for producing 750 GeV resonance $S$ and $\text{Br}_{S \to A'A'}$ is the branching ratio of this resonance decaying to two dark photons. $P\left(A'A' \to (e^+e^-)(e^+e^-)\big|\,\gamma\gamma\right)$ is the probability that two dark photons decay to electron-positron pairs inside the detector (within appreciable distance), passing the selection criteria for the diphoton events, and successful reconstruction. It is the most complicated object, depending on factors such as the detector geometry, the detector acceptance, the reconstruction efficiency, as well as the decay length of $A'$, and the mass of $A'$ that affects the size and the shape of the shower in the EM calorimeter. We will abbreviate $P\left(A'A' \to (e^+e^-)(e^+e^-)\big|\,\gamma\gamma\right)$ as $P_{\text{acc}}$. The existing excess in the diphoton channel found by ATLAS [345] is at the level of $\sigma_{\text{Signal}} \simeq 5 - 10$ fb, which corresponds to $\sim 16$ to 32 events.

**Production and decay of $S$ in a $U(1)_D$ model**

Data suggest that the total width of $S$ is around $5-45$ GeV, and therefore the narrow width approximation for $S$ suffices for our accuracy. The production cross section of $S$ through gluon fusion is given by

$$\sigma(pp \to S) = \frac{\pi^2}{8s\, m_S} \Gamma(S \to gg) \int_{m_S^2/s}^{1} \frac{dx}{x} f_g(x, m_S^2) f_g\left(\frac{m_S^2/s}{x}, m_S^2\right), \tag{5.6}$$

where $\sqrt{s} = 13$ TeV is the center of mass energy and $f_g(x, Q^2)$ is the gluon parton distribution function evaluated at $Q^2$. We assume that the decay width of $S \to gg$ entering in (5.6) is mediated by the loop of heavy vector-like fermions $T$. The actual constraints on $m_T$ would critically depend on $T$-fermion decay channels. To reduce the number of parameters to be scanned, we will adopt $m_T = 1$ TeV throughout, which is safe relative to direct searches. Note that for such a massive particle in the loops, the form factor of the effective $g - g - S$ vertex does not need to be taken into account. A very well known formula for the calculation of the width (*e.g.*, see [346]) gives

$$\Gamma(S \to gg) = \frac{\alpha_s^2}{32\pi^3} \frac{m_S^3}{m_T^2} \lambda_T^2 |\tau_T \left[1 + (1 - \tau_T) f(\tau_T)\right]|^2, \tag{5.7}$$

where $\tau_T = 4m_T^2/m_S^2$. In this expression, the invariant function $f(\tau)$ is quite familiar from the Higgs physics literature,

$$f(\tau) = \begin{cases} \arcsin^2\left(\sqrt{\tau^{-1}}\right), & \tau > 1 \\ -\frac{1}{4}\left[\log\left(\frac{1+\sqrt{1-\tau}}{1-\sqrt{1-\tau}}\right) - i\pi\right]^2, & \tau \le 1 \end{cases}. \tag{5.8}$$

The cross section (5.6) can be further improved by taking into account NLO corrections. With these expressions, we find that a fiducial value for the $\sigma_{pp \to S}$ cross section at $m_T \sim 1$ TeV and $\lambda_T \sim 1$ to be around 40 fb.

The branching ratio of $S$ to dark photons directly follows from the three decay channels of the heavy scalar: $S \to gg$, $S \to \bar{\psi}\psi$, and $S \to A'A'$,

$$\text{Br}_{S \to A'A} = \frac{\Gamma_{S \to A'A'}}{\Gamma_{S \to A'A'} + \Gamma_{S \to gg} + \Gamma_{S \to \bar{\psi}\psi}}. \tag{5.9}$$

If kinematically accessible, the decay of $S$ to dark fermions $\psi$ could be the largest:

$$\Gamma(S \to \bar{\psi}\psi) = \frac{\lambda_d^2}{8\pi} m_S \left(1 - \frac{4m_\psi^2}{m_S^2}\right)^{3/2}. \tag{5.10}$$

The $S \to A'A'$ decay is induced by the $\psi$ loop and is given by

$$\Gamma(S \to A'A') = \frac{\alpha_d^2}{64\pi^3} \frac{m_S^3}{m_\psi^2} \lambda_d^2 |\tau_\psi \left[1 + (1 - \tau_\psi) f(\tau_\psi)\right]|^2, \tag{5.11}$$
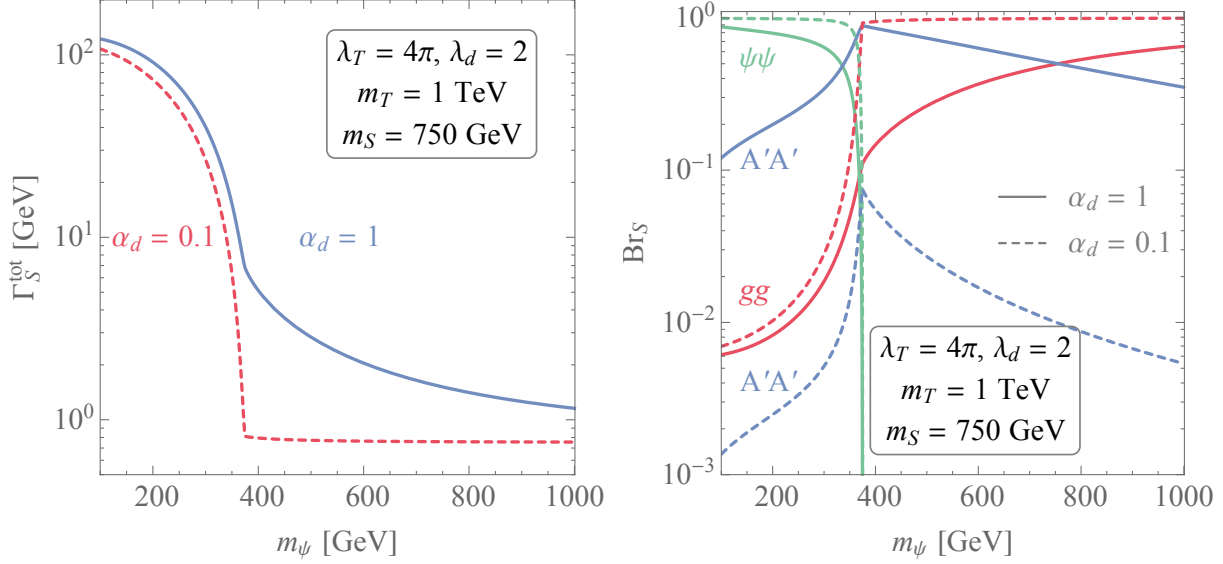
Figure 5.2: **Left**: Total decay width of $S$ with $\alpha_d = 1$ (blue, solid) and 0.1 (red, dashed). The values of other parameters used here are $m_T = 1$ TeV, $\lambda_d = 2$ and $\lambda_T$ is taken to the strong interaction limit, $\lambda_T = 4\pi$. **Right**: Branching ratios of $S$ for $S \to gg$ (red), $S \to \bar{\psi}\psi$ (green), and $S \to A'A'$ (blue) with $\alpha_d = 1$ (solid) and 0.1 (dashed), with the same choice of other parameters as in the left panel.

where $\tau_\psi = 4m_\psi^2/m_S^2$. Note that in this expression we have taken $m_{A'}$ to zero, as it is negligibly small compared to $m_S$ and $m_\psi$.

The total width and branching ratios of the $S$-resonance are illustrated in Fig. 5.2. We have taken $\lambda_T$ to what we will consider its uppermost value, $4\pi$, (which would imply a strongly interacting $S - T$ sector). We can observe that if the decays to dark fermions $\psi$ are allowed, one could easily achieve a width of the $S$ resonance of $\sim 40$ GeV. Rather large branching ratios to pairs of dark photons can be achieved for $\alpha_d \sim \mathcal{O}(1)$. We note in passing that the hierarchy of mass scales, $m_\psi \gg m_{A'}$ and large coupling constant $\lambda_d$ will create a variety of interesting effects for the dark matter phenomenology, should $\psi$ remain stable on cosmological time scales (see *e.g.* [34, 35]).

We now come to the most technically challenging part, the evaluation of $A'$ decays mimicking the diphoton signal, $P_{\text{acc}}$. In a hypothetical limit of an infinite detector with 100% efficiency and 100% faking rate for a dark photon as a regular photon, this probability is simply $(\text{Br}_{A' \to e^+ e^-})^2$. The branching of dark photons to electrons is well-known [78], and is

100% below the dimuon threshold, while the $A'$ width is given by

$$\Gamma_{A'\to l^+l^-} = \frac{\epsilon^2\alpha}{3}m_{A'}\sqrt{1 - \frac{4m_l^2}{m_{A'}^2}}\left(1 + \frac{2m_l^2}{m_{A'}^2}\right). \tag{5.12}$$

At higher $m_{A'}$ one has to include muon and hadronic decay channels, $i.e.$, $\Gamma_{A'} = \Gamma_{A'\to e^+e^-} + \Gamma_{A'\to\mu^+\mu^-} + \Gamma_{A'\to\text{hadronic}}$.

In practice, of course, there are strict geometric requirements where the decays of the dark photons must occur so that they can be confused with a real photon. Obviously, a very important requirement is that both dark photons decay before or inside the first layer of the EM calorimeter, which depends rather sensitively on the decay length. Suppose that the parent $S$ particle is produced almost at rest, and then decays into two dark photons, each of them carries energy around $m_S/2$, where $m_S$ is the mass of the heavy scalar $S$. Then the decay length of the dark photon can be written as

$$L_{A'}(\epsilon, m_{A'}) = \gamma_{A'}\beta_{A'}\tau_{A'}(\epsilon, m_{A'}) = \frac{m_S}{2m_{A'}}\sqrt{1 - \frac{4m_{A'}^2}{m_S^2}}\Gamma_{A'}^{-1}, \tag{5.13}$$

where $\beta_{A'}$ is the velocity of $A'$ observed in the fixed laboratory frame and $\gamma_{A'} \equiv 1/\sqrt{1 - \beta_{A'}^2}$ is the boost factor of $A'$. $\tau_{A'}(\epsilon, m_{A'})$ is the lifetime of $A'$ in its rest frame. Evidently, $\gamma_{A'} \gg 1$ and $\beta_{A'}$ is almost one. The decay length follows an approximate scaling

$$L_{A'} \propto (\epsilon m_{A'})^{-2} \times m_S \tag{5.14}$$

with largest deviations of this scaling at $m_{A'} \sim m_\rho$. Below the dimuon threshold, we have the following useful expression,

$$L_{A'}(\epsilon, m_{A'}) = 30 \text{ cm} \times \left(\frac{m_S}{750 \text{ GeV}}\right) \times \left(\frac{100 \text{ MeV}}{m_{A'}}\right)^2 \times \left(\frac{10^{-4}}{\epsilon}\right)^2. \tag{5.15}$$

These numbers immediately tell us that *currently allowed* region of the dark photon parameter space can indeed be compatible with dark photons decaying within reasonable distance inside the LHC detectors so that they can be confused with real photons. If initial boost distributions of $S$ particles, and angular dependences of its production and of detector geometry could have been neglected, then $P_{\text{acc}}$ would be determined by the relation between some relevant length scale of the detector, $L_{\text{det}}$, and $L_{A'}$.

$$P_{l<L_{\text{det}}} \propto 1 - \exp\{-L_{\text{det}}/L_{A'}\} \implies P_{\text{acc}} \propto (\text{Br}_{A'\to e^+e^-})^2 \times (P_{l<L_{\text{det}}})^2, \tag{5.16}$$

where $P_{l<L_{\text{det}}}$ is the probability of a single photon to decay inside $L_{\text{det}}$. This is of course a very crude formula that has to be carefully augmented for the detector geometry, boosts, and

other factors, which we will attempt to do in section Sec. 5.2. We also note that should one of the dark photons decay outside the detector, this would mimic the mono-photon signal with the probability that scales as

$$P_{\text{mono}} \propto 2 \times \text{Br}_{A' \to e^+ e^-} \times P_{l < L_{\text{det}}} \times P_{l > L_{\text{det}}}, \tag{5.17}$$

setting up the stage for an important constraint that would come from corresponding searches.

**Variations on the dark photon model**

In this subsection we would like to note that the dark photon model is not the only possibility for a weakly unstable light vector particles. Indeed, there are other UV complete choices based on anomaly-free symmetries, such as $B - L$, $L_{L1} - L_{L2}$ (where $L1$ and $L2$ stand for different lepton flavors) etc. If we take, for example, a model with $U(1)$-gauged $L_e - L_\tau$ symmetry, then the main couplings of its gauge boson $V$ to leptons are

$$\mathcal{L} = g_{L_e - L_\tau} V_\alpha \left( \bar{\nu}_e \gamma^\alpha \nu_e - \bar{\nu}_\tau \gamma^\alpha \nu_\tau + \bar{e} \gamma^\alpha e - \bar{\tau} \gamma^\alpha \tau \right) . \tag{5.18}$$

Here, $g_{L_e - L_\tau}$ is the $U(1)_{L_e - L_\tau}$ gauge coupling, so that the coupling to electrons is rescaled compared to the dark photon case as $e\epsilon \to g_{L_e - L_\tau}$. In the entire mass range from a few MeV to 3.6 GeV the vector boson $V$ decays to electrons and neutrinos, with equal probabilities so that $\text{Br}_{V \to e^+ e^-} = 0.5$.

Despite the fact that one can choose $g_{L_e - L_\tau}$ in the same range as $e\epsilon$ and thus adjust the decay length of $V$ to be commensurate with $L_{\text{det}}$, this model does not look as a good candidate to mimic the diphoton signal, for the following reasons. Firstly, $g_{L_e - L_\tau}$ is required to be very small, $g_{L_e - L_\tau} < 10^{-2}$, from the decay length requirements, which would correspond to a tiny $\alpha_d$. This in turn would require some additional model-building to generate an appreciable branching of $S$ to $VV$ states. Another reason is that this model will give a non-removable mono-photon signal due to the decay to neutrinos at a rate more than twice the diphoton signal, for any ratio of $L_{\text{det}}/L_V$. On account of these two difficulties, we will abandon further investigation of $U(1)_{L_e - L_\tau}$ models in connection to the 750 GeV resonance.

## 5.1.2   750 GeV Vector Scenario

If light unstable particles can indeed fake real photons at the LHC, new possibilities for the spin of the 750 GeV resonance open up. In this section we will consider an option of dark mediators being scalar and pseudo-scalar, while the decayed 750 GeV resonance being a spin-1 vector boson. Notice that this is a novel possibility bypassing the Landau-Yang theorem (see *e.g.* earlier related discussion in Ref. [347, 348]).
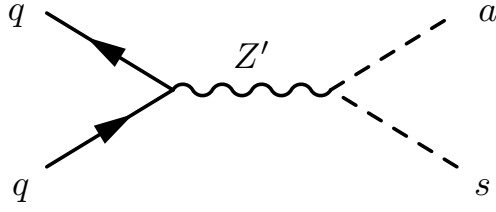
Figure 5.3: Feynman diagram for $q\bar{q} \to Z' \to sa$, where $Z'$ is the 750 GeV vector resonance and $s(a)$ is the light on-shell scalar (pseudo-scalar) that faking photons.

The scenario of this section is based on the following sequence,

$$q\bar{q} \to Z' \to sa \to (e^+e^-)(e^+e^-), \tag{5.19}$$

where all new particles $Z', s, a$ are assumed to be singlets under the SM gauge group. Scalar $s$ and pseudo-scalar $a$ can be combined in a complex scalar field

$$\mathcal{S} = s + ia, \tag{5.20}$$

that we assume is charged under some new $U(1)_D$ group with dark charge $Q_d = 1$. The mass of a heavy dark $Z'$ boson is taken around 750 GeV. The coupling of $Z'$ to the SM can again proceed via the kinetic mixing operator. To avoid confusion with the case of the previous section, we will call the heavy boson $Z'$ (while the light one is $A'$). The Feynman diagrams for the process is shown as Fig. 5.3.

The kinetic mixing operator will couple the $Z'$ to hypercharge of the SM particles (as opposed the electric charge in case of small vector mass). Since for the chosen $m_{Z'}$ mass scale

$$m_{Z'} \gg m_Z, \quad \epsilon_Y \ll 1,$$

the coupling between $Z'$ and SM fermions are given by

$$\epsilon_Y g'Y = \frac{\epsilon e Y}{\cos^2 \theta_W} \tag{5.21}$$

See Appendix 2.2.1 for more details.

The resulting effective Lagrangian reads

$$\mathcal{L}_{Z',\text{eff}} \supset \frac{1}{2}M_{Z'}^2 Z_\mu'^2 + \bar{f}_{L,R}i\slashed{D}f_{L,R} + |D_\mu\mathcal{S}|^2 - m_\mathcal{S}^2 |\mathcal{S}|^2 + \mathcal{L}_{\text{dec}}, \tag{5.22}$$

where

$$D_\mu = \partial_\mu - ieQ_f A_\mu - i\frac{g}{\cos\theta_W}\left(T_{L,R}^3 \cos^2\theta_W - Y_{L,R}\sin^2\theta_W\right)Z_\mu - i\left(g_{Z'}Q_d + \frac{\epsilon e Y_{L,R}}{\cos^2\theta_W}\right)Z_\mu' \tag{5.23}$$

and $f_{L,R}$ includes all left-handed/right-handed SM quarks and leptons. $Q_f$, $T^3_{L,R}$ and $Y_{L,R}$ represent their $U(1)_{\text{EM}}$, $SU(2)_L$, and $U(1)_Y$ charges respectively. $e$, $g$ and $g_{Z'}$ are electric coupling, weak coupling and the $U(1)_D$ gauge coupling, respectively. $\mathcal{L}_{\text{dec}}$ is the most "delicate" part of the Lagrangian that is responsible for the decays of $a$ and $s$ particles. Notice that one cannot simply write down $\lambda_s s\bar{e}e$ and $\lambda_a a\bar{e}i\gamma_5 e$ operators at the fundamental level, as they would explicitly violate both the SM and $U(1)_D$ gauge invariances. Nevertheless these operators can be in fact generalized to the following gauge invariant structures of higher dimension:

$$\mathcal{L}_{\text{dec}} = \lambda_s s(\bar{e}e) + \lambda_a a(\bar{e}i\gamma_5 e) \quad \rightarrow \quad \frac{\mathcal{S}\Phi}{\Lambda_\Phi^2} \times (\bar{L}_1 E_1 H) + (h.c.). \tag{5.24}$$

In this formula, $L_1$ and $E_1$ are the first generation left- and right-handed lepton fields, $H$ is the SM Higgs field bi-doublet, and $\Phi$ is the Higgs field of the dark sector with the charge of $-1$. For the purpose of our discussion, $H$ and $\Phi$ can be replaced by their vacuum expectation values, $v/\sqrt{2}$ and $v_d/\sqrt{2}$. $\Lambda_\Phi$ is some energy scale normalizing this effective operator, that now defines the effective Yukawa couplings as

$$\lambda_\mathcal{S} \equiv \lambda_s = \lambda_a = \frac{v v_d}{2\Lambda_\Phi^2}. \tag{5.25}$$

Since it is clear that displaced decays are only possible for $\lambda_\mathcal{S} \ll 1$ and typically as small as $10^{-4}$ while heavy $m_{Z'}$ implies a large dark vev $v_d$, the scale $\Lambda_\Phi$ can be well above the LHC energy reach. We leave it at that, without trying to provide further UV completion to the effective operator (5.24). A further uncertainty in this approach arises from a possibility of nontrivial lepton flavor structure of (5.24). To avoid possible complications, we will assume that these couplings are flavor-diagonal, and will limit $m_{s,a}$ to be below the dimuon threshold.

**Production and decay of $Z'$**

Going over to the production mechanism, we notice, of course, that $Z'$ does not couple to gluons, and have to be produced in $q\bar{q}$ fusion. Although the probability of finding (anti-)quarks inside the proton at high energy is smaller compared to that of gluons, the leading order contribution of this process is at tree-level and thus the cross section can be comparable to gluon-initiated but loop-suppressed processes. The production cross section of $Z'$ reads

$$\sigma(pp \rightarrow Z') = \int_0^1 dx_1 \int_0^1 dx_2 f_q(x_1, m_{Z'}^2) f_{\bar{q}}(x_2, m_{Z'}^2) \hat{\sigma} \left[ q\left(x_1 \frac{\sqrt{s}}{2}\right) \bar{q}\left(x_2 \frac{\sqrt{s}}{2}\right) \rightarrow Z' \right],$$
$$\tag{5.26}$$

where $\sqrt{s} = 13$ TeV is the center of mass energy and $f_q(x, Q^2)(f_{\bar{q}}(x, Q^2))$ is the quark (anti-quark) parton distribution function evaluated at $Q^2$. At the same time, the increase in parton luminosity between run I and run II for the production of the 750 GeV resonance is

less pronounced for $q\bar{q}$ compared to gluons, by about a factor of order 3. The decay channels of $Z'$ are similar to those of the SM $Z$-boson but with an additional channel, $Z' \to sa$ available in this model. The decay width to the SM fermions is given by

$$\Gamma(Z' \to f\bar{f}) = \frac{N_c}{12\pi} m_{Z'} \left(\frac{\epsilon e}{\cos^2 \theta_W}\right)^2 \sqrt{1 - \frac{4m_f^2}{m_{Z'}^2}} \left[\frac{Y_L^2 + Y_R^2}{2} + \frac{m_f^2}{m_{Z'}^2} \frac{6Y_L Y_R - Y_L^2 - Y_R^2}{2}\right],$$
(5.27)

where $N_c$ represents the number of colors of the SM fermions $(f)$ and $Y_L(Y_R)$ stands for the hypercharge of the left-handed (right-handed) SM fermions. The decay width of the "dark" $sa$ channel is

$$\Gamma(Z' \to sa) = \frac{g_{Z'}^2}{48\pi} m_{Z'} \left(1 - \frac{2(m_s^2 + m_a^2)}{m_{Z'}^2} + \frac{(m_s^2 - m_a^2)^2}{m_{Z'}^4}\right)^{3/2} \simeq \frac{g_{Z'}^2}{48\pi} m_{Z'}^2.$$
(5.28)

We take the limit $m_{s,a} \ll m_{Z'}$ in the second equality.

Fig. 5.4 shows the total width of $Z'$ (green, solid) as well as its partial widths $\Gamma(Z' \to f\bar{f})$ (blue, dotted) and $\Gamma(Z' \to sa)$ (red, dashed) for $\epsilon = 0.1$ and $m_s = m_a = 100$ MeV. $\Gamma(Z' \to f\bar{f})$ does not vary with $g_{Z'}$ since it only depends on $\epsilon$ while $\Gamma(Z' \to sa)$ is proportional to $g_{Z'}^2$ and therefore grows with $g_{Z'}$. One can also see that for small $g_{Z'} \sim 0.01$ the dominant decay branching ratio is from $Z' \to f\bar{f}$ and the total width of $Z'$ is also very small. However, for a large enough $g_{Z'} \sim 3$, not only the dominant channel becomes $Z' \to sa$, but also the width of $Z'$ can reach $\sim 45$ GeV due to $Z' \to sa$ decays without any difficulty. Therefore in the following analysis we use $g_{Z'} \sim 3$ as a representative point. Also notice that since the branching ratio of $Z' \to sa$ is close to 1 at that point, the parameter $g_{Z'}$ cancels in the branching ratio and has very small effect on subsequent considerations.

The decay lengths of $s$ and $a$ are as follows,

$$L_s(\lambda_s, m_s) = \frac{m_{Z'}}{2m_s} \sqrt{1 - \frac{4m_s^2}{m_{Z'}^2}} \Gamma_s^{-1}, \quad L_a(\lambda_a, m_a) = \frac{m_{Z'}}{2m_a} \sqrt{1 - \frac{4m_a^2}{m_{Z'}^2}} \Gamma_a^{-1},$$
(5.29)

with

$$\Gamma_s = \frac{m_s}{8\pi} \lambda_s^2 \left(1 - \frac{4m_e^2}{m_s^2}\right)^{3/2}, \quad \Gamma_a = \frac{m_a}{8\pi} \lambda_a^2 \left(1 - \frac{4m_e^2}{m_a^2}\right)^{1/2},$$
(5.30)

where $\Gamma_s$ and $\Gamma_a$ are total widths of $s$ and $a$, respectively. We only explore the region below the dimuon threshold so that one can have $\mathrm{Br}_{s \to e^+ e^-}$ and $\mathrm{Br}_{a \to e^+ e^-}$ of order one.
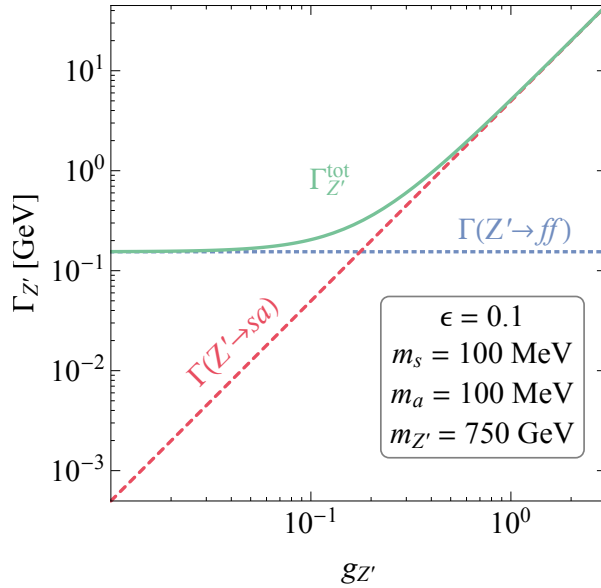
Figure 5.4: Total decay width of $Z'$ (green, solid) along with its partial widths $\Gamma(Z' \to f\bar{f})$ (blue, dotted) and $\Gamma(Z' \to sa)$ (red, dashed) for $\epsilon = 0.1$ and $m_s = m_a = 100$ MeV. $\Gamma(Z' \to f\bar{f})$ is independent of $g_{Z'}$ since it is only a function of $\epsilon$ whereas $\Gamma(Z' \to sa)$ is proportional to $g_{Z'}^2$.

## 5.2 Results

### 5.2.1 Geometry of LHC relevant for the diphoton signal

The ATLAS detector can be viewed as a series of ever-larger concentric cylinders around the beam line. From the inner region to the outer region, the main detector elements are silicon pixel and strip trackers, electromagnetic calorimeters (ECALs), hadron calorimeters (HCALs), and muon spectrometers. A 1/4 of the $z$ view of the detector is demonstrated in Fig. 5.5.

The inner detector tracking system is used to reconstruct primary vertices up to a radius in the transverse plane ($r$) less than 0.8 m [349]. Recently, ATLAS has upgraded the inner detector system and inserted another layer, the Insertable B-Layer (IBL) [350], near the beam-pipe with 0.03 m $< r <$ 0.04 m to enhance the tracking ability and overcome the increased pileup at the LHC run-II. Therefore we define the fiducial volume of the inner detector to be in the region 0.03 m $< r <$ 0.8 m. A photon passing through the fiducial volume of the inner detector can convert into an electron-positron pair, which leaves tracks in the fiducial volume. As a result, such photons are classified as converted photon candidates by the ATLAS collaboration.
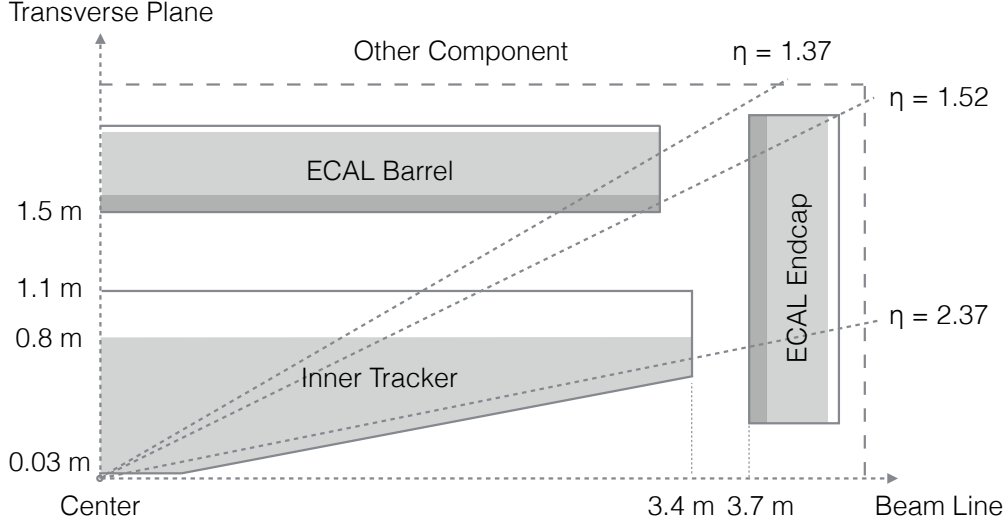
Figure 5.5: Relevant geometry of the ATLAS detector. Here we only show the configuration of the inner tracker and ECAL (1/4 of the $z$ view). Other components of the detector are not shown. The fiducial region of inner detector and ECAL are shaded with gray. The ECAL consists of three layers (see text for details), which we shaded with different tones of gray. We also specific values for the relevant geometry that used in the analysis. Other relevant parameters of the detector can be found in Tab. 5.1.

The ECAL (as well as HCAL) is composed of a barrel and two endcaps. The ATLAS ECAL is a lead-liqid argon sampling calorimeter. The relevant geometrical parameters of the ECAL components are summarized in Fig. 5.5 and Tab. 5.1 [351]. The ECAL consists of three layers, starting at $r = 1.5$ m. A photon is categorized as an unconverted photon candidate if it converts inside the region between 0.8 m and 1.5 m, consisting of the final part of the tracking system and a gap between the inner tracker and the first layer of the ECAL, since it does not leave any reconstructible tracks. In summary, the fiducial volumes of the event reconstruction for the converted and unconverted photons are 0.03 m$< r < 0.8$ m and 0.8 m$< r < 1.6$ m, respectively. Note that if the second layer of the ECAL is also included, the fiducial volume of the unconverted photons is 0.8 m$< r < 1.93$ m.

The inner detectors of ATLAS and CMS are very similar in geometrical coverage. As shown in the CMS TDR [352], the innermost tracker layer starts at $r \sim 44$ mm. The fiducial region of the calorimeter ends at 1.79 m. These numbers are not too different from those of ATLAS ($r = 31$ mm to 1.59 m, respectively in our paper). The slight difference in the significance between the two collaborations may be due to the fact that CMS has around 20% less data compared to that of ATLAS. In addition, the angular resolution of the EM calorimeter at ATLAS might be better in distinguishing the collimated $e^+e^-$ from a single

96

| ATLAS detector | |
| --- | --- |
| Inner tracker | Region: 0.03 m $< r <$ 1.1 m |
| | Fiducial: 0.03 m $< r <$ 0.8 m |
| | $\|\eta\| < 2.5$ |
| ECAL Barrel (EB) | Region: 1.15 m $< r <$ 2.25 m |
| | Fiducial: 1.5 m $< r <$ 1.93 m |
| | $\|\eta\| < 1.48$ |
| ECAL Endcap (EE) | Region: 3.4 m $< \|z\| <$ 6.57 m |
| | Fiducial: 3.7 m $< r <$ 4.13m |
| | $1.38 < \|\eta\| < 3.2$ |

Table 5.1: Geometric parameters and fiducial regions of inner trackers and ECALs of ATLAS. $r$ denotes the transverse radius from the beam line. $z$ denotes the distance from the center of the detector along the beam line. $\eta$ denotes the pseudorapidity with respect to the center of the detector.

photon. As a result, one could expect a potentially smaller excess at CMS. However, the slight discrepancy between ATLAS and CMS could be just statistical fluctuations. More data is required to make a conclusive statement.

## 5.2.2   Displaced Dark Mediator Decay Signal

In order to obtain a more realistic evaluation of $P_{\text{acc}}$ than the one given in Eq. (5.16), we need to take into account the distribution of the initial momentum of heavy resonances ($S$ or $Z'$) affecting the boosts of emerging light particles, which in turns translates into a distribution of the decay lengths $L_{A'}$ or $L_{s,a}$.

Different production mechanisms for $S$ and $Z'$ suggest differences in their boost factors. The scalar $S$ is produced through gluon fusion, which means that the initial states are similarly distributed. On the other hand, in our second example, $Z'$ is produced through $q\bar{q}$ initial states, which is asymmetric because it is more probable to find a quark than an antiquark in a proton due to differences in their parton distribution functions. As a consequence it is more likely that $Z'$ will have more of a longitudinal boost compared to $S$, while for the latter we find that the production-near-rest picture largely holds.

Suppose that the distribution of a heavy resonance initial velocities, or boosts, is given by $f(\beta)$. The function satisfies normalization condition

$$\int_{-1}^{1} f(\beta)d\beta = 1. \tag{5.31}$$

We simulate $f(\beta)$ using standard MC tools in practice. Furthermore, given the geometry of the detector is cylindrical, and that all decays of light particles to collimated $e^+e^-$ pairs within radial segments (distance from the origin) $r_{min}(\theta) < r < r_{max}(\theta)$ pass the photon selection criteria, $P_{acc}$ is proportional to

$$P_{acc} \propto P_{fid} \times (Br_{e^+e^-})^2, \tag{5.32}$$

where $P_{fid}$ is the probability for dark mediators decaying inside the fiducial regions. $P_{fid}$ can be expressed as

$$P_{fid} = \int_{-1}^{1} d\beta f(\beta) \int_{\theta_{1,min}}^{\theta_{1,max}} d\cos\theta_1 \frac{\gamma}{2}(1 - \beta\cos\theta_1) \left[\sin^2\theta_1 + \gamma^2(\cos\theta_1 - \beta)^2\right]^{-3/2}$$
$$\times \left(e^{-r_{1,min}/L_{L,1}} - e^{-r_{1,max}/L_{L,1}}\right) \left(e^{-r_{2,min}/L_{L,2}} - e^{-r_{2,max}/L_{L,2}}\right), \tag{5.33}$$

with

$$L_{L,1} = p_{L,1}\frac{\tau_{A'}}{m_{A'}} = \frac{p_0}{\sqrt{1 - \cos^2\theta_1 + \gamma^2(\cos\theta_1 - \beta)^2}}\frac{\tau_{A'}}{m_{A'}}, \tag{5.34}$$

$$L_{L,2} = p_{L,2}\frac{\tau_{A'}}{m_{A'}} = \frac{p_0}{\sqrt{1 - \cos^2\theta_1 + \gamma^2(\cos\theta_1 - \beta)^2}}\sqrt{\frac{1 - \cos^2\theta_1}{1 - \cos^2\theta_2}}\frac{\tau_{A'}}{m_{A'}} \tag{5.35}$$

are the decay lengths of the dark mediators 1 and 2 in the laboratory frame (denoted with subscript "$L$"). $\theta_1$ and $\theta_2$ are the polar angles of the dark mediators 1 and 2, respectively in the laboratory frame. $r_{i,min}$ and $r_{i,max}$ are lower and upper boundaries of $r_i$ of the fiducial volume, which both are functions of $\theta$. $\theta_{1,min}$ and $\theta_{1,max}$ represent lower and upper boundaries of $\theta_1$ of the fiducial region. Note that $\theta_1$ and $\theta_2$ are not independent. $\cos\theta_2$ can be expressed in terms of $\cos\theta_1$ and $\beta$

$$\cos\theta_2 = \cos\theta_2(\cos\theta_1, \beta) = -\frac{\beta^2\cos\theta_1 - 2\beta + \cos\theta_1}{\beta^2 - 2\beta\cos\theta_1 + 1}, \tag{5.36}$$

where $\beta$ is the velocity of the parent particle ($Z'$ or $S$) after the production with a boost factor $\gamma \equiv 1/\sqrt{1 - \beta^2}$. We refer the readers to Appendix A.3 for the more detailed derivation of the decay probability including the boost effect.

Given the geometry of the detector and the probability (A.51), we can calculate $P_{fid}$ for both 750 GeV scalar and vector resonance scenarios. We give the results for $P_{fid}$ for the 750 GeV scalar resonance scenario in Tab. 5.2 as an example. $P_{fid}$ a function of decay length $L_{A'}$. One can observe that as the decay length grows, the $P_{fid}$ drops precipitously.

From Eq. (5.32) to obtain the final $P_{acc}$, we still need to multiple the right hand side by the acceptance rate and diphoton reconstruction efficiency, i.e.,

$$P_{acc} = \epsilon_\gamma^2 \times A \times P_{fid} \times (Br_{e^+e^-})^2, \tag{5.37}$$

| Decay Length ($L_d$) | Converted | Unconverted 1 | Converted 1+2 | Unconverted 1+2 |
|:---:|:---:|:---:|:---:|:---:|
| 0.1 | 0.31 | $2.9 \times 10^{-8}$ | 0.32 | $2.9 \times 10^{-8}$ |
| 1 | 0.38 | $3.4 \times 10^{-2}$ | 0.42 | $5.0 \times 10^{-2}$ |
| 10 | $1.5 \times 10^{-2}$ | $3.9 \times 10^{-3}$ | $1.8 \times 10^{-2}$ | $7.4 \times 10^{-3}$ |
| 20 | $4.0 \times 10^{-3}$ | $1.1 \times 10^{-3}$ | $5.0 \times 10^{-3}$ | $2.2 \times 10^{-3}$ |
| 100 | $1.7 \times 10^{-4}$ | $5.1 \times 10^{-5}$ | $2.2 \times 10^{-4}$ | $1.0 \times 10^{-4}$ |

Table 5.2: Probabilities of dark photon decays inside the ATLAS detector, $P_{\text{fid}}$, for the 750 GeV scalar resonance scenario. Various decay length $L_d$ and fiducial regions are considered. Events with at least one of the decays occurring inside the tracker volume are categorized as "Converted". The "Unconverted 1" category includes events where both dark mediators decay inside the remaining part of the fiducial volume (gap region and the first layer of the ECAL). Similarly, the "Converted 1+2" and "Unconverted 1+2" categories are the generalization of the Converted and Unconverted 1 categories by including the second layer of the ECAL into the fiducial volume of the event reconstruction.

where $\epsilon_\gamma = 95\%$ is the reconstruction efficiency for a single photon [345]. The selection cuts on $|\eta|$ has already been considered in the calculation $P_{\text{fid}}$. The rest selection cuts in [345] are as follows:

$$E_{\text{T}}^{\gamma_1} > 40 \text{ GeV}, \quad E_{\text{T}}^{\gamma_2} > 30 \text{ GeV}, \quad E_{\text{T}}^{\gamma_1}/m_{\gamma\gamma} > 0.4, \quad E_{\text{T}}^{\gamma_2}/m_{\gamma\gamma} > 0.3. \tag{5.38}$$

We use Monte-Carlo simulation to implement above cuts and obtain the acceptance $A$. The resulting acceptance $A$ (after $|\eta|$ cuts) is 68% (84%) for 750 GeV scalar (vector) resonance scenario. Substituting the acceptance and efficiency back to Eq. (5.37), we get $P_{\text{acc}}$ that consequently yields $\sigma_{\text{Signal}}$ through Eq. (5.5).

### 5.2.3 Preferred Parameter Space for Light Dark Mediator

In this subsection we perform a "fusion" of all different components of our calculation in order to derive the allowed parameter space for light particles. Our strategy is to be conservative, which means we should allow the largest possible variations in the properties of the 750 GeV resonance. To that effect, we take the largest possible range for the coupling that regulates the production of $S$ through the gluon fusion, $0 \leq \lambda_T \leq 4\pi$. The upper boundary would correspond to the largest production cross section, and therefore admits the lowest possible $P_{\text{acc}}$. At this point we will also assume that every electron-positron decay of light particles is going to pass the photon selection criteria. Violation of this assumption in practice is possible for higher $A'$ masses, which would reduce the region of interest on the $\epsilon - m_{A'}$

Figure 5.6: Preferred parameter space (yellow shaded) in the $\epsilon^2$ versus $m_{A'}$ plane for dark photons that can explain the 750 GeV scalar resonance through faking photons. In the left and right panel, we vary the parameter $\alpha_d$ and $\lambda_T$ separately. The solid, dotted, and dashed lines in the left(right) panel respectively represent parameters corresponding to 30 observed diphoton events for $\alpha_d = 1$, 0.1, and 0.08 ($\lambda_T = 4\pi$, 4, and 1.3) with a fixed $\lambda_T = 4\pi$ ($\alpha_d = 1$). Other parameters in the calculation are set to be $\lambda_d = 2$, $m_\psi = 300$ GeV and $m_T = 1$ TeV. The purple-gray shaded regions are excluded by the mono-photon search at the ATLAS [353]. It excludes part of parameter space for $\alpha_d = 1$, $\lambda_T = 4\pi$ that we marked as purple-gray lines. Nevertheless, the mono-photon search does not further exclude preferred parameter space for smaller $\alpha_d$ and $\lambda_T$ values listed in the plot. In the plot, we also include current constraints and future prospects on the $\epsilon^2$ versus $m_{A'}$ plane for dark photons that decay directly to SM particles (see *e.g.* [342] and reference in Sec. I).

parameter space.

A fixed minimum value for the $P_{\rm acc}$ has, of course, two solutions in terms of $L_{A'}$. If the decay length is too short, all the decays will happen inside or close to the beam pipe, while if the decay length is too large, only a small finite number of $A'$ pairs would decay in or before the ECAL. For the dark photon model, we obtain the allowed region that would be consistent with our scenario for the 750 GeV resonance. The preferred part of the dark photon parameter space is shown in Fig. 5.6 with $m_T = 1$ TeV, $m_\psi = 300$ GeV, $\lambda_d = 2$ while $\lambda_T$ and $\alpha_d$ are varied. In Fig. 5.7, the same parameters as those of Fig. 5.6 are used except for $m_\psi = 600$ GeV, which corresponds to a narrow width as shown in the left panel of Fig. 5.2. (Notice that the choices of $m_\psi$ and $\alpha_d$ fit the reported widths of a possible 750 GeV
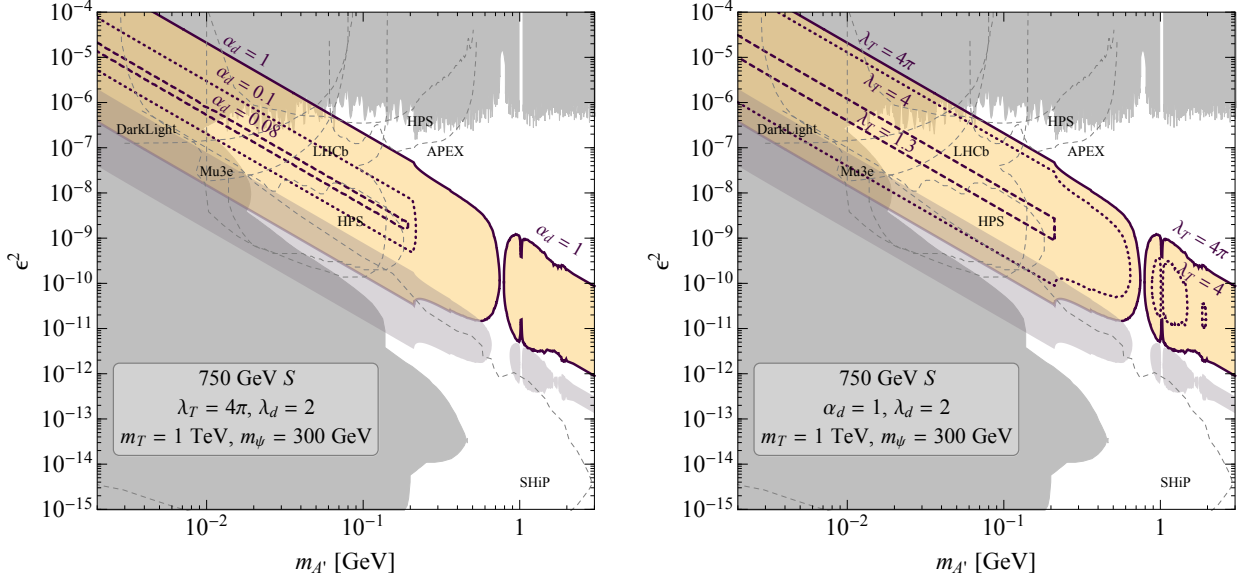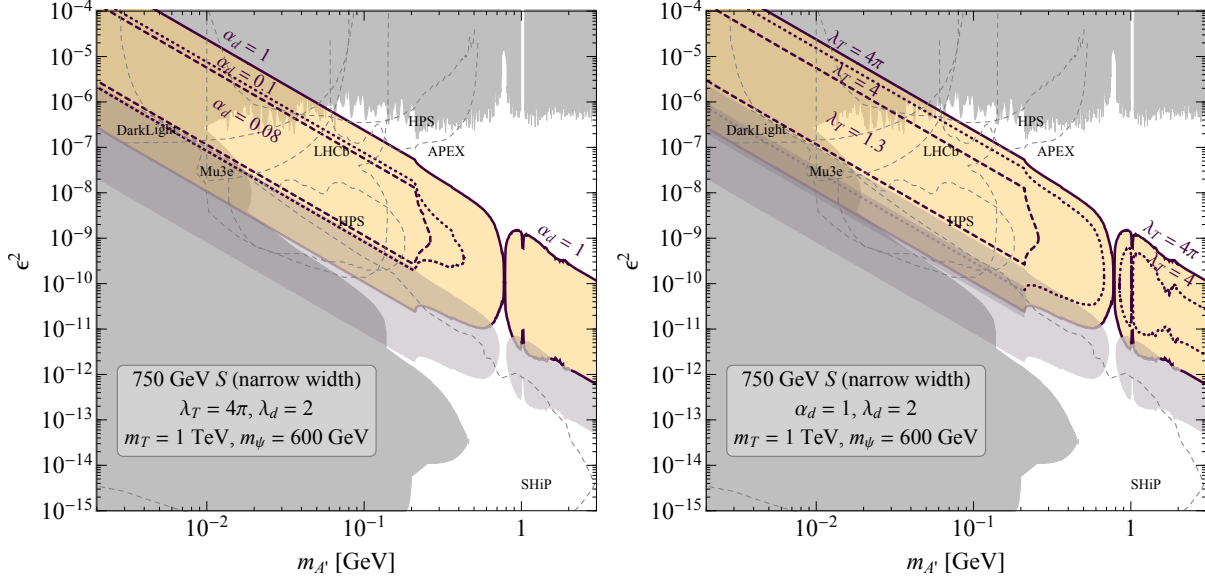
Figure 5.7: Preferred parameter space (yellow shaded) in the $\epsilon^2$ versus $m_{A'}$ plane for dark photons that can explain the 750 GeV scalar resonance. Similar to Fig. 5.6, but with $m_\psi = 600$ GeV. In this choice of parameter space the width of $S$ is narrow around 1 GeV.

resonance with $m_\psi = 300$ and $600$ correspond to wide and narrow widths, respectively.) The yellow shaded region is favored by the 750 GeV resonance. One can also see that the allowed parameter space has a band structure, which follows from the $L_{A'} \propto (\epsilon m_{A'})^{-2}$ scaling. Wiggles, deviations and a dip near 1 GeV occurs due to the enhancement of hadronic decays of $A'$ and the reduction of $\mathrm{Br}_{e^+e^-}$. In the left panel of the plot $\lambda_T$ is set to its maximum value while $\alpha_d$ is varied, while on the right panel $\alpha_d = 1$ and $\lambda_T$ is scanned. We observe that as the couplings diminish so does the allowed part of the parameter space. However, some allowed parameter space still exists for $\lambda_T \sim \mathcal{O}(1)$ or $\alpha_d \sim \mathcal{O}(0.1)$. It is also worth mentioning that above $m_{A'} = 2m_\mu$ there is an appreciable branching to muons, so that one should expect "fake photon" and muon pair, or two muon pair events appearing in the same model that should reconstruct to the same invariant mass.

On the whole, one can see that intensity frontier searches cannot fully exclude the suggested region of the model parameter space. It is easy to understand why: in the adopted LHC scenario, $A'$ particles have relatively small mixing angles $\epsilon \sim \mathcal{O}(10^{-4})$, which for most fixed target searches would not lead to detectable displaced decays. At the same time, it is too small a coupling to be currently ruled out by the search for "bumps" in the $e^+e^-$ spectrum. We also include the exclusion region imposed by the ATLAS mono-photon constraints [353]. This constraint comes from the situation when one $A'$ decays before or inside the ECAL faking a photon, while the second $A'$ completely escapes the detector before de-

caying. The current limit on the cross section is 6.1 (5.3) fb at 95% C.L. This constraint will be relevant for the longer $L_{A'}$, and this is seen in Figs. 5.6 and Fig. 5.7 with the gray band being parallel but below the yellow one. It is worth mentioning that future intensity frontier experiments can potentially exclude some part of preferred parameter space in Figs. 5.6 and Fig. 5.7. These projected limits are shown in dashed lines. In addition, with more data collected the mono-photon search should be able to provide a stronger constraint at the LHC run-II.

Next we present the result of the $Z'$ model in the $\lambda_{\mathcal{S}}^2 - m_{s/a}$ parameter space in Fig. 5.8 with various contours corresponding to $\epsilon = 0.05, 0.1$ and $0.2$. The left and right panels correspond to wide and narrow widths with $g_{Z'} = 3$ and $0.3$, respectively. As illustrated in Fig. 5.2 BR($Z' \to sa$) grows with the total width, and therefore the region enclosed by a contour in the left panel increases for a fixed value of $\epsilon$ compared to those in the right panel because of the larger branching fraction. The yellow shaded region are favored by the 750 GeV $Z'$ resonance while the gray shaded region is excluded by the mono-photon searches with $\epsilon = 0.2$. For $m_{s/a} = 0.1$ GeV one can have $\lambda_{\mathcal{S}}^2$ between $10^{-10}$ and $10^{-8}$. The allowed range of $\epsilon$ in the yellow shaded region is $0.02 \lesssim \epsilon \lesssim 0.2$. The lower limit is to ensure having enough production cross section while the upper limit comes from the measurement of the $Z$-boson mass and width [87]. Notice that the model with $\epsilon < 0.1$ and $g_d \gg g_1\epsilon$ is very difficult to constrain via "conventional" $q\bar{q} \to Z' \to \mu^+\mu^-$ searches due to a small branching ratio for the $Z'$ decay to SM particles, which leads to $\epsilon^4$ scaling of the signal.

## 5.3 Discussion

### 5.3.1 Potential Methods to Exclude Models with Dark Mediators

So far there is only limited amount of data available. However, with more data it is likely that one can statistically discriminate between real photon events and decays of dark mediators. While the properties of the photons are of course fully specified by QED and atomic physics, the main input parameters for the dark mediator decays will be its energy, mass and the decay length (such as $E_{A'}$, $m_{A'}$ and $L_{A'}$ as in the dark photon example). Below we outline important differences between the conversions of real photons and decays of dark mediators.

1. *Affinity of conversions to the material inside the detector.* Photons convert to pairs in the field of the nucleus, and therefore the distribution of conversion points roughly follows the number density of atoms weighted with the square of the atomic number, $Z^2 n_A$. The dark mediators, on the other hand, can decay anywhere in the detector,

102
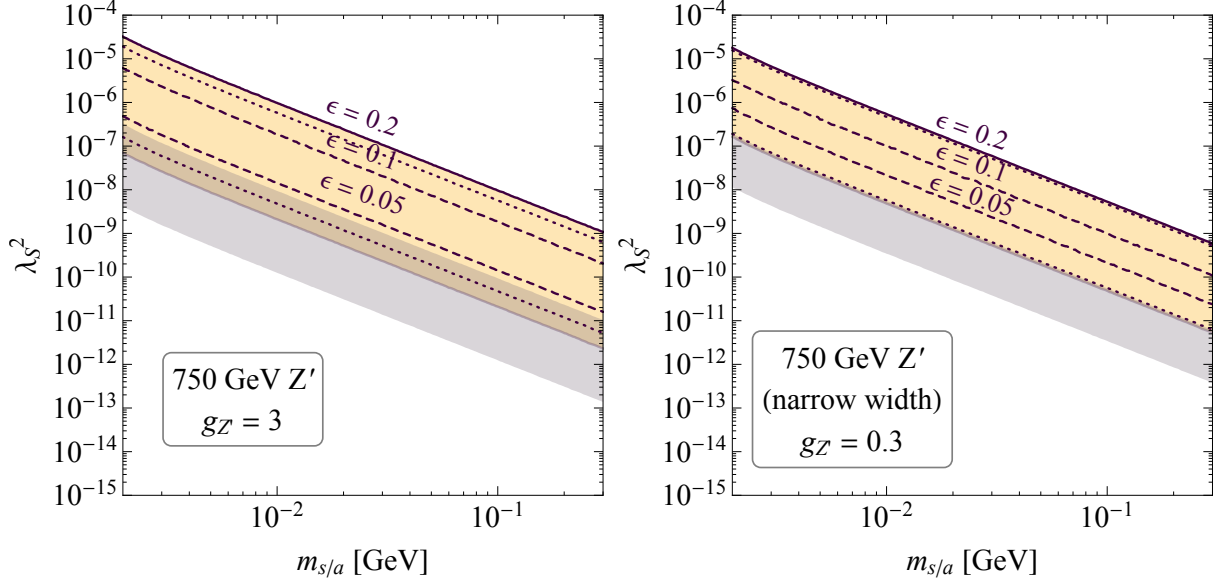
Figure 5.8: Preferred parameter space (yellow shaded) in the $\lambda_{\mathcal{S}}^2$ versus $m_{s/a}$ plane for dark scalars that can explain the 750 GeV vector resonance. The left and right panels correspond to large and narrow widths with $g_{Z'} = 3$ and 0.3, respectively. The solid, dotted, and dashed lines represent parameters corresponding to 30 observed diphoton events for $\epsilon = 0.2$, 0.1, and 0.05, respectively. The purple-gray shaded regions are excluded by the mono-photon search at ATLAS [353]. It excludes part of parameter space for $\epsilon = 0.2$ that we marked as a purple-gray line. The mono-photon search does not further exclude preferred parameter regions for $\epsilon = 0.1$ and 0.05.

including hollow parts. The distribution of vertices for the converted photon events should provide a useful discrimination.

2. *Events beyond the first layer of the ECAL.* The decays of dark mediators can occur in the ECAL *beyond* the first layer of the calorimeter, which would correspond to an unusual penetration depth for a regular photon. In fairness, the probability of decay within the second or third layer of the calorimeter is not very large for the models considered, and more data is needed for this criterion to become useful. But even with current statistics, the searches of "late converting" photons in association with regular photons is of interest and should be pursued.

3. *Distribution of converted vs unconverted events.* Exponential dependence on the distance travelled, for a short decay length $L_d$, will always enhance the fraction of fake unconverted events. That is most dark mediators at short $L_d$ will decay before reaching the ECAL. Therefore this can be a useful criterion for part of the parameter space.

4. *Energy distribution of electron-positron pairs.* It is well known that the electron-positron pairs created by Bethe-Heitler process (regular conversion) have an appreciable fraction of events with asymmetric energy distribution ($E_{e+} \gg E_{e-}$ or $E_{e-} \gg E_{e+}$) whereas a vast fraction of dark mediator decays has $E_{e+} \sim E_{e-}$. This fact is well appreciated in the direct dark photon searches. An abnormally low fraction of asymmetric pairs could be a signature of dark mediators.

5. *Shape and point of origin for the shower.* Unconverted photons may have a small but non-zero penetration depth inside the first layer of the ECAL, while dark photons decaying in the gap between the tracker and the ECAL enter the calorimeter as pairs, and thus shower immediately. This will affect the shape of the shower, its starting point, and possibly the energy reconstructed from the standard procedures.

6. *Abnormal separation of electron-positron pair.* In this chapter we have avoided the discussion of the drop in efficiency for converted and/or unconverted photons when the mass of the dark mediator become large. When a dark mediator such as $A'$ decays to the electron-positron pair, each electron receives a perpendicular momentum $p_\perp \sim m_{A'}/E_{A'}$. After some distance travelled, this may lead to an abnormally large separation of electrons and positrons, compared to a similar behavior of a regular conversion pair, when they cross a layer of the pixel detector and/or reach the ECAL. Detailed implementation of this criterion should determine the *maximum* mass for a dark mediator capable of faking a photon.

We believe that the possibility of dark mediators mimicking real photons deserves a closer look by the experimental collaborations. A few items outlined above may serve as a basis for developing a statistical procedure that would emphasize or suppress fake photons vs real photons and vice versa. It is also worth mentioning that due to the difference in the linear sizes of the ATLAS and CMS detectors (hence a different sensitivity to $L_d$), there can be an additional discriminating power in a combined treatment. Also, it may be that dark mediator decays create a large number of events that are neglected for one or many of the above reasons. Therefore a closer look in a sample with loosened criteria for photon identification may also contribute to constraining or validating dark mediator models.

## 5.4 Summary

In this chapter we have considered the exotic possibility that metastable BSM particles of low mass could be produced as a result of a heavy resonance decay. Being weakly unstable,

these particles decay to electron-positron pairs that may in fact resemble the conversion pairs originating from a regular photon. The prime candidates for such metastable particles are dark photons, as well as light scalars and pseudoscalars, which all have small branchings to neutrinos and therefore do not generate a large missing transverse momentum signal. We have examined both possibilities, without imposing very restrictive assumptions on the properties of the 750 GeV resonance. We have found that the parameter space for light particles (*e.g.* the dark photon models prefer a somewhat wide range of parameters along the $m_{A'}/(100 \text{ MeV}) \times (\epsilon/10^{-4}) \sim O(1)$ line) that emerges from this analysis is not excluded by the current limits. However, a number of new proposals at different stages of maturity exists [341, 354, 62, 343, 355] which will eventually probe deep inside the region of interest.

In the models we consider, the mono-photon searches provide an important constraint. Also, should the light particles be able to decay to muons, a search of two collimated muons plus a "fake photon" reconstructing to the same invariant mass is a promising search channel.

Irrespective of the future status of the 750 GeV resonance, it seems important for the experimental collaborators to build statistical discriminators that would allow (given enough data) to distinguish between regular SM photon events and would-be-photon dark mediator decays. We have provided a discussion of some avenues along which this problem might be addressed.

# Chapter 6

# Conclusion

In this thesis, we discussed the dark sector and its motivation, showed various models, and demonstrated several novel probes of the dark sector through rare muon decays, low-energy electron-positron colliders, and exotic Higgs decays. Those high-intensity experiments provide an unique opportunity to answer several major puzzles of particle physics, such as the nature of particle DM, through the exploration of the dark sector. We focused our dark sector searches on two specific types of models: the vector portal and the Higgs portal. We focused on dark force mediator masses ranging from a few MeV to $\mathcal{O}(10)$ GeV. We explored their searches in the visible decay scenario, where dark mediators decay directly to the SM particle, as well as the invisible decay scenario, where dark mediators decay into dark matter particle beyond the SM. In particular, we project that the future Mu3e experiment can probe the kinetic mixing for dark photons down to $\epsilon \sim 10^{-4}$ in its visible decay mode through the mass range from $\sim 10$ MeV to $\sim 100$ MeV. Future B-factory experiment can probe $\epsilon \sim 10^{-4}$ in dark photon (dark scalar) invisible decay mode through the mass range from $\sim 100$ MeV to $\sim 10$ GeV. Exotic Higgs searches at HL-LHC can probe the branching ratio for Higgs decaying into dark Higgs pairs down to $\mathrm{Br}(h \to 2s) \sim 10^{-2}$ through the $h \to b\bar{b}\mu^+\mu^-$ channel for the mass range from $\sim 10$ GeV to $\sim 60$ GeV. Within the next decade, our understanding of the dark sector can be improved significantly from those searches.

The recently reported 750 GeV diphoton excess from the LHC Run 2 yields excitement in both theory and experiment communities. If it is true, it will be the first BSM particle. We offered a possible explanation, from the dark sector perspective, about the excess through the idea that dark mediators can fake photons, and described the favorable parameter space for dark mediators for two scenarios: a 750 scalar resonance and a 750 GeV vector resonance. Future experimental input from LHC can help us to identify or falsify those scenarios.

Looking to the future, dark sector searches can be approaches from multiple directions, ranging from higher-intensity experiments to improved astrophysical and cosmological obser-

vations. They offer more opportunities to better understand particle physics and cosmology, and shines lights to the dark universe.

# Appendix A

# Technical Details

## A.1 Decay Rate Computation for 2HDM+S Light Scalar and Pseudoscalar

We will now outline how the branching ratios in Sec. 2.3 are calculated. We mostly follow [114, 113], neglecting hadronization effects. This is sufficient for our purposes of demonstrating the range of possible exotic Higgs decay phenomenologies in 2HDM+S.

The relevant part of the Lagrangian is

$$\mathcal{L} \supset -\sum_f \frac{m_f}{v} \left[ \bar{f}f \left( H_1^0 g_{H_1^0 f\bar{f}} + H_2^0 g_{H_2^0 f\bar{f}} \right) - i\bar{f}\gamma_5 f A^0 g_{A^0 f\bar{f}} \right] , \qquad (A.1)$$

where $f$ stands for SM charged fermions. Higgs-vector boson interactions are obtained from the kinematic terms of the vector bosons. The relevant terms are

$$\mathcal{L} \supset -\sum_V \frac{2m_V^2}{v} \left[ V_\mu V^\mu \left( H_1^0 g_{H_1^0 VV} + H_2^0 g_{H_2^0 VV} \right) \right] + \sum_{i=1,2} i\frac{m_Z}{v} g_{ZH_i^0 A^0} \partial_\mu Z^\mu H_i^0 A^0 . \qquad (A.2)$$

Given the the $A^0, H_{1,2}^0$ content of the singlet-like scalar $s$ and pseudoscalar $a$ in Eqs. (2.42) and (2.49), and the couplings in Tab. 2.1, the couplings $g_{sf\bar{f}}$, $g_{af\bar{f}}$, and $g_{sVV}$ can be derived.

The approach for calculating branching ratios is different for light Higgs mass above or below $\sim$ GeV. The theoretical uncertainties in the hadronic region of the latter case are very large, and an effective theory computation must be used.

### A.1.1 Light Singlet Mass Above 1 GeV

According to the discussion in Sec. 4.1.1, the relevant decay channel for the lightest Higgs scalar/pseudoscalar are $a/s \to f\bar{f}$, $a/s \to \gamma\gamma$, and $a/s \to gg$. Ref. [113] contains the decay

widths for the MSSM Higgs at tree-level and higher orders. We include the relevant formulas here, which are valid for the 2HDM+S and SM+S case after rescaling the Yukawa and gauge couplings by the small singlet mixing angle.

(i) **Decays to light SM fermion pairs $a/s \to f\bar{f}$.**

The tree level decay width of $\phi = a, s$ into fermion pairs is given by

$$\Gamma(\phi \to f\bar{f}) = \frac{N_c G_F}{4\sqrt{2}\pi} g_{\phi f\bar{f}}^2 m_\phi m_f^2 \beta_f^p,
\tag{A.3}$$

where the phase volume, $\beta$, is

$$\beta_f = \sqrt{1 - \frac{4m_f^2}{m_\phi^2}}
\tag{A.4}$$

with $p = 1(3)$ for $\phi$ = pseudoscalar $a$ (scalar $s$). For quarks, additional $\mathcal{O}(\alpha_s^2)$ and $\mathcal{O}(\alpha_s^3)$ QCD radiative corrections are taken into consideration

$$\Gamma(\phi \to q\bar{q}) = \frac{3G_F}{4\sqrt{2}\pi} g_{\phi q\bar{q}}^2 m_\phi \bar{m}_q^2 \beta_q^p \left(1 + \Delta_{qq} + \Delta_\phi^2\right).
\tag{A.5}$$

Here $\bar{m}_q$ stands for the running of the quark mass in the $\overline{\text{MS}}$ scheme with the renormalization scale $\mu = m_\phi$. This redefinition absorbs logarithms of masses of quarks from NLO QCD. The QCD correction factor $\Delta_{qq}$ for $\overline{\text{MS}}$ scheme is given by

$$\Delta_{qq} = 5.67\frac{\bar{\alpha}_s}{\pi} + (35.94 - 1.35N_f)\left(\frac{\bar{\alpha}_s}{\pi}\right)^2,
\tag{A.6}$$

where $N_f$ is the number of active light quarks. $\bar{\alpha}_s$ stands for the running of strong coupling up to three-loop order in QCD. Again we choose the renormalization scale $\mu = m_\phi$. Above $\sim$ GeV, $\alpha_s$ is small enough that perturbative QCD can give accurate results. $\Delta_\phi^2$ accounts for additional $\mathcal{O}(\alpha_s^2)$ corrections for $a$ and $h$,

$$\Delta_a^2 = \frac{\bar{\alpha}_s^2}{\pi^2}\left(3.83 - \log\frac{m_a^2}{m_t^2} + \frac{1}{6}\log^2\frac{\bar{m}_q^2}{m_a^2}\right)
\tag{A.7}$$

$$\Delta_s^2 = \frac{\bar{\alpha}_s^2}{\pi^2}\left(1.57 - \frac{2}{3}\log\frac{m_s^2}{m_t^2} + \frac{1}{9}\log^2\frac{\bar{m}_q^2}{m_s^2}\right)
\tag{A.8}$$

(ii) **Loop induced decays to photon pairs $a/s \to \gamma\gamma$.**

The couplings between Higgs scalars and $\gamma\gamma$ are induced by charged particle loops. The decay widths can be written as

$$\Gamma(a \to \gamma\gamma) = \frac{G_F \alpha^2 m_a^3}{128\sqrt{2}\pi^3}\left|\sum_f N_c Q_f^2 g_{af\bar{f}} A_{1/2}^a\left(\frac{m_a^2}{4m_f^2}\right)\right|^2
\tag{A.9}$$

$$\Gamma(s \to \gamma\gamma) = \frac{G_F \alpha^2 m_s^3}{128\sqrt{2}\pi^3}\left|\sum_f N_c Q_f^2 g_{sf\bar{f}} A_{1/2}^s\left(\frac{m_s^2}{4m_f^2}\right) + g_{sVV} A_1^s\left(\frac{m_s^2}{4m_W^2}\right)\right|^2,
\tag{A.10}$$

where $Q_f$'s are electric charges in units of $e$. The form factors for spin half and one particles, $A_{1/2}$ and $A_1$, are given by

$$A_{1/2}^a(x) = 2x^{-1}f(x) \tag{A.11}$$

$$A_{1/2}^s(x) = 2[x + (x-1)f(x)]x^{-2} \tag{A.12}$$

$$A_1^s(x) = -[2x^2 + 3x + 3(2x-1)f(x)]x^{-2} \tag{A.13}$$

with

$$f(x) = \begin{cases} \arcsin^2\sqrt{x} & x \leq 1 \\ -\frac{1}{4}\left[\log\frac{1+\sqrt{1-1/x}}{1-\sqrt{1-1/x}} - i\pi\right]^2 & x > 1 \end{cases}. \tag{A.14}$$

In the limit $x \to 0$

$$A_{1/2}^a \to 2 \tag{A.15}$$

$$A_{1/2}^s \to 4/3 \tag{A.16}$$

$$A_1^s \to -7 \tag{A.17}$$

We neglect the contributions of possible heavy BSM charged particles, which are generically highly suppressed.

Eq. (A.10) shows that the dominant contribution to $s \to \gamma\gamma$ for SM-like fermion couplings comes from $W$- and $t$-loops. The top loop also dominates $a \to \gamma\gamma$ but there is no $W$ contribution. However, $\alpha'$ and $\beta$-dependent factors in the couplings can also make the $b$ loop important. This occurs in type-II and type-IV models when $\tan\beta \times \tan\alpha'$ or $\tan\alpha$ is large for $s$ or $a$, respectively.

For the purposes of computing QCD correction we can treat $t$ in the heavy quark limit $(m_t \to \infty)$. The QCD corrections on $A_{1/2}(x)$ are then

$$A_{1/2}^a(x) \to A_{1/2}^a(x) \quad \text{(no NLO correction)} \tag{A.18}$$

$$A_{1/2}^s(x) \to \left(1 - \frac{\bar{\alpha}_s(m_s/2)}{\pi}\right)A_{1/2}^s(x) \tag{A.19}$$

Here the renormalization scale $\bar{\alpha}_s$ is chosen to be $\mu = m_s/2$. The above expressions are also valid for the scalar mass in the range $m_\phi < 2m_b$, but QCD corrections become more complicated near the $b$-threshold $m_\phi \gtrsim 2m_b$ [356, 357].

(iii) **Loop induced decays to gluon pairs $a, s \to gg$.**

Gluons are massless particles that couple to the Higgs dominantly via heavy quark loops, $Q = t, b, c$. The decay widths are given by

$$\Gamma(\phi \to gg) = \frac{G_F \bar{\alpha}_s^2 m_\phi^3}{36\sqrt{2}\pi^3} \left| \frac{3}{4} \sum_{Q=t,b,c} g_{\phi Q\bar{Q}} A_{1/2}^\phi \left( \frac{m_\phi^2}{4m_Q^2} \right) \right|^2. \tag{A.20}$$

Other potential heavy particle contributions are neglected. Adding NLO QCD corrections yields the decay width

$$\Gamma(a \to gg) = \frac{G_F \bar{\alpha}_s^2 m_a^3}{36\sqrt{2}\pi^3} \left| \frac{3}{4} \sum_{Q=t,b,c} g_{aQ\bar{Q}} A_{1/2}^a \left( \frac{m_a^2}{4m_Q^2} \right) \right|^2 \left( 1 + \left( \frac{97}{4} - \frac{7}{6}N_f \right) \frac{\bar{\alpha}_s}{\pi} \right) \tag{A.21}$$

$$\Gamma(h \to gg) = \frac{G_F \bar{\alpha}_s^2 m_s^3}{36\sqrt{2}\pi^3} \left| \frac{3}{4} \sum_{Q=t,b,c} g_{hQ\bar{Q}} A_{1/2}^s \left( \frac{m_s^2}{4m_Q^2} \right) \right|^2 \left( 1 + \left( \frac{95}{4} - \frac{7}{6}N_f \right) \frac{\bar{\alpha}_s}{\pi} \right), \tag{A.22}$$

where the renormalization scale of $\bar{\alpha}_s$ is $\mu = m_\phi$.

(iv) **Other Decay Channels of the lightest Higgs.**

Decays to $\gamma$+quarkonium final states are enhanced for pseudoscalar masses near the $2c, 2b$ thresholds. These are challenging to calculate [141], and we neglect them along with hadronization effects, which likely invalidates our quantitative results near the $B/D$-meson and quarkonia thresholds.

## A.1.2 Light Singlet Mass Below 1 GeV

For a sub-GeV (pseudo)scalar Higgs, hadronization effects dominate and the perturbative analysis is not valid above the pion threshold. The calculation of decay widths in this region is extremely difficult due to the QCD uncertainties in the hadronic final states. Light (pseudo)scalars that decay to two (three) pions would look similar to hadronic taus in an experimental analysis, and care would have to be taken not to reject them based on track quality requirements.

We now outline our methods for estimating the branching ratios in this low-mass regime.

(i) **Singlet-like scalar** $s$

For $m_s < 2m_e \simeq 1.02$ MeV, $\gamma\gamma$ decay is the only available channel. In the region $2m_e \leq m_s < 2m_\mu \simeq 211$ MeV, $e^+e^-$ rises and competes with $\gamma\gamma$. Br's of $\gamma\gamma$ may be enhanced in type-II, III, and IV by appropriate choice of $\tan\beta$ and $\alpha'$. In the region $2m_\mu \leq m_s < 2m_{\pi^0} \simeq 270$ MeV, $\mu^+\mu^-$ decay appears and replaces $e^+e^-$ to compete with $\gamma\gamma$.

Branching ratios are most difficult to estimate accurately in the mass window from the $\pi\pi$ threshold to about 1 GeV. $\mu^+\mu^-$ competes with $\gamma\gamma$, $\pi\pi$, $K\overline{K}$, and $\eta\eta$. Several methods are available for the estimation in this region, such as soft pion theory and the chiral Lagrangian method. All suffer from significant final-state uncertainties. According to Ref. [115], the perturbative spectator approximation gives a reasonable and relatively simple approximation of decay widths. They are given by[1]

$$\Gamma(s \to \gamma\gamma) = \frac{G_F \alpha^2 m_s^3}{128\sqrt{2}\pi^3} \left| \sum_f N_c Q_f^2 g_{sf\bar{f}} A_{1/2}^s \left( \frac{m_s^2}{4m_f^2} \right) - 7 g_{sVV} \right|^2 \tag{A.23}$$

$$\Gamma(s \to \mu\bar{\mu}, e\bar{e}) = \frac{G_F}{4\sqrt{2}\pi} m_s g_{s\mu\bar{\mu},e\bar{e}}^2 m_{\mu,e}^2 \beta_\mu^3 \tag{A.24}$$

$$\Gamma(s \to u\bar{u}, d\bar{d}) = \frac{3G_F}{4\sqrt{2}\pi} m_s g_{su\bar{u},d\bar{d}}^2 m_{u,d}^2 \beta_\pi^3 \tag{A.25}$$

$$\Gamma(s \to s\bar{s}) = \frac{3G_F}{4\sqrt{2}\pi} m_s g_{ss\bar{s}}^2 m_s^2 \beta_K^3 \tag{A.26}$$

$$\Gamma(s \to gg) = \frac{G_F \alpha_s^2 m_s^3}{36\sqrt{2}\pi^3} \left( \sum_q g_{sq\bar{q}} - (g_{su\bar{u}} + g_{sd\bar{d}})\beta_\pi^3 - g_{ss\bar{s}}\beta_K^3 \right)^2 \tag{A.27}$$

and we define the non-charm hadron decay width as

$$\Gamma(s \to had.) = \Gamma(s \to u\bar{u}) + \Gamma(s \to d\bar{d}) + \Gamma(s \to s\bar{s}) + \Gamma(s \to gg). \tag{A.28}$$

Another source of uncertainty in the Br estimation lies in the definition of the light quark mass. Different definitions render different Br's, especially to $\gamma\gamma$. For our computation, we use $m_u = m_d = 40$ MeV, $m_s = 450$ MeV, and $\alpha_s/\pi = 0.15$ as [115]. The values are chosen such that results from the spectator approximation method match results from the chiral Lagrangian method, but we emphasize that the uncertainties remain very large above the pion threshold.

(ii) **Singlet-like pseudoscalar $a$**

Below the $3\pi$ threshold ($m_a < 3m_{\pi^0} \simeq 405$ MeV), Br's of $a$ are similar to Br's of $h$ and dictated mostly by thresholds (and possibly a competitive decay to $\gamma\gamma$). Above the $3\pi$ threshold, decays of $a$ to $3\pi, \rho^0\gamma, \omega\gamma, \theta\pi\pi$ arise as $m_a$ increases and competes with $\mu^+\mu^-$ and $\gamma\gamma$ decays. We apply a similar spectator approximation as for the scalar case, with

---

[1]Here "s" stands for the strange quark in order to differentiate with the singlet-like scalar, $s$.

a threshold of twice the Kaon mass, $2m_K$, for strange quark final states [358],

$$\Gamma(a \to \gamma\gamma) = \frac{G_F \alpha^2 m_a^3}{128\sqrt{2}\pi^3} \Big| \sum_f N_c Q_f^2 g_{af\bar{f}} A_{1/2}^a \left(\frac{m_a^2}{4m_f^2}\right) \Big|^2 \tag{A.29}$$

$$\Gamma(a \to \mu\bar{\mu}, e\bar{e}) = \frac{G_F}{4\sqrt{2}\pi} m_a g_{a\mu\bar{\mu},e\bar{e}}^2 m_{\mu,e}^2 \beta_\mu \tag{A.30}$$

$$\Gamma(a \to u\bar{u}, d\bar{d}) = \frac{3G_F}{4\sqrt{2}\pi} m_a g_{au\bar{u},d\bar{d}}^2 m_{u,d}^2 \beta_\pi \tag{A.31}$$

$$\Gamma(a \to s\bar{s}) = \frac{3G_F}{4\sqrt{2}\pi} m_a g_{as\bar{s}}^2 m_s^2 \beta_K \tag{A.32}$$

$$\Gamma(a \to gg) = \frac{G_F \alpha_s^2 m_a^3}{16\sqrt{2}\pi^3} \left( \sum_q g_{aq\bar{q}} - (g_{au\bar{u}} + g_{ad\bar{d}})\beta_\pi - g_{as\bar{s}}\beta_K \right)^2 \tag{A.33}$$

$$\Gamma(a \to had.) \equiv \Gamma(a \to u\bar{u}) + \Gamma(a \to d\bar{d}) + \Gamma(a \to s\bar{s}) + \Gamma(a \to gg). \tag{A.34}$$

## A.2  Estimation of the Multi-jet QCD Backgrounds at LHC

The high rate of QCD multi-jet processes means that the possibility of two QCD jets 'faking' a pair of muons must be considered. This is a very rare process, occurring mostly due to heavy flavor decay inside of a jet with otherwise soft hadronic constituents that result in the muon passing isolation requirements. The rate for QCD jets resulting in a muon tag is estimated at $\sim 10^{-3}$ per $b/c$-jet [359, 360] and $\sim 10^{-4}$ per light flavor jet [266].

These backgrounds are notoriously difficult to simulate in full detail. As pointed out by [361], even large-scale full Monte Carlo simulations still lack the credibility to predict these fake muon backgrounds, and experimental analyses rely on data-driven methods to estimate their contributions.

A framework for the simulation of fake leptons was proposed in [266], in which differential mis-tag rates are derived from experimental information, then used to reweight event samples and hence obtain statistically reliable fake-lepton background distributions that preserve the kinematics of the source processes without simulating large numbers of events. This was successfully used to reproduce data-driven estimates of fake lepton backgrounds in [362, 363]. We will use this framework to very roughly estimate the size of QCD multi-jet background to our $2b2\mu$ search. Given the large uncertainties, our estimate of the number of fake leptons should only be considered as qualitative.

We simulate QCD multi-jet backgrounds, together with the irreducible DY and $t\bar{t}$ backgrounds, at leading order and at parton level in `MadGraph 5.1.14` [190]. We reweight the

events using the procedure in [266], then apply preselection cuts and compare the rates of multi-jet backgrounds to those of DY and $t\bar{t}$ backgrounds. Since the latter are included in our analyses (simulated to a much greater level of detail in `Sherpa 2.1.1` [267]), comparing irreducible to multi-jet backgrounds in this toy study will allow us to estimate the significance of lepton fakes to our analyses.

For the purpose of this estimate, we ignore the relatively small amount of momentum lost when the 'jet' is reconstructed as a muon. We only need the mis-tag rate as a function of jet $p_T$. In [266], this was parameterized by a simple linear function.

$$\epsilon_{j\to\mu}(p_{T_j}) = \epsilon_{200}\left[1 - (1-r_{10})\frac{200 - (p_{Tj}/\text{GeV})}{200 - 10}\right], \qquad (A.35)$$

where $\epsilon_{200} \equiv \epsilon_{j\to\mu}(200 \text{ GeV})$ and $r_{10} \equiv \epsilon_{j\to\mu}(10 \text{ GeV})/\epsilon_{j\to\mu}(200 \text{ GeV})$. We adopt the three fake-rate benchmarks derived in [266] for the rate of a light jet faking a muon at the 8 TeV LHC:

(a) $r_{10} = 0$, $\epsilon_{200} = 3.8 \times 10^{-4}$;

(b) $r_{10} = 0.5$, $\epsilon_{200} = 1.6 \times 10^{-4}$;

(c) $r_{10} = 1$, $\epsilon_{200} = 0.85 \times 10^{-4}$.

For the 14 TeV LHC, we adopt two benchmarks:

(A) the same parameters as (a);

(B) $r_{10} = 1$, $\epsilon_{200} = 1.7 \times 10^{-4}$.

For $b/c$-jets faking muons, we simply scale the mis-tag efficiency curve of the light jet by

$$\epsilon_{b\to\mu}(p_{Tb}) \approx 50 \times \epsilon_{j\to\mu}(p_{Tj}), \qquad (A.36)$$

$$\epsilon_{c\to\mu}(p_{Tc}) \approx 50 \times \epsilon_{j\to\mu}(p_{Tj}), \qquad (A.37)$$

as suggested in [359, 360]. (This may be pessimistic, see [364].)

After reweighting the multi-jet events ($4j$, $4c$, $4b$, $2b2j$, $2b2c$, $2c2j$) according to these fake rate curves and applying preselection criteria, we find that irreducible DY backgrounds appear dominant when requiring zero or two $b$-tags. Therefore, for the analyses presented in Sec. 4.1.2 and 4.1.2, fake muon backgrounds can be safely ignored. For a single $b$-tag, fake background may be competitive with DY and $t\bar{t}$ after the preselection cuts, but adding that channel in any case does not improve sensitivity. For the jet-substrcture analysis presented in Sec. 4.1.2, the fake background may be important, as there we require only one $b$-tag. For this, a careful experimental study, using a data-driven background estimate, is required.

## A.3  Decay Probability with Boost Effect

In this section, we derive the decay probability of dark mediators in the laboratory frame. We first start with the decay probability in the rest frame of the parent particle $S$ which can be written as

$$P_r = \int dW \frac{1}{L_{r,1}} e^{-r_1/L_{r,1}} \frac{1}{L_{r,2}} e^{-r_2/L_{r,2}} dr_1 dr_2, \tag{A.38}$$

with

$$dW = \frac{1}{4\pi p_0^2} d^3 p_{r,1} \delta(|\vec{p}_{r,1}| - p_0). \tag{A.39}$$

The normalization factor in Eq. A.39 is chosen such that $W = 1$ after carrying out the integration. $p_0 \simeq m_S/2$ is the magnitude of the momentum of the daughter particles and the subscript "$r$" indicates that the observable is in the rest frame of the parent particle. $r_i$ is the radial coordinate of the dark mediator $i$. We neglect the mass of the daughter particles since they are much lighter than the parent particle. The delta function is used to impose the on-shell condition. Note that the momenta of the two daughter particles are related $\vec{p}_{r,1} = -\vec{p}_{r,2}$ so the delta function requires both daughter particles to be on-shell. $r_i$ and $L_{r,i}$ are radial coordinate and the decay length of the daughter particle $i$ ($i = 1, 2$) in the rest frame of the parent particle. We also assume that the boost is only along the beam-pipe, i.e. the $z$ direction. Using a Lorentz transformation one can express the $z$ component of the momentum of the daughter particle in the rest frame in terms of the observables in the laboratory frame

$$p_r^z = \gamma(p_L^z - \beta E_L) \simeq \gamma\, p_L(\cos\theta - \beta), \tag{A.40}$$

where $p_L^z$ and $E_L$ are the $z$ component momentum and the energy of the daughter particle in the laboratory frame, respectively. The subscript $L$ indicates that the observable is in the laboratory frame. $\theta$ represents the polar angle of the daughter particles in the laboratory frame. We have used $p_L^z = p_L \cos\theta$ and $E_L \simeq p_L$ in the last step. $\beta$ is the relative velocity between the rest frame of the parent particle and the laboratory frame. The boost factor $\gamma = 1/\sqrt{1 - \beta^2}$. Similarly we obtain the following equations

$$dp_r^z = \gamma(1 - \beta \frac{p_L^z}{E_L}) dp_L^z \simeq \gamma(1 - \beta\cos\theta) dp_L^z, \tag{A.41}$$

$$|\vec{p}_r| = \sqrt{p_\perp^2 + \gamma^2(p_L^z - \beta E_L)^2} \simeq p_L \sqrt{\sin^2\theta + \gamma^2(\cos\theta - \beta)^2}, \tag{A.42}$$

where $p_\perp = p_L \sin\theta$ is the momentum of the daughter particle in the transverse plane. In the last steps of Eqs. A.41 and A.42 we have used the relations, $p_\perp = p_L \sin\theta$ and $p_L^z = p_L \cos\theta$.

Therefore the $\delta$ function in A.39 in the laboratory frame can be written as

$$\delta(|\vec{p}_r| - p_0) = \delta(p_L\sqrt{\sin^2\theta + \gamma^2(\cos\theta - \beta)^2} - p_0)$$

$$= \frac{1}{\sqrt{\sin^2\theta + \gamma^2(\cos\theta - \beta)^2}}\delta(p_L - \frac{p_0}{\sqrt{\sin^2\theta + \gamma^2(\cos\theta - \beta)^2}}). \qquad (A.43)$$

Likewise, $dW$ in the laboratory frame is as follows

$$dW = \frac{d\cos\theta}{2}dp_L\delta(p_L - \frac{p_0}{\sqrt{\sin^2\theta + \gamma^2(\cos\theta - \beta)^2}})$$

$$\times \gamma(1 - \beta\cos\theta)(\sin^2\theta + \gamma^2(\cos\theta - \beta)^2)^{-3/2}. \qquad (A.44)$$

Furthermore, based on the momentum conservation we know that there are relations between daughter particles 1 and 2.

$$p_{r,1}^z = -p_{r,2}^z, \qquad (A.45)$$

$$p_{\perp,1} = p_{\perp,2}. \qquad (A.46)$$

This gives rise to

$$p_{L,1}(\cos\theta_1 - \beta) = p_{L,2}(\cos\theta_2 - \beta), \qquad (A.47)$$

$$p_{L,1}\sin\theta_1 = p_{L,2}\sin\theta_2. \qquad (A.48)$$

One can solve Eqs. A.47 and A.48 for $\cos\theta_2$ and $p_{L,2}$,

$$\cos\theta_2 = -\frac{\beta^2\cos\theta_1 - 2\beta + \cos\theta_1}{\beta^2 - 2\beta\cos\theta_1 + 1}, \qquad (A.49)$$

$$p_{L,2} = \frac{p_0}{\sqrt{1 - \cos^2\theta_1 + \gamma^2(\cos\theta_1 - \beta)^2}}\sqrt{\frac{1 - \cos^2\theta_1}{1 - \cos^2\theta_2}}. \qquad (A.50)$$

In summary, the final formula for the decay probability in the laboratory frame is as follows:

$$P_L = \int d\beta f(\beta)dW\frac{1}{L_{L,1}}e^{-r_1/L_{L,1}}\frac{1}{L_{L,2}}e^{-r_2/L_{L,2}}dr_1 dr_2$$

$$= \int_{-1}^{1} d\beta f(\beta)\int_{-1}^{1}\frac{d\cos\theta_1}{2}\gamma(1 - \beta\cos\theta_1)(\sin^2\theta_1 + \gamma^2(\cos\theta_1 - \beta)^2)^{-3/2}$$

$$\times (e^{-r_{1,min}/L_{L,1}} - e^{-r_{1,max}/L_{L,1}})(e^{-r_{2,min}/L_{L,2}} - e^{-r_{2,max}/L_{L,2}}), \qquad (A.51)$$

where

$$L_{L,1} = p_{L,1}\frac{\tau_{A'}}{m_{A'}} = \frac{p_0}{\sqrt{1 - \cos^2\theta_1 + \gamma^2(\cos\theta_1 - \beta)^2}}\frac{\tau_{A'}}{m_{A'}}, \qquad (A.52)$$

$$L_{L,2} = p_{L,2}\frac{\tau_{A'}}{m_{A'}} = \frac{p_0}{\sqrt{1 - \cos^2\theta_1 + \gamma^2(\cos\theta_1 - \beta)^2}}\sqrt{\frac{1 - \cos^2\theta_1}{1 - \cos^2\theta_2}}\frac{\tau_{A'}}{m_{A'}}. \qquad (A.53)$$

We have used the delta function in the last step of Eq. A.51. Note that $p_0 \tau_{A'}/m_{A'}$ is the decay length of the daughter particles in the rest frame of the parent particle. $r_{i,min}$ and $r_{i,max}$ are lower and upper boundaries of $r_i$ of the fiducial volume. $\theta_{1,min}$ and $\theta_{1,max}$ are lower and upper boundaries of $\theta_1$ of the fiducial region. $f(\beta)$ is the normalized velocity distribution of the parent particle, *i.e.* $\int_{-1}^{1} d\beta f(\beta) = 1$. We use MadGraph5_aMC@NLO [146] to obtain $f(\beta)$ of the parent particle.

# Bibliography

[1] H. Weyl, *Gravitation und elektrizität, Sitzungsberichte der Königlich Preußischen Akademie der Wissenschaften (Berlin), Seite 465-478* **1** (1918) 465–478.

[2] N. Arkani-Hamed, F. Cachazo, and J. Kaplan, *What is the Simplest Quantum Field Theory?, JHEP* **09** (2010) 016, [`arXiv:0808.1446`].

[3] **Institute for Advanced Study** Collaboration, N. Seiberg, "What is Quantum Field Theory?." talk given at Future Prospects for Fundamental Particle Physics and Cosmology Workshop, May 2015.

[4] **Particle Data Group** Collaboration, K. A. Olive et al., *Review of Particle Physics, Chin. Phys.* **C38** (2014) 090001.

[5] J. H. Oort, *The force exerted by the stellar system in the direction perpendicular to the galactic plane and some related problems*, .

[6] F. Zwicky, *On the Masses of Nebulae and of Clusters of Nebulae, The Astrophysical Journal* **86** (Oct., 1937) 217.

[7] V. C. Rubin, W. K. J. Ford, and N. . Thonnard, *Rotational properties of 21 SC galaxies with a large range of luminosities and radii, from NGC 4605 /R = 4kpc/ to UGC 2885 /R = 122 kpc/, The Astrophysical Journal* **238** (June, 1980) 471–487.

[8] G. Steigman and M. S. Turner, *Cosmological Constraints on the Properties of Weakly Interacting Massive Particles, Nucl. Phys.* **B253** (1985) 375.

[9] **LUX** Collaboration, D. S. Akerib et al., *First results from the LUX dark matter experiment at the Sanford Underground Research Facility, Phys. Rev. Lett.* **112** (2014) 091303, [`arXiv:1310.8214`].

[10] K. J. Bae, J.-H. Huh, and J. E. Kim, *Update of axion CDM energy, JCAP* **0809** (2008) 005, [`arXiv:0806.0497`].

[11] **ADMX** Collaboration, S. J. Asztalos et al., *A SQUID-based microwave cavity search for dark-matter axions*, Phys. Rev. Lett. **104** (2010) 041301, [`arXiv:0910.5914`].

[12] Y. Kahn, B. R. Safdi, and J. Thaler, *A Broadband/Resonant Approach to Axion Dark Matter Detection*, `arXiv:1602.0108`.

[13] P. W. Graham and S. Rajendran, *New Observables for Direct Detection of Axion Dark Matter*, Phys. Rev. **D88** (2013) 035023, [`arXiv:1306.6088`].

[14] A. Boyarsky, O. Ruchayskiy, and M. Shaposhnikov, *The Role of sterile neutrinos in cosmology and astrophysics*, Ann. Rev. Nucl. Part. Sci. **59** (2009) 191–214, [`arXiv:0901.0011`].

[15] K. M. Zurek, *Asymmetric Dark Matter: Theories, Signatures, and Constraints*, Phys. Rept. **537** (2014) 91–121, [`arXiv:1308.0338`].

[16] K. Petraki and R. R. Volkas, *Review of asymmetric dark matter*, Int. J. Mod. Phys. **A28** (2013) 1330028, [`arXiv:1305.4939`].

[17] S. D. McDermott, H.-B. Yu, and K. M. Zurek, *Constraints on Scalar Asymmetric Dark Matter from Black Hole Formation in Neutron Stars*, Phys. Rev. **D85** (2012) 023519, [`arXiv:1103.5472`].

[18] Y. Nomura and J. Thaler, *Dark Matter through the Axion Portal*, Phys. Rev. **D79** (2009) 075008, [`arXiv:0810.5397`].

[19] P. Arias, D. Cadamuro, M. Goodsell, J. Jaeckel, J. Redondo, and A. Ringwald, *WISPy Cold Dark Matter*, JCAP **1206** (2012) 013, [`arXiv:1201.5902`].

[20] A. E. Nelson and J. Scholtz, *Dark Light, Dark Matter and the Misalignment Mechanism*, Phys. Rev. **D84** (2011) 103501, [`arXiv:1105.2812`].

[21] M. Baumgart, C. Cheung, J. T. Ruderman, L.-T. Wang, and I. Yavin, *Non-Abelian Dark Sectors and Their Collider Signatures*, JHEP **0904** (2009) 014, [`arXiv:0901.0283`].

[22] D. E. Morrissey, D. Poland, and K. M. Zurek, *Abelian Hidden Sectors at a GeV*, JHEP **0907** (2009) 050, [`arXiv:0904.2567`].

[23] **Muon G-2 Collaboration** Collaboration, G. Bennett et al., *Final Report of the Muon E821 Anomalous Magnetic Moment Measurement at BNL*, Phys.Rev. **D73** (2006) 072003, [`hep-ex/0602035`].

[24] M. Davier, A. Hoecker, B. Malaescu, and Z. Zhang, *Reevaluation of the Hadronic Contributions to the Muon g-2 and to alpha(MZ)*, *Eur.Phys.J.* **C71** (2011) 1515, [arXiv:1010.4180].

[25] M. Pospelov, *Secluded U(1) below the weak scale*, *Phys. Rev.* **D80** (2009) 095002, [arXiv:0811.1030].

[26] C.-Y. Chen, H. Davoudiasl, W. J. Marciano, and C. Zhang, *Implications of a light "dark Higgs" solution to the g-2 discrepancy*, *Phys. Rev.* **D93** (2016), no. 3 035006, [arXiv:1511.0471].

[27] B. W. Lee and S. Weinberg, *Cosmological Lower Bound on Heavy Neutrino Masses*, *Phys. Rev. Lett.* **39** (1977) 165–168.

[28] P. Jean et al., *Early SPI / INTEGRAL measurements of 511 keV line emission from the 4th quadrant of the Galaxy*, *Astron. Astrophys.* **407** (2003) L55, [astro-ph/0309484].

[29] C. Boehm and P. Fayet, *Scalar dark matter candidates*, *Nucl.Phys.* **B683** (2004) 219–263, [hep-ph/0305261].

[30] D. P. Finkbeiner and N. Weiner, *Exciting Dark Matter and the INTEGRAL/SPI 511 keV signal*, *Phys. Rev.* **D76** (2007) 083519, [astro-ph/0702587].

[31] **PAMELA Collaboration** Collaboration, O. Adriani et al., *An anomalous positron abundance in cosmic rays with energies 1.5-100 GeV*, *Nature* **458** (2009) 607–609, [arXiv:0810.4995].

[32] **Fermi-LAT** Collaboration, M. Ackermann et al., *Measurement of separate cosmic-ray electron and positron spectra with the Fermi Large Area Telescope*, *Phys. Rev. Lett.* **108** (2012) 011103, [arXiv:1109.0521].

[33] **AMS** Collaboration, M. Aguilar et al., *First Result from the Alpha Magnetic Spectrometer on the International Space Station: Precision Measurement of the Positron Fraction in Primary Cosmic Rays of 0.5–350 GeV*, *Phys. Rev. Lett.* **110** (2013) 141102.

[34] N. Arkani-Hamed, D. P. Finkbeiner, T. R. Slatyer, and N. Weiner, *A Theory of Dark Matter*, *Phys. Rev.* **D79** (2009) 015014, [arXiv:0810.0713].

[35] M. Pospelov and A. Ritz, *Astrophysical Signatures of Secluded Dark Matter*, *Phys. Lett.* **B671** (2009) 391–397.

[36] H. An, M. B. Wise, and Y. Zhang, *Effects of Bound States on Dark Matter Annihilation*, `arXiv:1604.0177`.

[37] L. Goodenough and D. Hooper, *Possible Evidence For Dark Matter Annihilation In The Inner Milky Way From The Fermi Gamma Ray Space Telescope*, `arXiv:0910.2998`.

[38] **Fermi-LAT** Collaboration, T. A. Porter and S. Murgia, *Observations of High-Energy Gamma-Ray Emission Toward the Galactic Centre with the Fermi Large Area Telescope*, 2015. `arXiv:1507.0468`.

[39] D. Hooper, N. Weiner, and W. Xue, *Dark Forces and Light Dark Matter*, *Phys. Rev.* **D86** (2012) 056009, [`arXiv:1206.2929`].

[40] C. Boehm, M. J. Dolan, C. McCabe, M. Spannowsky, and C. J. Wallace, *Extended gamma-ray emission from Coy Dark Matter*, *JCAP* **1405** (2014) 009, [`arXiv:1401.6458`].

[41] E. Bulbul, M. Markevitch, A. Foster, R. K. Smith, M. Loewenstein, and S. W. Randall, *Detection of An Unidentified Emission Line in the Stacked X-ray spectrum of Galaxy Clusters*, *Astrophys. J.* **789** (2014) 13, [`arXiv:1402.2301`].

[42] A. Boyarsky, O. Ruchayskiy, D. Iakubovskyi, and J. Franse, *Unidentified Line in X-Ray Spectra of the Andromeda Galaxy and Perseus Galaxy Cluster*, *Phys. Rev. Lett.* **113** (2014) 251301, [`arXiv:1402.4119`].

[43] D. P. Finkbeiner and N. Weiner, *An X-Ray Line from eXciting Dark Matter*, `arXiv:1402.6671`.

[44] M. Boylan-Kolchin, J. S. Bullock, and M. Kaplinghat, *The Milky Way's bright satellites as an apparent failure of LCDM*, *Mon. Not. Roy. Astron. Soc.* **422** (2012) 1203–1218, [`arXiv:1111.2048`].

[45] S. Garrison-Kimmel, M. Boylan-Kolchin, J. S. Bullock, and E. N. Kirby, *Too Big to Fail in the Local Group*, *Mon. Not. Roy. Astron. Soc.* **444** (2014), no. 1 222–236, [`arXiv:1404.5313`].

[46] E. J. Tollerud, M. Boylan-Kolchin, and J. S. Bullock, *M31 Satellite Masses Compared to LCDM Subhaloes*, Mon. Not. Roy. Astron. Soc. **440** (2014), no. 4 3511–3519, [`arXiv:1403.6469`].

[47] B. Moore, *Evidence against dissipationless dark matter from observations of galaxy haloes*, Nature **370** (1994) 629.

[48] R. A. Flores and J. R. Primack, *Observational and theoretical constraints on singular dark matter halos*, Astrophys. J. **427** (1994) L1–4, [`astro-ph/9402004`].

[49] A. B. Newman, T. Treu, R. S. Ellis, and D. J. Sand, *The Density Profiles of Massive, Relaxed Galaxy Clusters: II. Separating Luminous and Dark Matter in Cluster Cores*, Astrophys. J. **765** (2013) 25, [`arXiv:1209.1392`].

[50] S.-H. Oh et al., *High-resolution mass models of dwarf galaxies from LITTLE THINGS*, Astron. J. **149** (2015) 180, [`arXiv:1502.0128`].

[51] A. Loeb and N. Weiner, *Cores in Dwarf Galaxies from Dark Matter with a Yukawa Potential*, Phys.Rev.Lett. **106** (2011) 171302, [`arXiv:1011.6374`].

[52] S. Tulin, H.-B. Yu, and K. M. Zurek, *Beyond Collisionless Dark Matter: Particle Physics Dynamics for Dark Matter Halo Structure*, Phys. Rev. **D87** (2013), no. 11 115007, [`arXiv:1302.3898`].

[53] M. Kaplinghat, S. Tulin, and H.-B. Yu, *Dark Matter Halos as Particle Colliders: Unified Solution to Small-Scale Structure Puzzles from Dwarfs to Clusters*, Phys. Rev. Lett. **116** (2016), no. 4 041302, [`arXiv:1508.0333`].

[54] J. S. Bullock, *Notes on the Missing Satellites Problem*, `arXiv:1009.4505`.

[55] P. Gondolo, J. Hisano, and K. Kadota, *The Effect of quark interactions on dark matter kinetic decoupling and the mass of the smallest dark halos*, Phys. Rev. **D86** (2012) 083523, [`arXiv:1205.1914`].

[56] B. Bertoni, S. Ipek, D. McKeen, and A. E. Nelson, *Constraints and consequences of reducing small scale structure via large dark matter-neutrino interactions*, JHEP **04** (2015) 170, [`arXiv:1412.3113`].

[57] T. Bringmann, H. T. Ihle, J. Kersten, and P. Walia, *Suppressing structure formation at dwarf galaxy scales and below: late kinetic decoupling as a compelling alternative to warm dark matter*, `arXiv:1603.0488`.

[58] L. Randall and M. Reece, *Dark Matter as a Trigger for Periodic Comet Impacts*, *Phys. Rev. Lett.* **112** (2014) 161301, [arXiv:1403.0576].

[59] J. Fan, A. Katz, L. Randall, and M. Reece, *Dark-Disk Universe*, *Phys. Rev. Lett.* **110** (2013), no. 21 211302, [arXiv:1303.3271].

[60] Z. Chacko, H.-S. Goh, and R. Harnik, *The Twin Higgs: Natural electroweak breaking from mirror symmetry*, *Phys. Rev. Lett.* **96** (2006) 231802, [hep-ph/0506256].

[61] J. Shelton and K. M. Zurek, *Darkogenesis: A baryon asymmetry from the dark matter sector*, *Phys. Rev.* **D82** (2010) 123512, [arXiv:1008.1997].

[62] B. Echenard, R. Essig, and Y.-M. Zhong, *Projections for Dark Photon Searches at Mu3e*, *JHEP* **01** (2015) 113, [arXiv:1411.1770].

[63] R. Essig, J. Mardon, M. Papucci, T. Volansky, and Y.-M. Zhong, *Constraining Light Dark Matter with Low-Energy $e^+e^-$ Colliders*, *JHEP* **11** (2013) 167, [arXiv:1309.5084].

[64] D. Curtin et al., *Exotic decays of the 125 GeV Higgs boson*, *Phys. Rev.* **D90** (2014), no. 7 075004, [arXiv:1312.4992].

[65] D. Curtin, R. Essig, and Y.-M. Zhong, *Uncovering light scalars with exotic Higgs decays to $b\bar{b}\mu^+\mu^-$*, *JHEP* **06** (2015) 025, [arXiv:1412.4779].

[66] C.-Y. Chen, M. Lefebvre, M. Pospelov, and Y.-M. Zhong, *Diphoton Excess through Dark Mediators*, *JHEP* **07** (2016) 063, [arXiv:1603.0125].

[67] B. Holdom, *Two U(1)'s and Epsilon Charge Shifts*, *Phys.Lett.* **B166** (1986) 196.

[68] P. Galison and A. Manohar, *Two Z's or Not Two Z's?*, *Phys.Lett.* **B136** (1984) 279.

[69] K. R. Dienes, C. F. Kolda, and J. March-Russell, *Kinetic Mixing and the Supersymmetric Gauge Hierarchy*, *Nucl.Phys.* **B492** (1997) 104–118, [hep-ph/9610479].

[70] N. Arkani-Hamed and N. Weiner, *LHC Signals for a SuperUnified Theory of Dark Matter*, *JHEP* **0812** (2008) 104, [arXiv:0810.0714].

[71] R. Essig, J. Kaplan, P. Schuster, and N. Toro, *On the Origin of Light Dark Matter Species*, *Submitted to Physical Review D* (2010) [arXiv:1004.0691].

[72] C. Cheung, J. T. Ruderman, L.-T. Wang, and I. Yavin, *Kinetic Mixing as the Origin of Light Dark Scales*, arXiv:0902.3246.

[73] R. Essig, P. Schuster, and N. Toro, *Probing Dark Forces and Light Hidden Sectors at Low-Energy e+e- Colliders*, Phys. Rev. **D80** (2009) 015003, [arXiv:0903.3941].

[74] J. D. Bjorken, R. Essig, P. Schuster, and N. Toro, *New Fixed-Target Experiments to Search for Dark Gauge Forces*, Phys. Rev. **D80** (2009) 075018.

[75] J. D. Bjorken et al., *Search for Neutral Metastable Penetrating Particles Produced in the SLAC Beam Dump*, Phys. Rev. **D38** (1988) 3375.

[76] E. M. Riordan et al., *A Search for Short Lived Axions in an Electron Beam Dump Experiment*, Phys. Rev. Lett. **59** (1987) 755.

[77] A. Bross et al., *A Search for Shortlived Particles Produced in an Electron Beam Dump*, Phys. Rev. Lett. **67** (1991) 2942–2945.

[78] B. Batell, M. Pospelov, and A. Ritz, *Probing a Secluded U(1) at B-factories*, Phys. Rev. **D79** (2009) 115008.

[79] M. J. Strassler and K. M. Zurek, *Echoes of a Hidden Valley at Hadron Colliders*, Phys.Lett. **B651** (2007) 374–379, [hep-ph/0604261].

[80] M. J. Strassler, *Possible effects of a hidden valley on supersymmetric phenomenology*, hep-ph/0607160.

[81] M. Freytsis, G. Ovanesyan, and J. Thaler, *Dark Force Detection in Low Energy e-p Collisions*, JHEP **1001** (2010) 111, [arXiv:0909.2862].

[82] R. Essig, P. Schuster, N. Toro, and B. Wojtsekhowski, *An Electron Fixed Target Experiment to Search for a New Vector Boson A' Decaying to e+e-*, JHEP **1102** (2011) 009, [arXiv:1001.2557].

[83] J. Blumlein and J. Brunner, *New Exclusion Limits for Dark Gauge Forces from Beam-Dump Data*, Phys.Lett. **B701** (2011) 155–159, [arXiv:1104.2747].

[84] S. Andreas, C. Niebuhr, and A. Ringwald, *New Limits on Hidden Photons from Past Electron Beam Dumps*, Phys.Rev. **D86** (2012) 095019, [arXiv:1209.6083].

[85] M. Reece and L.-T. Wang, *Searching for the Light Dark Gauge Boson in Gev-Scale Experiments*, JHEP **0907** (2009) 051, [arXiv:0904.1743].

[86] **BaBar Collaboration** Collaboration, B. Aubert et al., *Search for Dimuon Decays of a Light Scalar Boson in Radiative Transitions* $\Upsilon \to \gamma A^0$, *Phys.Rev.Lett.* **103** (2009) 081803, [arXiv:0905.4539].

[87] A. Hook, E. Izaguirre, and J. G. Wacker, *Model Independent Bounds on Kinetic Mixing, Adv.High Energy Phys.* **2011** (2011) 859762, [arXiv:1006.0973].

[88] **KLOE-2 Collaboration** Collaboration, D. Babusci et al., *Limit on the production of a light vector gauge boson in phi meson decays with the KLOE detector, Phys.Lett.* **B720** (2013) 111–115, [arXiv:1210.3927].

[89] F. Archilli, D. Babusci, D. Badoni, I. Balwierz, G. Bencivenni, et al., *Search for a vector gauge boson in phi meson decays with the KLOE detector, Phys.Lett.* **B706** (2012) 251–255, [arXiv:1110.0411].

[90] **APEX** Collaboration, S. Abrahamyan et al., *Search for a new gauge boson in the A′ Experiment (APEX), Phys. Rev. Lett.* **107** (2011) 191804, [arXiv:1108.2750].

[91] H. Merkel, P. Achenbach, C. A. Gayoso, T. Beranek, J. Bericic, et al., *Search for light massive gauge bosons as an explanation of the* $(g-2)_\mu$ *anomaly at MAMI,* arXiv:1404.5502.

[92] J. B. Dent, F. Ferrer, and L. M. Krauss, *Constraints on Light Hidden Sector Gauge Bosons from Supernova Cooling,* arXiv:1201.2683.

[93] H. Davoudiasl, H.-S. Lee, and W. J. Marciano, *Dark Side of Higgs Diphoton Decays and Muon g-2, Phys.Rev.* **D86** (2012) 095009, [arXiv:1208.2973].

[94] H. Davoudiasl, H.-S. Lee, and W. J. Marciano, *'Dark' Z implications for Parity Violation, Rare Meson Decays, and Higgs Physics, Phys.Rev.* **D85** (2012) 115019, [arXiv:1203.2947].

[95] H. Davoudiasl, H.-S. Lee, I. Lewis, and W. J. Marciano, *Higgs Decays as a Window into the Dark Sector,* arXiv:1304.4935.

[96] M. Endo, K. Hamaguchi, and G. Mishima, *Constraints on Hidden Photon Models from Electron g-2 and Hydrogen Spectroscopy, Phys.Rev.* **D86** (2012) 095029, [arXiv:1209.2558].

[97] J. Balewski, J. Bernauer, W. Bertozzi, J. Bessuille, B. Buck, et al., *DarkLight: A Search for Dark Forces at the Jefferson Laboratory Free-Electron Laser Facility,* arXiv:1307.4432.

[98] **WASA-at-COSY Collaboration** Collaboration, P. Adlarson et al., *Search for a dark photon in the $\pi^0 \to e^+e^-\gamma$ decay, Phys.Lett.* **B726** (2013) 187–193, [arXiv:1304.0671].

[99] **HADES** Collaboration, G. Agakishiev et al., *Searching a Dark Photon with HADES, Phys.Lett.* **B731** (2014) 265–271, [arXiv:1311.0216].

[100] S. Andreas, S. Donskov, P. Crivelli, A. Gardikiotis, S. Gninenko, et al., *Proposal for an Experiment to Search for Light Dark Matter at the SPS*, arXiv:1312.3309.

[101] M. Battaglieri, S. Boyarinov, S. Bueltmann, V. Burkert, A. Celentano, et al., *The Heavy Photon Search Test Detector*, arXiv:1406.6115.

[102] **BaBar** Collaboration, J. Lees et al., *Search for a dark photon in e+e- collisions at BABAR*, arXiv:1406.2980.

[103] A. Adare, S. Afanasiev, C. Aidala, N. Ajitanand, Y. Akiba, et al., *Closing the Door for Dark Photons as the Explanation for the Muon g-2 Anomaly*, arXiv:1409.0851.

[104] D. Kazanas, R. N. Mohapatra, S. Nussinov, V. Teplitz, and Y. Zhang, *Supernova Bounds on the Dark Photon Using its Electromagnetic Decay*, arXiv:1410.0221.

[105] J. Blümlein and J. Brunner, *New Exclusion Limits on Dark Gauge Forces from Proton Bremsstrahlung in Beam-Dump Data, Phys. Lett.* **B731** (2014) 320–326, [arXiv:1311.3870].

[106] **CERN NA48/2** Collaboration, C. N. Collaboration, *Search for the dark photon in $\pi^0$ decays*, arXiv:1504.0060.

[107] **ATLAS** Collaboration, G. Aad et al., *Observation of a new particle in the search for the Standard Model Higgs boson with the ATLAS detector at the LHC, Phys.Lett.* **B716** (2012) 1–29, [arXiv:1207.7214].

[108] **CMS** Collaboration, S. Chatrchyan et al., *Observation of a new boson at a mass of 125 GeV with the CMS experiment at the LHC, Phys.Lett.* **B716** (2012) 30–61, [arXiv:1207.7235].

[109] **CMS** Collaboration, *Combination of standard model Higgs boson searches and measurements of the properties of the new boson with a mass near 125 GeV*, .

[110] **ATLAS** Collaboration, *Combined coupling measurements of the Higgs-like boson with the ATLAS detector using up to 25 $fb^{-1}$ of proton-proton collision data*, .

[111] D. E. Morrissey and M. J. Ramsey-Musolf, *Electroweak baryogenesis*, *New J.Phys.* **14** (2012) 125003, [`arXiv:1206.2942`].

[112] M. J. Strassler and K. M. Zurek, *Discovering the Higgs through highly-displaced vertices*, *Phys.Lett.* **B661** (2008) 263–267, [`hep-ph/0605193`].

[113] A. Djouadi, *The Anatomy of Electro-Weak Symmetry Breaking. II: The Higgs bosons in the Minimal Supersymmetric Model*, *arXiv* **hep-ph** (Mar, 2005) [`hep-ph/0503173v2`].

[114] A. Djouadi, *The Anatomy of Electro-Weak Symmetry Breaking. I: The Higgs boson in the Standard Model*, *arXiv* **hep-ph** (Mar, 2005) [`hep-ph/0503172v2`].

[115] J. Gunion, H. Haber, G. Kane, and S. Dawson, *The Higgs Hunter's Guide*. Frontiers in Physics, V. 80. Perseus Pub., 2000.

[116] R. Dermisek and J. F. Gunion, *New constraints on a light CP-odd Higgs boson and related NMSSM Ideal Higgs Scenarios*, *Phys.Rev.* **D81** (2010) 075003, [`arXiv:1002.1971`].

[117] B. Echenard, *Search for Light New Physics at B Factories*, *Adv.High Energy Phys.* **2012** (2012) 514014, [`arXiv:1209.1143`].

[118] **BaBar Collaboration** Collaboration, J. Lees et al., *Search for a Low-Mass Scalar Higgs Boson Decaying to a Tau Pair in Single-Photon Decays of Upsilon(1S)*, `arXiv:1210.5669`.

[119] D. McKeen, *Constraining Light Bosons with Radiative Upsilon(1S) Decays*, *Phys.Rev.* **D79** (2009) 015007, [`arXiv:0809.4787`].

[120] M. Lisanti and J. G. Wacker, *Discovering the Higgs with Low Mass Muon Pairs*, *Phys.Rev.* **D79** (2009) 115006, [`arXiv:0903.1377`].

[121] H. E. Haber and G. L. Kane, *The Search for Supersymmetry: Probing Physics Beyond the Standard Model*, *Phys.Rept.* **117** (1985) 75–263.

[122] J. E. Kim, *Light Pseudoscalars, Particle Physics and Cosmology*, *Phys.Rept.* **150** (1987) 1–177.

[123] R. Peccei and H. R. Quinn, *CP Conservation in the Presence of Instantons*, *Phys.Rev.Lett.* **38** (1977) 1440–1443.

[124] M. Trodden, *Electroweak baryogenesis: A Brief review*, `hep-ph/9805252`.

[125] G. Branco, P. Ferreira, L. Lavoura, M. Rebelo, M. Sher, et al., *Theory and phenomenology of two-Higgs-doublet models*, *Phys.Rept.* **516** (2012) 1–102, [`arXiv:1106.0034`].

[126] C.-Y. Chen, M. Freid, and M. Sher, *The Next-to-Minimal Two Higgs Doublet Model*, `arXiv:1312.3949`.

[127] A. Dery, A. Efrati, G. Hiller, Y. Hochberg, and Y. Nir, *Higgs couplings to fermions: 2HDM with MFV*, *JHEP* **1308** (2013) 006, [`arXiv:1304.6727`].

[128] W. Altmannshofer, S. Gori, and G. D. Kribs, *A Minimal Flavor Violating 2HDM at the LHC*, *Phys.Rev.* **D86** (2012) 115009, [`arXiv:1210.2465`].

[129] N. Craig, J. A. Evans, R. Gray, C. Kilic, M. Park, et al., *Multi-Lepton Signals of Multiple Higgs Bosons*, *JHEP* **1302** (2013) 033, [`arXiv:1210.0559`].

[130] J. Gunion, B. Grzadkowski, H. Haber, and J. Kalinowski, *LEP limits on CP violating nonminimal Higgs sectors*, *Phys.Rev.Lett.* **79** (1997) 982–985, [`hep-ph/9704410`].

[131] G. Belanger, B. Dumont, U. Ellwanger, J. Gunion, and S. Kraml, *Global fit to Higgs signal strengths and couplings and implications for extended Higgs sectors*, `arXiv:1306.2941`.

[132] P. Ferreira, R. Santos, M. Sher, and J. P. Silva, *Could the LHC two-photon signal correspond to the heavier scalar in two-Higgs-doublet models?*, *Phys.Rev.* **D85** (2012) 035020, [`arXiv:1201.0019`].

[133] D. S. Alves, P. J. Fox, and N. J. Weiner, *Higgs Signals in a Type I 2HDM or with a Sister Higgs*, `arXiv:1207.5499`.

[134] P. M. Ferreira, R. Santos, M. Sher, and J. P. Silva, *Implications of the LHC two-photon signal for two-Higgs-doublet models*, *arXiv* **hep-ph** (Dec, 2011) [`arXiv:1112.3277`].

[135] N. Craig and S. Thomas, *Exclusive Signals of an Extended Higgs Sector*, *JHEP* **1211** (2012) 083, [`arXiv:1207.4835`].

[136] N. Craig and A. Katz, *A Supersymmetric Higgs Sector with Chiral D-terms*, *JHEP* **1305** (2013) 015, [`arXiv:1212.2635`].

[137] Y. Bai, V. Barger, L. L. Everett, and G. Shaughnessy, *The 2HDM-X and Large Hadron Collider Data*, Phys.Rev. **D87** (2013) 115013, [`arXiv:1210.4922`].

[138] A. Azatov and J. Galloway, *Electroweak Symmetry Breaking and the Higgs Boson: Confronting Theories at Colliders*, Int.J.Mod.Phys. **A28** (2013) 1330004, [`arXiv:1212.1380`].

[139] B. A. Dobrescu and J. D. Lykken, *Coupling spans of the Higgs-like boson*, JHEP **1302** (2013) 073, [`arXiv:1210.3342`].

[140] C.-Y. Chen and S. Dawson, *Exploring Two Higgs Doublet Models Through Higgs Production, arXiv* **hep-ph** (Jan, 2013) [`arXiv:1301.0309`]. 21 pages, 13 figures; matches published version.

[141] M. Baumgart and A. Katz, *Implications of a New Light Scalar Near the Bottomonium Regime*, JHEP **1208** (2012) 133, [`arXiv:1204.6032`].

[142] D. Curtin, R. Essig, S. Gori, and J. Shelton, *Illuminating Dark Photons with High-Energy Colliders*, JHEP **02** (2015) 157, [`arXiv:1412.0018`].

[143] R. Essig, R. Harnik, J. Kaplan, and N. Toro, *Discovering New Light States at Neutrino Experiments*, Phys.Rev. **D82** (2010) 113008, [`arXiv:1008.0636`].

[144] A. Blondel, A. Bravar, M. Pohl, S. Bachmann, N. Berger, et al., *Research Proposal for an Experiment to Search for the Decay $\mu \to eee$*, `arXiv:1301.6113`.

[145] R. M. Djilkibaev and R. V. Konoplich, *Rare Muon Decay $\mu^+ \to e^+ e^- e^+ \nu_e \bar{\nu}_\mu$*, Phys.Rev. **D79** (2009) 073004, [`arXiv:0812.1355`].

[146] J. Alwall, R. Frederix, S. Frixione, V. Hirschi, F. Maltoni, et al., *The automated computation of tree-level and next-to-leading order differential cross sections, and their matching to parton shower simulations*, JHEP **1407** (2014) 079, [`arXiv:1405.0301`].

[147] **Particle Data Group** Collaboration, K. Olive et al., *Review of Particle Physics (RPP)*, Chin.Phys. **C38** (2014) 090001.

[148] **SuperB Collaboration** Collaboration, M. Baszczyk et al., *SuperB Technical Design Report*, `arXiv:1306.5655`.

[149] **BaBar Collaboration** Collaboration, B. Aubert et al., *The BaBar detector*, Nucl.Instrum.Meth. **A479** (2002) 1–116, [`hep-ex/0105044`].

[150] **BABAR** Collaboration, B. Aubert et al., *The BABAR Detector: Upgrades, Operation and Performance*, *Nucl.Instrum.Meth.* **A729** (2013) 615–701, [`arXiv:1305.3560`].

[151] Y. Kuno and Y. Okada, *Muon decay and physics beyond the standard model*, *Rev.Mod.Phys.* **73** (2001) 151–202, [`hep-ph/9909265`].

[152] R. Essig et al., *Working Group Report: New Light Weakly Coupled Particles*, in *Community Summer Study 2013: Snowmass on the Mississippi (CSS2013) Minneapolis, MN, USA, July 29-August 6, 2013*, 2013. `arXiv:1311.0029`.

[153] J. Goodman, M. Ibe, A. Rajaraman, W. Shepherd, T. M. Tait, et al., *Constraints on Dark Matter from Colliders*, *Phys.Rev.* **D82** (2010) 116010, [`arXiv:1008.1783`].

[154] M. Beltran, D. Hooper, E. W. Kolb, Z. A. Krusberg, and T. M. Tait, *Maverick Dark Matter at Colliders*, *JHEP* **1009** (2010) 037, [`arXiv:1002.4137`].

[155] Y. Bai, P. J. Fox, and R. Harnik, *The Tevatron at the Frontier of Dark Matter Direct Detection*, *JHEP* **1012** (2010) 048, [`arXiv:1005.3797`].

[156] J. Goodman, M. Ibe, A. Rajaraman, W. Shepherd, T. M. Tait, et al., *Constraints on Light Majorana Dark Matter from Colliders*, *Phys.Lett.* **B695** (2011) 185–188, [`arXiv:1005.1286`].

[157] P. J. Fox, R. Harnik, J. Kopp, and Y. Tsai, *Lep Shines Light on Dark Matter*, *Phys.Rev.* **D84** (2011) 014028, [`arXiv:1103.0240`].

[158] A. Rajaraman, W. Shepherd, T. M. Tait, and A. M. Wijangco, *Lhc Bounds on Interactions of Dark Matter*, *Phys.Rev.* **D84** (2011) 095013, [`arXiv:1108.1196`].

[159] P. J. Fox, R. Harnik, J. Kopp, and Y. Tsai, *Missing Energy Signatures of Dark Matter at the LHC*, *Phys.Rev.* **D85** (2012) 056011, [`arXiv:1109.4398`].

[160] P. J. Fox, R. Harnik, R. Primulando, and C.-T. Yu, *Taking a Razor to Dark Matter Parameter Space at the Lhc*, *Phys.Rev.* **D86** (2012) 015010, [`arXiv:1203.1662`].

[161] **CMS** Collaboration, S. Chatrchyan et al., *Search for Dark Matter and Large Extra Dimensions in pp Collisions Yielding a Photon and Missing Transverse Energy*, *Phys.Rev.Lett.* **108** (2012) 261803, [`arXiv:1204.0821`].

[162] **ATLAS Collaboration** Collaboration, G. Aad et al., *Search for dark matter candidates and large extra dimensions in events with a photon and missing transverse momentum in pp collision data at $\sqrt{s} = 7$ TeV with the ATLAS detector*, *Phys.Rev.Lett.* **110** (2013) 011802, [`arXiv:1209.4625`].

[163] H. An, R. Huo, and L.-T. Wang, *Searching for Low Mass Dark Portal at the LHC*, *Phys.Dark Univ.* **2** (2013) 50–57, [`arXiv:1212.2221`].

[164] P. J. Fox and C. Williams, *Next-to-Leading Order Predictions for Dark Matter Production at Hadron Colliders*, *Phys.Rev.* **D87** (2013) 054030, [`arXiv:1211.6390`].

[165] N. Zhou, D. Berge, and D. Whiteson, *Mono-everything: combined limits on dark matter production at colliders from multiple final states*, `arXiv:1302.3619`.

[166] E. A. Baltz, M. Battaglia, M. E. Peskin, and T. Wizansky, *Determination of dark matter properties at high-energy colliders*, *Phys.Rev.* **D74** (2006) 103521, [`hep-ph/0602187`].

[167] H. K. Dreiner, O. Kittel, and U. Langenfeld, *Discovery potential of radiative neutralino production at the ILC*, *Phys.Rev.* **D74** (2006) 115010, [`hep-ph/0610020`].

[168] H. K. Dreiner, O. Kittel, and U. Langenfeld, *The Role of Beam polarization for Radiative Neutralino Production at the ILC*, *Eur.Phys.J.* **C54** (2008) 277–284, [`hep-ph/0703009`].

[169] H. K. Dreiner, S. Heinemeyer, O. Kittel, U. Langenfeld, A. M. Weber, et al., *Mass Bounds on a Very Light Neutralino*, *Eur.Phys.J.* **C62** (2009) 547–572, [`arXiv:0901.3485`].

[170] C. Bird, P. Jackson, R. V. Kowalewski, and M. Pospelov, *Search for Dark Matter in B -¿ S Transitions with Missing Energy*, *Phys.Rev.Lett.* **93** (2004) 201803, [`hep-ph/0401195`].

[171] B. McElrath, *Invisible Quarkonium Decays as a Sensitive Probe of Dark Matter*, *Phys.Rev.* **D72** (2005) 103508, [`hep-ph/0506151`].

[172] P. Fayet, *Constraints on Light Dark Matter and U Bosons, from Psi, Upsilon, K+, Pi0, Eta and Eta-Prime Decays*, *Phys.Rev.* **D74** (2006) 054034, [`hep-ph/0607318`].

[173] C. Bird, R. V. Kowalewski, and M. Pospelov, *Dark Matter Pair-Production in B -¿ S Transitions*, *Mod.Phys.Lett.* **A21** (2006) 457–478, [`hep-ph/0601090`].

[174] **CLEO Collaboration** Collaboration, P. Rubin et al., *Search for Invisible Decays of the Upsilon(1S) Resonance*, *Phys.Rev.* **D75** (2007) 031104, [`hep-ex/0612051`].

[175] **Belle Collaboration** Collaboration, O. Tajima et al., *Search for invisible decay of the Upsilon(1S)*, *Phys.Rev.Lett.* **98** (2007) 132001, [`hep-ex/0611041`].

[176] Y. Kahn, M. Schmitt, and T. M. Tait, *Enhanced rare pion decays from a model of MeV dark matter*, *Phys.Rev.* **D78** (2008) 115002, [`arXiv:0712.0007`].

[177] A. E. Dorokhov and M. A. Ivanov, *Rare decay pi0 → e + e−: Theory confronts KTeV data*, *Phys.Rev.* **D75** (2007) 114007, [`arXiv:0704.3498`].

[178] P. Fayet, *U-boson production in e+ e- annihilations, psi and Upsilon decays, and Light Dark Matter*, *Phys.Rev.* **D75** (2007) 115017, [`hep-ph/0702176`].

[179] P. Fayet, *Invisible Upsilon decays into Light Dark Matter*, *Phys.Rev.* **D81** (2010) 054025, [`arXiv:0910.2587`].

[180] G. K. Yeghiyan, *Upsilon Decays into Light Scalar Dark Matter*, *Phys.Rev.* **D80** (2009) 115019, [`arXiv:0909.4919`].

[181] A. Dorokhov, M. Ivanov, and S. Kovalenko, *Complete structure dependent analysis of the decay P -¿ l+ l-*, *Phys.Lett.* **B677** (2009) 145–149, [`arXiv:0903.4249`].

[182] **BaBar Collaboration** Collaboration, P. del Amo Sanchez et al., *Search for Production of Invisible Final States in Single-Photon Decays of Upsilon(1S)*, *Phys.Rev.Lett.* **107** (2011) 021804, [`arXiv:1007.4646`].

[183] A. Badin and A. A. Petrov, *Searching for light Dark Matter in heavy meson decays*, *Phys.Rev.* **D82** (2010) 034005, [`arXiv:1005.1277`].

[184] B. Echenard, *Search for Low-Mass Dark Matter at BABAR*, *Mod.Phys.Lett.* **A27** (2012) 1230016, [`arXiv:1205.3505`].

[185] G. Calderini, *Search for Physics Beyond the Standard Model at BaBar and Belle*, *EPJ Web Conf.* **28** (2012) 04005, [`arXiv:1204.4281`].

[186] N. Borodatchenkova, D. Choudhury, and M. Drees, *Probing MeV Dark Matter at Low-Energy E+E- Colliders*, *Phys.Rev.Lett.* **96** (2006) 141802, [`hep-ph/0510147`].

[187] **BaBar Collaboration** Collaboration, B. Aubert et al., *Search for Invisible Decays of a Light Scalar in Radiative Transitions* $\Upsilon_{3S} \to \gamma$ *A0*, `arXiv:0808.0017`.

[188] J. Hewett, H. Weerts, R. Brock, J. Butler, B. Casey, et al., *Fundamental Physics at the Intensity Frontier*, `arXiv:1205.2671`.

[189] **BaBar Collaboration** Collaboration, J. Lees et al., *Time-Integrated Luminosity Recorded by the BABAR Detector at the PEP-II e+e- Collider*, `arXiv:1301.2703`.

[190] J. Alwall, M. Herquet, F. Maltoni, O. Mattelaer, and T. Stelzer, *MadGraph 5 : Going Beyond, JHEP* **1106** (2011) 128, [`arXiv:1106.0522`].

[191] **Belle II Collaboration** Collaboration, T. Abe, *Belle II Technical Design Report*, `arXiv:1011.0352`.

[192] **Belle II Collaboration** Collaboration, L. Piilonen, "Status and Prospects of SuperKEKB/Belle II." talk given at BNL Forum 2013.

[193] **BaBar Collaboration** Collaboration, J. Lees et al., *Study of Radiative Bottomonium Transitions Using Converted Photons, Phys.Rev.* **D84** (2011) 072002, [`arXiv:1104.5254`].

[194] P. deNiverville, M. Pospelov, and A. Ritz, *Observing a light dark matter beam with neutrino experiments, Phys.Rev.* **D84** (2011) 075020, [`arXiv:1107.4580`].

[195] **BES Collaboration** Collaboration, M. Ablikim et al., *Search for the invisible decay of J / psi in psi(2S) — pi+ pi- J / psi, Phys.Rev.Lett.* **100** (2008) 192001, [`arXiv:0710.0039`].

[196] **MiniBooNE Collaboration** Collaboration, R. Dharmapalan et al., *Low Mass WIMP Searches with a Neutrino Experiment: A Proposal for Further MiniBooNE Running*, `arXiv:1211.2258`.

[197] **E787 Collaboration** Collaboration, S. Adler et al., *Further search for the decay K+ -¿ pi+ nu anti-nu in the momentum region P ¡ 195 MeV/c, Phys.Rev.* **D70** (2004) 037102, [`hep-ex/0403034`].

[198] **E949 Collaboration** Collaboration, A. Artamonov et al., *New measurement of the $K^+ \to \pi^+\nu\bar{\nu}$ branching ratio, Phys.Rev.Lett.* **101** (2008) 191802, [`arXiv:0808.2459`].

[199] J. Brod, M. Gorbahn, and E. Stamou, *Two-Loop Electroweak Corrections for the $K- > \pi\nu\bar{n}u$ Decays, Phys.Rev.* **D83** (2011) 034030, [`arXiv:1009.0947`].

[200] **BNL-E949 Collaboration** Collaboration, A. Artamonov et al., *Study of the decay K+ -¿ pi+ nu anti-nu in the momentum region 140 ¡ P(pi) ¡ 199 MeV/c, Phys.Rev.* **D79** (2009) 092004, [arXiv:0903.0030].

[201] G. D'Ambrosio, G. Ecker, G. Isidori, and J. Portoles, *The Decays K -¿ pi l+ l- beyond leading order in the chiral expansion, JHEP* **9808** (1998) 004, [hep-ph/9808289].

[202] **E. T. Worcester for the ORKA collaboration** Collaboration, *ORKA, The Golden Kaon Experiment: Precision measurement of K+ -¿ pi+nunubar and other rare processes*, arXiv:1305.7245.

[203] **ORKA Collaboration** Collaboration, D. Bryman, "ORKA at Fermilab: Seeking New Physics with Measurements of the "Golden Kaon" Decay $K^+ \to \pi^+ \bar{\nu}\nu$." talk given at Argonne Intensity Frontier Workshop, April 2013.

[204] **NA62** Collaboration, "2013 NA62 status report to the CERN SPSC."

[205] T. Aoyama, M. Hayakawa, T. Kinoshita, and M. Nio, *Tenth-Order QED Contribution to the Electron g-2 and an Improved Value of the Fine Structure Constant, Phys.Rev.Lett.* **109** (2012) 111807, [arXiv:1205.5368].

[206] R. Bouchendira, P. Cladé, S. Guellati-Khélifa, F. Nez, and F. Biraben, *New Determination of the Fine Structure Constant and Test of the Quantum Electrodynamics, Physical Review Letters* **106** (Feb., 2011) 080801, [arXiv:1012.3627].

[207] D. Hanneke, S. Fogwell, and G. Gabrielse, *New Measurement of the Electron Magnetic Moment and the Fine Structure Constant, Physical Review Letters* **100** (Mar., 2008) 120801, [arXiv:0801.1134].

[208] B. Batell, M. Pospelov, and A. Ritz, *Exploring Portals to a Hidden Sector Through Fixed Targets, Phys.Rev.* **D80** (2009) 095024, [arXiv:0906.5614].

[209] **BABAR** Collaboration, B. Aubert et al., *Search for a Narrow Resonance in e+e- to Four Lepton Final States*, 0908.2821.

[210] F. Bossi, *The role of KLOE and KLOE-2 in the search for a secluded gauge sector*, arXiv:0904.3815.

[211] e.g. https://confluence.slac.stanford.edu/display/hpsg/.

[212] **A1** Collaboration, H. Merkel et al., *Search for Light Gauge Bosons of the Dark Sector at the Mainz Microtron, Phys. Rev. Lett.* **106** (2011) 251802.

[213] F. Archilli et al., *U boson searches at KLOE*, `1107.2531`.

[214] **DarkLight Collaboration** Collaboration, G. Bennett et al., *A proposal for the DarkLight experiment at the Jefferson Laboratory Free Electron Laser*, .

[215] B. Wojtsekhowski, D. Nikolenko, and I. Rachek, *Searching for a new force at VEPP-3*, `arXiv:1207.5089`.

[216] Y. Kahn and J. Thaler, *Searching for an invisible A' vector boson with DarkLight, Phys.Rev.* **D86** (2012) 115012, [`arXiv:1209.0777`].

[217] P. deNiverville, D. McKeen, and A. Ritz, *Signatures of sub-GeV dark matter beams at neutrino experiments, Phys.Rev.* **D86** (2012) 035022, [`arXiv:1205.3499`].

[218] S. Davidson, S. Hannestad, and G. Raffelt, *Updated bounds on millicharged particles, JHEP* **0005** (2000) 003, [`hep-ph/0001179`].

[219] H. K. Dreiner, J.-F. Fortin, C. Hanhart, and L. Ubaldi, *Supernovae Constraints on Dark Forces*, .

[220] H. K. Dreiner, J.-F. Fortin, J. Isern, and L. Ubaldi, *White Dwarfs constrain Dark Forces, Phys.Rev.* **D88** (2013) 043517, [`arXiv:1303.7232`].

[221] R. Essig, J. Mardon, and T. Volansky, *Direct Detection of Sub-Gev Dark Matter, Phys.Rev.* **D85** (2012) 076007, [`arXiv:1108.5383`].

[222] R. Essig, A. Manalaysay, J. Mardon, P. Sorensen, and T. Volansky, *First Direct Detection Limits on Sub-Gev Dark Matter from Xenon10, Phys.Rev.Lett.* **109** (2012) 021301, [`arXiv:1206.2644`].

[223] M. F. Altmann, G. Angloher, M. Bruckmayer, C. Bucci, S. Cooper, et al., *Results and plans of the CRESST dark matter search*, `astro-ph/0106314`.

[224] **DAMIC Collaboration** Collaboration, J. Barreto et al., *Direct Search for Low Mass Dark Matter Particles with CCDs, Phys.Lett.* **B711** (2012) 264–269, [`arXiv:1105.5191`].

[225] S. Gopalakrishna, S. Jung, and J. D. Wells, *Higgs boson decays to four fermions through an abelian hidden sector, Phys.Rev.* **D78** (2008) 055002, [`arXiv:0801.3456`].

[226] J. Jaeckel, M. Jankowiak, and M. Spannowsky, *LHC probes the hidden sector*, *Phys. Dark Univ.* **2** (2013) 111–117, [`arXiv:1212.3620`].

[227] C.-F. Chang, E. Ma, and T.-C. Yuan, *Multilepton Higgs Decays through the Dark Portal*, `arXiv:1308.6071`.

[228] A. Falkowski and R. Vega-Morales, *Exotic Higgs decays in the golden channel*, *JHEP* **12** (2014) 037, [`arXiv:1405.1095`].

[229] J. M. Cline, G. Dupuis, Z. Liu, and W. Xue, *The windows for kinetically mixed Z'-mediated dark matter and the galactic center gamma ray excess*, *JHEP* **08** (2014) 131, [`arXiv:1405.7691`].

[230] I. Hoenig, G. Samach, and D. Tucker-Smith, *Searching for dilepton resonances below the Z mass at the LHC*, *Phys. Rev.* **D90** (2014), no. 7 075016, [`arXiv:1408.1075`].

[231] U. Ellwanger, J. F. Gunion, C. Hugonie, and S. Moretti, *Towards a no lose theorem for NMSSM Higgs discovery at the LHC*, `hep-ph/0305109`.

[232] U. Ellwanger, J. F. Gunion, and C. Hugonie, *Difficult scenarios for NMSSM Higgs discovery at the LHC*, *JHEP* **0507** (2005) 041, [`hep-ph/0503203`].

[233] J. Cao, F. Ding, C. Han, J. M. Yang, and J. Zhu, *A light Higgs scalar in the NMSSM confronted with the latest LHC Higgs data*, *JHEP* **1311** (2013) 018, [`arXiv:1309.4939`].

[234] K. Cheung, J. Song, and Q.-S. Yan, *Role of $h \to \eta\eta$ in Intermediate-Mass Higgs Boson Searches at the Large Hadron Collider*, *Phys.Rev.Lett.* **99** (2007) 031801, [`hep-ph/0703149`].

[235] M. Carena, T. Han, G.-Y. Huang, and C. E. Wagner, *Higgs Signal for $h \to aa$ at Hadron Colliders*, *JHEP* **0804** (2008) 092, [`arXiv:0712.2466`].

[236] D. E. Kaplan and M. McEvoy, *Associated Production of Non-Standard Higgs Bosons at the LHC*, *Phys.Rev.* **D83** (2011) 115004, [`arXiv:1102.0704`].

[237] N. Adam, T. Aziz, J. Andersen, A. Belyaev, T. Binoth, et al., *Higgs Working Group Summary Report*, `arXiv:0803.1154`.

[238] A. Belyaev, S. Hesselbach, S. Lehti, S. Moretti, A. Nikitenko, et al., *The Scope of the $4\tau$ Channel in Higgs-strahlung and Vector Boson Fusion for the NMSSM No-Lose Theorem at the LHC*, `arXiv:0805.3505`.

[239] C. Englert, T. S. Roy, and M. Spannowsky, *Ditau Jets in Higgs searches, Phys.Rev.* **D84** (2011) 075026, [`arXiv:1106.4545`].

[240] **D0** Collaboration, V. Abazov et al., *Search for NMSSM Higgs Bosons in the* $h \to aa \to \mu\mu\,\mu\mu,\ \mu\mu\,\tau\tau$ *Channels Using* $p\bar{p}$ *Collisions at* $\sqrt{s} = 1.96$ *TeV*, *Phys.Rev.Lett.* **103** (2009) 061801, [`arXiv:0905.3381`].

[241] **CMS** Collaboration, S. Chatrchyan et al., *Search for a Non-Standard-Model Higgs Boson Decaying to a Pair of New Light Bosons in Four-Muon Final States*, `arXiv:1210.7619`.

[242] **CMS** Collaboration, S. Chatrchyan et al., *Search for Light Resonances Decaying into Pairs of Muons as a Signal of New Physics*, *JHEP* **1107** (2011) 098, [`arXiv:1106.2375`].

[243] **CMS** Collaboration, C. Collaboration, *Search for a non-standard-model Higgs boson decaying to a pair of new light bosons in four-muon final states*, .

[244] S. Chang, P. J. Fox, and N. Weiner, *Naturalness and Higgs Decays in the MSSM with a Singlet*, *JHEP* **0608** (2006) 068, [`hep-ph/0511250`].

[245] R. Dermisek and J. F. Gunion, *Escaping the Large Fine Tuning and Little Hierarchy Problems in the Next to Minimal Supersymmetric Model and* $h \to aa$ *Decays*, *Phys.Rev.Lett.* **95** (2005) 041801, [`hep-ph/0502105`].

[246] R. Dermisek and J. F. Gunion, *The NMSSM Solution to the Fine-Tuning Problem, Precision Electroweak Constraints and the Largest LEP Higgs Event Excess*, *Phys. Rev.* **D76** (2007) 095006, [`arXiv:0705.4387`].

[247] U. Ellwanger, C. Hugonie, and A. M. Teixeira, *The Next-to-Minimal Supersymmetric Standard Model*, *Phys.Rept.* **496** (2010) 1–77, [`arXiv:0910.1785`].

[248] M. J. Strassler, *Why Unparticle Models with Mass Gaps are Examples of Hidden Valleys*, `arXiv:0801.0629`.

[249] B. Coleppa, F. Kling, and S. Su, *Exotic Decays Of A Heavy Neutral Higgs Through HZ/AZ Channel*, *JHEP* **09** (2014) 161, [`arXiv:1404.1922`].

[250] A. Djouadi, *The Anatomy of electro-weak symmetry breaking. II. The Higgs bosons in the minimal supersymmetric model*, *Phys. Rept.* **459** (2008) 1–241, [`hep-ph/0503173`].

[251] A. Djouadi, *The Anatomy of electro-weak symmetry breaking. I: The Higgs boson in the standard model*, *Phys. Rept.* **457** (2008) 1–216, [hep-ph/0503172].

[252] J. Bernon, J. F. Gunion, Y. Jiang, and S. Kraml, *Light Higgs bosons in Two-Higgs-Doublet Models*, *Phys. Rev.* **D91** (2015), no. 7 075019, [arXiv:1412.3385].

[253] B. A. Dobrescu and K. T. Matchev, *Light Axion Within the Next-to-Minimal Supersymmetric Standard Model*, *JHEP* **0009** (2000) 031, [hep-ph/0008192].

[254] R. Dermisek and J. F. Gunion, *The NMSSM Close to the R-symmetry Limit and Naturalness in h → aa Decays for m_a < 2m_b*, *Phys.Rev.* **D75** (2007) 075019, [hep-ph/0611142].

[255] D. E. Morrissey and A. Pierce, *Modified Higgs Boson Phenomenology from Gauge or Gaugino Mediation in the NMSSM*, *Phys.Rev.* **D78** (2008) 075029, [arXiv:0807.2259].

[256] R. Peccei and H. R. Quinn, *Constraints Imposed by CP Conservation in the Presence of Instantons*, *Phys.Rev.* **D16** (1977) 1791–1797.

[257] E. Chun, *Natural mu term with Peccei-Quinn symmetry*, *Phys.Lett.* **B348** (1995) 111–114, [hep-ph/9411290].

[258] L. J. Hall and T. Watari, *Electroweak supersymmetry with an approximate U(1)(PQ)*, *Phys.Rev.* **D70** (2004) 115001, [hep-ph/0405109].

[259] D. G. Cerdeno, P. Ghosh, and C. B. Park, *Probing the two light Higgs scenario in the NMSSM with a low-mass pseudoscalar*, *JHEP* **06** (2013) 031, [arXiv:1301.1325].

[260] N. D. Christensen, T. Han, Z. Liu, and S. Su, *Low-Mass Higgs Bosons in the NMSSM and Their LHC Implications*, *JHEP* **1308** (2013) 019, [arXiv:1303.2113].

[261] J. Kozaczuk and S. Profumo, *Light NMSSM Neutralino Dark Matter in the Wake of CDMS II and a 126 GeV Higgs*, arXiv:1308.5705.

[262] U. Ellwanger and C. Hugonie, *The semi-constrained NMSSM satisfying bounds from the LHC, LUX and Planck*, *JHEP* **08** (2014) 046, [arXiv:1405.6647].

[263] N.-E. Bomark, S. Moretti, S. Munir, and L. Roszkowski, *A light NMSSM pseudoscalar Higgs boson at the LHC redux*, *JHEP* **02** (2015) 044, [arXiv:1409.8393].

[264] L. J. Hall, D. Pinner, and J. T. Ruderman, *A Natural SUSY Higgs Near 126 GeV*, *JHEP* **1204** (2012) 131, [`arXiv:1112.2703`].

[265] M. Badziak, M. Olechowski, and S. Pokorski, *New Regions in the NMSSM with a 125 GeV Higgs*, *JHEP* **1306** (2013) 043, [`arXiv:1304.5437`].

[266] D. Curtin, J. Galloway, and J. G. Wacker, *Measuring the t̄th coupling from same-sign dilepton +2b measurements*, *Phys. Rev.* **D88** (2013), no. 9 093006, [`arXiv:1306.5695`].

[267] T. Gleisberg, S. Hoeche, F. Krauss, M. Schonherr, S. Schumann, F. Siegert, and J. Winter, *Event generation with SHERPA 1.1*, *JHEP* **02** (2009) 007, [`arXiv:0811.4622`].

[268] H.-L. Lai, M. Guzzi, J. Huston, Z. Li, P. M. Nadolsky, J. Pumplin, and C. P. Yuan, *New parton distributions for collider physics*, *Phys. Rev.* **D82** (2010) 074024, [`arXiv:1007.2241`].

[269] **LHC Higgs Cross Section Working Group** Collaboration, S. Dittmaier et al., *Handbook of LHC Higgs Cross Sections: 1. Inclusive Observables*, `arXiv:1101.0593`.

[270] M. Cacciari, G. P. Salam, and G. Soyez, *The Anti-k(t) jet clustering algorithm*, *JHEP* **04** (2008) 063, [`arXiv:0802.1189`].

[271] D. Curtin, R. Essig, and B. Shuve, *Boosted Multijet Resonances and New Color-Flow Variables*, *Phys. Rev.* **D88** (2013) 034019, [`arXiv:1210.5523`].

[272] D. Curtin, P. Meade, and P.-J. Tien, *Natural SUSY in Plain Sight*, *Phys. Rev.* **D90** (2014), no. 11 115012, [`arXiv:1406.0848`].

[273] M. Cacciari, G. P. Salam, and G. Soyez, *FastJet User Manual*, *Eur. Phys. J.* **C72** (2012) 1896, [`arXiv:1111.6097`].

[274] **ATLAS** Collaboration, T. A. collaboration, *Calibration of b-tagging using dileptonic top pair events in a combinatorial likelihood approach with the ATLAS experiment*, .

[275] **ATLAS** Collaboration, T. A. collaboration, *Performance of shower deconstruction in ATLAS*, .

[276] **ATLAS** Collaboration, *Measurement of the b-tag Efficiency in a Sample of Jets Containing Muons with 5 fb1 of Data from the ATLAS Detector*, .

[277] **ATLAS** Collaboration, G. Aad et al., *Search for Higgs boson decays to a photon and a Z boson in pp collisions at $\sqrt{s}$=7 and 8 TeV with the ATLAS detector*, Phys. Lett. **B732** (2014) 8–27, [`arXiv:1402.3051`].

[278] M. Dasgupta, F. Dreyer, G. P. Salam, and G. Soyez, *Small-radius jets to all orders in QCD*, JHEP **04** (2015) 039, [`arXiv:1411.5182`].

[279] J. Thaler and K. Van Tilburg, *Identifying Boosted Objects with N-subjettiness*, JHEP **03** (2011) 015, [`arXiv:1011.2268`].

[280] J. M. Butterworth, A. R. Davison, M. Rubin, and G. P. Salam, *Jet substructure as a new Higgs search channel at the LHC*, Phys.Rev.Lett. **100** (2008) 242001, [`arXiv:0802.2470`].

[281] T. Plehn, G. P. Salam, and M. Spannowsky, *Fat Jets for a Light Higgs*, Phys.Rev.Lett. **104** (2010) 111801, [`arXiv:0910.5472`].

[282] D. Krohn, J. Thaler, and L.-T. Wang, *Jet Trimming*, JHEP **02** (2010) 084, [`arXiv:0912.1342`].

[283] G. D. Kribs, A. Martin, T. S. Roy, and M. Spannowsky, *Discovering the Higgs Boson in New Physics Events using Jet Substructure*, Phys. Rev. **D81** (2010) 111501, [`arXiv:0912.4731`].

[284] J. Thaler and L.-T. Wang, *Strategies to Identify Boosted Tops*, JHEP **07** (2008) 092, [`arXiv:0806.0023`].

[285] D. E. Kaplan, K. Rehermann, M. D. Schwartz, and B. Tweedie, *Top Tagging: A Method for Identifying Boosted Hadronically Decaying Top Quarks*, Phys. Rev. Lett. **101** (2008) 142001, [`arXiv:0806.0848`].

[286] J. M. Butterworth, A. R. Davison, M. Rubin, and G. P. Salam, *Jet substructure as a new Higgs search channel at the LHC*, AIP Conf. Proc. **1078** (2009) 189–191, [`arXiv:0809.2530`].

[287] Y. L. Dokshitzer, G. D. Leder, S. Moretti, and B. R. Webber, *Better jet clustering algorithms*, JHEP **08** (1997) 001, [`hep-ph/9707323`].

[288] M. Wobisch and T. Wengler, *Hadronization corrections to jet cross-sections in deep inelastic scattering*, in *Monte Carlo generators for HERA physics. Proceedings, Workshop, Hamburg, Germany, 1998-1999*, 1998. `hep-ph/9907280`.

[289] T. A. collaboration, *Search for resonances decaying to photon pairs in 3.2 fb$^{-1}$ of pp collisions at $\sqrt{s} = 13$ TeV with the ATLAS detector*, .

[290] **CMS** Collaboration, C. Collaboration, *Search for new physics in high mass diphoton events in proton-proton collisions at 13TeV*, .

[291] L. Landau, *On the angular momentum of a two-photon system, Dokl.Akad.Nauk Ser.Fiz.* **60** (1948) 207–209.

[292] C.-N. Yang, *Selection Rules for the Dematerialization of a Particle Into Two Photons, Phys.Rev.* **77** (1950) 242–245.

[293] S. D. McDermott, P. Meade, and H. Ramani, *Singlet Scalar Resonances and the Diphoton Excess*, `arXiv:1512.0532`.

[294] W. Chao, *Symmetries Behind the 750 GeV Diphoton Excess*, `arXiv:1512.0629`.

[295] P. S. B. Dev, R. N. Mohapatra, and Y. Zhang, *Quark Seesaw, Vectorlike Fermions and Diphoton Excess*, `arXiv:1512.0850`.

[296] C. W. Murphy, *Vector Leptoquarks and the 750 GeV Diphoton Resonance at the LHC*, `arXiv:1512.0697`.

[297] J. Ellis, S. A. R. Ellis, J. Quevillon, V. Sanz, and T. You, *On the Interpretation of a Possible $\sim$ 750 GeV Particle Decaying into $\gamma\gamma$*, `arXiv:1512.0532`.

[298] F. Wang, W. Wang, L. Wu, J. M. Yang, and M. Zhang, *Interpreting 750 GeV Diphoton Resonance in the NMSSM with Vector-like Particles*, `arXiv:1512.0843`.

[299] J. Kawamura and Y. Omura, *Diphoton excess at 750 GeV and LHC constraints in models with vector-like particles*, `arXiv:1601.0739`.

[300] M. J. Dolan, J. L. Hewett, M. Krämer, and T. G. Rizzo, *Simplified Models for Higgs Physics: Singlet Scalar and Vector-like Quark Phenomenology*, `arXiv:1601.0720`.

[301] B. Dutta, Y. Gao, T. Ghosh, I. Gogoladze, T. Li, Q. Shafi, and J. W. Walker, *Diphoton Excess in Consistent Supersymmetric SU(5) Models with Vector-like Particles*, `arXiv:1601.0086`.

[302] S.-F. Ge, H.-J. He, J. Ren, and Z.-Z. Xianyu, *Realizing Dark Matter and Higgs Inflation in Light of LHC Diphoton Excess*, `arXiv:1602.0180`.

[303] A. Alves, A. G. Dias, and K. Sinha, *The 750 GeV S-cion: Where else should we look for it?*, `arXiv:1512.0609`.

[304] D. Buttazzo, A. Greljo, and D. Marzocca, *Knocking on New Physics' door with a Scalar Resonance*, `arXiv:1512.0492`.

[305] R. Ding, L. Huang, T. Li, and B. Zhu, *Interpreting 750 GeV Diphoton Excess with R-parity Violation Supersymmetry*, `arXiv:1512.0656`.

[306] F. P. Huang, C. S. Li, Z. L. Liu, and Y. Wang, *750 GeV Diphoton Excess from Cascade Decay*, `arXiv:1512.0673`.

[307] L. Berthier, J. M. Cline, W. Shepherd, and M. Trott, *Effective interpretations of a diphoton excess*, `arXiv:1512.0679`.

[308] C. Cai, Z.-H. Yu, and H.-H. Zhang, *The 750 GeV diphoton resonance as a singlet scalar in an extra dimensional model*, `arXiv:1512.0844`.

[309] M. Son and A. Urbano, *A new scalar resonance at 750 GeV: Towards a proof of concept in favor of strongly interacting theories*, `arXiv:1512.0830`.

[310] K. Cheung, P. Ko, J. S. Lee, J. Park, and P.-Y. Tseng, *A Higgcision study on the 750 GeV Di-photon Resonance and 125 GeV SM Higgs boson with the Higgs-Singlet Mixing*, `arXiv:1512.0785`.

[311] M. Badziak, *Interpreting the 750 GeV diphoton excess in minimal extensions of Two-Higgs-Doublet models*, `arXiv:1512.0749`.

[312] X.-F. Han and L. Wang, *Implication of the 750 GeV diphoton resonance on two-Higgs-doublet model and its extensions with Higgs field*, *Phys. Rev.* **D93** (2016), no. 5 055027, [`arXiv:1512.0658`].

[313] S. Moretti and K. Yagyu, *The 750 GeV diphoton excess and its explanation in 2-Higgs Doublet Models with a real inert scalar multiplet*, `arXiv:1512.0746`.

[314] W.-C. Huang, Y.-L. S. Tsai, and T.-C. Yuan, *Gauged Two Higgs Doublet Model confronts the LHC 750 GeV di-photon anomaly*, `arXiv:1512.0726`.

[315] I. Chakraborty and A. Kundu, *Diphoton excess at 750 GeV: Singlet scalars confront triviality*, `arXiv:1512.0650`.

[316] H. Han, S. Wang, and S. Zheng, *Scalar Explanation of Diphoton Excess at LHC*, arXiv:1512.0656.

[317] S. Ghosh, A. Kundu, and S. Ray, *On the potential of a singlet scalar enhanced Standard Model*, arXiv:1512.0578.

[318] S. Kanemura, N. Machida, S. Odori, and T. Shindou, *Diphoton excess at 750 GeV in an extended scalar sector*, arXiv:1512.0905.

[319] C.-W. Chiang, M. Ibe, and T. T. Yanagida, *Revisiting Scalar Quark Hidden Sector in Light of 750-GeV Diphoton Resonance*, arXiv:1512.0889.

[320] A. Kobakhidze, F. Wang, L. Wu, J. M. Yang, and M. Zhang, *LHC 750 GeV diphoton resonance explained as a heavy scalar in top-seesaw model*, arXiv:1512.0558.

[321] W. Altmannshofer, J. Galloway, S. Gori, A. L. Kagan, A. Martin, and J. Zupan, *On the 750 GeV di-photon excess*, arXiv:1512.0761.

[322] A. Ahmed, B. M. Dillon, B. Grzadkowski, J. F. Gunion, and Y. Jiang, *Higgs-radion interpretation of 750 GeV di-photon excess at the LHC*, arXiv:1512.0577.

[323] A. Falkowski, O. Slone, and T. Volansky, *Phenomenology of a 750 GeV Singlet*, *JHEP* **02** (2016) 152, [arXiv:1512.0577].

[324] P. Agrawal, J. Fan, B. Heidenreich, M. Reece, and M. Strassler, *Experimental Considerations Motivated by the Diphoton Excess at the LHC*, arXiv:1512.0577.

[325] B. Dasgupta, J. Kopp, and P. Schwaller, *Photons, Photon Jets and Dark Photons at 750 GeV and Beyond*, arXiv:1602.0469.

[326] P. Draper and D. McKeen, *Diphotons from Tetraphotons in the Decay of a 125 GeV Higgs at the LHC*, *Phys.Rev.* **D85** (2012) 115023, [arXiv:1204.1061].

[327] X.-J. Bi, R. Ding, Y. Fan, L. Huang, C. Li, T. Li, S. Raza, X.-C. Wang, and B. Zhu, *A Promising Interpretation of Diphoton Resonance at 750 GeV*, arXiv:1512.0849.

[328] C. Boehm, T. A. Ensslin, and J. Silk, *Can Annihilating dark matter be lighter than a few GeVs?*, *J. Phys.* **G30** (2004) 279–286, [astro-ph/0208458].

[329] M. Pospelov, A. Ritz, and M. B. Voloshin, *Secluded WIMP Dark Matter*, *Phys.Lett.* **B662** (2008) 53–61, [arXiv:0711.4866].

[330] J. Chang, K. Cheung, and C.-T. Lu, *Interpreting the 750 GeV Di-photon Resonance using photon-jets in Hidden-Valley-like models*, `arXiv:1512.0667`.

[331] S. Chang, *A Simple U(1) Gauge Theory Explanation of the Diphoton Excess*, `arXiv:1512.0642`.

[332] L. Bian, N. Chen, D. Liu, and J. Shu, *A hidden confining world on the 750 GeV diphoton excess*, `arXiv:1512.0575`.

[333] S. Knapen, T. Melia, M. Papucci, and K. Zurek, *Rays of light from the LHC*, `arXiv:1512.0492`.

[334] U. K. Dey, S. Mohanty, and G. Tomar, *750 GeV resonance in the Dark Left-Right Model*, `arXiv:1512.0721`.

[335] H. Davoudiasl and C. Zhang, *A 750 GeV Messenger of Dark Conformal Symmetry Breaking*, `arXiv:1512.0767`.

[336] K. Das and S. K. Rai, *The 750 GeV Diphoton excess in a U(1) hidden symmetry model*, `arXiv:1512.0778`.

[337] K. Kaneta, S. Kang, and H.-S. Lee, *Diphoton excess at the LHC Run 2 and its implications for a new heavy gauge boson*, `arXiv:1512.0912`.

[338] Y. Jiang, Y.-Y. Li, and T. Liu, *750 GeV Resonance in the Gauged $U(1)'$-Extended MSSM*, `arXiv:1512.0912`.

[339] J.-H. Yu, *Hidden Gauged U(1) Model: Unifying Scotogenic Neutrino and Flavor Dark Matter*, `arXiv:1601.0260`.

[340] H. An, C. Cheung, and Y. Zhang, *Broad Diphotons from Narrow States*, `arXiv:1512.0837`.

[341] **HPS** Collaboration, S. Stepanyan, *Heavy photon search experiment at JLAB, AIP Conf.Proc.* **1563** (2013) 155–158.

[342] S. Alekhin et al., *A facility to Search for Hidden Particles at the CERN SPS: the SHiP physics case*, `arXiv:1504.0485`.

[343] P. Ilten, J. Thaler, M. Williams, and W. Xue, *Dark photons from charm mesons at LHCb, Phys. Rev.* **D92** (2015), no. 11 115017, [`arXiv:1509.0676`].

[344] C. Boehm, P. Fayet, and J. Silk, *Light and heavy dark matter particles*, *Phys.Rev.* **D69** (2004) 101302, [`hep-ph/0311143`].

[345] T. A. collaboration, *Search for resonances decaying to photon pairs in 3.2 fb$^{-1}$ of pp collisions at $\sqrt{s}$ = 13 TeV with the ATLAS detector*, .

[346] J. F. Gunion, H. E. Haber, G. L. Kane, and S. Dawson, *The Higgs Hunter's Guide*, *Front.Phys.* **80** (2000) 1–448.

[347] N. Toro and I. Yavin, *Multiphotons and photon jets from new heavy vector bosons*, *Phys.Rev.* **D86** (2012) 055005, [`arXiv:1202.6377`].

[348] M. Chala, M. Duerr, F. Kahlhoefer, and K. Schmidt-Hoberg, *Tricking Landau–Yang: How to obtain the diphoton excess from a vector resonance*, *Phys. Lett.* **B755** (2016) 145–149, [`arXiv:1512.0683`].

[349] **The ATLAS Collobration** Collaboration, T. A. Collobration, *Measurements of the photon identification efficiency with the ATLAS detector using 4.9 fb$^{-1}$ of pp collision data collected in 2011*, .

[350] O. Røhne, *Overview of the {ATLAS} insertable b-layer (ibl) project*, *Nuclear Instruments and Methods in Physics Research Section A: Accelerators, Spectrometers, Detectors and Associated Equipment* **731** (2013) 18 – 24. {PIXEL} 2012.

[351] **ATLAS** Collaboration, G. Aad et al., *Expected Performance of the ATLAS Experiment - Detector, Trigger and Physics*, `arXiv:0901.0512`.

[352] **CMS** Collaboration, G. L. Bayatian et al., *CMS physics: Technical design report*, .

[353] **ATLAS** Collaboration, G. Aad et al., *Search for new phenomena in events with a photon and missing transverse momentum in pp collisions at $\sqrt{s} = 8$ TeV with the ATLAS detector*, *Phys. Rev.* **D91** (2015), no. 1 012008, [`arXiv:1411.1559`]. [Erratum: Phys. Rev.D92,no.5,059903(2015)].

[354] J. Balewski, J. Bernauer, J. Bessuille, R. Corliss, R. Cowan, et al., *The DarkLight Experiment: A Precision Search for New Physics at Low Energies*, `arXiv:1412.4717`.

[355] **Belle-II** Collaboration, T. Abe et al., *Belle II Technical Design Report*, `arXiv:1011.0352`.

[356] M. Spira, A. Djouadi, D. Graudenz, and P. M. Zerwas, *Higgs Boson Production at the LHC*, *arXiv* **hep-ph** (Apr, 1995) [`hep-ph/9504378v1`].

145

[357] J. Fleischer, O. V. Tarasov, and V. O. Tarasov, *Analytical Result for the Two-Loop QCD Correction to the Decay $H \to 2\gamma$*, arXiv **hep-ph** (Jan, 2004) [hep-ph/0401090v2].

[358] R. Dermisek and J. F. Gunion, *New constraints on a light CP-odd Higgs boson and related NMSSM Ideal Higgs Scenarios*, arXiv **hep-ph** (Feb, 2010) [arXiv:1002.1971].

[359] Z. Sullivan and E. L. Berger, *Isolated leptons from heavy flavor decays - theory and data*, Phys. Rev. **D82** (2010) 014001, [arXiv:1003.4997].

[360] **CMS** Collaboration, S. Chatrchyan et al., *Search for anomalous production of events with three or more leptons in pp collisions at $\sqrt{(s)} = 8$ TeV*, Phys. Rev. **D90** (2014) 032006, [arXiv:1404.5801].

[361] Z. Sullivan and E. L. Berger, *The Missing heavy flavor backgrounds to Higgs boson production*, Phys. Rev. **D74** (2006) 033008, [hep-ph/0606271].

[362] **CMS** Collaboration, S. Chatrchyan et al., *Search for new physics in events with same-sign dileptons and b-tagged jets in pp collisions at $\sqrt{s} = 7$ TeV*, JHEP **08** (2012) 110, [arXiv:1205.3933].

[363] **CMS** Collaboration, S. Chatrchyan et al., *Search for new physics in events with same-sign dileptons and b jets in pp collisions at $\sqrt{s} = 8$ TeV*, JHEP **03** (2013) 037, [arXiv:1212.6194]. [Erratum: JHEP07,041(2013)].

[364] M. J. Flowerdew, *Electron fake rates and trigger efficiency*, ATLAS SM meeting 2007-03-22.